Modelling particle acceleration

in core-collapse supernova remnants inside circumstellar wind-blown bubbles

---

Samata Das

Univ.-Diss.

zur Erlangung des akademischen Grades
"doctor rerum naturalium"
(Dr. rer. nat.)
in der Wissenschaftsdisziplin "Astroteilchenphysik"

eingereicht an der
Mathematisch-Naturwissenschaftlichen Fakultät
Institut für Physik und Astronomie
der Universität Potsdam

Hauptbetreuer*in: Prof. Dr. Martin Pohl
Betreuer*innen: Prof. Dr. Huirong Yan

Gutachter*innen: Prof. Dr. Martin Pohl
Prof. Miroslav Filipovic
Prof. Alexandre Marcowith

Published online on the
Publication Server of the University of Potsdam:
https://doi.org/10.25932/publishup-61414
https://nbn-resolving.org/urn:nbn:de:kobv:517-opus4-614140

Dissertation

“Modelling particle acceleration in core-collapse supernova remnants inside circumstellar wind-blown bubbles”

Author:
Samata Das
Matriculation ID: 800900

Supervisors:
Prof. Dr. Martin Pohl
Prof. Dr. Huirong Yan
Mentor:
Dr. Andrew Taylor

zur Erlangung des akademischen Grades
"doctor rerum naturalium"
(Dr. rer. nat.)
in der Wissenschaftsdisziplin "Astroteilchenphysik"

eingereicht an der
Mathematisch-Naturwissenschaftlichen Fakultät
Institut für Physik und Astronomie
der Universität Potsdam

June 5, 2023

Dedicated to my adorable grandmother...

Declaration of Authorship

I, **Samata Das**, declare that this dissertation I submitted in fulfilment of the requirements for the degree of "Doctor rerum naturalium" (Dr. rer. nat.), adhere to the following code of academic conduct in accordance with the plagiarism policy of University of Potsdam, published on October 20, 2010:

- This manuscript is written by me, independently and without the use of aids or sources other than those specified here.
- All content that has been taken or has been informed by other published or unpublished work has been properly stated and referenced.
- The previously submitted parts of this manuscript for a degree or any other qualification at this University or any other institution have been clearly stated.

Samata Das

Institut für Physik und Astronomie

der Universität Potsdam

Place: Potsdam, Germany

Date: 05. 06. 2023

Abstract

Supernova remnants are considered to be the primary sources of galactic cosmic rays. These cosmic rays are assumed to be accelerated by the diffusive shock acceleration mechanism, specifically at shocks in the remnants. Particularly in the core-collapse scenario, these supernova remnant shocks expand inside the wind-blown bubbles structured by massive progenitors during their lifetime. Therefore, the complex environment of wind bubbles can influence the particle acceleration and radiation from the remnants. Further, the evolution of massive stars depends on their Zero Age Main Sequence mass, rotation, and metallicity. Consequently, the structures of the wind bubbles generated during the lifetime of massive stars should be considerably different. Hence, the particle acceleration in the core-collapse supernova remnants should vary, not only from the remnants evolving in the uniform environment but also from one another, depending on their progenitor stars.

A core-collapse supernova remnant with a very massive 60 $M_{\odot}$ progenitor star has been considered to study the particle acceleration at the shock considering Bohm-like diffusion. This dissertation demonstrates the modification in particle acceleration and radiation while the remnant propagates through different regions of the wind bubble by impacts from the profiles of gas density, the temperature of the bubble and the magnetic field structure. Subsequently, in this thesis, I discuss the impacts of the non-identical ambient environment of core-collapse supernova remnants on particle spectra and the non-thermal emissions, considering 20 $M_{\odot}$ and 60 $M\odot$ massive progenitors having different evolutionary tracks. Additionally, I also analyse the effect of cosmic ray streaming instabilities on particle spectra.

To model the particle acceleration in the remnants, I have performed simulations in one-dimensional spherical symmetry using *RATPaC* code. The transport equation for cosmic rays and magnetic turbulence in test-particle approximation, along with the induction equation for the evolution of the large-scale magnetic field, have been solved simultaneously with the hydrodynamic equations for the expansion of remnants inside the pre-supernova circumstellar medium.

The results from simulations describe that the spectra of accelerated particles in supernova remnants are regulated by density fluctuations, temperature variations, the large-scale magnetic field configuration and scattering turbulence. Although the diffusive shock acceleration mechanism at supernova remnant shock predicts the spectral index of 2 for the accelerated non-thermal particles, I have obtained the particle spectra that deviate from this prediction, in the core-collapse scenario. I have found that the particle spectral index reaches 2.5 for the supernova remnant with 60 $M_{\odot}$ progenitor when the remnant resides inside the shocked wind region of the wind bubble, and this softness persists at later evolutionary stages even with Bohm-like diffusion for accelerated particles. However, the supernova remnant with 20 $M_{\odot}$ progenitor does not demonstrate persistent softness in particle spectra from the influence of the hydrodynamics of the corresponding wind bubble. At later stages of evolution, the particle spectra illustrate softness at higher energies for

both remnants as the consequence of the escape of high-energy particles from the remnants while considering the cosmic ray streaming instabilities. Finally, I have probed the emission morphology of remnants that varies depending on the progenitors, particularly in earlier evolutionary stages. This dissertation provides insight into different core-collapse remnants expanding inside wind bubbles, for instance, the calculated gamma-ray spectral index from the supernova remnant with 60 $M_{\odot}$ progenitor at later evolutionary stages is consistent with that of the observed supernova remnants expanding in dense molecular clouds.

Zusammenfassung

Supernova-Überreste gelten als die Hauptquellen der galaktischen kosmischen Strahlung. Diese kosmische Strahlung wird vermutlich durch den Mechanismus der diffusiven Schockbeschleunigung beschleunigt, insbesondere durch Schocks in den Überresten. Insbesondere im Szenario des Kernkollapses werden diese Supernova-Überreste innerhalb der windgeblasenen Blasen aus, die von massiven Progenitoren während ihrer Lebenszeit. Daher kann die komplexe Umgebung der Windblasen die Teilchenbeschleunigung und die Strahlung der Überreste beeinflussen. Außerdem hängt die Entwicklung von massereichen Sternen von ihrer Masse, Rotation und Metallizität in der Nullzeit der Hauptreihe ab. Folglich sollten die Strukturen der Windblasen, die während der Lebensdauer massereicher Sterne erzeugt werden, sehr unterschiedlich sein. Folglich sollte die Teilchenbeschleunigung in den Kernkollaps Supernovaüberresten nicht nur von den Überresten unterscheiden, die sich in einer einheitlichen Umgebung, sondern auch voneinander, je nach ihren Vorgängersternen.

Ein Kernkollaps-Supernova-Überrest mit einem sehr massereichen 60 $M_\odot$ Vorläuferstern wurde betrachtet, um die Teilchenbeschleunigung am Schock unter Berücksichtigung der Bohm-ähnlichen Diffusion zu untersuchen. Diese Dissertation zeigt die Veränderung der Teilchenbeschleunigung und der Strahlung, während sich der Überrest durch verschiedene Regionen der Windblase ausbreitet, anhand der Profile der Gasdichte, der Temperatur der Blase und der Magnetfeldstruktur. Anschließend diskutiere ich in dieser Arbeit die Auswirkungen der nicht-identischen Umgebung von Supernova-Überresten auf die Teilchenspektren und die nicht-thermischen Emissionen unter Berücksichtigung von 20 $M_\odot$ und 60 $M_\odot$ massiven Vorläufern mit unterschiedlichen Entwicklungspfaden. Darüber hinaus analysiere ich auch die Auswirkungen von Instabilitäten der kosmischen Strahlung auf die Teilchenspektren.

Um die Teilchenbeschleunigung in den Überresten zu modellieren, habe ich Simulationen in eindimensionaler dimensionalen sphärischen Symmetrie mit dem RATPaC-Code durchgeführt. Die Transportgleichung für kosmische Strahlung und die magnetische Turbulenz in der Testteilchen-Näherung, zusammen mit der Induktionsgleichung Induktionsgleichung für die Entwicklung des großräumigen Magnetfeldes, wurden gleichzeitig mit den hydrodynamischen Gleichungen für die Expansion der Überreste im zirkumstellaren Medium vor der Supernova zirkumstellaren Mediums gelöst.

Die Ergebnisse der Simulationen beschreiben, dass die Spektren der beschleunigten Teilchen in Supernovaüberresten durch Dichtefluktuationen, Temperaturschwankungen, die großräumige Magnetfeldkonfiguration und Streuturbulenzen reguliert werden. Obwohl der Mechanismus der diffusiven Schockbeschleunigung im Supernova-Überrest einen Spektralindex von 2 für die beschleunigten nicht-thermischen Teilchen vorhersagt, habe ich im Szenario des Kernkollapses Teilchenspektren erhalten, die von dieser Vorhersage abweichen. Ich habe herausgefunden, dass der Spektralindex der Teilchen für den Supernova-Überrest mit einem 60 $M_\odot$ Vorläufer 2,5 erreicht, wenn sich der Überrest in der geschockten

Windregion der Windblase befindet, und diese Schwäche bleibt auch in späteren Entwicklungsstadien bestehen, selbst bei einer Bohm-ähnlichen Diffusion für beschleunigte Teilchen. Der Supernova-Überrest mit 20 $M_\odot$ Vorläufer zeigt jedoch keine anhaltende Weichheit in Teilchenspektren durch den Einfluss der Hydrodynamik der entsprechenden Windblase. In späteren Entwicklungsstadien zeigen die Teilchenspektren für beide Überreste eine Weichheit bei höheren Energien als Folge des Entweichens hochenergetischer Teilchen aus den Überresten unter Berücksichtigung der Instabilitäten des kosmischen Strahlenstroms. Schließlich habe ich die Emissionsmorphologie der Überreste untersucht, die je nach den Vorläufern variiert, insbesondere in früheren Entwicklungsstadien. Diese Dissertation gibt Aufschluss über verschiedene Kernkollapsüberreste, die sich in Windblasen ausdehnen. So stimmt beispielsweise der berechnete Gammastrahlen-Spektralindex des Supernova-Überrests mit 60 $M_\odot$ Vorläufer in späteren Entwicklungsstadien mit dem der beobachteten Supernova-Überreste überein, die sich in dichten Molekülwolken ausdehnen.

Acknowledgements

I would like to express my sincere gratitude to the following people, without whom I would not have been able to complete this dissertation.
Firstly, I am very thankful to my PhD supervisor Prof. Martin Pohl, whose guidance, thoughtful questions, and insight into the subject steered me through this doctoral study. I am also grateful to him for providing me with the opportunity of carrying out research in the Theoretical Astroparticle physics group at Deutsche Elektronen-Synchrotron DESY, Zeuthen and Institute for Physics and Astronomy in the University of Potsdam.
Secondly, lots of thanks to Dr. Andrew Taylor for his comments about my research work during my PhD committee meetings and also for refereeing my papers internally.
I am grateful to Dr. Robert Brose, not only because he instructed me on the *RATPaC* but also for his enthusiasm and willingness to assist throughout my research with great optimism. I am also thankful to him for the proofreading and valuable remarks for the improvement of this dissertation.
Further, I am very thankful to Dr. Iurii Sushch for his critical comments and questions during the research discussions, which helped me to improve my work.
I acknowledge Dr. Dominique M.-A. Meyer for his efforts to produce data which are essential to initialise my work.
I would also like to acknowledge reviewers Prof. Alexandre Marcowith and Prof. Miroslav Filipovic, as well as the chairman and members of the doctoral examination committee.
Last but not least, I want to express my gratitude to my parents, Sipra and Gour Chandra Das, my best friend Minnie, and my aunts Uma Singh and Rita Chakraborty from the bottom of my heart for their continuous encouragement, enormous support and faith in me all time. Further, I am greatly indebted to my grandparents as without their blessings I would not have made it.

List of publications

Peer-reviewed publications:

- Samata Das, Robert Brose, Dominique M. A. Meyer, Martin Pohl, Iurii Sushch, and Pavlo Plotko. Spectral softening in core-collapse supernova remnant expanding inside wind-blown bubble., 661:A128, May 2022. doi: 10.1051/0004- 6361/202142747*
- Sushch, I., Brose, R., Pohl, M., Plotko, P., & Das, S. 2022, ApJ, 926, 140
- Bhatt, M., Sushch, I., Pohl, M., et al. 2020, Astroparticle Physics,123, 102490

Submitted article:

- Samata Das, Robert Brose, Martin Pohl, Dominique M. A. Meyer, and Iurii Sushch. "Particle acceleration, escape and non-thermal emission from core-collapse supernovae inside non-identical wind-blown bubbles"-submitted in A&A *

* These projects are the parts of this thesis.

List of abbreviations

CR	cosmic ray
CRs	cosmic rays
SNR	supernova remnant
SNRs	supernova remnants
Cas A	Cassiopeia A
DSA	Diffusive shock acceleration
ISM	interstellar medium
ZAMS	zero age main sequence
PNS	proto-neutron star
CSM	circumstellar medium
MS	Main-sequence
H-R	Hertzsprung-Russel
RSG	Red supergiant
BSG	Blue supergiant
WR	Wolf-Rayet
LBV	Luminous Blue Variable
PIC	Particle-in-cell
HD	hydrodynamic
MHD	magnetohydrodynamic
MPI	Message Passing Interface
RATPaC	Radiation Acceleration Transport Parallel Code
WENO3	3^{rd}-Weighted-essentially-non-oscillatory scheme
HLL	Harten-Lax-Van Leer approximate Riemann Solver
RK	Runge-Kutta method
HLLC	Harten-Lax-Van Leer approximate Riemann Solver that restores with the middle contact discontinuity
CFL	Courant-Friedrich-Lewy
MPI	Message Passing Interface
E-BOSS	Extensive stellar Bow Shock Survey
CMB	cosmic microwave background

GZK Greisen-Zatsepin-Kuzmin

VFP Vlasov-Fokker-Planck

Contents

List of Figures

List of Tables

1 Introduction

The journey towards the discovery of cosmic rays (CRs) [1] started in 1785, from the quest to explain the spontaneous discharge of the closed and isolated torsion balance electrometer, illustrated in Figure 1.0.1. Although C.A. de Coulomb presumed the reason for this discharge could be the dust particles in the ambient air, this problem remained speculative for over a hundred years. In 1900, J Elster, H Geitel, and CTR Wilson suggested that radioactive substances in the atmosphere could be responsible for the conductivity of the air and CTR Wilson first mentioned this emanation as ". . . radiation from sources outside our atmosphere" [2]. Later on, Franz Linke first investigated this penetrating radiation with balloon flights, followed by several studies. Finally, in 1912 a series of successful investigations by V. F. Hess with balloon flights confirmed that [3]: ". . . radiation of high penetration power hits our atmosphere from top" and this radiation is known as CRs at the present time. Even though CRs are extensively studied since their discovery, the main sources are still not distinctly identified. However, the supernova remnants (SNRs) are considered to be the most promising sources of galactic CRs.

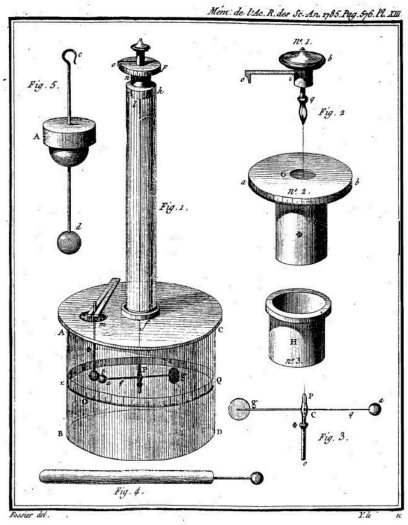

Figure 1.0.1: Torsion balance electrometer Image credit: *Coulomb - First Memoir On Electricity and Magnetism (1785)*

In 1934, Baade and Zwicky [4, 5] postulated the existence of "super-novae" and proposed their connection with the production of CRs. Later on, as an outcome of the advancement in radio astronomy, direct evidence of radio emission was detected in SNRs, Cassiopeia A (Cas A), followed by the observations of the Crab Nebula, Tycho's, Kepler's supernovae and so on, as the radio sources [6]. Eventually, the synchrotron radiation was suggested to explain the radio emission from SNRs [7, 8] and also Fermi proposed the well-known Fermi acceleration mechanism of energetic particles [9] which is acceleration of charged particles through the stochastic interaction with moving magnetic clouds. However, this original form of the Fermi acceleration process was not efficient enough to explain the observed flux of cosmic rays. Then, on the basis of Fermi's idea, it was proposed that supernova remnant (SNR) shock waves can efficiently accelerate particles to very high energy [10–12] and this process is called Diffusive shock acceleration (DSA) which currently the widely accepted model of particle acceleration in SNRs.

Supernovae, one of the most energetic systems of our galaxy, can be classified generally into two categories based on the explosion processes, thermonuclear supernovae and core-collapse supernovae. Thermonuclear supernova is thought to arise from the white dwarf progenitor whether the other one

[1]: Walter et al. (2012), 'Early history of cosmic particle physics'

[2]: Wilson (1901), 'On the Ionisation of Atmospheric Air'

[3]: Hess (1912), 'Über Beobachtungen der durchdringenden Strahlung bei sieben Freiballonfahrten'

[4]: Baade et al. (1934), 'On Super-Novae'

[5]: Baade et al. (1934), 'Cosmic Rays from Super-Novae'

[6]: Dubner et al. (2015), 'Radio emission from Supernova Remnants'

[7]: Alfvén et al. (1950), 'Cosmic Radiation and Radio Stars'

[8]: Kiepenheuer (1950), 'Cosmic Rays as the Source of General Galactic Radio Emission'

[9]: Fermi (1949), 'On the Origin of the Cosmic Radiation'

[10]: Bell (1978), 'The acceleration of cosmic rays in shock fronts - I.'

[11]: Bell (1978), 'The acceleration of cosmic rays in shock fronts - II.'

[12]: Blandford et al. (1980), 'Supernova shock acceleration of cosmic rays in the Galaxy.'

Figure 1.0.2: The bubble nebula, NGC 7635, HST 2016- Located at 2.7kpc, formed by the O-type star BD+60°2522 with stellar mass of $27 \pm 7\, M_{\odot}$ [13] Image credit: *NASA, ESA, Hubble Heritage Team*

[13]: Toalá et al. (2020), 'The Bubble Nebula NGC 7635 - testing the wind-blown bubble theory'

is generated from the explosion of a massive star ($> 8\, M_{\odot}$). The massive progenitors of core-collapse supernovae form wind-blown bubbles during their entire lifespan, for instance, the bubble nebula shown in Figure 1.0.2 and consequently, core-collapse supernovae evolve inside wind bubbles, unlike the thermonuclear supernovae which expand in the pristine interstellar medium (ISM).

The aim of this dissertation is "Modelling particle acceleration in core-collapse supernova remnants inside circumstellar wind-blown bubbles".
The structure of this thesis is as follows: I begin with an introduction to core-collapse supernovae in Chapter 2. An overview of supernovae classification and a synopsis of the core-collapse process are provided. Then I discuss briefly the stellar evolution followed by the detailed structure of stellar wind-blown bubbles. Further, I mention the structure of the supernova remnant.

Chapter 3 describes briefly the SNR paradigm of galactic CRs along with the particle acceleration by the Fermi mechanism. Further, I discuss the different non-thermal emissions from the SNR together with the observational signatures.

Chapter 4 reviews the numerical methods to probe the particle acceleration at the SNR shock, followed by the overview of the numerical simulation method which is applied in this dissertation. Further, I discuss the implemented changes in the pre-existing code to achieve the aim of this thesis.

Chapter 5 discuss the particle acceleration in the core-collapse SNR by applying the Bohm-like diffusion coefficient for particles. This chapter elaborately demonstrates the effect of the hydrodynamics of stellar wind bubbles on the spectral shape of accelerated particles at the SNR shock. Moreover, the impact of the SNR expansion inside the wind bubble on the resulting emission from the remnant is analysed.

Chapter 6 demonstrates the change in particle acceleration and emissions if SNRs evolve through non-identical wind bubbles shaped by different progenitors. Further, in this Chapter, the time-dependent diffusion coefficient is taken into account which is derived from the self-consistent treatment of scattering magnetic turbulence. Hence, the impact of this time-dependent diffusion coefficient in the acceleration of the particles in comparison to the simplified Bohm-like scenario is explored.

In Chapter 7, I provide an overview of this dissertation along with a discussion about future possibilities in this regard.

Core-collapse supernovae and their remnants

2

The field of core-collapse supernovae starts to develop with the breakthrough of Baade and Zwicky in 1934 [5] that the collapse of an ordinary star to a neutron star energises a supernova. This remarkable finding is followed by the discovery of neutrons by Chadwick [14] and the conjecture of neutron stars by Landau in 1932 [15]. The theory of supernovae evolve a long way since the discovery of Baade and Zwicky and a lot of insights is solved, however, some questions still remain undetermined. In this chapter, I begin with the classification of supernovae, and then I provide an overview of the core-collapse process and stellar evolution. In the end, I discuss stellar wind bubbles along with the formation and evolution of supernova remnants.

2.1 Classification of supernovae

The early days of supernova observations indicated that two types of supernovae exist such as Type I which has no hydrogen lines and Type II which demonstrates strong hydrogen lines. Although this convention of classifying supernovae is still continued, there are different subcategories in both Type I and Type II supernovae based on spectroscopy and the shape of light curves as shown in Figure 2.1.1. Type II supernovae are always formed from core-collapse events while Type I supernovae can be born from thermonuclear explosions as well as core-collapse events. Spectroscopic class Type Ia [16] having Silicon absorption lines are associated with thermonuclear explosions and according to the prediction of the volume-limited Lick Observatory Supernova Search [17] this subcategory includes ~ 24% of all supernovae. The other two subcategories of Type I supernovae, Type Ib and Type Ic, comprising ~ 19% of all supernovae originate from hydrogen-poor core-collapse. Type Ic supernovae are mainly found in the most luminous regions of galaxies which indicates that these supernovae are from very massive progenitors and most interestingly they are also associated with long-duration gamma-ray bursts [18]. Type IIP (plateau) are the most common sub-type of Type II and almost 40% of all supernovae. Red supergiants with hydrogen envelopes are considered to be the progenitors of this sub-type and the progenitor stars are predicted to have $8.5\,M_{\odot} - 16.5\,M_{\odot}$ zero age main sequence (ZAMS) masses [19]. Type IIL (linear) supernovae are characterised by the linear decline of the light curve and they may have yellow supergiant progenitors. Further, Type IIb is the transitional supernovae in which at earlier stages of evolution strong hydrogen lines exist but at

[14]: Chadwick (1932), 'Possible Existence of a Neutron'

[15]: Yakovlev et al. (2013), 'L D Landau and the concept of neutron stars'

[16]: Elias et al. (1985), 'Type I supernovae in the infrared and their use as distance indicators.'

[17]: Li et al. (2011), 'Nearby supernova rates from the Lick Observatory Supernova Search - II. The observed luminosity functions and fractions of supernovae in a complete sample'

[18]: Kelly et al. (2008), 'Long γ-Ray Bursts and Type Ic Core-Collapse Supernovae Have Similar Locations in Hosts'

[19]: Smartt (2009), 'Progenitors of core-collapse supernovae'

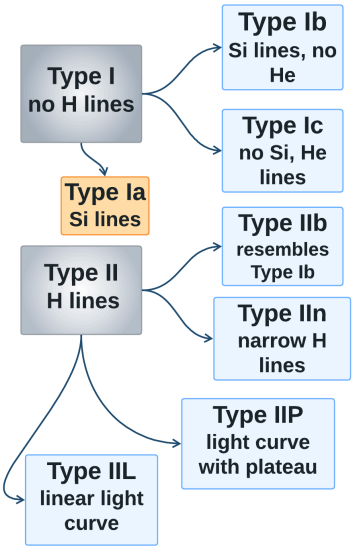

Figure 2.1.1: Classification of supernovae based on spectroscopy and shape of the light curve.
The orange and blue boxes indicate the thermonuclear and core-collapse supernovae respectively. The following abbreviations are taken - hydrogen (H), helium (He), silicon (Si)

later times the hydrogen lines disappear and the supernovae of this sub-type transit to Type Ib. The optical spectrum at the maximum brightness of Cas A suggests that it is a remnant of type IIb supernova [20]. Finally, Type IIn demonstrates narrow hydrogen emission lines and these narrow lines can be interpreted as the slowly-moving material during the interaction of the supernova shock wave with the dense circumstellar material. This observational classification scheme of supernovae has evolved over time since the historical classification by Minkowski [21] from the spectroscopy of 14 observed supernova events. As the observed spectrum of supernovae should carry the signatures of the physical properties of the progenitor, it may be more reasonable to classify supernovae based on the stellar classification [22] in the current age when millions of events are observed.

The discussed classification where the core-collapse events cover a vast observational perspective suggests the diversity of progenitors at pre-supernova stages. Therefore, regardless of the evolutionary tracks of massive stars ($> 8\,M_{\odot}$), they will ultimately end their life through core collapse.

[20]: Krause et al. (2008), 'The cassiopeia A supernova was of type IIb'

[21]: Minkowski (1941), 'Spectra of Supernovae'

[22]: Gal-Yam (2016), 'Observational and Physical Classification of Supernovae'

[23]: Langer (2012), 'Presupernova Evolution of Massive Single and Binary Stars'

[24]: Woosley et al. (2002), 'The evolution and explosion of massive stars'

2.2 Core-collapse mechanism

The life of massive stars ($> 8M_{\odot}$) proceeds through several evolutionary and dynamic phases at the end towards core-collapse supernovae and our understanding of the insight into this mechanism has continually evolved. Although there are different proposals that drive core-collapse explosions, such as neutrino-driven explosion mechanism, magneto-rotational explosion mechanism, acoustic mechanism and so on, the neutrino-driven explosion is the most ubiquitous and well-studied among them. I provide a synopsis of the core-collapse event here along with a schematic, shown in Figure 2.2.1. I would refer the reader studies in [23, 24] for thorough reviews of the evolution of massive stars.

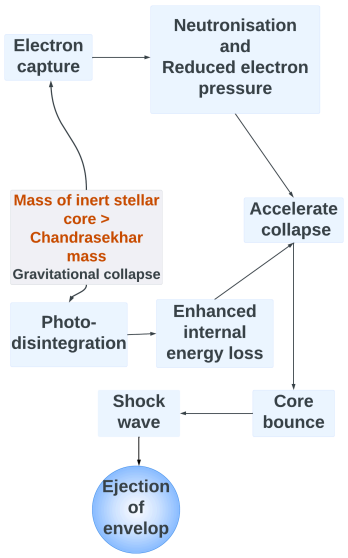

Figure 2.2.1: Schematic of explosion mechanism of core-collapse

1. Collapse of core: A massive star evolves through successive stages of core and shell burning and ultimately reaches the silicon fusion stage which eventually develops an iron core. Until this stage, the star is in the hydrostatic equilibrium where the nuclear fusion stabilises the enormous stellar mass against gravitational collapse. The pressure from ions, electrons, and photons equilibrates the gravitational force. However, after the formation of the iron core, further nuclear fusion is not possible as iron is the most stable atom with maximum nuclear binding energy per nucleon and the core becomes inert. This inert core can still be balanced against gravitational collapse by electron degeneracy pressure if the mass of the core is less than the Chandrasekhar mass ($M_{\rm ch}$) limit and for iron-dominating composition, $M_{\rm ch} \approx (1.3 - 1.7)\,M_{\odot}$. However, gravitational collapse ensues as electrons become relativistic in the high temperature and density ($\geq 10^9\,{\rm gm\,cm^{-3}}$) of the

$M_{\rm ch} \approx 1.44 \left(\frac{Y_e}{0.5}\right)^2 \{1 + \left(\frac{S_e}{\pi Y_e}\right)^2\} M_{\odot}$
$Y_e \Rightarrow$ number of electrons per baryon,
$S_e \Rightarrow$ entropy of electrons in the core.

core and two following processes may start to expedite the contraction of the core under gravity.

Electron capture: At very high-density, free electron captures can be possible and this process leads to "neutronization" of the plasma. This also reduces the support of electron degeneracy pressure in the core.

Electron capture- $p + e^- \rightarrow \nu_e + n$
$p \Rightarrow$ proton, $e^- \Rightarrow$ electron, $\nu_e \Rightarrow$ neutrino, $n \Rightarrow$ neutron

Photo-disintegration: In the very hot core (10^{10} K), highly energetic photons can break heavy nuclei into lighter ones which reduce the internal energy of the gas. Thus, photo-disintegration ultimately accelerates the free-fall collapse of the core by decreasing the pressure of the gas.

Photo-disintegration-
$^{26}Fe + \gamma \rightarrow 13\,^4He + 4n$
$Fe \Rightarrow$ iron, $\gamma \Rightarrow$ photon, $He \Rightarrow$ helium, $n \Rightarrow$ neutron

2. Neutrino trapping and core bounce: The neutrinos, produced by electron capture interact through coherent scattering with the present heavier nuclei in the core, but towards the end of the collapse when the density of the core becomes $> 10^{11}\,\mathrm{gm\,cm^{-3}}$ the core turns into the opaque region for neutrinos, as well as their diffusion velocity becomes smaller than the in-fall velocity of the outer core. Thus, the neutrinos are trapped in the core. This gravitation collapse of the core continues until the core density approaches nuclear density ($\rho_{\mathrm{nuc}} \approx 10^{14}\,\mathrm{gm\,cm^{-3}}$). If the central density exceeds ρ_{nuc}, the inner core becomes repulsive and it bounces back, so-called "core bounce". Further, at this time, a nascent proto-neutron star (PNS) is formed in the centre.

[25]: Raffelt (2007), 'Supernova neutrino observations: What can we learn?'
[26]: Odrzywolek et al. (2007), 'Future neutrino observations of nearby pre-supernova stars before core-collapse'

3. Shock formation and break out: The interaction between the outward-moving inner core and the supersonic inward flow of materials from the outer part of the core generates an outward shock wave. During this shock breaks out into the material of the outer core, the stellar medium becomes transparent for neutrinos and so, the neutrinos do not remain trapped which results in the so-called "neutrino burst". Here, I want to mention that this incidence of neutrino burst was detected from supernova SN 1987A in the Large Magellanic Cloud, several hours before the optical explosion of the supernova [25, 26].

[27]: Burrows (2013), 'Colloquium: Perspectives on core-collapse supernova theory'
[28]: Janka et al. (2016), 'Physics of Core-Collapse Supernovae in Three Dimensions: A Sneak Preview'
[29]: Couch (2017), 'The mechanism(s) of core-collapse supernovae'

Further, This outward shock stalls soon after its formation as the photo-disintegration and neutrino burst cause a considerable energy loss and so, the pressure of the matter behind this shock fails to overcome the ram pressure of the in-falling outer core. Consequently, the shock turns into an accretion shock. The inward flow of the outer core still persists, which feeds an accretion flow on the PNS.

Problem: What re-energises the stalled shock and helps it to move outwards and drives stellar explosion, so-called core-collapse supernovae? Currently, this is still a topic of research [27–29].

[30]: Wilson (1985), 'Supernovae and Post-Collapse Behavior'

4. Revival of shock and explosion: Wilson [30] proposed that neutrinos may play a crucial role in shock revival and introduced "delayed neutrino-heating mechanism". According to this proposal, the shock is revived because a fraction

of neutrinos deposits energy behind the shock front. There is a reference radius called "neutrinosphere" (R_ν), shown in this Figure 2.2.2 at approximately 50 km and at this radius, neutrinos from PNS decouple from matter. Outside "neutrinosphere", neutrinos start to interact with material and transfer energy from the neutrino field to matter. A region called "gain region" is built up behind the shock where neutrino heating is dominated. The heating in this "gain region" is sufficient enough to increase the pressure behind the shock above the ram pressure of the in-falling material and hence, revive the shock. Here, I want to mention that the success of shock revival can depend on the mass of the star as the higher mass accretion rate from the outer core can resist the expansion of the stalled shock. This shock propagates through the stellar plasma until it reaches the stellar surface and after that, the supernova blast wave becomes visible.

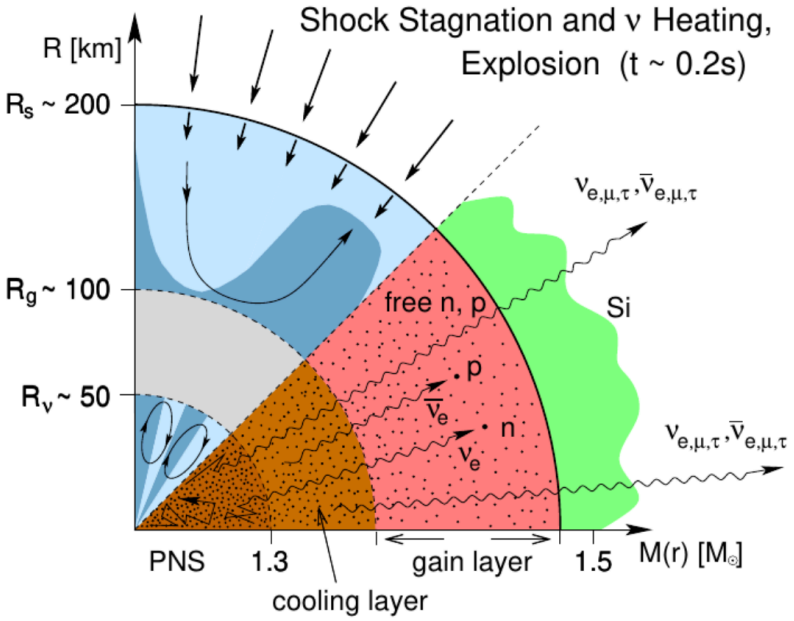

Figure 2.2.2: A snapshot of neutrino-driven core-collapse explosion. Formation of gain layer and deposition of neutrino energy behind the stalled shock, from [31].
R_ν, R_g, R_s are the radius of "neutrinosphere", gain radius and shock radius respectively.

[31]: Janka et al. (2007), 'Theory of core-collapse supernovae'

This supernova blast wave from a core-collapse event propagates inside the ambient medium, shaped by massive stars during their lifetime through the stellar winds. Therefore, the structure of this modified circumstellar medium (CSM) depends on stellar winds from different evolutionary stages. So, it is crucial to understand the properties of stellar winds in different stages of stellar life in order to get a complete picture of the evolution of supernovae. Hence, I provide an outline of stellar evolution at this point.

2.3 Stellar evolution

The evolution of massive stars depends on their ZAMS mass, metallicity and rotation. Metallicity affects the stellar luminosity by regulating opacity inside the star. The stellar

rotation mainly influences the time span of a star's Main-sequence (MS) phase by inducing mixing in the stellar interior. The metallicity- and rotation-dependent stellar evolution is discussed elaborately in [32–34]. In this dissertation, I only

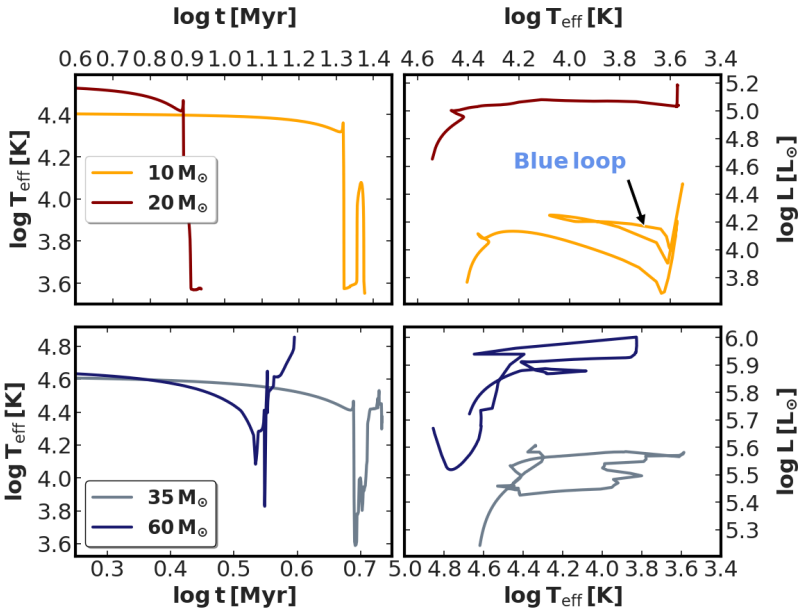

Figure 2.3.1: Evolutionary tracks of massive stars from the ZAMS to the pre-supernova stage considering no stellar rotation and an initial solar metallicity using Geneva stellar models [35, 36] In the left panels, the variations in effective temperature ($T_{\rm eff}$) with the age of stars are shown and in the right panels, Hertzsprung-Russell diagram (H-R) diagram, the change in stellar luminosity (L) with $T_{\rm eff}$ are plotted for stars with different ZAMS masses, indicated in the Figure.

study the core-collapse supernovae which originate from non-rotating massive stars with solar metallicity, hence here I mention the evolutionary tracks of massive stars depending on their ZAMS mass [37].

Stars spend most of their lifespan in the MS stage and during this stage, the luminosity and temperature of a star do not change significantly. For example, in Figure 2.3.1, 10 $M_\odot$ and 20 $M_\odot$ stars stay in MS for 20.5 Myr and 7.5 Myr, respectively and the effective temperature ($T_{\rm eff}$) as well as luminosity (L) remain almost unchanged in this time period. Furthermore, the MS lifetime of a star is its ZAMS mass-dependent. The lower-mass stars evolve slower than more massive ones. For instance, the 10 $M_\odot$ star evolves through this stage for approximately 20.5 Myr whereas 60 $M_\odot$ star stays in MS only for almost 3.2 Myr. In addition to this, the stellar evolutionary tracks illustrated in Hertzsprung-Russel (H-R) diagram, become more complicated with the increasing initial mass of stars. The outline of the evolution of massive stars is as follows,

- Stars with ZAMS mass 8 $M_\odot$ - 20 $M_\odot$ evolve through the Red supergiant (RSG) phase after MS, and then may grow to Blue supergiant (BSG) by forming the "blue loop", characterised by a sharp increase in effective temperature, indicated in the corresponding H-R diagram. Finally, they return to the RSG stage.
- 20 $M_\odot$ - 30 $M_\odot$ stars generally evolve through the RSG stage in post-MS evolution.
- 30 $M_\odot$ - 200 $M_\odot$ stars turn into Wolf-Rayet (WR) stars in pre-supernova stage. Stars with initial mass above 50 $M_\odot$ may grow to the Luminous Blue Variable (LBV) star instead of the RSG star before the WR phase.

$T_{\rm eff}$ $\Rightarrow$ stellar surface temperature assuming star as a spherical black body
$L = 4\pi R^2 \sigma {T_{\rm eff}}^4$
R $\Rightarrow$ stellar radius
σ $\Rightarrow$Stefan-Boltzmann constant

[32]: Hirschi et al. (2008), 'Stellar Evolution at Low Metallicity'
[33]: Meynet et al. (2000), 'Stellar evolution with rotation. 5. Changes in all the outputs of massive star models'
[34]: Sanyal, D. et al. (2017), 'Metallicity dependence of envelope inflation in massive stars'
[35]: Ekström, S. et al. (2012), 'Grids of stellar models with rotation - I. Models from 0.8 to 120 M solar metallicity (Z = 0.014)'
[36]: Yusof et al. (2022), 'Grids of stellar models with rotation VII: models from 0.8 to 300–M– at supersolar metallicity (Z = 0.020)'
[37]: Woosley et al. (1993), 'The evolution of massive stars including mass loss - Presupernova models and explosion'

[38]: Eldridge et al. (2006), 'The circumstellar environment of Wolf-Rayet stars and gamma-ray burst afterglows'

[39]: Geen et al. (2020), 'The geometry and dynamical role of stellar wind bubbles in photoionized H–ii regions'

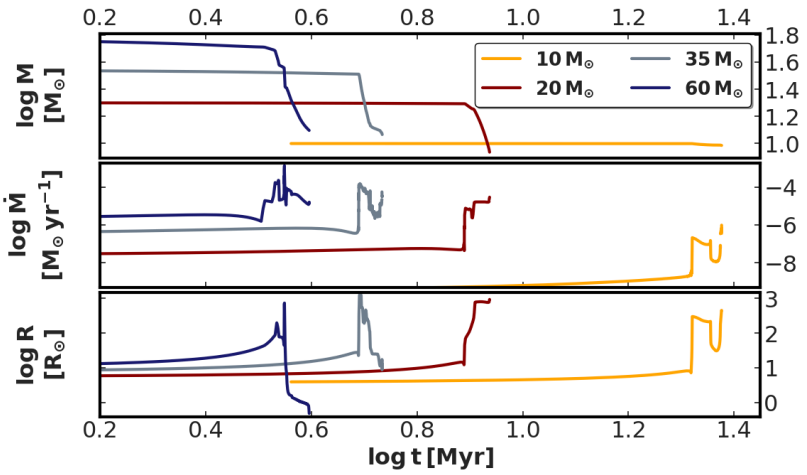

Figure 2.3.2: Evolution of stellar mass (M), mass-loss rate ($\dot{M}$), stellar radius (R) during different stages of evolution for stars with different ZAMS masses, mentioned in the Figure following the evolutionary track referred in Figure 2.3.1

Figure 2.3.2 suggests that during the MS stage, the mass-loss rate and stellar radius are hardly changed. As soon as the stars enter into the RSG phase and LBV phase for 60 $M_\odot$ star, in Figure 2.3.2, the mass-loss rate along with the size of the star increases, approximately around 8 Myr and 3.4 Myr for 20 $M_\odot$ and 60 $M_\odot$ stars, respectively. Later on, during WR phase for very massive stars, the stellar radius drastically decreases. Hence, the velocity of stellar wind, according to Comment 2.3.1 should decrease during the RSG and LBV phases and increase during the WR phase. Further, the wind density ($\rho_{\rm wind}$) related to mass-loss rate ($\dot{M}$), stellar radius, and stellar wind velocity by,

Comment 2.3.1

Stellar wind velocity ($V_{\rm wind}$) should relate to the escape velocity ($V_{\rm esc}$) of materials from the gravitational pull of stars, so $V_{\rm wind} \propto V_{\rm esc}$ [38]. The escape velocity of a luminous star reads, $V_{\rm esc} = \frac{2GM(1-\Gamma)}{R}$
$G \Rightarrow$ Gravitational constant
$\Gamma \Rightarrow$ Eddington factor, a correction factor from radiation pressure on free electrons to the Newtonian gravity [39].

$$\rho_{\rm wind} = \frac{\dot{M}}{4\pi R^2 V_{\rm wind}} \tag{2.3.1}$$

Throughout the lifetime of stars, the properties of the stellar wind like mass-loss rate, stellar wind velocity as well as density of wind vary as shown in Figure 2.3.2. Consequently, these stellar winds from different evolutionary ages of massive stars can structure the CSM complicatedly and also form stellar wind-blown bubbles. The modified CSM during the complete lifetime of the massive stars is discussed elaborately in Chapters 5 and 6.

Comment 2.4.1

The simulated wind bubble from a test run is purposefully shown here to provide the reader with the outline of the stellar wind bubble structure in a very simple scenario where only one stellar wind is involved.

2.4 Stellar wind-blown bubble

[40]: Avedisova (1972), 'Formation of Nebulae by Wolf-Rayet Stars.'
[41]: Weaver et al. (1977), 'Interstellar bubbles. II. Structure and evolution.'

Massive stars lose a significant amount of mass in the form of stellar wind that interacts with the ambient ISM and forms a stellar wind bubble. Analytically, the structure of the bubble was predicted by [40, 41]. Figure 2.4.1 demonstrates (i) the schematic of the wind bubble structure and (ii) a numerically simulated wind bubble formed by a stellar wind shown as a test run (see Comment 2.4.1). When the supersonic stellar wind collides with ambient ISM, a double-shock structure, consisting of an outer shock propagating inside

the ISM, located at R_B in Figure 2.4.1 and a reverse shock, so-called "wind-termination shock" is created. The wind-termination shock, denoted by R_{WT} in Figure 2.4.1 separates

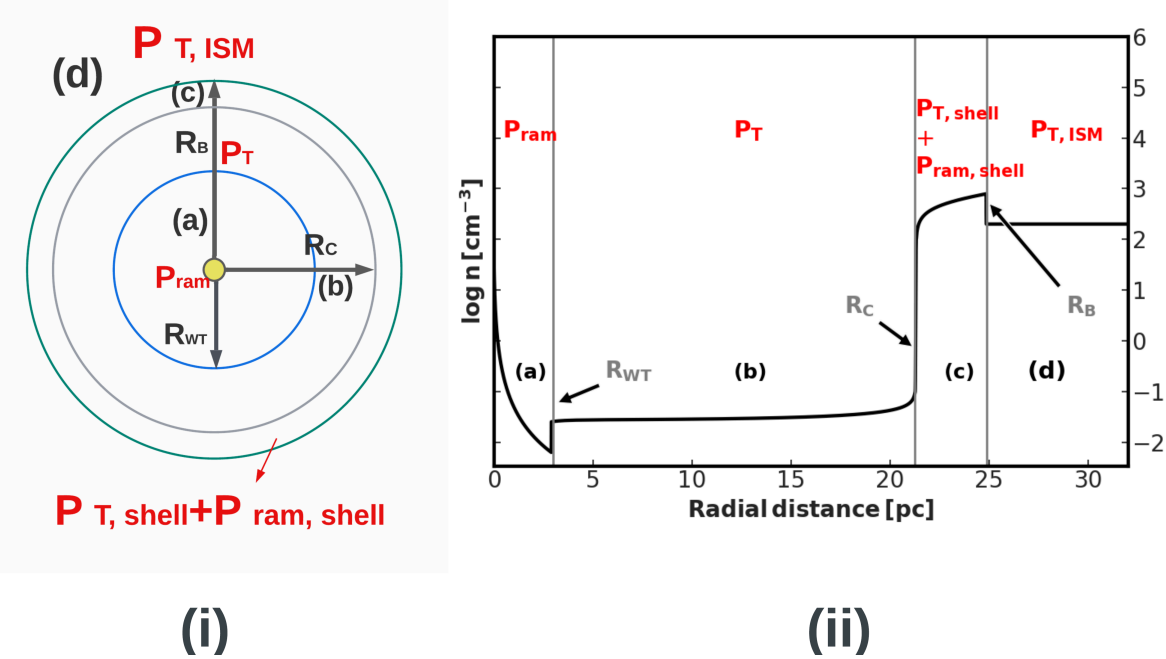

Figure 2.4.1: Schematic of stellar wind bubble and Numerically simulated stellar wind bubble
(i) Structure of wind bubble
(ii) Number density (n) profile of stellar wind bubble computed in a test run by Numerical hydrodynamic simulation using *PLUTO* code [42]:
Bubble created by a stellar wind in ISM number density 200 $\mathrm{cm^{-3}}$ with velocity 2200 $\mathrm{km\,s^{-1}}$ and mass-loss rate $4 \times 10^{-5}\ M_\odot\ \mathrm{yr^{-1}}$ after 0.9 Myr adiabatically, computed in one-dimensional spherical symmetry.
(a)-(d) mark different regions of wind bubble filled by: (a) Free stellar wind, (b) Shocked stellar wind, (c) Shocked ISM, (d) ambient ISM. R_{WT}, R_C, and R_B are the radius of wind termination shock, bubble contact discontinuity, and bubble outer shock, respectively.
Pressures in different regions for hydrodynamic interaction between stellar wind and ISM are indicated. P_{ram}, P_T are the ram pressure of supersonic stellar wind and the thermal pressure of shocked stellar wind, respectively. $P_{T,shell}$, $P_{ram,shell}$, $P_{T,ISM}$ are the thermal and ram pressure of the shock ISM, and thermal pressure of ambient ISM, respectively.

free-streaming stellar wind from the shocked stellar wind region. There is also a contact discontinuity, corresponding to the transition between the shocked stellar wind and shocked interstellar material. Further, the region between contact discontinuity and bubble outer shock is referred to as the "shell". Thus, the wind bubble comprises four different regions. Further, as the wind properties depicted in Figure 2.3.2 during the MS stage are almost constant, assuming the adiabatic expansion of the wind bubble, the time evolution of the bubble can be analytically expressed in the MS stage as [41],

[42]: Mignone et al. (2007), 'PLUTO: A Numerical Code for Computational Astrophysics'

$$R_B(t) = 27 \left(\frac{L_w}{10^{36}\ \mathrm{erg\,s^{-1}}}\right)^{1/5} \left(\frac{n_0}{1\ \mathrm{cm^{-3}}}\right)^{-1/5} \left(\frac{t}{1\ \mathrm{Myr}}\right)^{3/5} \mathrm{pc} \tag{2.4.1}$$

where t and n_0 refer to evolution time and ambient atomic number density, respectively. L_w represents the wind mechanical luminosity $L_w = 1/2 \dot{M} V_{wind}^2\ \mathrm{erg\,s^{-1}}$. The estimated

value of R_B using Equation 2.4.1 is ~ 22 pc considering the wind parameters mentioned in Figure 2.4.1 which reasonably agrees with $R_B \sim 25$ pc in numerically simulated wind bubble, shown in Figure 2.4.1.

[43]: Heiligman (1980), 'Planetary nebulae and the interstellar magnetic field'

[44]: van Marle, A. J. et al. (2015), 'Shape and evolution of wind-blown bubbles of massive stars: on the effect of the interstellar magnetic field'

[45]: Cowie et al. (1977), 'The evaporation of spherical clouds in a hot gas. I. Classical and saturated mass loss rates.'

[46]: Spitzer (1962), *Physics of Fully Ionized Gases*

Dynamics:

Pressure-driven wind: Initially, at the MS stage stellar wind hits the ambient ISM and converts its kinetic energy to thermal energy and consequently, the shocked stellar wind region turns into a bubble of hot gas. Then, the position of the wind-termination shock is determined by the balance between the ram pressure exerted by the free supersonic stellar wind and the thermal pressure of the shocked stellar wind. At the outer shock of the bubble, the thermal pressure of ambient unshocked ISM balances against the thermal pressure and ram pressure of the shell arising from the propagation of the shell of shocked ISM material in ambient ISM. Thus, the expansion of the wind bubble in ISM is governed by hydrodynamic interaction. If the bubble expands inside the magnetised ISM, the magnetic pressure of ambient ISM, depending on the angle between the direction of the bubble's expansion with the magnetic field, along with the thermal pressure is applied to the outer shock of the bubble, externally. So, the large-scale ISM magnetic field can change the shape of the wind bubble by reducing the expansion rate perpendicularly to the magnetic field, predicted in [43]. Consequently, to maintain the pressure balance at the outer shock the ram pressure of the shell increases and from the conservation of magnetic field flux, field strength should be compressed in the shell. Therefore, the thermal pressure of the shocked wind should increase to conserve the pressure equilibrium at contact discontinuity, and hence, the location of the wind-termination shock becomes closer to the star. The influence of the ISM magnetic field on the dynamics of the wind bubble was investigated in [44] and this study demonstrated that the strongly magnetised ISM leads to the formation of the highly asymmetric bubble.

Comment 2.4.2

Mass-flux from the shell, region (c) to the hot shocked wind, region (b) ($\dot{M}_b$) according to the classical evaporation theory [45], $\dot{M}_b = \frac{16\pi\mu C}{25k} T^{\frac{5}{2}} R_c$.
where μ, T, k are the mean molecular weight of ISM material and temperature of region (b), Boltzmann constant, respectively. Thermal conductivity is defined by, $\kappa = CT^{5/2}$ where $C = 6\times10^{-7}$ erg K$^{7/2}$ s^{-1} cm^{-1} [46].

Energy loss: After the pressure-driven expansion of the wind bubble in the adiabatic limit, following Equation 2.4.1, thermal energy transfer from the hot interior of the bubble, region (b) in Figure 2.4.1 to shell, region (c) takes place through the contact discontinuity, R_c. In response to this thermal flux in the outward direction, an inward flux, described in Comment 2.4.2 of the shocked interstellar material induces which is associated with the evaporation of material during the passage through the contact discontinuity, along with the radiative cooling in the interface.

Comment 2.4.3

H II regions: Photo-ionised ISM by Ultra Violet radiation from hot stars. These regions can have different sizes and shapes-ultra compact (< 0.1 pc) to giant ($\approx$ 100 pc)

Wind bubble inside H II region: Another complication in the wind bubble scenario can arise if the bubble expands inside the H II region which gives rise to different complex structures like shells, clouds and fingers. Freyer et al. [47, 48] have studied this interesting interaction between wind bubbles and H II region numerically considering time-dependent

[47]: Freyer et al. (2003), 'Massive Stars and the Energy Balance of the Interstellar Medium. I. The Impact of an Isolated 60 M– Star'
[48]: Freyer et al. (2006), 'Massive Stars and the Energy Balance of the Interstellar Medium. II. The 35 M– Star and a Solution to the "Missing Wind Problem"'

ionisation, radiation transfer along with the heating and cooling processes using the stellar wind parameters from the evolution history of 60 $M_\odot$ and 35 $M_\odot$ stars in two-dimension and the simulated X-ray emission with 35 $M_\odot$ star is inline with the observed X-ray luminosity from the WR bubble S308, shown in Figure 2.4.2. This study is extended in [39] using radiative magnetohydrodynamic (MHD) simulations in three-dimension with different massive stars in the presence of turbulent ISM which suggests the generation of an aspherical and chaotic wind bubble including "chimney"- and "plumes"-like structures.

[49]: Toalá et al. (2012), 'X-RAY EMISSION FROM THE WOLF–RAYET BUBBLE S 308*'

Figure 2.4.2: S308 WR bubble: Composite images in optical lines and soft X-ray bands.
The bubble is located at the distance of 1.5 kpc and is generated by Wolf-Rayet star HD 50896 which evolved from a rotating star with ZAMS mass 40 $M_\odot$. The thick ionised shell and bubble interior, marked by blue colour indicates the diffuse X-ray emission at 0.1 − 1keV. The optical shell is visible in [O III] and $H\alpha$, distinguished by green and red colours, respectively. [49]
Image credit:J.A. Toala and M.A. Guerrero (IAA-CSIC), Y.-H. Chu and R.A. Gruendl (UIUC), S.J. Arthur (CRyA - UNAM), R.C. Smith (NOAO/CTIO), and S.L. Snowden (NASA/GSFC) and G.Ramos-Larios (IAM) and ESA

Runaway star and bow shock: The supersonic motion of the massive star with the strong stellar wind with respect to the ambient medium also distorts the generated wind bubble and produces an arc-like structure, so-called a bow shock [50] at the boundary of the wind bubble and ambient medium, shown in Figures 2.4.3 and 2.4.4. These bow shocks are detected in different wavelengths, starting from the first detection in optical line emission [O III] [51] to non-thermal radio emission [52] in recent times along with the detection in mid-infrared. The infrared emission is re-emitted starlight by the dust grains swept by the bow shock. The mid-infrared is the most appropriate waveband to detect the bow shock of specifically runaway MS and RSG stars, predicted in theory [53, 54]. This prediction supports the success of the Extensive stellar Bow Shock Survey (E-BOSS) in mid-infrared [55] and search of the mid-infrared stellar bow shocks in the Milky way [56] which catalogued 73 and 709 bow shock candidates, respectively.

[50]: van Buren et al. (1988), 'Bow Shocks and Bubbles Are Seen around Hot Stars by IRAS'

[51]: Gull et al. (1979), 'Discovery of two distorted interstellar bubbles.'

[52]: Pereira, V. et al. (2016), 'Modeling nonthermal emission from stellar bow shocks'

[53]: Meyer et al. (2014), 'Models of the circumstellar medium of evolving, massive runaway stars moving through the Galactic plane'

[54]: Henney et al. (2019), 'Bow shocks, bow waves, and dust waves – I. Strong coupling limit'

[55]: Peri et al. (2015), 'E-boss: An extensive stellar bow shock survey-ii. catalogue second release'

[56]: Kobulnicky et al. (2016), 'A COMPREHENSIVE SEARCH FOR STELLAR BOWSHOCK NEBULAE IN THE MILKY WAY: A CATALOG OF 709 MID-INFRARED SELECTED CANDIDATES'

The location of the contact discontinuity of bow shock (R_0), so-called stand-off distance [57, 58] is determined by the pressure balance between the stellar wind and ISM, given by- $\rho_{\rm wind}\, V^2_{\rm wind} = \rho_{\rm ISM}\, V^2_\star$, where $\rho_{\rm ISM}$, $V_\star$ are ISM gas density and velocity of stellar motion with respect to ISM. Therefore, using Equation 2.3.1, the stand-off distance reads,

[57]: Baranov et al. (1971), 'A Model of the Interaction of the Solar Wind with the Interstellar Medium'

[58]: Wilkin (1996), 'Exact Analytic Solutions for Stellar Wind Bow Shocks'

$$R_0 = \sqrt{\frac{\dot{M}\, V_{\rm wind}}{4\pi \rho_{\rm ISM}\, V_\star^2}} \tag{2.4.2}$$

[59]: Toalá et al. (2016), 'X-RAY OBSERVATIONS OF BOW SHOCKS AROUND RUNAWAY O STARS. THE CASE OF ζ OPH AND BD+43°3654'

[60]: Gvaramadze et al. (2012), '– Oph and the weak-wind problem'

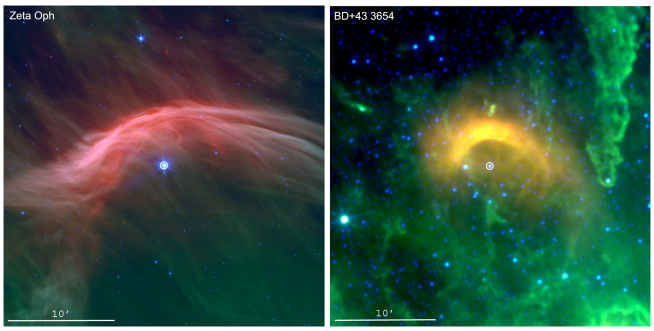

Figure 2.4.3: Observations of the bow shocks [59] Composite mid-infrared images of ζ Oph and $BD + 43°3654$- the red, green, and blue correspond to Spitzer MIPS $24\mu m$, IRAC $8\mu m$, and IRAC $4.5\mu m$, respectively for ζ Oph. For $BD + 43°3654$ the red, green, and blue correspond to WISE $22\mu m$, $12\mu m$, and $4.6\mu m$.

[61]: Van den Eijnden et al. (2022), 'Radio detections of IR-selected runaway stellar bow shocks'

Hence, Equation 2.4.2 suggests a promising way to determine the stellar mass-loss rate ($\dot{M}$) by constraining the other quantities in this equation [60]. Consequently, it also signifies the rapidly evolving instrumentation of radio detection of the bow shock [61] as although, the detection of bow shocks is favourable mainly in infrared waveband, constraining the ISM gas density from this emission is quite uncertain in the presence of dust grains [62].

[62]: Mackey, Jonathan et al. (2016), 'Detecting stellar-wind bubbles through infrared arcs in Hregions'

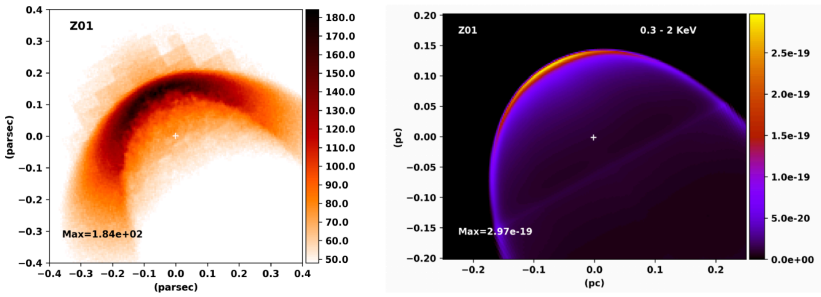

Figure 2.4.4: Simulated bow shock in infrared and X-ray emissions for ζ Ophiuchi, calculated in [63], estimating the distance of the star 112 pc and the stellar space velocity 26.5km s^{-1}, Z01 model. The left panel demonstrates the synthetic infrared emission maps of the bow shock in units of MJy $ster^{-1}$ at 24 μm. The right panel demonstrates the synthetic soft X-ray (0.3 − 2 KeV) emission map. Coordinates are in parsecs relative to the position of the star (white cross) and the colour scale is from zero to maximum in erg cm^{-2} s^{-1} $arcsec^{-2}$.

[63]: Green et al. (2022), 'Thermal emission from bow shocks-II. 3D magnetohydrodynamic models of ζ Ophiuchi'

The massive stars after exploding through the core-collapse mechanism, described in Section 2.2 forms an object called core-collapse SNRs.

2.5 Supernova remnant (SNR)

Comment 2.4.4

I refer the reader [64] for a review of stellar wind bubbles.

[64]: Mackey (2022), 'Interaction between massive star winds and the interstellar medium'

The supernova explosion gives rise to supersonic stellar ejecta which interacts with the ambient CSM and generates a blast wave. Initially, SNR consists of the stellar ejecta in a hot expanding bubble surrounded by the swept-up CSM material and an outer blast wave or outer shock. This blast wave will eventually lead to the formation of another shock which moves back towards the supernova ejecta. This shock is called reverse shock and the blast wave, propagating outward through the CSM is called forward shock. A contact

discontinuity is present between these two shocks and it separates the shocked ejecta from the shocked CSM. The basic structure of SNR is illustrated in Figure 2.5.1.

The evolution of SNR can be divided into four main stages [65, 66] such as 1. the **free expansion phase/ejecta dominated phase**, 2. the **Sedov-Taylor phase/adiabatic expansion phase**, 3. the **pressure-driven phase/radiative phase**, 4. the **dissipative phase/merging phase**. These four respective stages are beneficial to understand the dynamics of an SNR during its evolution, however, in reality, it is quite hard to specify the stage of SNR. Furthermore, specifically for SNR expanding inside the wind bubble, different parts of the remnant can be in separate stages depending on the ambient medium, for instance, SNR RCW 86, also known as $G315.4-2.3$, comprising fast shock, is in the free expansion phase in the northeast while in the southwest, the remnant is evolving through the radiative phase, described in Figure 2.5.2 and Comment 2.5.1.

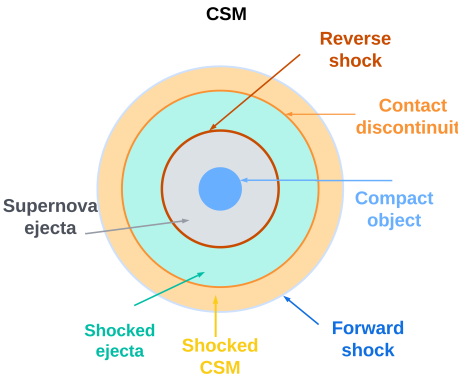

Figure 2.5.1: Structure of SNR

Definition 2.5.1 *Equilibrium between two plasmas with different properties creates an evolution of boundary in the form of a narrow layer on the gyro-kinetic scale. This layer is called* ***discontinuity****.*
Shock: *This discontinuity is characterised by the non-vanishing normal mass flux in its rest frame.*
Contact discontinuity: *Through this discontinuity, there is no normal mass flux in its rest frame.*

Comment 2.5.1

RCW 86: The supernova explosion for this remnant may not be located in the middle of the wind bubble but is slightly offset. the shock front has already reached the ambient shell in the southwest but not in the northeast direction [67, 68]. Consequently, in the southwest rim the shock velocity is $\approx$ 500 km s^{-1} and X-ray emission is mainly thermal whereas in the northeast direction shock velocity is 6000 $\pm$ 2800 km s^{-1} and the probable source of X-ray emission is synchrotron emission [69].

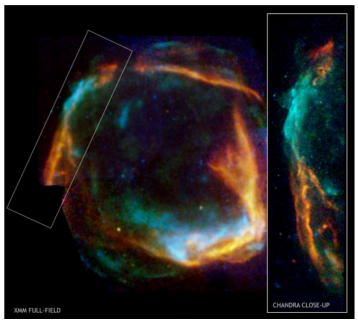

Figure 2.5.2: X-ray emission from RCW 86 remnant.
Composite image from the Chandra and XMM-Newton X-ray observations. The colour code is as follows: Red 0.5 – 1 keV, Green 1 – 1.95 keV, Blue 1.95 – 6.6 keV. The image depicts the XMM-Newton image of the entire remnant. The right panel shows the Chandra image of the Northeast rim as a close-up.
Image credit: ESA/XMM-Newton, NASA/CXC: University of Utrecht (J.Vink)

1. Free expansion phase: In this phase, the very fast shock (velocity $\approx 10^4$ km s^{-1}), created by the supernova explosion, expands with no resistance inside the CSM of density $\rho_{\rm CSM}$. As the energy of the explosion ($E_{\rm SN}$) is carried by the stellar ejecta with mass ($M_{\rm ej}$), the expansion velocity of the SNR outer shock can be approximated as $V_{\rm sh} \approx (2E_{\rm SN}/M_{\rm ej})^{1/2}$. In this stage, the SNR outer shock radius $R_{\rm sh}$ at evolution time t reads $R_{\rm sh} \approx V_{\rm sh}\, t$. Further, [70] describes that the supernova ejecta density ($\rho_{\rm ej}$) follows power-law distribution in radius (r), $\rho_{\rm ej} \propto r^{-n_{\rm ej}}$ at the early expansion stage. Then,

[65]: Woltjer (1972), 'Supernova Remnants'
[66]: Leahy et al. (2017), 'A Python Calculator for Supernova Remnant Evolution'
[67]: Vink (2012), 'Supernova remnants: the X-ray perspective'
[68]: Williams et al. (2011), 'RCW 86: A TYPE Ia SUPERNOVA IN A WIND-BLOWN BUBBLE'
[69]: Helder et al. (2011), 'TEMPERATURE EQUILIBRATION BEHIND THE SHOCK FRONT: AN OPTICAL AND X-RAY STUDY OF RCW 86'
[70]: Chevalier (1982), 'Self-similar solutions for the interaction of stellar ejecta with an external medium.'

SNR expansion can be described by a self-similar equation [67],

$$R_{\rm sh} \propto t^{\beta} \qquad \text{where} \quad \beta = \frac{n_{\rm ej} - 3}{n_{\rm ej} - s} \tag{2.5.1}$$

where s represents the index of power-law radial dependence of density, for example in the core-collapse scenario, $\rho_{\rm CSM} \propto r^{-2}$ and for Type-Ia, the ambient density is typically constant. Therefore, for Type-Ia supernovae, s=0, $n_{\rm ej} = 7$, hence $\beta = 0.57$ and for core-collapse scenario, s=2, $n_{\rm ej} = 9$, hence $\beta = 0.86$.

The free expansion phase terminates when the mass of swept-up CSM material ($M_{\rm swept-up}$) by the SNR outer shock becomes comparable to $M_{\rm ej}$.

[71]: Truelove et al. (1999), 'Evolution of Nonradiative Supernova Remnants'

[72]: Sedov (1946), 'Propagation of strong shock waves'
[73]: Taylor (1950), 'The Formation of a Blast Wave by a Very Intense Explosion. I. Theoretical Discussion'

$$M_{\rm swept-up} = (4\pi/3)\, \rho_{\rm CSM}\, R_{\rm d}^3 = M_{\rm ej} \tag{2.5.2}$$

Therefore, the characteristics mass, length and time scale for the transition from the free expansion phase to the Sedov-Taylor phase can be expressed as [71],

$$\begin{aligned} M_{\rm ch} &\equiv M_{\rm ej} \\ R_{\rm ch} &\equiv M_{\rm ej}^{1/3} \rho_{\rm CSM}^{-1/3} \\ t_{\rm ch} &\equiv E_{\rm SN}^{-1/2} M_{\rm ej}^{5/6} \rho_{\rm CSM}^{1/3} \end{aligned} \tag{2.5.3}$$

2. Sedov-Taylor phase: During this stage, the SNR expands inside the CSM adiabatically. The dynamics of the remnant is governed by [72, 73],

$$\begin{aligned} R_{\rm sh} &= \left(\xi \frac{E_{\rm SN} t^2}{\rho_{\rm CSM}}\right)^{1/5} \\ V_{\rm sh} &= \frac{dR_{\rm sh}}{dt} = \frac{2}{5}\frac{R_{\rm sh}}{t} \end{aligned} \tag{2.5.4}$$

where $\xi = 2.026$ for non-relativistic and mono-atomic gas. Further, at this stage the radiative energy loss is negligible and the cooling of plasma occurs only because of expansion. During the free expansion stage, the SNR reverse shock expands outwards with respect to the observer's frame but in this stage, the reverse shock starts to propagate towards the supernova ejecta. Further, at this stage $\beta = 2/(5-s)$ from Equation 2.5.1, so $\beta = 0.67$ for core-collapse scenario which is comparable with $\beta = 0.63 \pm 0.02$, derived from X-observation of young SNR Cas A [74].

3. Radiative phase: With the evolution of the SNR inside the CSM, the forward shock velocity decreases and, consequently, the temperature (T_d) of the downstream plasma (described in Comment 2.5.2) falls following the jump conditions at the shock, described in 3.3.1. Then, below a critical temperature of 10^6 K, free electron capturing by the ionised atoms begin with the production of line emissions. This radiative cooling process further slows down the expansion and the mass of swept-up material gradually increases like snow-plough piled-up snow. Thus, this phase is called the radiative phase or snow-plough phase.

Comment 2.5.2

Downstream plasma: The material which is already shocked by the SNR shock.
Upstream plasma: The material which is ahead of the SNR shock.

Comment 2.5.4

Comparison between the theoretical estimation of supernova expansion parameters and simulated values: I initiate a system of expanding core-collapse SNR inside the wind bubble, shown in Figure 2.4.1 considering $M_{ej} = 3\,M_\odot$ and simulate the SNR evolution. Initially, while the remnant is propagating through free stellar wind region, $\beta \approx 0.84 - 0.88$. Then, after entering into the shocked wind region, the ambient density becomes almost constant, CSM number density (n_{CSM})= 0.1 cm^{-3}. Consequently, $R_{ch} \approx$ 10pc and t_{ch} = 1800yrs and after this age β becomes $\sim$ 0.65 in the Sedov-Taylor phase. Although in this simulation, SNR forward shock radius depends on the interactions between the remnant and CSM, still, I get comparable values of β from numerical simulation.

Comment 2.5.3

Rayleigh-Taylor instability [75]**:** A hydrodynamic instability generated at the interface of two fluids of different densities. This instability is produced at the contact discontinuity of the SNR and this breaks the spherical symmetry of this SNR system and leads to "finger"-like structures.

4. Dissipative phase: At this stage, the expansion velocity of the remnant reduces below the local ISM dispersion velocity and the remnant merges with the ambient medium [76].

Next step: I want to mention that bow shocks and wind bubbles are the potential sources of particle acceleration [77] along with the SNRs, specifically as stellar clusters [78] and superbubbles [79]. However, in this dissertation, I will only discuss the particle acceleration at SNR, elaborately. Chapter 3 will give the reader insight into the SNR, as a source of galactic CRs through the description of the microphysics of particle acceleration.

[75]: Fraschetti, F. et al. (2010), 'Simulation of the growth of the 3D Rayleigh-Taylor instability in supernova remnants using an expanding reference frame'

[76]: T Chiad et al. (2015), 'Determination of Velocity and Radius of Supernova Remnant after 1000 yrs of Explosion'

[77]: del Valle et al. (2018), 'Nonthermal Emission from Stellar Bow Shocks'

[78]: Aharonian, F. et al. (2022), 'A deep spectromorphological study of the emission surrounding the young massive stellar cluster Westerlund 1'

[79]: Vieu et al. (2022), 'Cosmic ray production in superbubbles'

SNRs: sources of galactic CRs 3

CRs are the charged particles with energies between 1 MeV – 100 EeV [80] that spread throughout the Universe and during their propagation from the sources to the earth, they get diffused energy-dependently by the large-scale magnetic field along with the small-scale turbulence, present in their passage. Consequently, this diffusion of CRs prevents the retracing of cosmic ray (CR) sources and, also provides the softer spectral index of CRs on the earth than that is at the sources. In this chapter, I begin with a discussion of the CR spectrum observed on the earth followed by a discussion about SNRs as the dominant sources of galactic CRs, considering the galactic CR energy budget. Then, I provide an outline of the Fermi mechanism of CR acceleration. In the end, I discuss different non-thermal emission processes from SNRs along with the observational evidence.

3.1 CR spectrum

CRs, arriving at the Earth comprise majorly protons (∼ 87%), Helium nuclei (∼ 12%) and a small fraction of heavier elements [81]. Generally, the chemical composition of CRs is close to the cosmic abundance with a few exceptions of over-abundance for some elements like Lithium, Beryllium, and Boron. These elements are called secondary CRs, produced in the spallation of Carbon and Oxygen [82].

Comment 3.1.1

Measurements of CRs:
CRs are detected when they eventually reach the Earth.
Direct measurements: Satellite-borne experiments like PAMELA [83], space-based observations like AMS-02 [84] on the International Space Station, ballon-borne experiments like ATIC [85] directly measures the primary CRs below TeV energies.
Indirect measurements: Ground-based techniques to probe higher energy bands using the extensive air shower [86]. When the particles eventually reach the ground at the end of the air shower, they can be detected by different observations, for example, Tibet, Kascade, and Auger observatories [87].

The state-of-the-art techniques and instrumentation in the area of the CR detection mentioned in Comment 3.1.1, can be merged into a single CR spectrum, consisting of the flux (N)

[80]: Grenier et al. (2015), 'The nine lives of cosmic rays in galaxies'

[81]: Blasi (2013), 'The origin of galactic cosmic rays'

[82]: Kulsrud (2005), *Plasma Physics for Astrophysics*

[83]: Adriani et al. (2011), 'PAMELA Measurements of Cosmic-Ray Proton and Helium Spectra'

[84]: Aguilar et al. (2013), 'First Result from the Alpha Magnetic Spectrometer on the International Space Station: Precision Measurement of the Positron Fraction in Primary Cosmic Rays of 0.5–350 GeV'

[85]: Ganel et al. (2005), 'Beam tests of the balloon-borne ATIC experiment'

[86]: Kampert et al. (2012), 'Extensive air showers and ultra high-energy cosmic rays: a historical review'

[87]: Engel (2012), 'Indirect Detection of Cosmic Rays'

of particles per energy (E) band, shown in Figure 3.1.1. Low energetic CRs with $E < 10$ GeV are affected by solar activity [88]. Above approximately $E \sim 100$GeV, the shape of the CR energy spectrum is well described by,

[88]: Potgieter (2013), 'Solar modulation of cosmic rays'

$$\frac{dN}{dE} = E^{-s}, \quad s \equiv \text{spectral index} \tag{3.1.1}$$

[89]: Fisk et al. (2011), 'ACCELERATION OF GALACTIC COSMIC RAYS IN THE INTERSTELLAR MEDIUM'

The spectral index, $s \sim 2.7$ in the energy region between approximately $E \sim 100$ GeV to so-called "knee" at $E \sim 3$ PeV. Beyond "knee", the energy spectrum softens with $s \sim 3.1$, up to so-called "ankle" at $E \sim 5$EeV. At "ankle" the spectral index flattens again to $s \sim 2.75$ [89] and finally the CR flux becomes negligible around $40 - 60$ EeV. This cut-off energy of CRs is limited by theoretically predicted Greisen-Zatsepin-Kuzmin (GZK) cutoff [90], described in comment 3.1.2. Whether the origin of CRs is galactic or extra-galactic, can be determined by the Larmor radius (R_g) of CRs.

[90]: Greisen (1966), 'End to the Cosmic-Ray Spectrum?'

Comment 3.1.2

GZK cutoff: High energy protons ($E \sim 50$EeV) can interact with cosmic microwave background (CMB) photons (γ_{CMB}) and produce pions through Δ-resonance, which reduces the energy of parent protons.
$p + \gamma_{CMB} \rightarrow \Delta^+ \rightarrow p + \pi^0$
$p + \gamma_{CMB} \rightarrow \Delta^+ \rightarrow n + \pi^+$

$$R_g = \frac{p}{ZeB} \approx 1.07 \left(\frac{Z}{e}\right)^{-1} \left(\frac{E}{10^{18}\text{eV}}\right) \left(\frac{B}{\mu\text{G}}\right)^{-1} \text{kpc} \tag{3.1.2}$$

for a particle with charge Z, and momentum, energy p, E, respectively, gyrating in a uniform magnetic field B.

CRs with energies above "ankle" are most likely to have an extra-galactic origin as their Larmor radius is larger than the size of the galactic disc whereas the source of CRs with energy below "knee" is galactic [80].

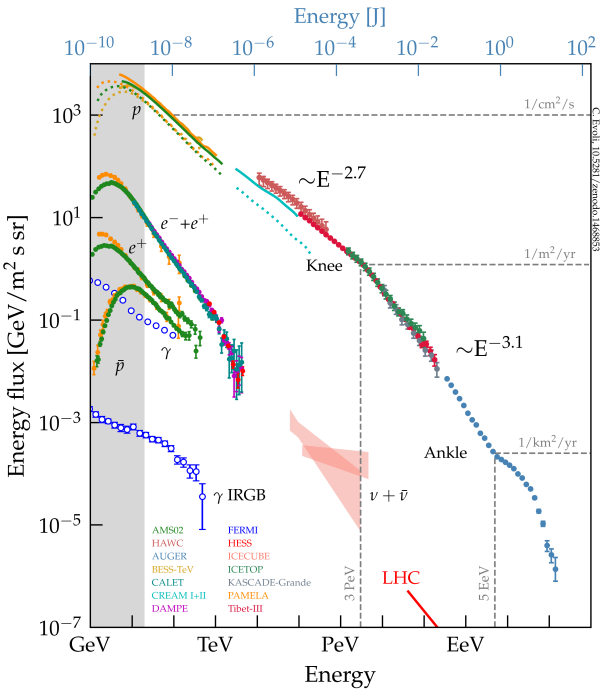

[91]: Evoli (2020), *The Cosmic-Ray Energy Spectrum*

Figure 3.1.1: CR spectrum as detected by various direct and indirect measurements.
The variation in the energy spectral index at energy $E \approx 3$ PeV is indicated in the spectrum. CRs with energies above $E \approx 5$ EeV originate at extragalactic sources. The energy range 3 PeV – 5 EeV marks the transition from galactic CRs to extragalactic CRs.
Image Credit: Carmelo Evoli [91]

3.2 Galactic CR energy budget

The measured flux of CRs shows that the local CR energy density (ρ_{CR}) near the sun is $\rho_{CR} \sim 1\,\mathrm{eV\,cm^{-3}}$. The volume of the Milky Way (V_G) is given by, $V_G = \pi\, r^2\, d \approx 10^{67}\,\mathrm{cm^3}$, considering radius, $r = 16\,\mathrm{kpc}$ and thickness $d = 3\,\mathrm{kpc}$. Typically, CR spends $\tau_G \approx 10^7\,\mathrm{yr} \sim 3 \times 10^{14}\,\mathrm{s}$ in the Milky Way before escaping into the intergalactic space [92]. Therefore, the corresponding rate of energy loss (L_{CR}) will be,

[92]: Gaisser (1990), *Cosmic rays and particle physics.*

$$L_{CR} \sim \frac{\rho_{CR}\, V_G}{\tau_G} \sim 5 \times 10^{40}\,\mathrm{erg\,s^{-1}} \tag{3.2.1}$$

Then, to maintain the steady energy density of galactic CRs, the injection and acceleration of new CRs are necessary. Estimating the rate of one supernova explosion every 30 years and $E_{SN} = 10^{51}\mathrm{erg}$, the average energy injection rate by SNRs will be approximately $10^{42}\mathrm{erg\,s^{-1}}$. Although this estimation can be uncertain, this rough energy approximation is certainly sufficient to compensate for the energy loss from the Milky Way. Hence, SNRs can be considered the prominent sources of galactic CRs and therefore, at this point, it becomes crucial to understand the acceleration mechanism of CRs which energise CRs in the SNRs.

[93]: Prunty (2021), 'Conditions Across the Shock: The Rankine-Hugoniot Equations'

3.3 CR acceleration mechanism

CRs are thought to be accelerated at SNR shocks by the Fermi acceleration mechanism. There are two types of Fermi accelerations, First-order or DSA [10, 11] and second-order [9]. First-order Fermi acceleration or DSA is the considered acceleration process for particles at the SNR shocks.

Before I start with a mathematical description of the Fermi acceleration mechanism, I want to provide the reader, with the formulations of jump conditions at the SNR shock.

3.3.1 Jump conditions at the SNR shock

According to Definition 2.5.1, shock is formed between two plasmas with different properties and an abrupt change in density, flow velocity, pressure, and temperature characterises this shock. Further, it is possible to relate the upstream and downstream properties of the shock through specific conditions as the flux of mass, momentum, and energy are conserved across the shock surface. These specific conditions are known as "Rankine-Hugoniot" jump conditions [93].

Considering ρ,**V**, P, E are fluid density, velocity, thermal pressure, and the total energy density, respectively with

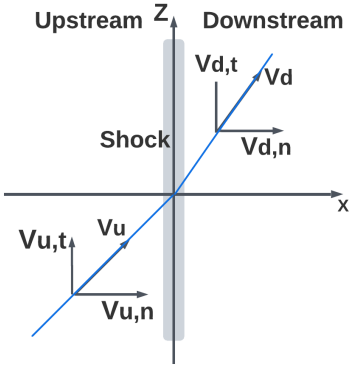

Figure 3.3.1: Schematic of the flow at the planar, oblique shock in the shock rest frame.
The shock is in the x-z plane and the velocity vector (**V**) reads $\mathbf{V} = V_n\hat{\mathbf{e}}_x + V_t\hat{\mathbf{e}}_z$, V_n and V_t are normal and tangential components of the flow, respectively. The subscripts u and d indicate upstream and downstream, respectively

respect to the shock rest frame, conservation laws of mass flux, x-component of momentum flux, y-component of momentum flux, energy flux, respectively across an infinitely thin shock, illustrated in Figure 3.3.1, gives the following Rankine-Hugoniot jump conditions:

$$\begin{aligned} \rho_u V_{u,n} &= \rho_d V_{d,n} \\ \rho_u V_{u,n}^2 + P_u &= \rho_d V_{d,n}^2 + P_d \\ \rho_u V_{u,n} V_{u,t} &= \rho_d V_{d,n} V_{d,t} \\ \frac{V_u^2}{2} + \frac{\gamma}{\gamma-1}\frac{P_u}{\rho_u} &= \frac{V_d^2}{2} + \frac{\gamma}{\gamma-1}\frac{P_d}{\rho_d} \end{aligned} \tag{3.3.1}$$

where γ is the adiabatic index. From Equations 3.3.1, so-called "shock adiabat" can be represented as,

$$\frac{\gamma}{\gamma-1}\left(\frac{P_d}{\rho_d} - \frac{P_u}{\rho_u}\right) = \frac{1}{2}\left(\frac{1}{\rho_d} + \frac{1}{\rho_u}\right)(P_d - P_u) \tag{3.3.2}$$

Density jump/Compression ratio→ $\frac{\rho_d}{\rho_u} = r$
Normal velocity jump → $\frac{V_{d,n}}{V_{u,n}}$
Pressure jump → $\frac{P_d}{P_u}$
Temperature jump → $\frac{T_d}{T_u}$

Now, normal upstream sonic Mach number ($\mathcal{M}_n$) defines as, $\mathcal{M}_n = V_{u,n}/c_s = \sqrt{\frac{\rho_u V_u^2}{\gamma P_u}}\cos\theta_s$, where c_s is the sound speed in front of shock and θ_s is the inclination angle of the incoming flow with respect to the direction of the shock normal. Then the jump conditions, described in Definition 3.3.1 at an infinitely thin shock in its rest frame define as,

$$\begin{aligned} r = \frac{\rho_d}{\rho_u} &= \frac{(1+\gamma)\mathcal{M}_n^2}{(\gamma-1)\mathcal{M}_n^2 + 2} \\ \frac{V_{d,n}}{V_{u,n}} &= \frac{(\gamma-1)\mathcal{M}_n^2 + 2}{(1+\gamma)\mathcal{M}_n^2} \\ V_{d,t} &= V_{u,t} \\ \frac{P_d}{P_u} &= 1 + \frac{2\gamma}{1+\gamma}\left(\mathcal{M}_n^2 - 1\right) \\ \frac{T_d}{T_u} &= \frac{\left[(1-\gamma) + 2\gamma\mathcal{M}_n^2\right]\left[2 + (\gamma-1)\mathcal{M}_n^2\right]}{(1+\gamma)^2\mathcal{M}_n^2} \end{aligned} \tag{3.3.3}$$

Hence, in strong shock limit, $\mathcal{M}_n^2 >> 1$ compression ratio (r) will be 4, considering $\gamma = 5/3$ for mono-atomic gas.
For the contact discontinuity, defined in Definition 2.5.1, jump conditions read,

$$V_{u,n} = V_{d,n} = 0 \qquad P_u = P_d \tag{3.3.4}$$

The conservation of y-momentum flux and energy flux, both are satisfied trivially. Therefore, plasmas at the two sides of contact discontinuity are constrained only by Equations 3.3.4.

Comment 3.3.1

I mention here that particles with Larmor radius larger than the shock thickness, $\lambda_{sh} = \frac{V_u}{\Omega_i}$ where Ω_i is the ion gyrofrequency, can "see" the shock as a discontinuity and involve in the shock acceleration process. This is known as "injection" process which connects the distribution of particles in thermal plasma with the non-thermal particle distribution but this required criterion is difficult to be obtained by the thermal electrons for their lower rest mass and consequently, reduced Larmor radius. Therefore, the pre-acceleration processes of electrons, for instance, the shock-surfing acceleration, shock drift acceleration are may be required to get them involved in the DSA process at the shock [94, 95]. I discuss the injection process for this dissertation in Section 4.1.

[94]: Li et al. (2018), 'Electron shock-surfing acceleration in the presence of magnetic field'
[95]: Bohdan et al. (2019), 'Kinetic Simulations of Nonrelativistic Perpendicular Shocks of Young Supernova Remnants. II. Influence of Shock-surfing Acceleration on Downstream Electron Spectra'

3.3.2 Fermi acceleration

1. Second-order Fermi acceleration: According to the original Fermi approach, charged particles are scattered by the randomly moving magnetic field inhomogeneities, so-called "magnetic mirrors", referred to by Fermi. Particles interact with the magnetic perturbations (magnetic turbulence) through both the "head-on" and "tail-on" collisions, as illustrated in Figure 3.3.2 and head-on collisions lead to energy gain in particles whereas during tail-on collisions, particles loss energy. However, the head-on collisions are more frequent than the tail-on collisions as the probability of a head-on collision is proportional to $(V_{CR} + v\cos\theta)$ while for a tail-on collision, the probability is proportional to $(V_{CR} - v\cos\theta)$, $\theta \equiv$ pitch angle [96]. Hence, the average increase in energy per collision through this random process, referred to as the stochastic process reads,

[96]: Longair (2011), *High Energy Astrophysics*

$$\left\langle \frac{\Delta E}{E} \right\rangle = \frac{8}{3}\frac{v^2}{c^2} \tag{3.3.5}$$

where particle energy is E, assuming particles are relativistic ($V_{CR} \approx$ c, where c is the speed of light) and particles are ran-

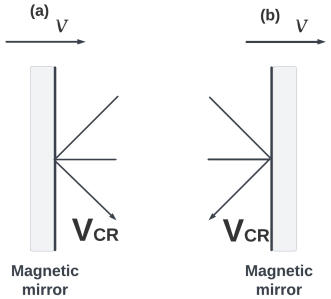

Figure 3.3.2: Schematic of the encounter of a particle with magnetic mirror (a) head-on collision, (b) tail-on collision. Magnetic mirrors or magnetic turbulence, in reality, move with velocity v and particle velocity is V_{CR} in the observer's reference frame.

domly scattered in pitch angle. This stochastic acceleration is considered to play an important role in particle acceleration in the ISM, by interacting with randomly moving interstellar magnetised clouds [97]. Although the second-order Fermi acceleration is not an efficient acceleration process in SNRs compared to the DSA, [98] proposed that TeV− emissions from the shell-type SNR, RXJ1713.7 − 3946 can be explained by stochastic acceleration of electrons in the SNR forward shock downstream by turbulent plasma waves, by considering this acceleration as a diffusion process in the energy space. Further, [99] represented that the stochastic acceleration process can influence the electron spectra in Type Ia Tycho's SNR and, hence, the emission at radio band.

[97]: Strong et al. (1998), 'Propagation of cosmic-ray nucleons in the galaxy'

[98]: FAN et al. (2013), 'STOCHASTIC ELECTRON ACCELERATION IN SNR RX J1713.7-3946'

[99]: Wilhelm, A. et al. (2020), 'Stochastic re-acceleration and magnetic-field damping in Tycho´s supernova remnant'

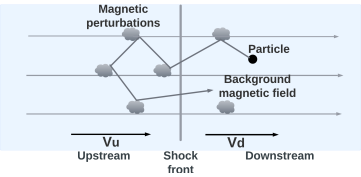

Figure 3.3.3: Schematic of the DSA of a particle in a non-relativistic parallel SNR shock with respect to the shock rest frame.
Particle is scattered from the magnetic fluctuations present in both sides of shock and cross the shock many times which energise the particle. Here, V_u and V_d are upstream and downstream flow speeds in the shock rest frame.

2. First-order Fermi acceleration or DSA: The first-order Fermi acceleration process can be divided into two categories, linear DSA, also known as test-particle limit if the pressure exerted by the accelerated particles is dynamically unimportant in the system and also the shock structure remains unaffected in this scenario, and non-linear DSA if the pressure of accelerated particles influences the dynamics of the system along with the modification in shock structure. In this thesis, I only consider the DSA mechanism in test-particle limit as the acceleration process of particles in SNRs.

a. Test-particle limit: This is the acceleration process of particles in the presence of collision-less astrophysical shock with the existing magnetic field fluctuations in shock upstream and downstream regions. In this scenario, particles are scattered by these magnetic fluctuations and perform random walks that lead to the shock-crossing several times, as represented in Figure 3.3.3 and gain energy in each crossing.

The shape of the particle spectrum can be derived, resulting from this acceleration mechanism through (i) the statistic of random walk, and (ii) the solution of the Vlasov-Fokker-Planck (VFP) equation [100, 101].
(i) The main assumption for the derivation of particle spectra through the statistic of random walk is the isotropic scattering of particles by magnetic field fluctuations in upstream and downstream of the shock. Further, in this process, considering infinite plane parallel shock, any particle in the shock upstream can return to the shock whereas downstream particles can be advected and, then never come back to the shock vicinity.
I consider that a particle with energy E_0 and momentum p_0 in the shock rest frame crosses the shock at an angle θ from the upstream region. Then, the energy of the particle in the downstream rest frame by Lorentz transformation is given by, $E_0' = \gamma_v(E_0 + p_0 v \cos\theta)$, v, γ_v are described in Comment 3.3.2. Therefore, energy gain (ΔE) in the half cycle, upstream to downstream is,

[100]: Krymskii (1977), 'A regular mechanism for the acceleration of charged particles on the front of a shock wave'
[101]: Blandford et al. (1978), 'Particle acceleration by astrophysical shocks.'

Comment 3.3.2

$V_u \rightarrow$ upstream flow speed in the shock rest frame
$V_d \rightarrow$ downstream flow speed in the shock rest frame
$v = V_u - V_d \rightarrow$ upstream flow speed in downstream rest frame ≡ downstream flow speed in upstream rest frame. The corresponding Lorentz factor is γ_v

$$\frac{\Delta E}{E_0} = \frac{v}{\mathrm{c}} \cos\theta \tag{3.3.6}$$

assuming the shock is non-relativistic and particle is relativistic, $\gamma_v \rightarrow 1$, $E_0 = p_0\mathrm{c}$.
The probability (p) that the particle crosses the shock can be expressed as, $p(\theta) = 2\cos\theta \sin\theta d\theta$ following Comment 3.3.3. Therefore, the average energy gain, by averaging the Equation 3.3.6 over the probability distribution would be,

Comment 3.3.3

Rate of shock crossing by particle $\rightarrow$ c $\cos\theta$
Number of particles between θ and $\theta + d\theta \rightarrow \propto \sin\theta\, d\theta$
$0 < \theta < \frac{\pi}{2}$

$$\begin{aligned} \text{half} - \text{cycle} \rightarrow \left\langle \frac{\Delta E}{E}_0 \right\rangle &= \frac{2}{3}\frac{v}{c} \\ \text{full} - \text{cycle} \rightarrow \left\langle \frac{\Delta E}{E}_0 \right\rangle_{\text{up-down-up}} &= \frac{4}{3}\frac{v}{c} \end{aligned} \tag{3.3.7}$$

Therefore, the energy of the particle after (k+1)th cycle is $E_{\mathrm{k+1}} = (1 + \frac{4}{3}\frac{v}{c})E_{\mathrm{k}} = \beta E_{\mathrm{k}}$. Then, the number of particles within the accelerator after k cycles are $N = N_0 P^{\mathrm{k}}$ with energy above $E = E_0\beta^{\mathrm{k}}$, if P is the probability that particles remain within the accelerator after each cycle and N_0 is the initial number of particles. Hence,

$$\begin{aligned} \log\left(\frac{N}{N_0}\right)/\log\left(\frac{E}{E_0}\right) &= \frac{\log P}{\log\beta} \\ \text{Integral spectrum} \rightarrow N(>E) &= N_0\left(\frac{E}{E_0}\right)^{\frac{logP}{log\beta}} \\ \text{Differential spectrum} \rightarrow n(E) &\propto E^{\left(-1+\frac{logP}{log\beta}\right)} \end{aligned} \tag{3.3.8}$$

Comment 3.3.4

$\rho_{\mathrm{CR}} \rightarrow$ Density of accelerated particles near the shock
c $\cos\theta \rightarrow$ particle velocity across the shock
ρ_{CR} is isotropic $\rightarrow$ $d\rho_{\mathrm{CR}} = \frac{\rho_{\mathrm{CR}}}{4\pi} d\Omega$
$R_{\mathrm{in}} = \int_{\text{up-down}} \mathrm{c}\cos\theta d\rho_{\mathrm{CR}}$
$= \frac{\rho_{\mathrm{CR}}\mathrm{c}}{4\pi}\int_0^{\frac{\pi}{2}} \cos\theta\sin\theta d\theta \int_0^{2\pi} d\phi$
$= \frac{\rho_{\mathrm{CR}}\mathrm{c}}{4}$
Particles advected in downstream $\rightarrow R_{\mathrm{out}} = \rho_{\mathrm{CR}} V_{\mathrm{d}}$

Calculation of P: If R_{in} is the rate of particles at the beginning of a cycle and R_{out} is the rate of particles that leave the system after one cycle, then $R_{\mathrm{out}}/R_{\mathrm{in}} = 1 - P = \frac{4V_{\mathrm{d}}}{\mathrm{c}}$, from the calculations shown in Comment 3.3.4. So, $P = 1 - \frac{4V_{\mathrm{d}}}{c}$, $\beta = \left(1 + \frac{4}{3}\frac{V_{\mathrm{u}} - V_{\mathrm{d}}}{c}\right)$. Then, considering $\log(1+x) \approx x$,

$$n(E) \propto E^{\left(-1-\frac{3V_{\mathrm{d}}}{V_{\mathrm{u}}-V_{\mathrm{d}}}\right)} \tag{3.3.9}$$

In strong shock approximation, from Equations 3.3.1,

$$n(E) \propto E^{-2} \tag{3.3.10}$$

Although using the statistic of random walk, the differential spectral shape depending on energy band can be calculated for relativistic particles, for the more general form of spectral shape also for non-relativistic particles can be derived from the solution of the VFP equation.

(ii) The VFP equation is given by,

$$\frac{\partial f}{\partial t} + \mathbf{V}_{\mathrm{CR}}.\frac{\partial f}{\partial \mathbf{r}} - q\left(\mathbf{E} + \mathbf{V}_{\mathrm{CR}} \times \mathbf{B}\right)\frac{\partial f}{\partial \mathbf{p}} = C\left(f\right) \quad (3.3.11)$$

where $f\left(\mathbf{r}, \mathbf{p}\right) d^3\mathbf{r} d^3\mathbf{p}$ is the total number of CRs in phase space volume $d^3\mathbf{r} d^3\mathbf{p}$ and $C\left(f\right)$ represents the scattering of accelerated particles by small-scale fluctuations in the magnetic field and **E, B,** $\mathbf{V}_{\mathrm{CR}}$ is the electric field, large-scale magnetic field, and velocity of accelerated particles, q represents the particle charge. Only considering the particle diffusion by the large-scale magnetic field and neglecting the large-scale electric and magnetic field, Equation 3.3.11 can be written as

$$\frac{\partial f}{\partial t} + \mathbf{V}_{\mathrm{CR}}.\frac{\partial f}{\partial \mathbf{r}} = C\left(f\right) \quad (3.3.12)$$

Now if f is defined in the local fluid rest frame and the shock is at $x = 0$ position in its rest frame and plasma flows through shock with velocity V in the x-direction, then in the local fluid rest frame Equation 3.3.12 reads,

$$\frac{\partial f}{\partial t} + \left(V_{\mathrm{CR},x} + V\right)\frac{\partial f}{\partial x} - \frac{\partial u}{\partial x} p_x \frac{\partial f}{\partial p_x} = C(f). \quad (3.3.13)$$

where $V_{\mathrm{CR},x}$ refers to the velocity of accelerated particles in x-direction. Now, the distribution function can be written as the sum of spherical harmonics [102],

[102]: Bell et al. (2006), 'Fast electron transport in laser-produced plasmas and the KALOS code for solution of the Vlasov–Fokker–Planck equation'

$$f\left(x, p, t\right) = \sum_{l,m} f_l^m\left(x, p, t\right) P_l^{|m|}\left(\cos\theta\right) \exp\left(im\phi\right) \quad (3.3.14)$$

where $f_l^{-m} = \left(f_l^m\right)^\star$, $p_x = p\cos\theta$, $p_y = p\sin\theta\cos\phi$, $p_z = p\sin\theta\sin\phi$ and $P_l^{|m|}$ is the Legendre polynomial. Therefore, only including the terms with $l < 2$, f can be defined as, $f = f_0(p) + f_1(p).p_x/p$ where $f_0 = f_0^0$ and $f_1 = f_1^0$. Then, in terms of f_0 [103],

[103]: Reville et al. (2013), 'Universal behaviour of shock precursors in the presence of efficient cosmic ray acceleration'

$$\frac{\partial f_0}{\partial t} + V\frac{\partial f_0}{\partial x} + \frac{V_{CR}}{3}\frac{\partial f_1}{\partial x} - \frac{1}{3}\frac{\partial V}{\partial x}p\frac{\partial f_0}{\partial p} = 0 \tag{3.3.15}$$

From the steady state solution for f_1, $V_{CR}\frac{\partial f_0}{\partial x} = -\nu f_1$, ν scattering frequency. Thus, Equation 3.3.15 becomes,

$$\frac{\partial f_0}{\partial t} + V\frac{\partial f_0}{\partial x} - \frac{\partial}{\partial x}\left(\frac{V_{CR}^2}{3\nu}\frac{\partial f_0}{\partial x}\right) - \frac{1}{3}\frac{\partial V}{\partial x}p\frac{\partial f_0}{\partial p} = 0$$
$$\frac{\partial f_0}{\partial t} = -\mathbf{V}.\nabla f_0 + \frac{1}{3}(\nabla.\mathbf{V})\,p\frac{\partial f_0}{\partial p} + \nabla\left(\frac{V_{CR}^2}{\nu}\nabla f_0\right) \tag{3.3.16}$$

and for relativistic particles, $\frac{c^2}{\nu} = D_B$, so-called Bohm diffusion coefficient. Integrating Equation 3.3.15 with respect to x from immediate downstream to upstream of the shock gives,

$$\frac{V_{CR}}{3}(f_{1u} - f_{1d}) = \frac{V_u - V_d}{3}p\frac{\partial f_0}{\partial p} \tag{3.3.17}$$

Steady state solution:
For no escape of particles far upstream, the diffusive drift balances the advective flow. So, $V_u f_0 + f_{1u}V_{CR}/3 = 0$.
CR advect with background fluid- $f_{1d} = 0$. Hence, using Equation 3.3.1

$$\frac{p}{f_0}\frac{\partial f_0}{\partial p} = -\frac{V_u}{V_u - V_d} = -\frac{3r}{r-1}$$
$$\Rightarrow f_0 \propto p^{-\frac{3r}{r-1}} \rightarrow n(p) \propto p^{-\frac{r+2}{r-1}} \tag{3.3.18}$$

Then, in strong shock approximation, $n(p) \propto p^{-2}$ and

$$n(E) = \begin{cases} \propto E^{-\frac{3}{2}}, & \text{in non} - \text{relativistic case} \\ \propto E^{-2} & \text{in relativistic limit} \end{cases} \tag{3.3.19}$$

The spectral index for CR distribution roughly agrees with the observations of emissions from SNRs and the CR spectrum, observed on earth, shown in Figure 3.1.1. However, the spectral shape predicted by the DSA mechanism can be significantly influenced by the magnetic amplification, arising

from the CR streaming instabilities. [104, 105] demonstrated that the CR spectra from SNR can become softer at higher energies while the higher energetic particles escape from the shock vicinity as a consequence of inefficient confinement resulting from the weak driving of Alfvén waves. Additionally, [106] analytically presented that the spectral shape of electrons and protons can vary as the result of magnetic field amplification. Therefore, understanding the spectral form of accelerated particles in a more realistic way involves the study of magnetic field amplification.

[104]: Celli et al. (2019), 'Exploring particle escape in supernova remnants through gamma rays'

[105]: Brose et al. (2020), 'Cosmic-ray acceleration and escape from post-adiabatic supernova remnants'

[106]: Cristofari et al. (2021), 'Cosmic ray protons and electrons from supernova remnants'

Maximum achievable CR energy: According to the DSA, the average time ($t_{\rm cycle}$) required to complete a cycle from entering downstream, coming back upstream, and then re-entering the upstream is given by [107] considering only the relativistic particles,

$$\left\langle t_{\rm cycle} \right\rangle = \frac{4}{\rm c}\left(\frac{D_{\rm u}(E)}{V_{\rm u}} + \frac{D_{\rm d}(E)}{V_{\rm d}}\right) \tag{3.3.20}$$

[107]: Drury (1983), 'REVIEW ARTICLE: An introduction to the theory of diffusive shock acceleration of energetic particles in tenuous plasmas'

where $D_{\rm u}$, $D_{\rm d}$ are diffusion coefficients for the upstream and downstream regions, respectively. Hence, the acceleration time ($t_{\rm acc}$) to gain energy E reads by using Equation 3.3.7 and then, using the shock jump conditions from Equations 3.3.3,

$$t_{\rm acc} = \frac{\left\langle t_{\rm cycle} \right\rangle}{\frac{\Delta E}{E}} = \begin{cases} \frac{3}{V_{\rm u}-V_{\rm d}}\left(\frac{D_{\rm u}(E)}{V_{\rm u}} + \frac{D_{\rm d}(E)}{V_{\rm d}}\right) \\ \frac{3r}{r-1}\left(\frac{D_{\rm u}(E)}{V_{\rm s}^2} + \frac{rD_{\rm d}(E)}{V_{\rm s}^2}\right) \end{cases} \tag{3.3.21}$$

[108]: Parizot, E. et al. (2006), 'Observational constraints on energetic particle diffusion in young supernovae remnants: amplified magnetic field and maximum energy'

where $V_{\rm s}$ is the shock velocity in the upstream rest frame. This equation 3.3.20 implies that the energy dependence of diffusion coefficients which varies according to the type of magnetic turbulence regulates the energy-dependent acceleration time. Then, considering the Bohm-like diffusion, described in Definition 3.3.1 can be expressed as following [108],

[109]: Berezhko, E. G. et al. (2003), 'Confirmation of strong magnetic field amplification and nuclear cosmic ray acceleration in SN 1006'

Definition 3.3.1 ***Bohm-like diffusion:*** *Mean free path of the particle equals its gyro-radius and this diffusion coefficient using Equation 3.1.2 is expressed as* $D(E) = \frac{1}{3}R_{\rm g}{\rm c} \propto E$

$$t_{\rm acc} \approx 2.2\frac{D(E)}{V_{\rm s}^2}\frac{3r}{r-1} \tag{3.3.22}$$

where $D(E)$ is the diffusion coefficient in the upstream region.

Definition 3.3.2 ***Precursor length:*** *The balance between diffusive flux and advective flux produces an exponential precursor ahead of the shock. If CR number density is* $n_{\rm cr}$ *in upstream of the shock, then,* $-D\frac{\partial n_{\rm cr}}{\partial x} = V_{\rm s}n_{cr} \Rightarrow n_{\rm cr} = n_{\rm s}\exp(-x/L_{\rm pre})$*, where* $n_{\rm s}$ *is CR number density at the shock,* x *is distance ahead of shock and* $L_{\rm pre}$ *is precursor length,* $L = \frac{D}{V_{\rm s}}$.

In SNRs, the maximum achievable energy by particles is limited spatially by the equivalence of precursor length ($L_{\rm pre}$), defined in Definition 3.3.2 and the size of the upstream region ($R_{\rm u} \approx 0.1\,R_{\rm SNR}$, described in [109], $R_{\rm SNR} \equiv$ SNR radius) and temporally, by the comparability of $t_{\rm acc}$ and the age of the

remnant(t_{age}). Therefore, the maximum achievable energy (E_{max}) reads using Equation 3.1.2,

$$E_{max} \approx 10^{12} \left(\frac{Z}{e}\right) \left(\frac{B}{1\mu G}\right) \left(\frac{t_{age}}{1000yr}\right) \left(\frac{V_s}{10^3 km\,s^{-1}}\right)^2 \quad eV \tag{3.3.23}$$

This estimation involves uncertainty because of the considered simplifications and for electrons, the maximum achievable energy should be controlled by the energy loss of synchrotron and inverse Compton emissions, described in Section 3.4 but still, it is efficient to get the E_{max} quite accurately for protons in the Bohm regime. For instance, I numerically calculate the proton spectrum at SNR forward shock for the remnant evolution inside the wind bubble in Figure 2.4.1, considering the Bohm-like diffusion and upstream magnetic field 5μ G. I get $E_{max,num} \sim 50$TeV numerically at $t_{age} = 200$yr when $V_s \sim 8000 km\,s^{-1}$ and Equation 3.3.23 gives $E_{max} = 64$TeV $\approx 1.3 E_{max,num}$. Further, if I consider in the scenario of Kepler's SNR, $E_{max} \approx 30$TeV, which is far below than "knee", for proton, by taking $t_{age} = 400$yr, $V_s = 5000\,km\,s^{-1}$, and $B = 3\,\mu$G $\equiv$ magnetic field of ISM. However, [108] estimated a very high downstream magnetic field for Kepler's SNR along with Tycho's SNR, SN 1006, and so on using the test-particle approximation, which is not compatible with the ISM magnetic field in the upstream region. This study proposes the scenario of the non-linear DSA [110] and the amplification of the upstream magnetic field in reality.

[110]: Ellison et al. (2004), 'Hydrodynamic simulation of supernova remnants including efficient particle acceleration'

b. Non-linear DSA: The acceleration of particles at SNR shock is considered to be in the non-linear regime if the pressure of accelerated particles (P_{CR}) becomes dynamically important for the hydrodynamic evolution of the system and it occurs when P_{CR} exceeds 10% of shock ram pressure (P_{ram}) [111]. In this scenario, the dominant P_{CR} of higher energetic particles modifies the shock structure by pushing the upstream plasma away from the shock and, thus creating a density and velocity gradient ahead of the shock, so-called dynamic precursor and, hence structures the particle spectrum [112, 113].

[111]: Kang et al. (2010), 'DIFFUSIVE SHOCK ACCELERATION IN TEST-PARTICLE REGIME'

[112]: Malkov et al. (2001), 'Nonlinear theory of diffusive acceleration of particles by shock waves'
[113]: Berezhko et al. (2009), 'A Simple Model of Nonlinear Diffusive Shock Acceleration'

Figure 3.3.4 illustrates the modified plasma flow in shock upstream by the back-reaction of the highly energetic particles and the flow velocity gradually decreases from far upstream to near upstream region. Therefore, the characteristic compression ratios for this modified shock can be defined as $r_{sub-shock} < 4$ and $r_{total} \rightarrow 7$ using the immediate downstream flow speed u_1 and far downstream flow speed u_0, from Comment 3.3.6, following shock jump conditions. From Definition 3.3.2, as the higher energetic particles have larger precursor lengths than with lower energy ones, they "feel" the larger compression ratio, r_{tot}. Consequently, the produced particle spectra by the modified shock should be

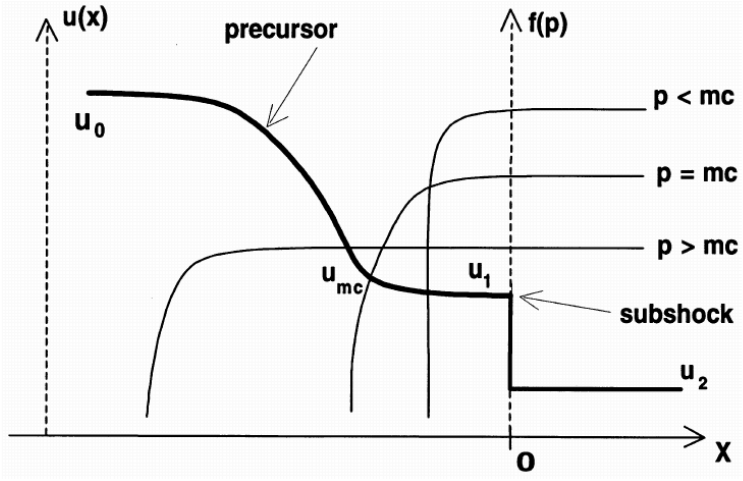

Figure 3.3.4: Schematic of the modified shock from [113].
The plasma velocity u(x) and the spatial distribution function, f(p) of the accelerated particle at different momentum are shown by heavy and light solid lines, respectively. The transition in flow velocity $u_{mc} \rightarrow u_1$ is provided by the non-relativistic particles whereas the transition $u_0 \rightarrow u_{mc}$ is created by the relativistic particles.

concave shape- softer at lower energy and harder at higher energy in comparison to the p^{-2} spectrum in Equation 3.3.18. However, the hard spectra at higher energy bands contrast with the generally predicted softer source spectra from the gamma-ray emissions of galactic SNRs [114, 115]. In this context, [116] numerically demonstrated that the non-linear DSA along with the amplified magnetic fields in the downstream region produces softer spectra which is consistent with the observational evidence.

Comment 3.3.6

For relativistic gas, the adiabatic index, $\gamma \rightarrow \frac{4}{3}$. Then, for strong shock approximation, the upper limit of $r_{tot} \rightarrow 7$, from Equation 3.3.3.

3.3.3 MHD turbulence

Plasma turbulence is ubiquitous in astrophysical flows and being charged particles, CRs are influenced by magnetic waves. In the acceleration process of CRs in the SNR, different wave modes of MHD turbulence present in the upstream and downstream regions of the SNR shock act as scattering centres of the CRs.

The waves of MHD turbulence can be derived from the MHD equations [117] described in Appendix A and the dispersion relation of MHD waves from the linearisation of these equations reads,

$$\left(\omega^2 - k_{\parallel}^2 v_A^2\right)\left(\omega^4 - k^2\left(c_s^2 + v_A^2\right)\omega^2 + k^2 k_{\parallel} c_s^2 v_A^2\right) = 0 \tag{3.3.24}$$

where $k_{\parallel}$ is the wave number component along the mean magnetic field, $v_A (= B_0/\sqrt{4\pi\rho_0}$, with B_0, ρ_0 are unperturbed magnetic field and density, respectively) is the Alfvén speed. Solution of this relation in Equation 3.3.24 provides three

[114]: Ahnen et al. (2017), 'A cut-off in the TeV gamma-ray spectrum of the SNR Cassiopeia A'
[115]: Malkov et al. (2011), 'Mechanism for spectral break in cosmic ray proton spectrum of supernova remnant W44'

[116]: Caprioli et al. (2020), 'Kinetic Simulations of Cosmic-Ray-modified Shocks. II. Particle Spectra'

[117]: Kirk et al. (1994), *Plasma astrophysics / J.G. Kirk, D.B. Melrose, E.R. Priest ; edited by A.O. Benz and T.J.-L. Courvoisier*

types of waves- "fast" magnetosonic wave, "slow" magnetosonic wave, and Alfvén wave with angular frequency ω_+, ω_-, and ω_A, respectively.

$$\omega_\pm = k\sqrt{\frac{v_A^2 + c_s^2}{2}}\left(1 \pm \sqrt{1 - \frac{4k_\parallel^2 c_s^2 v_A^2}{k^2(v_A^2 + c_s^2)^2}}\right)^{\frac{1}{2}} \qquad (3.3.25)$$

$$\omega_A = k_\parallel v_A$$

In the absence of the magnetic field, only the fast-mode wave exists among these three wave modes and its velocity is close to the standard sound wave while in highly magnetised plasma, the velocity of the fast-mode wave becomes close to the Alfvén velocity. [118] proposed that the fast-mode waves are the significant instabilities, responsible for the stochastic re-acceleration process for already accelerated particles by DSA in the SNR shock downstream region.

[118]: Pohl, M. et al. (2015), 'Reacceleration of electrons in supernova remnants'

Moreover, Alfvén waves are considered the major scattering centres for CRs in SNRs, specifically formed in the upstream region of the shock [10]. While the accelerated particles at the SNR shock with a streaming velocity faster than v_A with respect to the upstream plasma, try to escape the shock upstream they generate Alfvén waves with wavelength comparable to their corresponding Larmor radius, R_g. The concentration gradient of those accelerated particles gives rise to the Alfvén waves [119] and, then, generated Alfvén waves scatter the higher energetic particles which reduce their streaming velocity. Therefore, the particles are again involved in the DSA and cross the shock several times and hence, increase their energy through the cycle of shock crossing. This is known as the "resonant" streaming instability because of the spatial resonance between the wavelength of Alfvén waves and R_g of CRs and, further, this process continues self-consistently as CR flux in upstream with reasonable R_g drives the Alfvén waves and those waves deflect CRs, and so on. This instability saturates if the magnetic perturbation (δB) becomes comparable to the large-scale magnetic field (B_0) present in the upstream plasma

[10]: Bell (1978), 'The acceleration of cosmic rays in shock fronts - I.'

[119]: Skilling (1975), 'Cosmic Ray Streaming—III SELF-CONSISTENT SOLUTIONS'

Furthermore, the upstream magnetic field can be amplified beyond $\delta B/B_0 \sim 1$ through non-resonant streaming instability which grows rapidly at small scale ($\ll R_g$ of particles close to E_{max}) [120, 121]. The saturated magnetic field (δB_{sat}) is given by, $\frac{\delta B_{sat}^2}{4\pi} \sim \frac{V_s}{c} U_{cr}$, where U_{cr} is the energy density of CRs in near upstream region. Although, [106] argued that the saturation level should be $\propto V_s^{3/2}$ for the non-resonant scenario.

[120]: Lucek et al. (2000), 'Non-linear amplification of a magnetic field driven by cosmic ray streaming'
[121]: Bell (2004), 'Turbulent amplification of magnetic field and diffusive shock acceleration of cosmic rays'

This non-resonant instability saturates by the back-reaction of the thermal plasma to the CR-streaming or by a modification of the bulk flow [122, 123] and for both cases, the saturation

[122]: Riquelme et al. (2009), 'NONLINEAR STUDY OF BELL'S COSMIC RAY CURRENT-DRIVEN INSTABILITY'
[123]: Kobzar et al. (2017), 'Spatio-temporal evolution of the non-resonant instability in shock precursors of young supernova remnants'

level does not depend on the ambient magnetic field or the initial turbulence level. But the timescale for the growth of the turbulence is limited and required to be much shorter than the shock capture timescale, $D(p)/V_s^2$ [124]. Further, [125] calculated that to grow the non-resonant mode to the saturation level, not even a single exponential growth cycle is available and this implies the saturation level cannot be attained. Therefore, the amplified magnetic field will still depend on the ambient field strength, and hence, for the core-collapse scenario, the field of the progenitor stellar wind [126] can influence the amplified field strength.

Although [127, 128] described that the reasonably fast shock with $V_s > (\frac{4cv_A^2}{\eta_{acc}})^{1/3}$, where $\eta_{acc} \rightarrow$ acceleration efficiency that mainly exists during the early stage of supernova evolution is necessary for the scattering of particles near the E_{max} by the non-resonant instability generated magnetic field fluctuations, the scattering efficiency of CRs or the energy transfer from the streaming of CRs to these modes is still unclear and also their contribution in the increase of maximum energy of the particles in SNR. [125] demonstrated that for the efficient amplification of the magnetic field in this scenario, the modification in the particle spectral index is negligible for the accelerated particles at SNR shocks. Considering the non-resonant modes is out of scope in this dissertation anyway and I consider only the Alfvén waves as the scattering centre of CRs which can efficiently modify the particle spectra in the SNR which is in line with the observations [105] as well as the dynamics of CRs in the presence of these waves were widely studied.

3.4 Non-thermal emissions

As CRs are diffused during the propagation from their source to the earth in the presence of the magnetic field, it is impossible to track their sources directly. However, CRs are connected with astrophysical messengers such as photons and neutrinos as in the SNRs, mainly the accelerated electrons undergo synchrotron radiation and inverse Compton scattering, and on the other hand, the high-energetic protons produce neutral pion-decay emission. Hence, the SNR becomes observable in a wide range from radio waveband to very high energy gamma-rays and can be observed with different advanced instrumentation, mentioned in 3.4.1. Besides these above-mentioned non-thermal emissions, thermal emission originating from the hot plasma inside the remnant exists and this emission overlaps with the non-thermal component up to the X-ray band. In reality, for the X-ray emissions in the remnants, thermal components from low temperature and high temperature are prominent at low and high energy ends, respectively and in the intermediate energy range, synchrotron emission is dominant [133, 134].

[124]: Niemiec et al. (2008), 'Production of Magnetic Turbulence by Cosmic Rays Drifting Upstream of Supernova Remnant Shocks'

[125]: Pohl (2021), 'Time-dependent treatment of cosmic-ray spectral steepening due to turbulence driving'

[126]: Inoue et al. (2021), 'Direct Numerical Simulations of Cosmic-ray Acceleration at Dense Circumstellar Medium: Magnetic-field Amplification and Maximum Energy'

[127]: Amato et al. (2006), 'Non-linear particle acceleration at non-relativistic shock waves in the presence of self-generated turbulence'

[128]: Zirakashvili et al. (2008), 'Diffusive Shock Acceleration with Magnetic Amplification by Nonresonant Streaming Instability in Supernova Remnants'

[129]: Weisskopf et al. (2000), 'Chandra X-ray Observatory (CXO): overview'

[130]: Atwood et al. (2009), 'The Large Area Telescope on the Fermi Gamma-Ray Space Telescope Mission'

[131]: Aharonian et al. (2007), 'First ground-based measurement of atmospheric Cherenkov light from cosmic rays'

[132]: Salazar et al. (2008), 'Ground detectors for the study of cosmic ray showers'

Comment 3.4.1

Detection of photons: Space-based observatories like Chandra, XMM-Newton, NuStar for X-ray and Fermi-LAT telescope for gamma-rays [129, 130].
Ground-based Atmospheric Cherenkov Telescopes [131, 132] like VERITAS, HESS, and MAGIC for very high-energy gamma-ray detection and HAWC, LHAASO to detect gamma-ray emissions above TeV energies.

[133]: Reynolds (1998), 'Models of Synchrotron X-Rays from Shell Supernova Remnants'

[134]: Borkowski et al. (2001), 'Thermal and nonthermal X-ray emission in supernova remnant RCW 86'

Further, the thermal X-ray emission is seen as line emission with the synchrotron continuum and the non-thermal X-ray components are generally persistently present during the SNR lifetime in certain energy bands without the significant contribution from the thermal counterpart. In this thesis, I study only the non-thermal emissions, synchrotron radiation, inverse Compton scattering, and neutral pion-decay emission from the SNRs.

3.4.1 Synchrotron radiation

Relativistic electrons gyrating around the magnetic field lines radiate their energy in the form of electromagnetic waves, this is known as synchrotron radiation. This process was widely studied in [135, 136].

[135]: BLUMENTHAL et al. (1970), 'Bremsstrahlung, Synchrotron Radiation, and Compton Scattering of High-Energy Electrons Traversing Dilute Gases'
[136]: Schwinger (1949), 'Quantum Electrodynamics. III. The Electromagnetic Properties of the Electron—Radiative Corrections to Scattering'

The rate of total energy loss of an electron with energy E_e gyrating in the magnetic field B can be expressed as-

$$-\dot{E}_{e,syn} = \frac{4}{3}\sigma_T c U_B \gamma_L^2 \beta^2 \tag{3.4.1}$$

assuming the isotropic pitch angle distribution for the electron arising from the irregularities in the magnetic field and here σ_T refers the Thomson cross-section $U_B(= B^2/8\pi)$ denotes the magnetic field energy density, γ_L is the Lorentz factor and β is the electron velocity in the unit of c.

Comment 3.4.2

Thomson cross-section:
$\sigma_T = \frac{8\pi}{3}\left(\frac{e^2}{m_e c^2}\right)^2 = 6.6524 \times 10^{-25}\,cm^2$, where m_e is the electron mass.

This energy loss from the electron is transferred to electromagnetic radiation and, so, the emitted radiation ($\propto B^2$) would be directly linked to the magnetic field in the system. In the relativistic limit, the total synchrotron power ($P_{syn}(\nu)$) emitted by a single electron follows,

$$\begin{aligned} P_{syn}(\nu) &= \frac{\sqrt{3}e^3 B_\perp}{2\pi m_e c^2}\left(\frac{\nu}{\nu_c}\right)\int_{\nu/\nu_c}^{\infty} K_{5/3}(\eta)d\eta \\ &= \frac{\sqrt{3}e^3 B_\perp}{2\pi m_e c^2} F\left(\frac{\nu}{\nu_c}\right) \end{aligned} \tag{3.4.2}$$

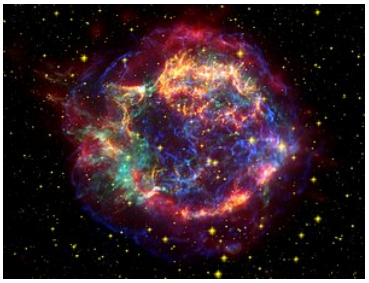

Figure 3.4.1: Multi-wavelength observation of Cas A:
The current age of Cas A is ≈ 300yrs and diameter is ≈ 3pc. The filaments of cool gas are observed in visible yellow light and the blue colour traces the high-energy X-ray emissions.
Image credit- Spitzer Space Telescope for infrared data (red), Hubble Space Telescope for optical emission (yellow), X-ray data from Chandra (blue and green)

.

where ν is the frequency of the emitted radiation, $B_\perp$ is the magnetic field perpendicular to the direction of the electron propagation, $\nu_c = \frac{3\gamma_L^2 e B_\perp}{2m_e c}$ refers to the critical frequency, and $K_{5/3}$ denotes the modified Bessel function of order 5/3. The function $F(\frac{\nu}{\nu_c})$ peaks near $\nu \sim 0.3\nu_c$. The total power spectrum, $P_{syn}(\nu)$ radiated by a population of electrons can be calculated by integrating $P_{syn}(\nu)$ over the electron distribution, for instance, the power-law distributed electrons,

$\frac{dN_e}{d\gamma_L} \propto \gamma_L^{-s}$ produces the synchrotron power that also follows a power-law,

Comment 3.4.3

For non-thermal synchrotron emission, $\gamma_L \approx \sqrt{\frac{\nu}{\nu_L}}$, where $\nu_L = \frac{eB}{2\pi m_e c}$

$$P_{syn}(\nu) \propto \nu^{-\frac{s-1}{2}} \equiv \nu^{\alpha}$$
$$\alpha = -\frac{s-1}{2} \tag{3.4.3}$$

In reality, the electron spectra can be a broken power law instead of a power law with a specific index. This situation is quite clear in the case of Cas A, shown in Figure 3.4.1. The spectral index from radio to infrared is demonstrated in Figure 3.4.2 taken from [137], which implies a deviation from $\alpha = -0.5$, predicted if $s = 2$ from the standard DSA. Further, the non-thermal synchrotron spectrum will also have a characteristic cut-off, following the magnetic field and the cut-off of the electron spectrum.

[137]: Domček et al. (2020), 'Mapping the spectral index of Cas A: evidence for flattening from radio to infrared'

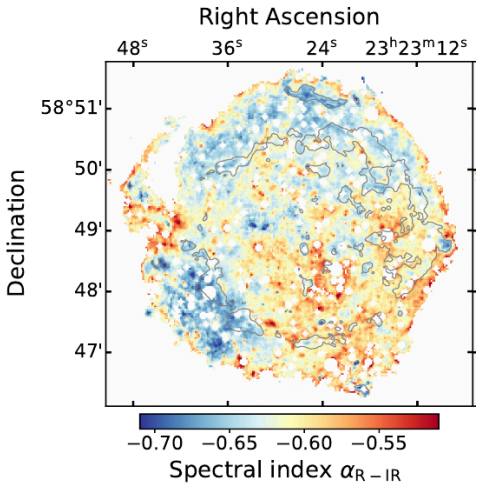

Figure 3.4.2: Radio to mid-infrared spectral index map of Cas A from [137]. The mean radio spectral index for Cas A is $\alpha_R \sim -0.77$ and radio to infrared spectra index $\alpha_{R-IR} \sim -0.61$.

3.4.2 Inverse Compton scattering

The inverse Compton scattering occurs during the interaction between the high-energetic electrons and low-energy photons. In this process, electrons transfer energy to photons and upscatter them to higher energies which can be in the gamma-ray energy band. The inverse Compton scattering process was studied in [136], [138].

[138]: Coppi et al. (1990), 'Reaction rates and energy distributions for elementary processes in relativistic pair plasmas'

I consider that the energy of the photon is E_{rad} in the laboratory frame and E'_{rad} in the electron rest frame. Then, the Klein-Nishina formula representing the total cross section σ_{IC} for the inverse Compton scattering can be written as [96],

$$\sigma_{IC} = 2\pi\left(\frac{e^2}{m_e c^2}\right)^2\left[\frac{1+\epsilon}{\epsilon^2}\left(\frac{2(1+\epsilon)}{1+2\epsilon} - \frac{1}{\epsilon}\ln(1+2\epsilon)\right) + \frac{1}{2\epsilon}\ln(1+2\epsilon) - \frac{1+3\epsilon}{(1+2\epsilon)^2}\right] \tag{3.4.4}$$

where $\epsilon = \frac{E'_{rad}}{m_e c^2}$. Then, if E'_{rad} is less than the electron rest mass energy, $E'_{rad} \ll m_e c^2$, then after scattering by the electron the energy of the photon in the electron rest frame remains same. This approximation is called the "Thomson" limit. Further, if E'_{rad} is comparable or higher than the electron rest mass energy, then this is known as "Klein-Nishina" limit.

$$\sigma_{IC} \approx \begin{cases} \sigma_T & \text{Thomson limit} \\ \frac{3}{8}\sigma_T \frac{1}{\epsilon}(\ln(2\epsilon) + \frac{1}{2}) & \text{Klein-Nishina limit} \end{cases} \tag{3.4.5}$$

In Thomson limit, the rate of energy loss for electrons while interacting with a photon field of energy U_{rad} which can be expressed as, $U_{rad} = n_{rad} E_{rad}$, where $n_{rad} \rightarrow$ photon number density, is given by,

$$-\dot{E}_{e,IC} = \frac{4}{3}\sigma_T c U_{rad} \gamma_L^2 \beta^2 \tag{3.4.6}$$

So, the ratio of inverse Compton to synchrotron radiation energy losses-

$$\frac{\dot{E}_{e,IC}}{\dot{E}_{e,syn}} = \frac{U_{rad}}{U_B} \tag{3.4.7}$$

Further, in this Thomson regime, the spectral index of the emitted photons is the same as the synchrotron radiation from the same power-law distribution of electron energies.

For SNRs, inverse Compton emission originates mainly from the scattering of the photons from CMB in the Thomson limit. Besides, scattering of the optical photons and infrared photons which can be in the Klein-Nishina limit can also contribute to inverse Compton emission from the remnant, depending on the location of the SNR in the galactic disk. In this context, [139] estimated that the contribution of infrared and optical photons to inverse Compton emission is not significant to that of CMB photons except for SNRs residing near the Galactic centre.

[139]: Porter et al. (2006), 'Inverse compton emission from galactic supernova remnants: effect of the interstellar radiation field'

3.4.3 Pion-decay emission

The interaction of accelerated higher energetic protons with the thermal plasma in the remnant gives rise to the emission of gamma-ray photons. In this process, initially, the inelastic collision between hadrons produces pions and among them, the neutral pion decays into gamma rays and the produced gamma rays carry $\sim$ 17% kinetic energy of protons in GeV – TeV energies [140].

[140]: Hinton et al. (2009), 'Teraelectron-volt astronomy'

$$\begin{aligned} p + p &\rightarrow \pi^+ + \pi^- + \pi^0 + X \\ \pi^0 &\rightarrow \gamma + \gamma \end{aligned} \tag{3.4.8}$$

The spectral production rate ($Q_{s,T}$) of gamma-ray, formed in the collisions of projectile particles of type s, that are accelerated particles in SNR shock, with target material T, present in the ambient plasma is given by,

$$Q_{s,T} = n_T \int N_{CR,s}(E_{CR}) \beta c \sigma_{s,T} \left(\frac{dN_\gamma}{dE}\right)_{s,T} dE_{CR} \tag{3.4.9}$$

where $N_{CR,s}$, E_{CR} are the differential CR density of respective species s, and the total energy per CR nucleon, respectively, E refers to the energy of gamma-ray, n_T, $\sigma_{s,T}$ are the number density of respective target nuclei and the inelastic cross-section for corresponding collisions, respectively, and $(\frac{dN_\gamma}{dE})_{s,T}$ is the multiplicity spectrum of gamma rays. The cross-section, $\sigma_{s,T}$ hardly changes in the higher energy range, 100 GeV – 100 TeV and the spectral index of produced gamma-ray spectra roughly follow the spectral index of the distribution of parent protons. Further, to produce gamma-ray through neutral pion-decay, the protons should have minimum energy of 280 GeV [141].

[141]: Drury et al. (1993), 'The gamma-ray visibility of supernova remnants: a test of cosmic ray origin'

The ambient medium of the core-collapse SNRs is chemically enriched as the CSM, structured by the stellar winds from massive stars contains the distribution of heavy materials, including carbon, oxygen, and iron along with hydrogen and helium [142]. Furthermore, the chemical composition and, hence the metallicity of stellar winds in different stages of stellar evolution should be varied [143]. Therefore, the hadronic gamma-ray emissions from the remnants should differ while the SNR evolves through the ambient medium created by the progenitor star during evolutionary ages because of the change in target materials, according to Equation 3.4.9. Figure 3.4.3 demonstrates this change in hadronic gamma-ray emission on account of the presence of different compositions in the ambient medium.

[142]: Szécsi, Dorottya et al. (2015), 'Low-metallicity massive single stars with rotation - Evolutionary models applicable to I Zwicky'

[143]: Bhatt et al. (2020), 'Production of secondary particles in heavy nuclei interactions in supernova remnants'

The gamma-ray spectra in [143] from an SNR residing in five

Components	ISM	RSG	WN	WO	WC
Hydrogen	0.71	0.639	0.20	0.0	0.0
Helium	0.28	0.349	0.78	0.14	0.55
Oxygen	2.06e-3	5.41e-3	0.0	0.24	0.05
Nitrogen	0.0	3.1e-3	1.5e-2	0.0	0.0
Carbon	2e-3	1.42e-3	1e-4	0.62	0.4
Iron	4e-4	1.35e-3	1.4e-3	0.0	1.6e-3

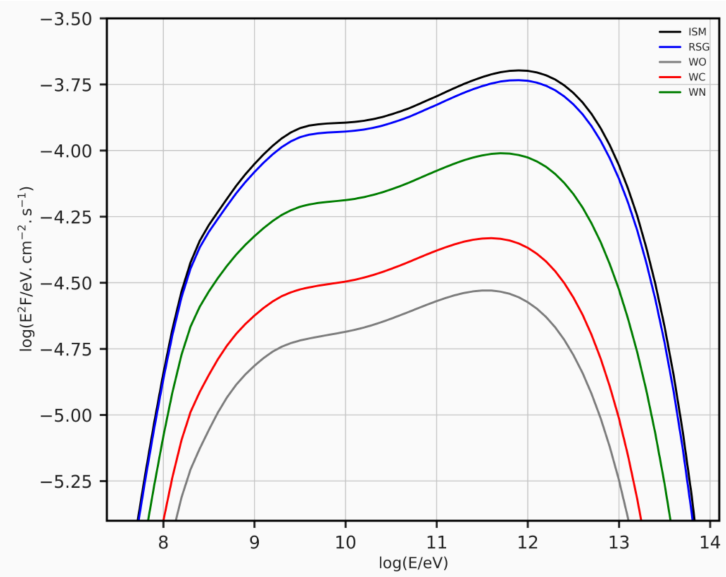

Figure 3.4.3: Hadronic gamma-ray spectra from a core-collapse SNR inside different stellar winds from [143].
Upper: Table of the mass fractions of different elements considered for the wind models.
Lower: Simulated gamma-ray spectra by using RATPaC (described in Chapter 4) from neutral pion-decay from an SNR expanding through the ambient medium with density $\rho_{\rm CSM} \propto r^{-2}$ where r is the radial distance from the star. The ambient medium is constructed considering the compositions of 5 scenarios such as ISM, RSG wind, and three different WR winds like WC, WO, and WN depending on the abundance of Carbon, Oxygen and Nitrogen. These simulated gamma-ray spectra show the corresponding cut-off energy shifts to the lower energies in the presence of heavier components in the stellar winds.

different environments depict that the wind material with heavy composition for WO, WC, and WN stars produces fewer gamma rays in comparison to the RSG wind and ISM with the similar compositions. This occurs because the number density of accelerated particles by the SNR shock scale with the number density of the plasma as described in Equation 4.1.2 and the number density of the plasma drops with the mass number if the plasma has the fixed mass density. Additionally, for the heavier composition, the cut-off energy for the gamma-ray spectra shifts to lower energies as the cut-off energy is proportional to the charge number. These results indicate that the observed gamma-ray spectrum from an SNR can be related to the higher cut-off energy of CRs if those CRs are heavy nuclei.

Therefore, the gamma-ray photons can be emitted from both the inverse Compton scattering and pion-decay emissions. This makes the determination of the gamma-ray origin quite challenging. For the SNRs located in the dense medium, the most probable gamma-ray origin should be hadronic as the gamma-ray spectra directly depend on the density of target

material, from Equation 3.4.9. Further, the characteristic cut-off of pion-decay emission at 280 MeV and the different spectral shapes of the leptonic and hadronic gamma-ray emissions may constrain the gamma-ray origin, as shown in Figure 3.4.4 through the gamma-ray emission from the SNR IC443 which demonstrates the low-energy cut-off in the gamma-ray spectra.

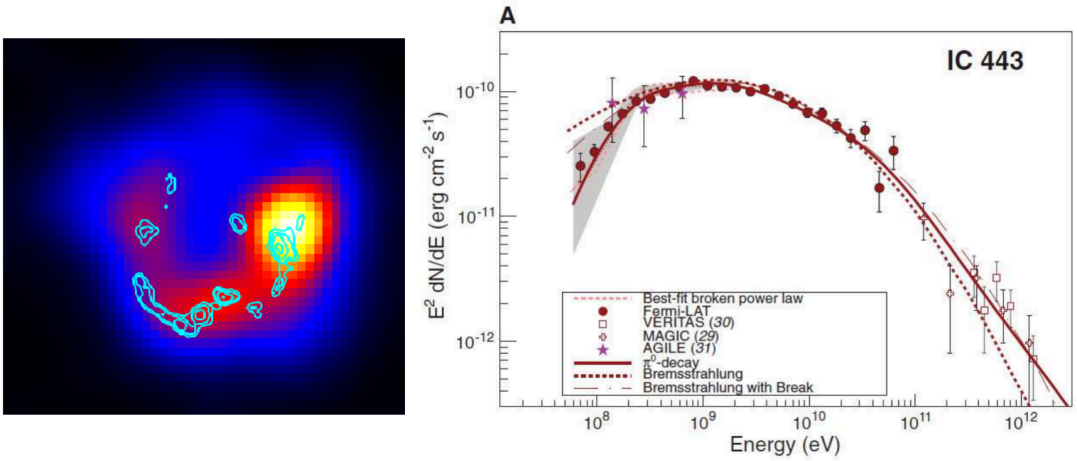

Figure 3.4.4: Gamma-ray emission from IC443
Left image: Gamma-ray emission from IC443 emitting from the region near SNR shock while it collides with the dense ISM material. The light blue contours show the density distribution of ISM gas, heated by the SNR shock.
Image credit- Cosmic-ray Research Division, Institute for Space–Earth Environmental Research, Nagoya University
Right image: Gamma-ray spectra of the SNR IC 443 and fitted models from [144, 145] shows the characteristic low-energy cut-off- implies to the hadronic-origin.

Next step: In this Chapter, I mention the particle acceleration mechanism at the SNR shock and the non-thermal emissions from the SNRs through the theoretical approach. The following Chapter 4 will provide the reader with a method of numerical modelling elaborately regarding particle acceleration.

[144]: Sasaki (2014), 'Multi-Wavelength View of Supernova Remnants'
[145]: Ackermann et al. (2013), 'Detection of the Characteristic Pion-Decay Signature in Supernova Remnants'

Numerical method- simulation of CR acceleration in SNR

4

In the DSA mechanism, particles are scattered off from MHD fluctuations, present in the downstream and upstream plasma of the SNR shock that induces the energy gain of particles by crossing the shock which I explain in Chapter 3. This acceleration mechanism has been studied by several state-of-the-art numerical techniques, for instance, the complete study of the generation of plasma instabilities along with the electron and ion dynamics based on kinetic Particle-in-cell (PIC) simulations [146, 147] described briefly in Comment 4.0.1. Although this PIC method provides many insights into the structure of SNR shocks and the microphysics [148], this method is quite computationally expensive as it includes the spatial and temporal scale larger than several ion-gyro radii or ion-gyro times, respectively with the resolution of small electron scales typically the skin depth defined in Definition 4.0.1, simultaneously.

Definition 4.0.1 ***Skin depth*** **($\lambda_{s,e}$):** *This is one of the fundamental length scales of plasma physics and for electrons, this is defined as:*

$$\lambda_{s,e} = \frac{c}{\omega_{pe}} \sim (5.3 \times 10^5\,\mathrm{cm}) \left(\frac{n_e}{1\,\mathrm{cm}^{-3}}\right)^{-1/2}$$

where ω_{pe} is the the plasma frequency, and n_e refers the medium density.

Hence, simulations based on the PIC method are temporally constrained to the scales of the order of a few to a few hundred ion-gyro times because of the computational expense. Consequently, the achieved time span from these simulations is much smaller than the acceleration time of the particles to the highest energies which are considered to be comparable with the lifetime of the SNR, typically a few thousand years as expressed in Equation 3.3.23 and also spatially, PIC simulations are restricted up to approximately $10^3 - 10^4$ km while typically for SNRs, the spatial size is several parsecs. Therefore, to limit the computational expense, arbitrarily reduced ratios of ion and electron masses, m_i/m_e, as well as very fast SNR shocks (> 0.1c) are generally considered in these simulations [149].

Comment 4.0.1

PIC method: Plasma is considered an ensemble of computational particles having charge and mass which can be located between the grid points. Electromagnetic fields

[146]: Amano et al. (2008), 'ELECTRON SHOCK SURFING ACCELERATION IN MULTIDIMENSIONS: TWO-DIMENSIONAL PARTICLE-IN-CELL SIMULATION OF COLLISIONLESS PERPENDICULAR SHOCK'

[147]: Umeda et al. (2009), 'ELECTRON ACCELERATION AT A LOW MACH NUMBER PERPENDICULAR COLLISIONLESS SHOCK'

[148]: Marcowith et al. (2016), 'The microphysics of collisionless shock waves'

[149]: Pohl et al. (2020), 'PIC simulation methods for cosmic radiation and plasma instabilities'

[150]: Birdsall et al. (1991), *Plasma Physics via Computer Simulation*

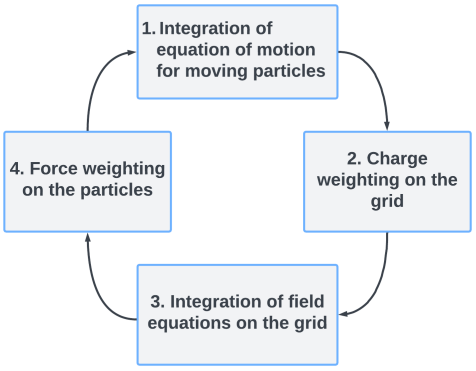

Figure 4.0.1: Computational cycle for PIC code, based on [150].

and charge and current densities (ρ_q, j) are defined at grid points. Figure 4.0.1 represents the cycle of computation.
1. Particle position ($\mathbf{x}$) and velocity ($\mathbf{v}$) at certain time point, t by advancing time from $t - \Delta t$ are derived from, $m\dot{\mathbf{v}} = q\,(\mathbf{E} + \mathbf{v} \times \mathbf{B})$, $\dot{\mathbf{x}} = \mathbf{v}$, where $\mathbf{E}$, $\mathbf{B}$ are the electric and magnetic field, respectively, q refers as particle charge.
2. (ρ_q, j) on the grid point are computed from ($\mathbf{x}$, $\mathbf{v}$) using weighting schemes like nearest-grid-point and cloud-in-cell methods.
3. Maxwell's equations are solved for deriving $\mathbf{E}$ and $\mathbf{B}$ on the grid point.
4. Similarly to the charge weighting, electromagnetic fields acting on particles are interpolated from the grid points using weighting schemes to calculate $\mathbf{x}$ and $\mathbf{v}$ at advanced time points.

However, [151] discussed that the pre-acceleration of thermal electrons, described in Comment 3.3.1 strongly depends on the choice of the parameters like m_i/m_e, the SNR shock velocity, the angle between the magnetic field and the shock normal (θ_{Bn}) as well as the shock Alfvénic Mach number ($\mathcal{M}_A$), and sonic Mach number ($\mathcal{M}_n$). Besides, there is another approach, called the PIC-hybrid method [152], where the computational expense is reduced by treating ions as particles and electrons as massless fluid, thus eliminating the electron kinetics. This method seems to provide efficient particle acceleration in the presence of quasi-parallel shocks, approximately up to $\theta_{Bn} < 50°$. But, the PIC-MHD approach [153, 154] where non-thermal ions and thermal gas are treated as individual particles and fluid, respectively shows that oblique shocks with $\theta_{Bn} \approx 70°$ can efficiently accelerate particles. Therefore, these simulations suggest that the particle acceleration is quite dependent on the simulation methods as well as parameters, which regulate the DSA mechanism by constraining the formation of magnetic field instabilities in the shock upstream [155].

Cosmic ray acceleration at the SNR shock was also probed by using a different numerical approach where both the thermal plasma and CRs are treated as two different fluids [156] during the lifetime of SNR in three dimensions. This approach demonstrates the effect of the magnetic obliquity-dependent shock acceleration of particles on the shock dynamics and the connection between the upstream magnetic field configurations and CR distributions. This approach can produce the TeV− gamma-ray morphology for SNRs, SN 1006 and Vela Jr reasonably consistent with observations [157, 158], by considering dominant advective CR transport. However, this method is incapable of predicting the spectral shape of accelerated particles in simulations as CRs are treated as a fluid although the spectral information is crucial to characterise the non-thermal emissions from SNRs, discussed in Section

[151]: Riquelme et al. (2010), 'Electron Injection by Whistler Waves in Non-relativistic Shocks'

[152]: Caprioli et al. (2014), 'Simulations of Ion Acceleration at Non-relativistic Shocks. I. Acceleration Efficiency'

[153]: Marle et al. (2018), 'On magnetic field amplification and particle acceleration near non-relativistic astrophysical shocks: particles in MHD cells simulations'

[154]: Marle et al. (2022), 'Diffusive Shock Acceleration at Oblique High Mach Number Shocks'

[155]: Kumar et al. (2021), 'Nonthermal Particle Acceleration at Highly Oblique Nonrelativistic Shocks'

[156]: Pfrommer et al. (2017), 'Simulating cosmic ray physics on a moving mesh'

[157]: Pais et al. (2018), 'The effect of cosmic ray acceleration on supernova blast wave dynamics'

[158]: Pais et al. (2020), 'Constraining the coherence scale of the interstellar magnetic field using TeV gamma-ray observations of supernova remnants'

3.4.

Another effective way to explore the shock acceleration in SNRs is by treating the thermal plasma as a fluid with considering the kinetics of CRs as discussed in [159, 160] which ensures the derivation of the spectral shapes of accelerated particles during the lifetime of SNRs with the feasible computational expense. This method is applied to obtain the DSA mechanism in test-particle approximation at the SNR shock in this thesis using Radiation Acceleration Transport Parallel Code (RATPaC) [161, 162].

In this chapter, I give an overview of this code structure followed by the implemented changes to achieve the aim of this thesis: "Modelling particle acceleration in core-collapse SNRs inside circumstellar wind-blown bubbles". In this dissertation, I only look into the DSA mechanism at the SNR forward shock. Modelling the DSA process time-dependently

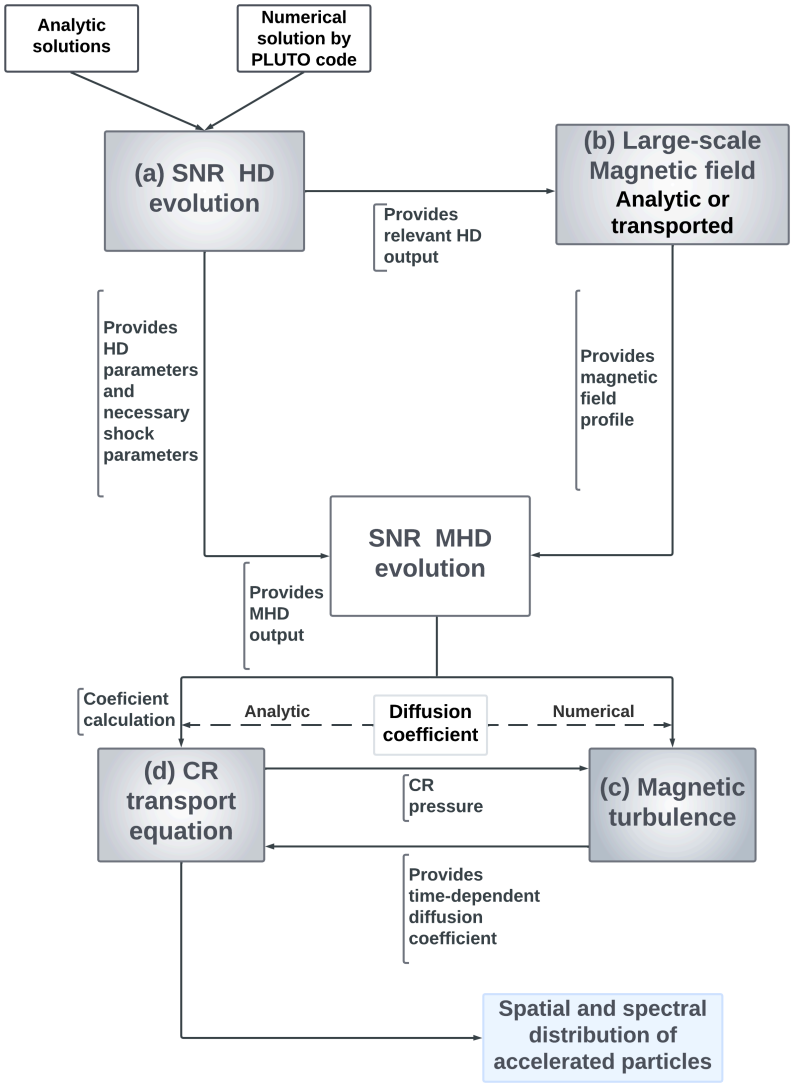

Figure 4.0.2: Structure of RATPaC. RATPaC is a fully time-dependent Python code that uses the FiPy-package [163] to solve partial differential equations numerically. The filled-grey boxes represent the major modules of the code to solve: (a) HD, (b) induction equation if the transported mode is used, (c) transport equation for scattering magnetic turbulence if diffusion coefficient is calculated time-dependently, and (d) CR transport equation. I discuss these equations later in this chapter. Finally, the spatial and spectral distribution of accelerated particles has been achieved time-dependently through the DSA.

at the SNR shock with test-particle approximation in 1-dimensional spherical symmetry comprises different necessary constituents which are the hydrodynamic (HD) evolution of the SNR, the evolution of large-scale magnetic field

[159]: Ptuskin et al. (2010), 'SPECTRUM OF GALACTIC COSMIC RAYS ACCELERATED IN SUPERNOVA REMNANTS'
[160]: Zirakashvili et al. (2012), 'Numerical simulations of diffusive shock acceleration in SNRs'

[161]: Telezhinsky, I. et al. (2012), 'Time-dependent escape of cosmic rays from supernova remnants, and their interaction with dense media'
[162]: Telezhinsky et al. (2013), 'Acceleration of cosmic rays by young core-collapse supernova remnants'

[163]: Guyer et al. (2009), 'FiPy: Partial Differential Equations with Python'

profile, a prescription for diffusion, and finally the solution of the CR transport equation.
In *RATPaC*, these components are directed to different modules as schematically represented in Figure 4.0.2 with their functionality and this construction of the code ensures to deal with these modules in multiple scenarios with different complexities. For instance, the required diffusion coefficient for the solution of the CR transport equation, expressed in Equation 4.1.1 can be calculated by simply using the Bohm-like diffusion coefficient or by solving the transport equation for the magnetic turbulence, numerically in a complicated framework. Further, the communication between these modules is established through a separate module called solver. The CR transport equation is solved time-dependently to derive the distribution of accelerated particles in the phase-space at every time step and thus, the particle spectra are obtained time-dependently.

4.1 CR transport equation

The time-dependent transport equation for the differential number density of CRs, $N(r, p, t)$ can be obtained from Equation 3.3.16,

$$\frac{\partial N}{\partial t} = \nabla(D\nabla N - \mathbf{u}N) - \frac{\partial}{\partial p}\left(\dot{p}N - \frac{\nabla.\mathbf{u}}{3}Np\right) + Q \quad (4.1.1)$$

where D is the spatial diffusion coefficient, $\dot{p}$ corresponds to energy loss rate, synchrotron losses and inverse Compton losses for electrons and Q represents the source term.
This CR transport equation is solved numerically by transforming the spatial coordinate from r to $r^\star$, discussed in Definition 4.1.1 and by transforming the momentum coordinate p to $\ln p$ in order to capture the evolving SNR size from sub-parsec to tens of parsec scale and in momentum from the injection in a few tens of MeV/c to the cut-off range in TeV/c scale.

Definition 4.1.1 ***Radial coordinate transformation in RATPaC:*** *The SNR shock-centred coordinate is defined as,* $r_0 = \frac{r}{R_{\rm sh}(t)}$, *where* r *refers the radial coordinate, and* $R_{\rm sh}(t)$ *is the time-dependent SNR shock radius.*
To get a better spatial resolution near the shock, $\Delta r_0/R_{\rm sh}(t) \approx 10^{-6}$, *the radial coordinate transformed as,*
$r_0 - 1 = (r^\star - 1)^3$.
In RATPaC, the size of computation domain in $r^\star$*-coordinate is a free parameter and for the spatial outer grid boundary* $r^\star \gg 1$ *in this uniform coordinate system of* $r^\star$, *the extension of grid*

boundary to several tens of shock radius in the non-uniform coordinate system of r_0. Consequently, higher energetic particles can be tracked in the simulation that have already escaped from the vicinity of the shock but are still inside the far upstream region.

After this coordinate transformation, the CR transport equation is calculated in test-particle approximation in *RATPaC* by using the *FiPy* package. In this dissertation, to constraint, the simulation in test-particle approximation CR pressure is always kept below 10% of the shock ram pressure [111] by regulating the particle injection parameter, described below. Although [164] demonstrated that CR-feedback has an impact on driving the galactic outflows in ISM when CRs escape the SNR at the late evolutionary stage, CR-feedback is beyond the scope of this thesis.

[164]: Simpson et al. (2016), 'The Role of Cosmic-Ray Pressure in Accelerating Galactic Outflows'

Injection of particles

The source term in the CR transport equation is defined by,

$$Q = \eta_{\mathrm{inj}} n_{\mathrm{u}} \left(V_{\mathrm{sh}} - u_{\mathrm{u}}\right) \delta\left(R - R_{\mathrm{sh}}\right) \delta\left(p - p_{\mathrm{inj}}\right) \qquad (4.1.2)$$

where η_{inj} is the injection efficiency, n_{u} and u_{u} are the upstream plasma number density and velocity in the simulation frame, respectively, V_{sh} refers to the SNR forward shock velocity in the simulation frame which is observers frame and p_{inj} represents the momentum of injected particles.
Following the thermal leakage injection model from [165], p_{inj} is defined as, $p_{\mathrm{inj}} = \xi\, p_{\mathrm{th}}$ where ξ is the injection parameter, and p_{th} refers the momentum at the thermal peak of Maxwell distribution in the downstream region at temperature T_{d}, hence $p_{\mathrm{th}} = \sqrt{2 m k_{\mathrm{B}} T_d}$, m referees the mass of corresponding CR constituents. This considered injection model is a simplified prescription and specifically, for electrons which require pre-acceleration to a certain energy level to get involved in the DSA at the shock as described in Comment 3.3.1. However, the injection parameter is necessary to define the injection momentum in this model and so, the consideration of the electron pre-acceleration is not needed. Further, the acceleration of electrons well above a few tens of MeV energy is focused on in this dissertation and hence, the details about the pre-acceleration mechanism for electrons are out of scope.
Here, the injection efficiency, η_{inj} is calculated under the condition that the total number of particles in the non-thermal spectrum equals the number of particles in Maxwell distribution with momentum greater than p_{inj}. Thus, η_{inj} can be expressed as,

[165]: Blasi et al. (2005), 'On the role of injection in kinetic approaches to non-linear particle acceleration at non-relativistic shock waves'

$$\eta_{\rm inj} = \frac{4}{3\pi^{1/2}} \left(r_{\rm sub} - 1\right) \xi^3 \exp\left(-\xi^2\right) \tag{4.1.3}$$

where $r_{\rm sub}$ represents the compression ratio for sub-shock calculated in the shock rest frame. As mentioned in Comment 3.3.1, pre-acceleration of CR electron is necessary to participate in the DSA mechanism at the shock but in this simplified thermal leakage model, the relevant parameters for CR electron injection are considered in such a way so that the considering the detailed pre-acceleration process is not required. Furthermore, I have injected electrons and protons at the same injection parameter, ξ in the simulations in this thesis, so the electron-to-proton ratio at higher energy can be determined by their mass ratio, $K_{\rm ep} \sim \sqrt{m_{\rm e}/m_{\rm p}}$ [166].

[166]: Pohl (1993), 'On the predictive power of the minimum energy condition. I-Isotropic steady-state configurations'

To calculate the different terms mentioned in the CR transport equation, the profiles for HD parameters, large-scale magnetic field configuration and diffusion coefficient for accelerated particles are necessary and hence, I describe the other modules of *RATPaC* with these respective contributions.

[167]: Cox (1972), 'Cooling and Evolution of a Supernova Remnant'

4.2 Hydrodynamics

The HD evolution of SNRs is calculated in two different modes in *RATPaC*. One mode uses the analytic solutions of different phases, described in Section 2.5 of the SNR, and another one solves the HD evolution of the SNR during its lifetime through numerical solutions by using *PLUTO* code [42].
In the framework of the analytic solution, the SNR hydrodynamics is prescribed by using the self-similar solutions, described in [70] during the free-expansion stage while the Sedov-Taylor dynamics, provided by Equation 2.5.4 is calculated following the derivation by [167].
However, the derivation of the HD evolution of the core-collapse SNR (see Definition 4.2.2) inside the complex wind bubble as discussed in Section 2.4, demands the time-dependent numerical solutions for finding the distributions of hydrodynamic parameters such as flow density, velocity, pressure, and temperature along with the SNR shock parameters like shock radius and velocity. Therefore, I only use the *PLUTO* code for solving the SNR hydrodynamics.

[168]: LeVeque (2002), *Finite Volume Methods for Hyperbolic Problems*
[169]: Toro (2009), 'Riemann Solvers and Numerical Methods for Fluid Dynamics: A Practical Introduction'

Comment 4.2.1

Finite volume method: This method provides the weak solution of partial differential equations, specifically given by the conservation laws in integral form. In this scheme, the computational domain is divided into a finite number of non-overlapping control volumes, so-called cells. Then, the integral form of conservation law is discretised and imposed on each cell [168, 169]. In each cell, the solution is defined as the cell average of the conserved quantity over the finite volume of the individual cell.

PLUTO code is applied to solve the Euler HD equations in this dissertation that read,

$$\frac{\partial}{\partial t}\begin{pmatrix}\rho\\ \mathbf{m}\\ E\end{pmatrix}+\nabla.\begin{pmatrix}\rho\mathbf{u}\\ \mathbf{m}\mathbf{u}+P\mathbf{I}\\ (E+P)\mathbf{u}\end{pmatrix}^{T}=\begin{pmatrix}0\\ 0\\ S\end{pmatrix} \tag{4.2.1}$$

$$\frac{\rho\mathbf{u}^2}{2}+\frac{P}{\gamma-1}=E;\quad \gamma=\frac{5}{3} \tag{4.2.2}$$

where ρ, $\mathbf{u}$, $\mathbf{m}$, P, E, and S refer to the mass density, velocity, momentum density, thermal pressure, the total energy density including the sum of specific internal energy and specific kinetic energy, and the source–sink term, respectively, and $\mathbf{I}$ is the unit tensor. I describe the design of *PLUTO* code along with the computation of HD equations using this code below.

***PLUTO* code:** This code is written in C programming language and provides solutions for hypersonic flows even in the presence of discontinuities in different geometries like Cartesian, cylindrical, and spherical along with in one, two, and three dimensions, efficiently. *PLUTO* has been constructed to solve the conservation law in the form of a set of partial differential equations,

$$\frac{\partial \mathbf{U}}{\partial t}=-\nabla.\mathbf{T}(\mathbf{U})+\mathbf{S}(\mathbf{U}) \tag{4.2.3}$$

where $\mathbf{U}$ refers to the state vector of conservative quantity, $\mathbf{T}(\mathbf{U})$ and $\mathbf{S}(\mathbf{U})$ are defined as the rank 2 tensor, rows of which are the fluxes of each component of $\mathbf{U}$ and source-sink terms, respectively, based on the finite volume method using Godunov-type high-resolution shock-capturing scheme [170] as the building block, where the computation of the numerical fluxes at cell interfaces is executed by applying the solution of a Riemann problem.
According to the finite volume method formulation defined in Comment 4.2.1, Equation 4.2.3 can be written as, $\partial_t\, \mathrm{U}_1(\mathrm{x},t)+\partial_x \mathrm{f}(\mathrm{U}_1(\mathrm{x},t))=0$ in one dimension, neglecting the source term, where U_1, $\mathrm{f}(\mathrm{U}_1)$ are one of the conservative quantities and the corresponding flux, respectively. Now, for the one-dimensional computational domain as shown in Figure 4.2.1, in the semi-discrete scheme, the integration of the above conservation equation over the cell $\mathrm{W_i}$ gives [171],

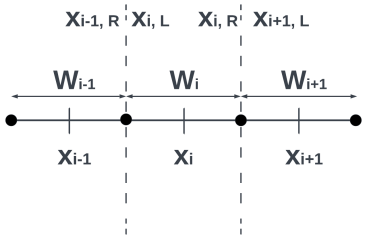

Figure 4.2.1: Schematic of computational cells in one dimension: The cell $\mathrm{W_i}$ and neighbouring cells $\mathrm{W_{i\pm1}}$ with cell centres $\mathrm{x_i}$, and $\mathrm{x_{i\pm1}}$, respectively. The size of each cell is Δx considering their uniformity. The vertical dotted lines indicate the interface between two cells, located at $\mathrm{x_{\pm,L/R}}$.

[170]: Godunov (1959), 'A difference method for the numerical computation of discontinuous solutions of hydrodynamic equations'

[171]: Haider et al. (2018), 'A high-order interpolation for the finite volume method: The Coupled Least Squares reconstruction'

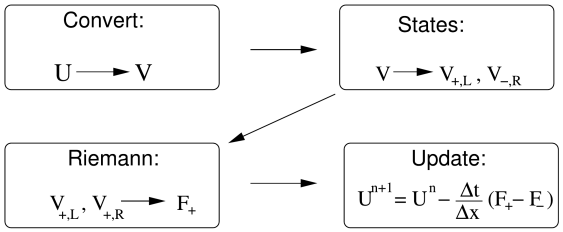

Figure 4.2.2: Schematic of the structure of *PLUTO* code from [42].

$$\begin{aligned}\partial_t\, q_i(t) &= -\frac{1}{\Delta x}\left[f_{i+\frac{1}{2}(t)} - f_{i-\frac{1}{2}}(t)\right] \\ &= -\frac{1}{\Delta x}\left[F\left(\omega_i[\mathbf{Q}(t)](x^L_{i+\frac{1}{2}}), \omega_{i+1}[\mathbf{Q}(t)](x^R_{i+\frac{1}{2}})\right)\right. \\ &\left. - F\left(\omega_i[\mathbf{Q}(t)](x^R_{i-\frac{1}{2}}), \omega_{i-1}[\mathbf{Q}(t)](x^L_{i-\frac{1}{2}})\right)\right] \end{aligned} \tag{4.2.4}$$

where,
1. $q_i(t)$ is the cell average of $U_1(x,t)$ for W_i cell
2. The vector $\mathbf{Q}(t) = (q_1(t), q_2(t), q_3(t), \ldots, q_N(t))^T$ for N cells
3. From the definition of the $q_i(t)$, calculation of the integral of fluxes $f_{i\pm1/2}$ require reconstructing the point-wise values of U_1 at the integration points on the left and right faces and in this process numerical process of high-order should be involved. $\omega_i[\mathbf{Q}(t)](x)$ is the interpolation function for reconstruction.
4. $F(q_L, q_R)$ is the numerical flux function.

The integration in Equation 4.2.3 is performed numerically by reconstruct-solve-average strategy in 4 steps in *PLUTO* code, as illustrated in Figure 4.2.2.

1. **Conversion:** The solution of Equation 4.2.3 can be formulated using the state vector of primitive or physical quantities, $\mathbf{V}$ instead of $\mathbf{U}$, for Equation 4.2.1, $\mathbf{U} = (\rho, \mathbf{m}, E)^T$ and $\mathbf{V} = (\rho, \mathbf{u}, P)^T$. The reason is that those chosen primitive variables impose physical constraints, for example, pressure positivity, subluminal speed, and so on, directly. Therefore, the first step is the conversion from conserved quantities to primitive variables, $\mathbf{U} \rightarrow \mathbf{V}$.
2. **Reconstruction:** The left and right states of the primitive variable for their defined values at the cell centre are computed through the interpolation routine as described through Equation 4.2.4, $\mathbf{V}_{\pm,L/R} = I(\mathcal{P}, \mathbf{V})$ where I refers to the interpolation routine, $\mathcal{P}$ is the piecewise polynomial approximation. This reconstruction method should satisfy different constraints like monotonicity to avoid spurious oscillations near discontinuities, pressure positivity and so on. In this dissertation, to solve the Euler HD equations I use 3^{rd}-Weighted-essentially-non-oscillatory scheme (WENO3) reconstruction inside a cell using 3-point stencil $S \equiv \{W_{i-1}, W_i, W_{i+1}\}$ [172]

[172]: Jiang et al. (1996), 'Efficient Implementation of Weighted ENO Schemes'

as shown in Figure 4.2.1.
3. **Riemann solver:** The Riemann problem involves a conservation equation and an initial condition, described by the piecewise constant data set, separated by a discontinuity, for instance, Riemann problems, $RP_{i,R}(V_i, V_{i+1})$ and $RP_{i,L}(V_{i-1}, V_i)$ at the interface $x_{i\pm1/2}$, for Figure 4.2.1 to get the corresponding numerical flux function, $F_\pm$, where ± refers to left (−) and right (+) cells of the corresponding cell. In this dissertation, I use the Harten-Lax-Van Leer approximate Riemann Solver that restores with the middle contact discontinuity (HLLC) [173] for solving the hydrodynamic evolution of SNRs.
4. **Temporal evolution:** Time marching algorithm provides the conservative quantities, at $t + \Delta t$, where Δt refer to the time step, by knowing their value at t, hence, $\mathbf{U}(t), F_\pm \implies \mathbf{U}(t+1)$. The time evolution of hydrodynamic simulations in this thesis is performed using 3^{rd}-order Runge-Kutta method (RK) method [174].

[173]: (1994), 'Restoration of the contact surface in the HLL-Riemann solver'

[174]: Jameson et al. (1981), 'Numerical Solution of the Euler Equations by Finite Volume Methods Using Runge-Kutta Time Stepping Schemes'

[175]: Courant et al. (1967), 'On the Partial Difference Equations of Mathematical Physics'

Definition 4.2.1 ***Courant-Friedrich-Lewy (CFL) condition:*** *This condition states as in a single time step Δt, any characteristic signal cannot cross more than one computational grid Δx, [175]. Therefore, this limits the time step following-*

$$\Delta t = \text{CFL.} \min\left(\frac{\Delta x}{v_\lambda}\right) \tag{4.2.5}$$

where v_λ is the largest signal velocity. The CFL number does not exceed 0.5 for the HD simulations in this thesis.

[176]: Gottlieb et al. (1997), 'On the Gibbs Phenomenon and its Resolution'

Comment 4.2.2

The solution of conservation laws can be oscillatory around the discontinuities. This is known as the **Gibbs phenomenon** [176]. This type of spurious oscillation can produce unphysical negative density or pressure that makes the code fail. Therefore, numerical stability can be obtained by choosing the suitable reconstruction method and solver so that the density and pressure never become negative at any cell during the lifetime of the SNR.

Further, I choose the specific reconstruction method and the Riemann solver combination to reduce the numerical oscillations and stabilise the HD simulations, discussed in Comment 4.2.2.

Implementation of *PLUTO* code in *RATPaC*: Although in test-particle approximation the HD equations are solved using *PLUTO*, independently from *RATPaC*, HD output is needed to pass efficiently from *PLUTO* to *RATPaC* during the simulation run time. For this, *PLUTO* is compiled as a shared C-library by replacing its main file and function with a dummy and then this shared library is loaded in *RATPaC* using the Ctypes structure class. This part of the code existed already before I start my simulations and was elaborately described in [177].

[177]: Brose (2020), 'From dawn till dusk : modelling particle acceleration in supernova remnants'

In *PLUTO*, $T = \frac{p}{\rho}\frac{\mu m_p u^2}{k_B}$, where μ, m_p are mean molecular weight and proton mass respectively, and k_B refers to Boltzmann constant

The HD parameters, ρ, $\mathbf{u}$, P, and temperature (T) are calculated by using *PLUTO*. Then, the location of the SNR shocks, specifically SNR forward shock in this thesis, the velocity of forward shock and HD parameters in the corresponding near downstream and upstream regions are calculated in *RATPaC* by getting HD data from *PLUTO*. Further, a shock resharpening strategy is implemented to get rid of the numerical smearing because of the jump conditions at the shock,

discussed in Equation 3.3.1. I state these issues by mentioning both the existing version and the newly implemented version during my PhD in the scenario of core-collapse SNRs in Section 4.4.

Definition 4.2.2 ***Initialise the supernova explosion inside the CSM for numerical modelling in one-dimension-***
The distribution of the supersonic stellar ejecta, resulting from supernova explosion discussed in Section 2.5 is needed to assume for modelling the SNR evolution inside the CSM as performing the simulation of supernova explosion mechanism is beyond the scope. The distribution of ejecta material depends on the explosion mechanism of the supernova. Here, I describe the stellar ejecta profile which is considered to initialise the structure of the core-collapse SNR for solving HD equations in this thesis.
The ejecta profile suggested by Chevalier [70], ejecta distribution extends to infinity. Following the Chevalier's formulation,

$$\rho_{\rm ej}(r) = \begin{cases} \rho_{\rm c}, & r \leq r_c \\ \rho_{\rm c}\left(\frac{r}{r_{\rm c}}\right)^{-n_{\rm ej}} & r > r_c \ , \end{cases} \tag{4.2.6}$$

$$u_{\rm ej}(r) = \frac{r}{T_{\rm SN}} \tag{4.2.7}$$

where $\rho_{\rm ej}$, $u_{\rm ej}$ refer to the ejecta density structure and velocity, respectively, $\rho_{\rm c}$ and $r_{\rm c}$ are the density of the inner plateau region and the radius of the transition point from the constant density region to the power-law distribution, respectively, $n_{\rm ej}$ is the power-law index of the outer ejecta and $T_{\rm SN}$ is the time since the supernova explosion. Further, the primary purpose of constructing the ejecta profile is to provide the stellar ejecta mass ($M_{\rm ej}$) after integrating over the radius up to the ejecta radius and supernova explosion energy ($E_{\rm ej}$) as the total kinetic energy of the ejecta. Therefore, using Equations 4.2.6 and 4.2.7,

$$\begin{aligned} M_{\rm ej} &= 4\pi \int_0^\infty r^2 \rho_{\rm ej}(r)\,{\rm d}r = 4\pi\rho_{\rm c} r_{\rm c}^3 \frac{n_{\rm ej}}{3\left(n_{\rm ej}-3\right)} \\ E_{\rm ej} &= 2\pi \int_0^\infty r^2 \rho_{\rm ej} u_{\rm ej}^2(r)\,{\rm d}r = \frac{2\pi\rho_{\rm c}}{T_{\rm SN}^2} r_{\rm c}^5 \frac{n_{\rm ej}}{5\left(n_{\rm ej}-5\right)}. \end{aligned} \tag{4.2.8}$$

Considering $M_{\rm ej}$ and $E_{\rm ej}$ as constraints, $r_{\rm c}$ and $\rho_{\rm c}$ can be ex-

pressed as,

$$r_c = \sqrt{\frac{10}{3}\frac{E_{ej}}{M_{ej}}\frac{n_{ej}-5}{n_{ej}-3}T_{SN}}$$
$$\rho_c = \frac{M_{ej}}{4\pi r_c^3}\frac{3\left(n_{ej}-3\right)}{n_{ej}}. \tag{4.2.9}$$

However, the ejecta distribution up to infinity cannot be applicable to numerical simulation and also the ejecta radius, R_{ej} should be finite as this is limited by the ejecta speed and feedback from pushing away the ambient CSM. Therefore, in RATPaC, the ejecta profile is modelled as,

$$\rho_{ej}(r) = \begin{cases} \rho_c, & r \le r_c \\ \rho_c \left(\frac{r}{r_c}\right)^{-n_{ej}}, & r_c < r \le R_{ej} \end{cases} \tag{4.2.10}$$

where outer radius of ejecta, R_{ej} is defined as the multiple of r_c, $R_{ej} = x r_c$. Hence, in the initialisation of the ejecta profile, I use the following expressions for r_c and ρ_c,

$$r_c = \left(\frac{10}{3}\frac{E_{ej}}{M_{ej}}\frac{n_{ej}-5}{n_{ej}-3}\frac{1-\frac{3}{n_{ej}}x^{3-n_{ej}}}{1-\frac{5}{n_{ej}}x^{5-n_{ej}}}\right)^{1/2} T_{SN} \tag{4.2.11}$$

$$\rho_c = \frac{M_{ej}}{4\pi r_c^3}\frac{3\left(n_{ej}-3\right)}{n_{ej}}\left(1-\frac{3}{n_{ej}}x^{3-n_{ej}}\right)^{-1} \tag{4.2.12}$$

considering, M_{ej}, E_{ej} are stored within the ejecta radius R_{ej}. Hence, using Equations 4.2.11, and 4.2.12, exact values for M_{ej} and E_{ej} can be obtained, regardless of the value of x. Therefore, technically any value of x can be taken for defining ejecta distribution, but R_{ej} should be considerably small because of the presence of CSM in the surroundings. Additionally, a lower value of x results in larger $\rho_{ej}(R_{ej})$ that can cause a sharp and high-density jump between ejecta distribution and the ambient density which may attribute to the numerical instability. Therefore, x should be chosen reasonably to maintain numerical stability. In this context, [178] also described the ejecta radius as a free parameter in the numerical study with the core-collapse SN ejecta.

[178]: Whalen et al. (2008), 'The destruction of cosmological minihalos by primordial supernovae'

4.3 Magnetic field

The magnetic field configuration inside SNRs is crucial for determining the diffusion coefficients and hence, for calculating the acceleration time (t_{acc}) for the particles with different energies, described in Definition 3.3.1 and Equation 3.3.22. Further, the magnetic field profile is also important

for regulating the energy loss of the electrons gyrating in the field and therefore, for calculating the synchrotron emissions from SNRs by following the expressions in the Equations 3.4.1 and 3.4.2.
The total magnetic field strength $B_{\rm tot}$ including the contribution from the magnetic turbulence to the background large-scale magnetic field is given by,

$$B_{\rm tot} = \sqrt{B^2 + B^2_{\rm turb}}\,, \tag{4.3.1}$$

where B and $B_{\rm turb}$ are the large-scale and turbulent magnetic fields, respectively.

4.3.1 Large-scale magnetic field profile

In *RATPaC*, there is a possibility to use different large-scale magnetic field profiles which are pre-defined inside the code together with the computation of the magnetic field induction equation using the HD parameters.

Analytic solution

One of the reasonable approximations about the magnetic field structure is considering the highly disordered upstream magnetic which gets compressed at the SNR shock. The radial component of the upstream magnetic field is not compressed but two tangential components are compressed at the shock, and hence, following [179] the magnetic compression ratio (r_B) becomes,

[179]: Marcowith, A. et al. (2010), 'Post-shock turbulence and diffusive shock acceleration in young supernova remnants'

$$r_{\rm B} = \sqrt{\frac{1 + 2r_{\rm sub}}{3}} \quad \text{and} \quad B_{\rm d} = r_{\rm B}\, B_{\rm u} \tag{4.3.2}$$

where $B_{\rm d}$, $B_{\rm u}$ are the downstream and upstream magnetic field strength, respectively. Therefore, for strong shock, $B_{\rm d} = \sqrt{11} B_{\rm u}$. This prescription for magnetic field configuration is denoted by the compressed magnetic field mode in *RATPaC* with the assumption of a constant $B_{\rm u}$. I model the DSA at the core-collapse SNR forward shock by considering this simple configuration as a test run to understand the direct influence of only HD on particle spectra as shown in Figure 4.3.2.

[180]: Pohl et al. (2005), 'Magnetically limited X-ray filaments in young supernova remnants'

Further, another reasonable analytic mode of the magnetic field profile in *RATPaC* is considering the damped downstream magnetic field. In this scenario, the turbulence formed in the upstream region and at the SNR shock by CR streaming instabilities is transferred to the shock downstream and eventually damped in the absence of turbulence driving [180]. Hence, the magnetic field profile in the downstream region can be parametrised as, $B_{\rm d}(r) = B_{\rm f} + (B_{\rm n} - B_{\rm f}) \exp\left(\frac{r - R_{\rm sh}}{l_{\rm d}}\right)$,

where R_{sh} refer to the SNR shock radius, B_f, B_n are far downstream and near downstream magnetic field, respectively, l_d refer to the damping length scale. [181] demonstrated the non-thermal emission from Vela Jr. SNR by using this magnetic field profile from *RATPaC* and Figure 4.3.1 shows in the SNR forward shock downstream, the comparison between this damped magnetic field and the numerical solution of the magnetic field, discussed below.

[181]: Sushch, Iurii et al. (2018), 'Modeling of the spatially resolved nonthermal emission from the Vela Jr. supernova remnant'

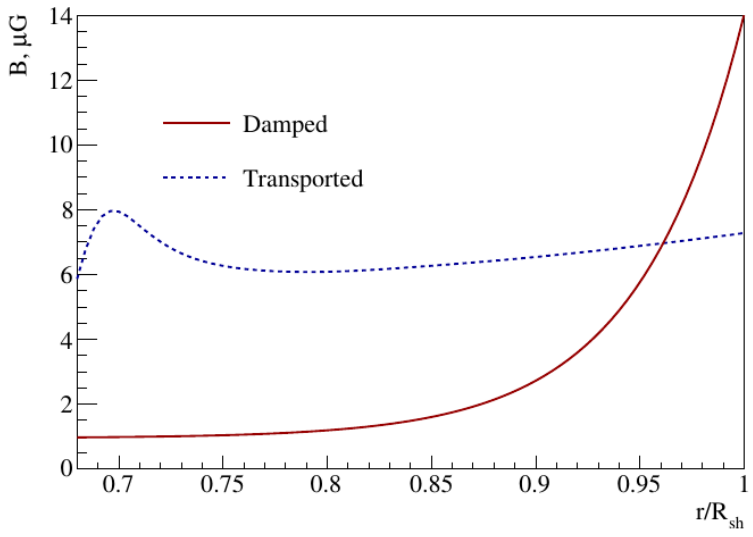

Figure 4.3.1: Comparison of radially dependent magnetic field strength including downstream magnetic field damping scenario and transported magnetic field from [181].
The profiles as the function of normalised radius show the magnetic field between contact discontinuity and the forward shock for Vela Jr. SNR where the red solid line represents the profile for the damped magnetic field scenario and the blue dashed line shows the transported magnetic field. The dissimilarities in field profiles lead to predicting the different radio, X-ray emissions and gamma-ray emission, and morphology, described in [181].

Numerical solution

Assuming the SNR is filled with a perfectly conducting fluid, the evolution of the frozen-in magnetic field (**B**) can be computed by applying the induction equation,

$$\frac{\partial \mathbf{B}}{\partial t} = \nabla \times (\mathbf{u} \times \mathbf{B}) \tag{4.3.3}$$

This equation is solved in one-dimensional spherical symmetry by using the *FiPy* package [163] in the co-moving frame of the shock in the $r^\star$ co-ordinate defined in Definition 4.1.1, by separating the radial and toroidal components of the magnetic field [162]. In this scenario, the upstream magnetic field profile should be considered and then, the numerical solution of Equation 4.3.3 provides the downstream magnetic field structure time-dependently during the lifetime of the SNR. Hence, the upstream magnetic field is transported to the downstream region through the shock, so I denote this magnetic field module as transported magnetic field in this thesis.

Figure 4.3.2 demonstrates the transported magnetic field (B_{tran}) configuration by assuming the CSM magnetic field in the upstream and the magnetic field peaks at contact discontinuity region in this scenario. B_{tran} also gives the different

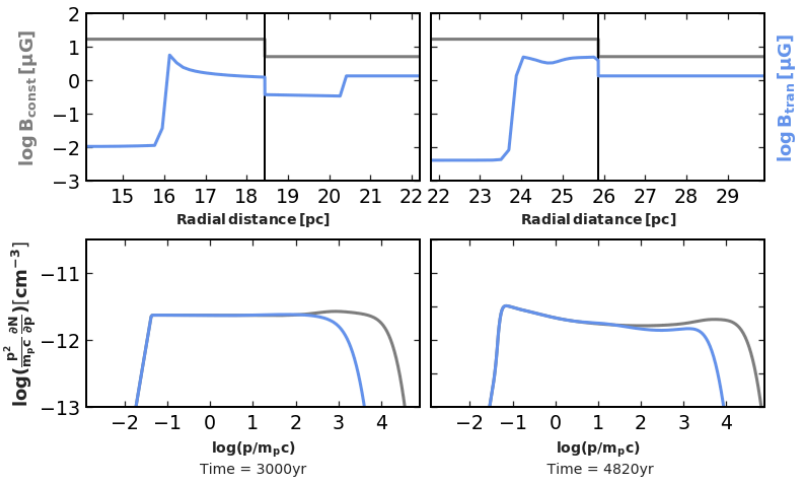

Figure 4.3.2: Large-scale magnetic field profile and influence on particle spectra.
The demonstrated transported magnetic field profiles and particle spectra correspond to core-collapse SNR with 60 $M_\odot$ progenitor described in Chapter 5. The first row depicts the configuration of two magnetic field profiles- the grey line denotes the constant upstream magnetic field compressed at the downstream scenario ($B_{\rm const}$), considering $B_{\rm u} = 5\mu$G and blue line represents the transported magnetic field $B_{\rm tran}$. The second row illustrates the volume-averaged SNR forward shock downstream proton spectra where N refers to the differential number density of CRs. The vertical lines show the SNR forward shock position.

values of the downstream magnetic field depending on evolution time which identifies the oversimplification of considering the constant upstream magnetic field compressed at the downstream scenario ($B_{\rm const}$) which is constant throughout the SNR evolution. Using these two magnetic field profiles while keeping the other parameters of DSA the same, I get proton spectra with different cut-offs and slightly different spectral shapes specifically at the higher energies. For $B_{\rm const}$ scenario, the maximum achievable energy by protons can be overestimated by the simplified analytic assumption. The CSM magnetic field and corresponding particle spectra are described in Chapter 5, elaborately.

Definition 4.3.1 ***Magnetic field in the SNR ejecta interpolated with the CSM magnetic field to initialise the large-scale magnetic field for numerical simulation:*** *The initial magnetic field in the supernova ejecta follows,*

$$B_{\rm ej}(r) \propto 1/r^2$$

satisfying $\nabla \cdot \mathbf{B_{ej}} = 0$ *and* $\nabla \times (\mathbf{u_{ej}} \times \mathbf{B_{ej}}) = 0$ *for both the radial and the toroidal field components. The normalisation is considered to provide a volume-averaged magnetic field of* $B_{\rm ej,0}$ *when the SNR radius is* $r_{\rm ej,0}$ *as described in [162]. Therefore, the magnetic field in ejecta can be expressed as,*

$$B_{\rm ej}(r, t_0) = \left(\frac{B_{\rm ej,0}}{\sqrt{3}}\right)\left(\frac{r_{\rm ej,0} R_{\rm ej}}{r\, R_{\rm sh}(t_0)}\right)^2 \quad r \le R_{\rm ej}$$

where t_0 *are the SNR shock radius and starting time of simulation, respectively.*

4.3.2 Magnetic turbulence

In Section 3.3.3, I describe the CR scattering from different MHD waves in the remnant and I only consider Alfvén waves

as the scattering centre of CRs in this dissertation. The spatial and temporal evolution of the magnetic turbulence spectrum can be expressed by a continuity equation for magnetic spectral energy density per logarithmic bandwidth, $E_{\rm w}(r, k, t)$, as described in Comment 4.3.1 and reads following [182], In *RATPaC*, this transport equation for magnetic turbulence is calculated in one-dimensional spherical symmetry in the co-moving frame of the shock in the $r^\star$ coordinate, defined in Definition 4.1.1 by using the *FiPy* package.

Comment 4.3.1

If $B_{\rm turb}$ is small-scale magnetic field amplitude from the contribution of Alfvén waves, then the total energy density in the waves will be,
$< {B_{\rm turb}}^2 > = 4\pi \int W_{\rm w}\, dk$
$= \quad 4\pi \int E_{\rm w}\, d\, \ln k$
where $W_{\rm w}$, and $E_{\rm w}$ are magnetic spectral energy density per interval in k and $\ln k$.

$$\frac{\partial E_{\rm w}}{\partial t} = -\nabla \cdot (\mathbf{u} E_{\rm w}) - k\frac{\partial}{\partial k}(k^2 D_{\rm k}\frac{\partial}{\partial k}\frac{E_{\rm w}}{k^3}) + 2(\Gamma_{\rm g} - \Gamma_{\rm d})E_{\rm w} \tag{4.3.4}$$

[182]: Brose et al. (2016), 'Transport of magnetic turbulence in supernova remnants'

where k, $D_{\rm k}$ represent the wave-number, diffusion coefficient in wave-number space, and $\Gamma_{\rm g}$, $\Gamma_{\rm d}$ are growth and damping rates, respectively. The diffusion coefficient in wave-number space is given by,

$$D_{\rm k} = \frac{k^2}{\tau_{\rm s}(k)} \tag{4.3.5}$$

where $\tau_{\rm s}(k)$ refers to the magnetic spectral energy transfer time scale.

Wave cascading

According to the classical picture of turbulence [183, 184], if the source of turbulence energy is injected into a system at the length scale, $\lambda_{\rm max}$ comparable to the system, then, this drives eddies at the same length scale, followed by the energy cascading or the energy transfer at a constant rate ϵ from large to the small length scale by the dispersion of large eddies to small eddies. Thus, the energy transfer to the small length scale, $\lambda_{\rm min}$ where the viscosity becomes dominant. In the Kolmogorov treatment, the eddy turnover time connected to length scale λ is λ/u_λ for the eddy size of λ with characteristic velocity u_λ and this also refers to the time scale for energy transfer from the length scale λ to smaller ones. Further, this process predicts the spectrum $E_{\rm w} \sim \epsilon^{\frac{2}{3}} k^{-\frac{2}{3}}$, so-called Kolmogorov spectrum.
Therefore, the magnetic spectral energy transfer time scale, $\tau_{\rm s}(k)$ and the diffusion coefficient $D_{\rm k}$ should depend on the cascade phenomenology, and hence turbulence cascading can be empirically written as $D_{\rm k} = k^3\, v_{\rm A} \sqrt{\frac{E_{\rm w}}{2B^2}}$ where $v_{\rm A}$ refer to the velocity of Alfvén wave, by using Equation 4.3.5 [185, 186]. Furthermore, since $v_{\rm A}$ depends on the total magnetic field, $B_{\rm tot}$, $D_{\rm k}$ depends more sensitively on $E_{\rm w}$ when the

[183]: Kolmogorov (1991), 'Dissipation of Energy in the Locally Isotropic Turbulence'
[184]: Richardson et al. (2007), *Weather Prediction by Numerical Process*

[185]: Zhou et al. (1990), 'Models of inertial range spectra of interplanetary magnetohydrodynamic turbulence'
[186]: Schlickeiser (2002), *Cosmic Ray Astrophysics*

turbulent field becomes amplified beyond the amplitude of the large-scale field, hence-

$$D_{\rm k} \propto \begin{cases} \sqrt{E_{\rm w}} & for \quad E_{\rm w} \ll B^2/8\pi \\ E_{\rm w} & for \quad E_{\rm w} \gg B^2/8\pi \end{cases} \tag{4.3.6}$$

Wave amplification

In section 3.3.3, I discuss that higher energetic particles streaming with super-Alfvén speed generate Alfvén waves with wavelengths comparable to the gyro-radius of the particles. Hence, if the Alfvén waves are considered as the scattering centres for CRs, the resonance condition is given by,

$$k_{\rm res} = \frac{qB}{pc} \tag{4.3.7}$$

where $k_{\rm res}$ represents the resonant wave number, and q is the particle charge, and p is the particle momentum. Additionally, I also explain in section 3.3.3 that although non-resonant streaming instability of the CRs may also be responsible to amplify the magnetic field beyond $B_{\rm turb}/B \sim 1$, the energy transfer from CRs to these modes is quite uncertain along with the wave spectrum of the cosmic-ray diffusion coefficient. Also, this amplification process and its spatial profiles are highly nonlinear. Therefore, understanding the non-resonant modes and their relation to the diffusion coefficient can be beneficial but these are beyond the scope of this dissertation. Further, [187] suggested that non-resonant CR streaming instabilities are likely the dominant way of magnetic field amplification specifically during the free expansion phases and early Sedov-Taylor phase of SNR, when the SNR shock is relatively faster, but at later times resonant modes provide efficient amplification. So, the growth term, based on resonant streaming instability [188] is enhanced by a linear factor A to consider the influence of non-resonant instabilities to amplify the magnetic field and hence, in *RATPaC*, the wave amplification is defined as,

[187]: Amato et al. (2009), 'A kinetic approach to cosmic-ray-induced streaming instability at supernova shocks'

[188]: Skilling (1975), 'Cosmic ray streaming - I. Effect of Alfvén waves on particles.'

$$\Gamma_{\rm g} = A \frac{v_{\rm A} p^2 v}{3E_{\rm w}} \left| \frac{\partial N}{\partial r} \right| \tag{4.3.8}$$

where v is the particle velocity. In this thesis, $A = 10$ is considered for simulation presented in Chapter 6 as this value of A agrees with the observations of historical SNRs [189] and also this estimates the growth rates of CR streaming instabilities during the early stages of SNR evolution in a

[189]: Brose, R. et al. (2021), 'Morphology of supernova remnants and their halos'

dense environment [190, 191]. Furthermore, as the growth rate of the resonant streaming instability [10] is increased by the factor 10, the turbulent field can be amplified to $B_{\rm turb} > B$ during the initial stages of the SNR evolution. The magnetic field is reached its peak amplitude at the position of the shock and drops quickly in the downstream region because of the efficient cascading which is consistent with the magnetic field profile suggested by [180].

[190]: Marcowith et al. (2018), 'Core-collapse supernovae as cosmic ray sources'
[191]: Brose et al. (2022), 'Core-collapse supernovae in dense environments–particle acceleration and non-thermal emission'

Wave damping

The turbulence can be damped by different processes, such as ion-cyclotron damping and neutral-charged collision.

Ion-cyclotron damping: Alfvén waves with wavelengths comparable to the gyro-radius of the thermal plasma interact with the thermal plasma. This turbulence energy transfer to the small-length scale can heat the plasma. Then, the damping term based on this mechanism can be defined as [192],

[192]: Threlfall et al. (2010), 'Alfvèn wave phase-mixing and damping in the ion cyclotron range of frequencies'

$$\Gamma_{\rm d} = \frac{v_{\rm A} c k^2}{2\omega_{\rm P}} \tag{4.3.9}$$

where $\omega_{\rm P}$ is the ion-plasma frequency.

Neutral-charged collision: The Alfvén wave with the wavelength between λ_1 and λ_2 cannot exist in the partially ionised medium as a consequence of the collision between neutral particles and ions [193]. However, this process of Alfvén wave damping is important in the presence of the molecular cloud at low temperature.

$\lambda_1 \equiv \pi v_{\rm A} \tau_{\rm ni}$, where $\tau_{\rm ni} \Rightarrow$ collision time scale for neutral particles

$\lambda_2 \equiv 4\pi v_{\rm A}^{\star} \tau_{\rm in}, v_{\rm A}^{\star} \Rightarrow$ Alfvén speed in the ions, $\tau_{\rm in} \Rightarrow$ collision time scale for ions

[193]: Kulsrud et al. (1969), 'The Effect of Wave-Particle Interactions on the Propagation of Cosmic Rays'

Therefore, in the absence of molecular clouds in the simulations presented in this thesis, I only apply ion-cyclotron damping without considering the generated heat for the dissipation of Alfvén waves at small length scales. This may modify the particle spectrum near the injection momentum.

Initial turbulence

As an initial condition, a magnetic turbulence source spectrum is needed, to amplify the magnetic turbulence and start to solve Equation 4.3.4, numerically. I assume a magnetic turbulence spectrum which provides a diffusion coefficient, D_0 of a factor of 100 lower than that for the Galactic propagation of CRs [194],

[194]: Thielemann et al. (2011), 'Massive Stars and Their Supernovae'

$$D_0 = \left(10^{27}\,{\rm cm^2\,s^{-1}}\right)\left(\frac{pc}{10\,{\rm GeV}}\right)^{\frac{1}{3}}\left(\frac{B}{3\mu\,{\rm G}}\right)^{-\frac{1}{3}} \tag{4.3.10}$$

Therefore, the growth of Alfvén waves, damping, spectral energy transfer through cascading, and the spatial transport of waves in Equation 4.3.4 suggest that the magnetic turbulence spectra should demonstrate a complicated shape, shown in Figure 4.3.3. In this Figure, the spectra at the shock depict that the turbulence is driven by the particles with all energies. Low-energy particles should be dominant in the shock vicinity, hence, the growth of the turbulence is quicker at the large wave number scale. Further, at large wave number scale or small length scale, cascading becomes important, and thus, the interplay between growth term and cascade constraints the shape of the turbulence spectra. The sharp cut-off at the low wave number scale indicates that particles beyond the corresponding energy can escape the shock vicinity and in the upstream turbulence spectra, there is a corresponding peak in turbulence, driven by those particles at their escaping energy. Then, with time evolution, the cut-off at the low wave number in the spectra is shifting to lower wave numbers which indicates that the maximum achievable energy of particles or escaping energy with time increases because of the effect of the amplified magnetic field.

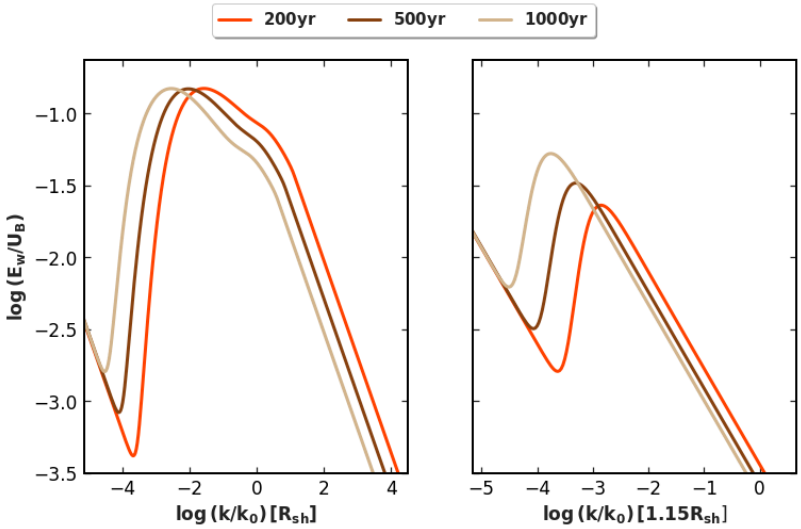

Figure 4.3.3: Spectral evolution of magnetic turbulence energy density, E_w. The demonstrated evolution of E_w corresponds to core-collapse SNR with 60 $M_\odot$ progenitor star, described in Chapter 6. Here, U_B refers to the energy density of the large-scale magnetic field, k_0 is the wave number corresponding to the length scale 7×10^{10} cm used for normalisation. The spectra in the left panel are the turbulence spectrum at SNR forward shock radius, R_{sh} and the right panel demonstrates the spectra in the upstream region, at 1.15 R_{sh} at the different mentioned ages of SNR.

[195]: Lagage et al. (1983), 'The maximum energy of cosmic rays accelerated by supernova shocks'
[196]: Schure et al. (2010), 'Time-dependent particle acceleration in supernova remnants in different environments'

4.3.3 Diffusion coefficient

The diffusion coefficient is directly connected to the acceleration time scale, the distribution of particles in the SNR, and the maximum attainable energy of particle [195, 196]. I use two recipes to calculate the diffusion coefficients in this dissertation such as Bohm-like diffusion, defined in Definition 3.3.1 and time-dependent diffusion coefficient derived from the magnetic turbulence spectrum written in Equation 4.3.4.

Bohm-like diffusion coefficient: In this scenario, the diffusion coefficient reads,

$$D_{\rm B} = \zeta \frac{cR_{\rm g}}{3} = \zeta \frac{pc}{qB} \tag{4.3.11}$$

where $R_{\rm g}$ refers to the gyro-radius of particles and ζ is the efficiency factor. In *RATPaC*, this diffusion coefficient is applied in the entire downstream region of SNR forward shock and in the far upstream region beyond $2R_{\rm sh}$, the Galactic diffusion coefficient is considered. The transition region between Bohm-like and Galactic diffusion coefficients is connected by an exponential profile, describe in [197]. I discuss the particle acceleration in the core-collapse remnant using this type of diffusion coefficient in Chapter 5.

[197]: Telezhinsky, I. et al. (2012), 'Time-dependent escape of cosmic rays from supernova remnants, and their interaction with dense media'

Time-dependent diffusion coefficient: The diffusion coefficient for CRs derived from $E_{\rm w}$ can be expressed as,

$$D_{\rm r} = \frac{4v}{3\pi} R'_{\rm g} \frac{U_{\rm B}}{E_{\rm w}} \tag{4.3.12}$$

where $U_{\rm B}$ is the energy density of the large-scale magnetic field and here $R'_{\rm g}$ represents the gyro-radius of particles in the total magnetic field, $B_{\rm tot}$. The diffusion coefficient is calculated numerically for simulations, described in Chapter 6.

4.4 Modification in *RATPaC*

I study the DSA mechanism at the core-collapse SNR forward shock that expands inside the complex wind-blown bubble, described in Section 2.4, formed by its progenitor. During the evolution, the SNR forward shock interacts with different discontinuities present in the bubble and creates respective transmitted and reflected shocks like the evolution of SNR with $35\,M_\odot$ progenitor shown in [198] in one dimension. Also, Figure 4.4.1 shows the change in the structure of the wind bubble created by $20\,M_\odot$ progenitor with wind parameters shown in Figure 2.3.2 after a few collisions between the wind bubble and the SNR forward shock. Besides, the wind bubble structure after the collision in this Figure 4.4.1, depicts the reverse shock moving towards the interior of SNR after merging with the reflected shock created by the SNR-CSM interactions. I elaborately explain this particular wind bubble in Chapter 6 and here this is mentioned to demonstrate the complications in HD parameters resulting from the evolution of the core-collapse SNR inside the CSM shaped by its progenitor. Thus the scenario of the SNR-wind bubble system becomes convoluted in comparison to the type Ia SNR that evolves in the uniform ambient medium. Although, *RATPaC* works reasonably well in Type Ia scenarios [105], the following modifications in the code are necessary to deal with the complex core-collapse framework.

[198]: Dwarkadas (2005), 'The Evolution of Supernovae in Circumstellar Wind-Blown Bubbles. I. Introduction and One-Dimensional Calculations'

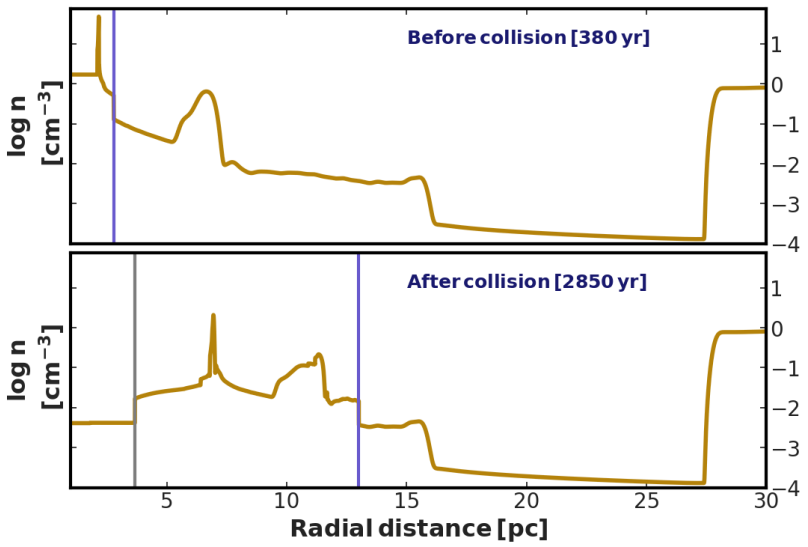

Figure 4.4.1: Flow number density (n) profiles before and after interactions between SNR forward shock and CSM structures.
The presented scenario indicates the evolution of SNR inside the wind bubble created by the 20 $M_\odot$ progenitor. I discuss this wind bubble structure elaborately in Chapter 6. Here, I mention this particular scenario to provide a glimpse of the complex density structure only after a few interactions of the SNR-CSM. The blue vertical line refers to the position of the SNR forward shock at different times and the grey vertical line denotes the reverse shock moving towards the interior of SNR after merging with the reflected shock created by the SNR-CSM interactions.

4.4.1 Shock finding

As Equations 4.1.1, 4.3.3, 4.3.4 are solved spatially in the shock-centred coordinate system, discussed in Definition 4.1.1, locating the shock position, specifically for this dissertation, finding the SNR forward shock position and its velocity in the simulation frame are crucial. Here, I describe the shock-finding method for the SNR forward shock that is applied to perform numerical simulations in this dissertation.
I start by considering the SNR forward shock as the only shock in the system and the output HD data from *PLUTO* code is used for the shock finding.
Older version: By definition, at the position of the SNR forward shock, the spatial gradient of plasma flow velocity should be maximum, as shown in Plot (a) of Figure 4.4.2. Numerically, the spatial gradient of flow velocity can be expressed as,

$$\frac{\partial u}{\partial r} \sim \frac{\Delta u}{\Delta r} \sim \frac{u_{\rm i} - u_{i+3}}{3\Delta r} \tag{4.4.1}$$

where $u_{\rm i}$ is the flow velocity at i-th computational cell and Δr is the size of each cell. Three cells are taken for this calculation as the shock always spreads over more than one cell, and so does the velocity jump. To find out the SNR forward shock position, the highest velocity gradient is searched for, and then, around that specific cell a logistic function is fitted in a window with 20 bins, 15 downstream and 4 upstream. The form of this fitted logistic function is,

$$\frac{u\,(x) - u_{\rm min}}{u_{\rm max} - u_{\rm min}} = \frac{1}{1 + \exp(k(x - x_{\rm sh}))}, \qquad x = \frac{r - r_{\rm min}}{r_{\rm max} - r_{\rm min}} \tag{4.4.2}$$

where $r_{\rm min}$, $r_{\rm max}$ are spatial coordinates in the fitted window at the inner and outer end, respectively and $u_{\rm min}$, $u_{\rm max}$ are minimum and maximum flow velocities in the window, respectively, k is the steepness of logistic function, and $x_{\rm sh}$ is the shock radius in normalised coordinate, x. Thus, the shock radius, $R_{\rm sh}$ is calculated from the fitted parameters. Further, the shock velocity in the simulation reference frame is calculated following,

$$V_{\rm sh} \sim \frac{R_{\rm sh}\,(t_2) - R_{\rm sh}\,(t_1)}{t_2 - t_1} \tag{4.4.3}$$

where t_1 and t_2 are preceding and succeeding time points, respectively.
Further, finding the shock in the total computational domain at every time step along with the evaluation of shock velocity is computationally expensive. Hence, to optimise the shock finding algorithm, if the shock position $R_{\rm sh,new}$ at a later time is at a particular distance away from the shock position at the one-time step before, $R_{\rm sh,old}$, say $R_{\rm sh,new} > R_{\rm sh,old} + 5\Delta r$, then the shock velocity is calculated, otherwise the new shock position is updated by keeping the shock velocity constant. Then, the code searches for the shock in a region $\pm 0.5\%$ around $R_{\rm sh,new}$ at the next time step. As *RATPaC* is run in parallel computing mode using Message Passing Interface (MPI), every core searches if the shock position $R_{\rm sh,new}$ is located in the respective domain and if so, that particular core tries to find the shock position at the next time step followed by communication and passing this message or shock location to other cores. If more than one core finds the probable new shock positions in their domains, the full HD data from all cores are combined followed by searching for the shock on the total computational domain around $R_{\rm sh,new}$. If both processes, local and global searches cannot find the exact shock location, the simulation fails.
This algorithm for defining the shock location and velocity works efficiently if only one shock is involved, say the SNR forward shock or reverse shock. However, in the core-collapse scenario, multiple shocks and contact discontinuities are present, as shown in Figure 4.4.2 which involves the system of the SNR-wind bubble for a simple test run.
Implemented version: Here I present the arising difficulties in the shock-finding method with the corresponding solutions.

1. If the SNR forward shock begins to interact with very dense material, shock velocity gradually decreases. Consequently, the older version of the shock-finder starts to locate another

Comment 4.4.1

If the SNR forward shock interacts with any structure of the wind bubble, transmitted and reflected shocks are generated. The reflected shock resulting from the collision between SNR forward shock and wind termination shock interacts with the contact discontinuity between SNR forward shock and reverse shock and again moves outward by reflecting back. Then, this shock eventually merges with SNR forward shock, shown in Plot (c) of Figure 4.4.2. Thus, by multiple collisions, a number of outward and inward-moving shocks are created that with time merges with SNR forward and reverse shock, respectively. In our one-dimensional simulation, this situation is enhanced.

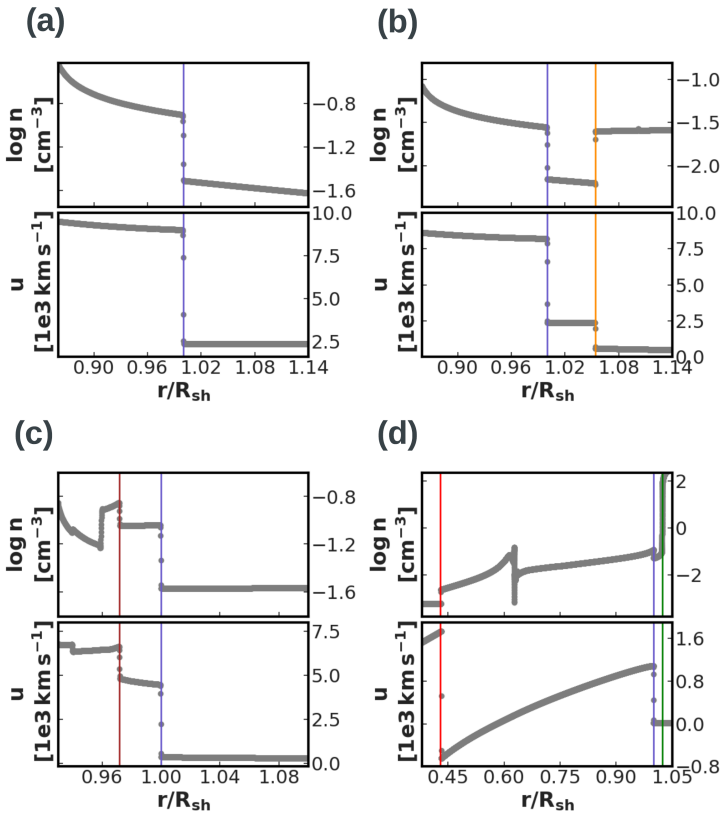

Figure 4.4.2: Flow number density (n) and flow velocity (u) profile for different interactions between SNR forward shock and CSM structures for a simple test run.
The presented scenario denotes the evolution of SNR inside the wind bubble shown in Figure 2.4.1 as a simplified test case. The SNR ejecta profile is defined following Definition 4.2.2 where $M_{ej} = 3M_{\odot}$ and $E_{ej} = 10^{51}$erg. In the plots, the blue vertical lines denote the SNR forward shock.
The SNR forward shock (a) propagates inside the free stellar wind region.
(b) is about to collide with wind termination shock. The orange vertical line shows the wind termination shock.
(c) is about to merge with another outgoing shock, indicated by the brown vertical line.
(d) start to climb the wind bubble contact discontinuity, shown by the green vertical line. The red vertical line refers to a fast reverse shock, resulting from SNR-wind bubble interaction.

shock if the velocity gradient at that location is greater than that at the SNR forward shock. For example, Plot (d) in Figure 4.4.2 illustrates the SNR forward shock interaction with wind bubble contact discontinuity and also a fast reverse shock (see Comment 4.4.1) and the flow velocity gradient is maximum at the reverse shock.
Solution: The solution to this complication is to include the density compression ratio at the probable SNR forward shock location. So, if the highest velocity gradient is found by the code around i-th cell as in Equation 4.4.1, $\frac{\rho_i}{\rho_{i+3}}$ is calculated followed by defining the compression ratio checking range. If the compression ratio is reasonable, then that specific position is located as the forward shock, otherwise, that specific position is blinded for the next search followed by the continuation of the search for the maximum velocity gradient.

2. If another shock is about to interact with the SNR forward shock by tail-on collision, as shown in Plot (c) in Figure 4.4.2, and the separation between these two shocks becomes less

than 15 bins, the logistic fit function in Equation 4.4.2 would become incapable to locate the accurate forward shock position for a brief time span depending on the relative velocity between the forward shock and the colliding shock. Consequently, the injection coefficient in Equation 4.1.2 becomes incorrect and so does the simulated particle spectrum.
Solution: Firstly, the logistic function is fitted with 10 bins, 5 downstream and 4 upstream and then the fit parameters provide the reasonably accurate position of the SNR shock in high spatially resolved HD data, in order of $\sim 10^{-4} - 10^{-5}$ pc for at least the time step of 1.0 yr to solve the CR transport equation (see comment 4.4.2).

Comment 4.4.2

During dealing with the shock-finding method, I calculated the particle spectra only by solving HD equations and CR transport equation, considering the constant compressed magnetic field as described in Section 4.3.1 and Bohm-like diffusion, described in Section 4.3.3. Solving specifically the transport equation for magnetic turbulence often needs a time step less than 1.0 yr.

In the second step, the SNR forward shock velocity in the simulation frame is calculated from the mass-flux jump around the forward shock instead of applying Equation 4.4.3 and this method is beneficial to get rid of the uncertainty in shock velocity, resulting from the inaccuracy in measured shock radius (see Comment 4.4.3). The expression of shock velocity in the simulation frame in terms of mass flux jump ($M_{\mathrm{u-d}}$) by considering the conservation of mass flux in the SNR forward shock rest frame is,

$$V_{\mathrm{sh}} = \frac{M_{\mathrm{u-d}}}{\rho_{\mathrm{u,HD}}(1 - k_{\mathrm{m}})} \tag{4.4.4}$$

where $k_{\mathrm{m}} = \frac{u_{\mathrm{u,HD}} - A}{u_{\mathrm{d,HD}}}$, $A = \frac{M_{\mathrm{u-d}}}{\rho_{\mathrm{u,HD}}}$ and $\rho_{\mathrm{u,HD}}$, $u_{\mathrm{u,HD}}$, $u_{\mathrm{d,HD}}$ are the upstream plasma density, upstream and downstream plasma flow velocity in the simulation frame, respectively and I use here HD subscripts as these upstream and downstream parameters are calculated directly from the HD data but the upstream and downstream parameters used in Equations 4.1.1, 4.3.3, 4.3.4 are from resharpening, discussed later in Section 4.4.2. The shock velocity from Equation 4.4.4 gives the reasonable compression ratio for sub-shock, r_{sub} and also injection efficiency in Equation 4.1.2, for single shock along with for the merging of shocks with the SNR forward shock, propagating in the same direction. Therefore, for these scenarios, the calculation of shock velocity from mass-flux jump is implemented.

Comment 4.4.3

Acknowledgement- Velocity calculation from mass-flux jump was suggested by my PhD supervisor Prof. Dr. Martin Pohl. The calculation regarding the derivation of Equation 4.4.4 is also done by him.

Further, detecting any structure in close proximity to the SNR forward shock is crucial for the implementation of shock velocity calculation from the jump of mass flux for the mentioned scenarios and also to control the reasonable temporal resolution of the simulation, discussed later in Section 4.4.3. Additionally, capturing if the SNR forward shock is about to collide particularly with any dense material or wind bubble contact discontinuity is necessary as updating the forward shock velocity if the SNR forward shock propagates by a certain distance away after one time step later, from its previous position, $R_{\mathrm{sh,new}} > R_{\mathrm{sh,old}} + 5\Delta r$, as discussed for the older version is not reasonable if the forward shock collides any dense material. The forward shock velocity in the sim-

ulation frame starts to decrease gradually in this situation, and so, the forward shock takes more time steps to exceed 5 grid points away from its previous position. However, the forward shock velocity in the simulation frame changes in the meantime and this leads to providing wrong injection efficiency for solving the CR transport equation. Therefore, calculating forward shock velocity at every time step during the SNR-dense material interactions should be reasonable.

Locating any shocks around SNR forward shock:

(i) First, a search window around the forward shock, R_{sh} is defined and for this, consider R_{sh} is located approximately at the computational grid i, then the search window would be $[i \pm 15, i \pm 4]$ for ahead (+) and behind (−) the SNR forward shock. To get rid of the complication of the search window related to very fine or coarse spatial resolution, there is also a possibility to define the search window with the 0.09 pc range ahead and behind the shock, excluding the region $[R_{sh} - 0.001\,\text{pc}, R_{sh} + 0.001\,\text{pc}]$ and this window range is, of course, valid only if R_{sh} is reasonably away from the inner boundary of the total computational grid. The reason for excluding the region extremely close to R_{sh} is to get rid of the forward shock itself.

(ii) Searching for the maximum velocity gradient and checking the respective density compression ratio, similarly as discussed for the SNR forward shock.

These procedures locate if there is any shock around the SNR forward shock and their location, for example, the wind termination shock and another outgoing shock behind the SNR forward shock in Plot (b) and (c) are found before their merging.

Finding the contact discontinuity:

(i) Searching for the density jump which is not associated with a velocity jump is the possible location of the contact discontinuity.

These changes in shock finding work reasonably well in the complicated scenarios of core-collapse SNR and along with these, another scheme, called shock resharpening in *RATPaC* should be modified specifically during the tail-on collision of SNR forward shock with another shock.

4.4.2 Resharpening

In the profiles of HD parameters like ρ, $\mathbf{u}$, P and T, calculated using *PLUTO* code, the SNR forward shock spread over several cells as shown in Figure 4.4.2. Therefore, to ensure a sharp jump from downstream to upstream, as discussed in the Rankine-Hugoniot jump conditions by Equation 3.3.1, the HD data of these parameters is re-sharpened. The process is after finding the SNR forward shock, the HD data in the range of 8 bins, 4 bins near-upstream and 4 bins near-downstream of the shock is replaced by the extrapolated values using the HD data further beyond 4 bins upstream and downstream region. Further, I want to mention that reasonably high-solution HD data is required for negligible

deviation of the extrapolated values from the proper data. So, the resulting data provides a sharp transition at SNR forward shock, named resharpened data. This resharpened data is mapped on the non-uniform grid of *RATPaC*, defined in Definition 4.1.1. From these resharpened data, near-upstream and near-downstream parameters are calculated, for instance, the $n_{\mathrm{u}}, u_{\mathrm{u}}, r_{\mathrm{sub}}$ in Equation 4.1.2, 4.1.3, where r_{sub} is calculated by,

$$r_{\mathrm{sub}} = \frac{V_{\mathrm{sh}} - u_{\mathrm{u}}}{V_{\mathrm{sh}} - u_{\mathrm{d}}} \tag{4.4.5}$$

where u_{d} is the flow velocity of the near-downstream of forward shock in the simulation frame.
This method of resharpening is not accurate when a shock

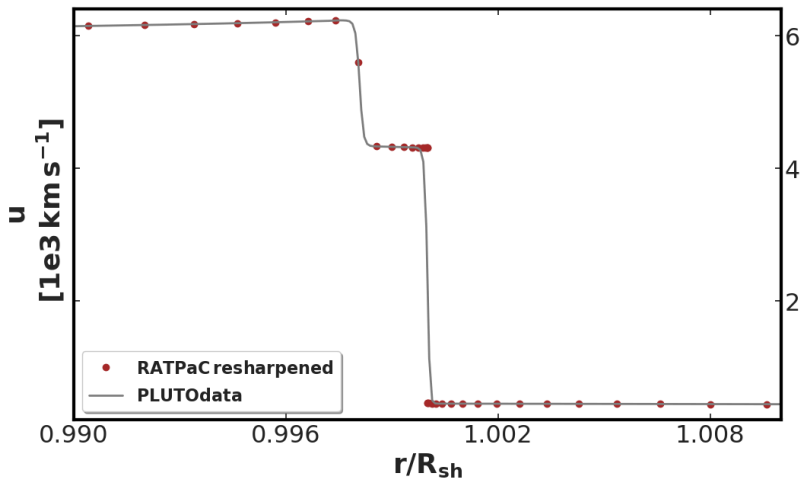

Figure 4.4.3: *RATPaC* resharpened velocity profile.
Flow velocity from *PLUTO* data by solid grey line and resharpened data by points are plotted. This plot shows the shock merging for the core-collapse SNR described in Figure 4.4.2.

from the downstream region approaches the SNR forward shock, as shown in Figure 4.4.3. If this approaching shock reaches within 4 bins in *RATPaC* grid in the near-downstream of SNR forward shock, then because of the linear extrapolation using far downstream points, measurement of u_{d} becomes inaccurate and the resharpening resumes to work properly after this tail-on collision. This incorrectness in a calculation of u_{d}, results in wrong r_{sub} and injection efficiency in Equation 4.1.3. Here, I want to mention that in this simulation, there is a limit to temporal and spatial resolution. Performed tests with different spatial and temporal resolutions suggest that the effect of shock merging on the particle spectra is resolution-dependent and the effect is enhanced at poor resolution and the spectra show amplified hardness at high energy. However, the theoretical calculations in Appendix B suggest that particles can observe the compression ratio from both shocks for less than a single acceleration time.

Thus, shock merging should not produce any significant spectral features in particle spectra and this collision only increases the acceleration rate of particles by increasing the SNR forward shock velocity and consequently higher maximum attainable energy by particles. This instant change in

shock velocity and maximum attainable energy can result in the brightening of the non-thermal X-ray and TeV emissions on very short time scales as shown in [199] and the observed rapid variation in non-thermal X-ray filaments of the Tycho's SNR [200] may be a consequence of the boosting of the forward shock by tail-on collision with another shock.
Further, analysis of the effect of shock merging on particle spectra by [201] shows a similar conclusion. Therefore, to get rid of the effect of resolution limitation in the simulation during shock merging, the resharpened values of HD parameters at 4 bins near-downstream of SNR forward shock are replaced by the resharpened values at those bins when the two shocks are separated by more than 4 bins in *RATPaC* grid. As the temporal resolution is quite high, with the time step of 0.2yr, and also the spatial resolution in the order of $10^{-4} - 10^{-5}$ pc, the resharpening starts to work after a very brief time period, depending on the velocity of merging shocks. This modification in resharpening produces reasonable $r_{\rm sub}$ and finally, the particle spectra even when SNR evolves through very complicated wind bubbles created by massive stars where multiple numbers of shock merging happen, described in Chapters 5 and 6.

[199]: Sushch et al. (2022), 'Leptonic Non-thermal Emission from Supernova Remnants Evolving in the Circumstellar Magnetic Field'

[200]: Okuno et al. (2020), 'Time Variability of Nonthermal X-Ray Stripes in Tycho's Supernova Remnant with Chandra'

[201]: Vieu et al. (2020), 'Particle acceleration at colliding shock waves'

4.4.3 Time step

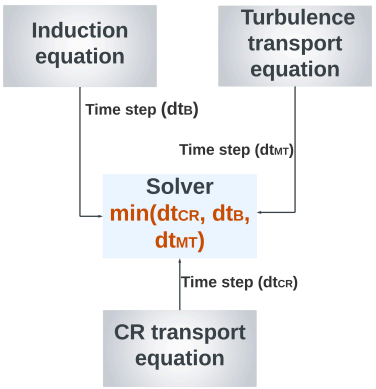

Figure 4.4.4: Schematic of time step control by Solver: Solver gets information about the time step from CR transport equation, magnetic field induction equation and transport equation of magnetic turbulence and finds the minimum time step among them and that would be the time step of the simulation.

An implicit treatment is applied to solve the partial differential equations, Equations 4.1.1, 4.3.3, 4.3.4 using the *FiPy* package. Consequently, the CFL condition discussed in Definition 4.2.1 is not strictly maintained while solving these equations. However, in *RATPaC* while solving Equation 4.3.4 for magnetic field turbulence, approximately 100 times reduced time steps in comparison to the time step for CR transport equation is necessary for the initial evolution of the SNR to amplify the initial source turbulence, expressed in Equation 4.3.10 to avoid the effect from the coarse temporal resolution on the simulated turbulence spectra.

The communication between the CR transport equation, magnetic field induction equation and magnetic field turbulence transport equation is set up in the solver module of *RATPaC*. Figure 4.4.4 shows schematically that the solver finds the minimum time step among suitable time steps for the CR transport equation ($\mathrm{d}t_{\rm CR}$), induction equation ($\mathrm{d}t_{\rm B}$), the transport equation for magnetic turbulence ($\mathrm{d}t_{\rm MT}$) and selects that time step as the simulation time step in *RATPaC*. Here, it should be noted that the time step for the HD equations is fully controlled by *PLUTO* code and independent of the time step in *RATPaC* simulation but I want to mention that the time step of HD equations should be greater than the *RATPaC* simulation.

Old version: In the older version of *RATPaC*, the time steps in different modules are set up manually, depending on the age of SNR, as shown in Table 4.1 and Table 4.2 for the *RATPaC* simulations. Similarly, time steps are considered

time (in yr)	dt_{CR} (in yr)
t < 0.1	0.001
0.1<= t <1	0.01
1.0<= t <10.0	0.05
10.0<= t <20.0	0.25
20.0<= t <50.0	1.0
50.0<= t <100.0	5.0
100.0<= t <1000.0	25.0
t>= 1000.0	50.0

Table 4.1: Time step for simulation without including the transport of the magnetic turbulence

time (in yr)	dt_{CR} (in yr)
t < 0.1	0.0002
0.1<= t <1	0.001
1.0<= t <10.0	0.01
10.0<= t <20.0	0.05
20.0<= t <50.0	0.1
50.0<= t <100.0	0.34
100.0<= t <499.0	1.0
499.0<= t <998.0	2.0
998.0<= t <2000.0	5.0
t>= 2000.0	25.0

Table 4.2: Time step for simulation including the transport of the magnetic turbulence

for Equations 4.3.3, 4.3.4. If this manual time stepping is used for the simulations with SNR inside the complex wind bubble in the presence of different interactions between SNR forward shock and CSM, discussed in Section 4.4.1, then, evidently interactions would be skipped by the code, specifically at later times and also, to implement the calculation of shock velocity and resharpening during shock collision, discussed in Section 4.4.2, choosing time steps appropriately is crucial. Although the high temporal resolution is needed at the time of interaction, performing the whole simulation with that same temporal resolution or reasonably small time steps to prevent the skipping of the interactions will be computationally expensive and simulation for the evolution of the core-collapse SNR within the CSM for an extended time period, say 7×10^4 yrs becomes difficult to achieve. The difficulties related to the time-stepping are enhanced if the transport equation for the magnetic turbulence is included in the simulations as shown in Table 4.2.
Therefore, an automated time-stepping or adapted time-stepping method is implemented to perform the simulation involving the core-collapse remnant.

Comment 4.4.4

In *RATPaC*, 400 bins are considered in spatial coordinate and 560 bins are in momentum coordinate. Therefore, the phase space can be represented by (r_i, p_j) where $i = 1, 2, 3, \ldots, 400$ and $j = 1, 2, 3, \ldots, 560$.

Implemented version: The adaptive time stepping method in *RATPaC* calculates the suitable time step for simulations at a given time, based on the relative deviation of calculated quantities in partial differential equations with respect to their values at the preceding time.
For example, the distribution of CRs, $N_{old}(r_i, p_j, t_{old})$ in phase space, described in Comment 4.4.4 is calculated by solving Equation 4.1.1. To determine the next time step at time t_{old}:
1. The method initially assumes the time step is $dt_{CR,ini}$ where $dt_{CR,ini} = 0.0009$yr. Taking this value as a possible time step,

CR distribution, $N_{\rm new}(r_{\rm i}, p_{\rm j}, t_{\rm new})$ is calculated at the time, $t_{\rm CR,new} = t_{\rm CR,old} + {\rm d}t_{\rm CR,ini}$.
2. The relative deviation $\delta N_{\rm rel}$ of $N_{\rm new}$ with respect to $N_{\rm old}$ is calculated in the phase space and the permissible range of the average of these relative deviations ($\overline{\delta N_{\rm rel}}$) is defined, say 0.5 % − 1.5 %. This range is fixed to avoid the very small as well as considerably large time steps.

$$\delta N_{\rm rel} = \left| \frac{N_{\rm new} - N_{\rm old}}{N_{\rm old}} \right| \tag{4.4.6}$$

Comment 4.4.5

If ${\rm d}t_{\rm CR}$, ${\rm d}t_{\rm B}$, ${\rm d}t_{\rm MT}$ provides larger time steps at later times and if any shock-shock collision happens during this time period that will not be detected by the relative change in CR distribution, magnetic field strength or turbulence spectral energy density and skipped by the simulation. So, the information provided by *HydroControl* helps to capture the interaction by controlling time steps before the collision.

3. If the calculated $\overline{\delta N_{\rm rel}}$ lies in this permissible range then $dt_{\rm ini}$ would be the time step. Otherwise, if the $\overline{\delta N_{\rm rel}}$ is smaller than the defined range, then the method chooses time step 1.25 times ${\rm d}t_{\rm CR,ini}$ and repeats the process. If $\overline{\delta N_{\rm rel}}$ is greater than the permissible range, then the next chosen time step is ${\rm d}t'_{\rm CR} = {\rm d}t_{\rm CR,ini}/1.25$ and repeats the process.

Similarly, the time steps for the induction equation, ${\rm d}t_{\rm B}$ and the time steps for the transport equation of magnetic turbulence, ${\rm d}t_{\rm MT}$ are evaluated using the relative deviation of magnetic field strength and turbulence spectral energy density, respectively.
Apart from choosing these appropriate time steps for different modules in the code, an additional part, called *HydroControl*, which passes the information from the shock finding algorithm, is described in Section 4.4.1 to the solver about the structures around the SNR forward shock is implemented (see Comment 4.4.5). Through this module, before the scenario of shock merging, the time step can be controlled by restricting the time step $\leq$ 0.2yr for the simulations. This helps to apply the modified resharpening technique, described in Section 4.4.2 for the shock-shock tail-on collisions if in any case, the time step calculated from the different modules is reasonably large. Further, while the SNR forward shock is approaching another incoming shock from ahead and also contact discontinuity, the time step is controlled to be $\leq$ 0.5yr by the *HydroControl*. These mentioned time steps are chosen based on the reasonable results in CR distributions in simulations.
Hence, in the implemented version, the time step of the simulation is determined from the minimum of ${\rm d}t_{\rm CR}$, ${\rm d}t_{\rm B}$, and ${\rm d}t_{\rm MT}$ based on relative deviation measurement, in the absence of structures around SNR. Otherwise, reasonably small time steps are fixed to be as upper limits for the respective interactions of the SNR and the structures in CSM by *HydroControl*. This automated time-stepping method helps simulations to be completed in an achievable time span and this also follows a systematic procedure for the determination of time step in comparison to the manual assumption, as shown in Table 4.1 and Table 4.2.
For instance, Figure 4.4.5 demonstrates the time steps of *RATPaC* simulation by applying the manual and automated

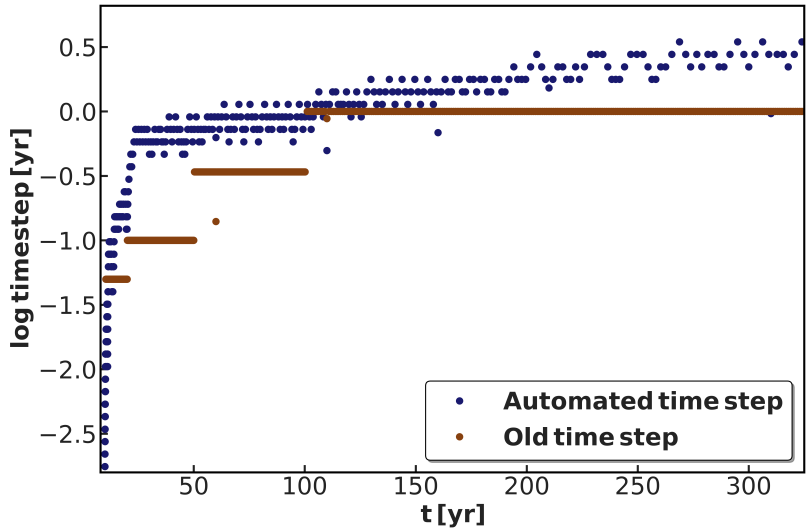

Figure 4.4.5: Comparison between automated time stepping and manual time stepping.
Here time steps of the simulation are shown by using time-stepping in the older version of *RATPaC* mentioned in Table 4.2 by brown dots and by applying implemented automated time-stepping by blue dots for the SNR evolution in the wind bubble shown in Figure 2.4.1 as a test run before the SNR shock hits the wind termination shock. In this scenario, transport equations for CRs and scattering turbulence are solved simultaneously with the magnetic field induction equation in *RATPaC* and of course, the HD equations are also solved by *PLUTO* code. This is to be noted that here at 60 years and 110 years, time steps are reduced which is clearly visible for specifically manual time stepping and this indicates that the code writes the output data at these specific times.

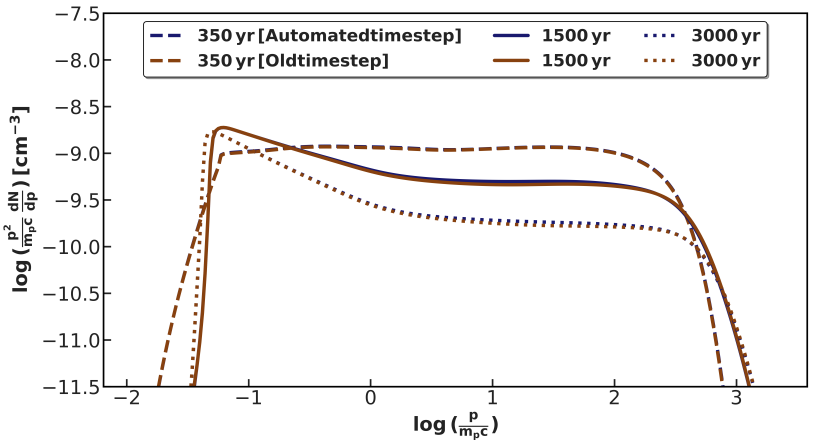

Figure 4.4.6: Comparison of spectra of total volume-averaged downstream of SNR forward shock computed using the old time step and automated time step schemes.
The proton spectra at different times from these two schemes show consistency and the maximum deviation calculated by $\frac{\left|\frac{p}{m_p c}\frac{dN}{dp}\right|_{\rm auto} - \left|\frac{p}{m_p c}\frac{dN}{dp}\right|_{\rm old}}{\left|\frac{p}{m_p c}\frac{dN}{dp}\right|_{\rm old}} \times 100\% \lesssim 7\%$ for different evolutionary ages and energy bands.

time steps for the SNR evolution inside the wind bubble shown in Figure 2.4.1 as a test run. The automated time steps are calculated including the transport equation for CRs and scattering magnetic turbulence together with the induction equation except for the interaction regime. Further, I have used the same strategy for these both time-stepping schemes during the SNR-CSM interactions and limited the maximum time-stepping to 10 yrs. In this situation, if these simulations are continued for 3000 yrs, the simulation runtime with the automated time-stepping speeds up by around factor $\sim$ 2.5 in comparison to the simulation with manual time-stepping. Further, the calculated proton spectra by both schemes are also consistent as shown in Figure 4.4.6. So, using the automated time step scheme is advantageous specifically for the evolution of the SNR inside a complex wind bubble as discussed in Chapters 5 and 6, and the speed-up of the simulation runtime will be more if the simulation is continued for a longer time.

Next step- In this Chapter, I describe the numerical method to solve the DSA at the SNR forward shock by using *RATPaC*

code. The following Chapters 5 and 6 will provide the reader with details about the particle acceleration at core-collapse SNRs inside wind bubbles, shaped by massive stars, by applying Bohm-like diffusion coefficient and time-dependent diffusion coefficient from CR streaming instabilities, respectively. In Chapter 5, the modified versions of the shock finding and resharpening from Sections 4.4.1 and 4.4.2 are implemented and the whole simulation is performed using 1 yr time-stepping except during the interactions between the SNR-CSM structures where the mentioned upper limits of time steps in *HydroControl* are used. In Chapter 6, modified time step method from Section 4.4.3 is also executed.

Particle acceleration in core-collapse SNR in Bohm-like diffusion regime

5

The presented study in this chapter is already published in [202] and I restate this respective analysis with minor modifications.

SNRs are the dominant sources of Galactic CRs below the "knee" energy [81, 203]. The acceleration mechanism that is able to accelerate CRs to this high energy, is considered to be the DSA process [9, 10, 107] and its non-linear modification [204]. The DSA process predicts the spectra of accelerated particles at the SNR shock should follow a power law in energy, as expressed in Equation 3.3.19 with an exponential cut-off at the maximum achievable energy that is limited spatially by the size, temporally by the age of the SNR, and also by radiative energy losses and adiabatic cooling. In recent years, different observations in the TeV band, such as HESS, VERITAS, MAGIC, HAWC, and LHAASO and in the GeV band, AGILE and *Fermi*-LAT have been collecting an ample amount of data regarding SNRs, providing crucial insight and constraints for theoretical models. Based on these observations, spectral measurements of gamma-ray emissions from different SNRs, for instance, IC443 [205], Cas A [206], SN 1006 [207], and the Tycho's SNR [208] suggest a considerable softening in comparison to the DSA predicted power law index and theoretically, these scenarios of softness in spectra can be modelled and explained in different ways. For example, the spectral shape of W44 is explained by diffusive re-acceleration of Galactic CRs in [209], but was found implausible in other studies by considering the large thickness of radiative shocks and the paucity of Galactic CRs to be re-accelerated [210]. Further, other theoretical predictions involve re-acceleration in fast-mode turbulence downstream of the SNR forward shock [211], the fast motion of downstream turbulence [212], and inefficient particle confinement in the vicinity of the SNR caused by the weak driving of Alfvén waves [104, 105].

The CR acceleration at SNR shocks depends on the type of the SNR as well as the HD and magnetic field structure of its environment. The type of the progenitor star can also leave imprints in the morphology of the core-collapse SNR, e.g. [198], [213]. CR acceleration at SNR shocks inside stellar wind bubbles was investigated by various studies including [214, 215] considering Bohm diffusion of energetic particles. Further, the modifications in particle spectra in the core-collapse scenario with RSG and WR progenitors were studied by [162] for simplified flow profiles and [199] probed the impact of the CSM magnetic field on electron spectra and subsequent non-thermal emissions, focusing on the SNR

[202]: Das et al. (2022), 'Spectral softening in core-collapse supernova remnant expanding inside wind-blown bubble'

[204]: Ellison et al. (1997), 'Galactic Cosmic Rays from Supernova Remnants. II. Shock Acceleration of Gas and Dust'

[205]: Acciari et al. (2009), 'Observation of Extended Very High Energy Emission from the Supernova Remnant IC 443 with VERITAS'

[206]: Abdo et al. (2010), 'Fermi-Lat Discovery of GeV Gamma-Ray Emission from the Young Supernova Remnant Cassiopeia A'

[207]: Acero et al. (2010), 'First detection of VHE gamma-rays from SN 1006 by HESS'

[208]: Acciari et al. (2011), 'Discovery of TeV Gamma-ray Emission from Tycho's Supernova Remnant'

[209]: Cardillo et al. (2016), 'Supernova remnant W44: a case of cosmic-ray reacceleration'

[210]: de Oña Wilhelmi et al. (2020), 'SNR G39.2-0.3, an hadronic cosmic rays accelerator'

[211]: Pohl, M. et al. (2015), 'Reacceleration of electrons in supernova remnants'

[212]: Caprioli et al. (2020), 'Kinetic Simulations of Cosmic-Ray-modified Shocks. II. Particle Spectra'

[213]: Dwarkadas (2007), 'The Evolution of Supernovae in Circumstellar Wind Bubbles. II. Case of a Wolf-Rayet Star'

[214]: Berezinskii et al. (1989), 'Radiation from young SN II shells produced by cosmic rays accelerated in shock waves'

[215]: Berezhko et al. (2000), 'Kinetic theory of cosmic ray and gamma-ray production in supernova remnants expanding into wind bubbles'

propagation from the free wind region in the wind bubble to the shocked wind region. In both studies, the complete HD evolution of the CSM during the lifetime of the progenitor was not considered. However, a realistic picture of the CSM at the pre-supernova stage can potentially impose better constraints than these already demonstrated analyses.
In addition, the amplified magnetic field by resonant and non-resonant CR streaming instabilities regulate the spectrum of turbulence, and consequently the diffusion coefficient as well as the maximally attainable particle energy at any point in time during the evolution of the remnant [105]. A detailed consideration of turbulent magnetic field is beyond the scope of this Chapter. In Chapter 6, particle acceleration, as well as radiation from the remnant are explored considering self-consistent magnetic field amplification along with realistic hydrodynamics.

In this Chapter, the change in spectra of accelerated particles at the SNR forward shock that evolves through different regions of the stellar wind bubble, simulated using an evolutionary track for a star with ZAMS mass of $60 M_\odot$ is explored. This study also includes the effects of CSM magnetic field The influence of interactions between SNR and different discontinuities present in the bubble on the particle spectra is demonstrated and the obtained CR spectra in this scenario are softer than standard DSA predictions for strong shocks. Although the SNR with $60\ M_\odot$ progenitor is not a frequent event [216], this is fascinating as emissions from SNR with very massive progenitor star can be predicted theoretically. Moreover, a $60 M_\odot$ star is regarded to evolve through an LBV phase instead of an RSG phase and ends its life as a WR star as described in Section 2.3 and the respective evolutionary phases leave imprints in the morphology of the ambient medium, and hence, on the particle spectra.

[216]: Jennings et al. (2014), 'The Supernova Progenitor Mass Distributions of M31 and M33: Further Evidence for an Upper Mass Limit'

5.1 Numerical methods

The DSA of CRs in the test-particle approximation is modelled by using *RATPaC* and *PLUTO* code as described in Chapter 4. For the discussed study in this Chapter, the CR transport equation, HD equations and magnetic field induction equation are solved simultaneously. Although I elaborately describe the numerical modelling for particle acceleration at the SNR shock in Chapter 4, in this section I provide a brief presentation about the considered parameters for this specific Chapter.

5.1.1 Hydrodynamics

The numerical study with the core-collapse SNR inside a wind bubble includes the following steps:
(a) Construction of CSM at the pre-supernova stage: The

wind bubble simulation is not performed by me. I have been provided the pre-calculated HD parameters of the CSM at the pre-supernova stage as shown in Figure 5.1.1. Please see Comment 5.1.1. Here, I summarise the simulation method to the reader for the purpose of understanding the background of the simulations with SNR inside the CSM, done by me.

Comment 5.1.1

Acknowledgement- Wind bubble simulations during the lifetime of massive stars are performed by Dr. Dominique M.-A. Meyer.

An HD simulation using *PLUTO* code in one-dimensional spherical symmetry is performed to simulate the wind bubble created by a non-rotating $60M_{\odot}$ star at solar metallicity from ZAMS to the pre-supernova stage. For this simulation, 50000 equally spaced grid points are taken in the computational domain $[O, R_{\rm max}]$ with origin O and $R_{\rm max} = 150\,{\rm pc}$. To start the simulation, a radially symmetric spherical supersonic stellar wind is injected into a small spherical region of radius 0.06pc at the origin using the stellar evolutionary track for a star with ZAMS mass $60M_{\odot}$, described in [217], assuming ISM with uniform number density, $n_{\rm ISM} = 1{\rm atom\,cm^{-3}}$. In this case, Equations 4.2.1, and 4.2.2 are integrated with a second-order RK method using Harten-Lax-Van Leer approximate Riemann Solver (HLL) in *PLUTO* code. Optically thin

[217]: Groh, Jose H. et al. (2014), 'The evolution of massive stars and their spectra - I. A non-rotating 60 Mar from the zero-age main sequence to the pre-supernova stage'

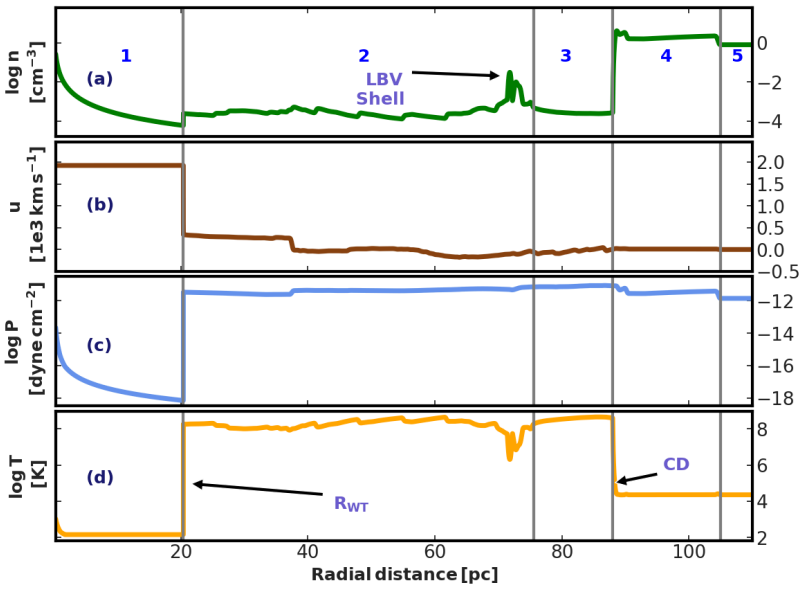

Figure 5.1.1: Pre-supernova CSM profiles of the number density, n, in panel (a), the flow speed, u, in panel (b), the thermal pressure, P, in panel (c), and the temperature, T, in panel (d), for the 60$M_{\odot}$ progenitor
Vertical grey lines mark the boundary of the free stellar wind (region 1), the shocked LBV and WR wind (region 2), the shocked wind from the O and B phases (region 3), the shocked ISM (region 4), and the ambient ISM (region 5). R_{WT} is the radius of the wind termination shock, LBV shell denotes the dense shell created by the interaction between LBV wind and WR wind, and CD represents the contact discontinuity of wind bubble between shocked wind and shocked ISM.

cooling and radiative heating terms are included through the source-sink term, $S = \Phi(T, \rho)$ in Equation 4.2.1 using the cooling and heating laws discussed in [218],

[218]: Meyer et al. (2014), 'Models of the circumstellar medium of evolving, massive runaway stars moving through the Galactic plane'

$$\Phi(T, \rho) = n^2(\Gamma(T) - \Lambda(T)) \tag{5.1.1}$$

where n is the particle number density, Γ is the rate for radiative heating from the effect of photo-ionised gas [219] and Λ is the rate of optically thin cooling following [220].
Further, CFL condition, mentioned in Definition 4.2.1 constrains the time steps for this simulation, initialised as $CFL = 0.1$.
The CSM evolution during the lifetime of the $60M_{\odot}$ star is

[219]: Bochkarev (1989), 'Book Review: D. E. Osterbrock Astrophysics of Gaseous Nebulae and Active Galactic Nuclei'

[220]: Wiersma et al. (2009), 'The effect of photoionization on the cooling rates of enriched, astrophysical plasmas'

followed for 3.95 million years until the pre-supernova stage. Then, this simulated CSM is assumed as the initial state of introducing the SNR in the simulation. This model is a one-dimensional equivalent of the two-dimensional simulation in [221] for the static-star scenario.

[221]: Meyer et al. (2020), 'Wind nebulae and supernova remnants of very massive stars'

(b) Modelling of the supernova ejecta profile: Supernova ejecta profile is defined following Definition 4.2.2. For the HD simulation of SNR evolution, the age of the remnant is considered to be $T_{SN} = 3\,\mathrm{yr}$. Further, x, n_{ej}, M_{ej}, and E_{ej} in Equations 4.2.11 and 4.2.12 are taken to be 2.5, 9, 11.75 $M_\odot$, and 10^{51}erg, respectively. Initially, ejecta temperature is set to 10^4K.

Definition 5.1.1 *Ejecta mass is defined as,*

$$M_{ej} = M_\star - \int_{t_{t_{ZAMS}}}^{t_{preSN}} \dot{M}(t)dt - M_{CompactObject}(1.4M_\odot)$$

where $M_\star$ is the ZAMS mass of the star and $\int_{t_{t_{ZAMS}}}^{t_{preSN}} \dot{M}(t)dt$ represents the total mass loss by the star during its lifetime from ZAMS (t_{ZAMS}) to the pre-supernova stage (t_{preSN}).

(c) Hydrodynamic modelling to study SNR shock evolution: To initiate the supernova explosion, the supernova ejecta profile is inserted into and interpolated with the pre-supernova CSM where the SNR ejecta extends to approximately 0.023pc. Equations 4.2.1 and 4.2.2 are solved considering the source-sink term, S as zero and HLLC solver using *PLUTO* code. Then, numerical simulation is performed in one-dimensional spherical symmetry with uniformly spaced grid cells in spatial resolution of about 4×10^{-4} pc. This high-resolution grid of HD applied for the SNR evolution inside CSM is reconstructed using the linear interpolation method on the pre-supernova CSM grid. This very high-resolution grid for the HD parameters which is a factor 7.5 finer than that used for the pre-supernova wind bubble is beneficial for resharpening the hydro data as discussed in Section 4.4.2 to ensure a sharp transition in HD parameters at the SNR shock.

5.1.2 Magnetic field

In the presence of the different evolutionary stages of the massive star [222], the construction of the CSM magnetic field is quite complex. Therefore, for simplicity, the CSM magnetic field is parametrised by applying background information about the stellar magnetic field instead of modelling the CSM magnetic field by performing MHD simulations for the entire lifetime of the $60M_\odot$ star.

[222]: Mackey et al. (2020), 'Simulations of Magnetised Stellar-Wind Bubbles'

Stellar mass and magnetic field are carried away by the wind of a rotating star. In the presence of a weak magnetic field, the flow speed can be described as for a non-magnetic wind

and the magnetic field becomes frozen-in [223]. Hence, the radial component of stellar magnetic field is expressed from Gauss's law ($\nabla \cdot \mathbf{B} = 0$) as,

[223]: Cassinelli (1991), 'Wolf-Rayet Stellar Wind Theory (review)'

$$B_{\rm r} = B_\star \frac{R_\star^2}{r^2}. \tag{5.1.2}$$

Further, the toroidal field for a rotating star in the equatorial plane [224] of rotation reads,

[224]: Ignace et al. (1998), '"WCFields": A Magnetic Rotating Stellar Wind Model from Wind Compression Theory'

$$B_\phi = B_\star \frac{u_{\rm rot} R_\star}{u_{\rm wind} r} \qquad r >> R_\star\ , \tag{5.1.3}$$

following [225, 226], where $B_\star$ and $R_\star$ are the stellar surface magnetic field and radius, respectively, $u_{\rm rot}$ and $u_{\rm wind}$ represent the surface rotational velocity in the equatorial plane and the radial wind speed, respectively. Equations 5.1.2, 5.1.3 suggest that the toroidal field will be dominant except for the region at very close to the stellar surface. Thus, the radial component should have an impact only during the first days of the SNR evolution as described in [227], and therefore, consideration of radial field is beyond the scope of this paper. The CSM magnetic field ($B_{\rm CSM}$) is parametrised by taking into account the stellar wind properties of a non-rotating $60 M_\odot$ star and the rotation of the WR star as the $60 M_\odot$ star becomes a WR star at the pre-supernova stage. In order to do so, the surface magnetic field and stellar radius are considered to be 1000 G and 6 $R_\odot$, respectively, following [228]. The wind speed and surface rotational velocity are approximated to 2000 km s^{-1} and 100 km s^{-1}, respectively, from [229, 230]. Further, the magnetic field is compressed by a factor of 4 at the wind termination shock following the corresponding density jump. In this parametrisation, the field strength in the shocked wind region, region 2 and region 3 in Figure 5.1.1 is assumed constant as a significantly more realistic model involves MHD simulations and hence the structure of the stellar magnetic field at the injection point of the stellar wind during the entire evolution of the progenitor star. Accordingly, the magnetic field in the regions denoted in Fig. 5.1.1 can be written as,

[225]: Chevalier et al. (1994), 'Magnetic shaping of planetary nebulae and other stellar wind bubbles'
[226]: Garcı–a-Segura et al. (1999), 'Hydrodynamics of ring nebulae: magnetic vs. non-magnetic hydro-models'

[227]: Inoue et al. (2021), 'Direct Numerical Simulations of Cosmic-ray Acceleration at Dense Circumstellar Medium: Magnetic-field Amplification and Maximum Energy'

[228]: Crowther (2007), 'Physical properties of Wolf-Rayet stars'

[229]: Ignace et al. (1996), 'Equatorial Wind Compression Effects across the H-R Diagram'
[230]: Chené et al. (2010), 'Large-scale Periodic Variability of the Wind of the Wolf-Rayet Star WR 1 (HD 4004)'

$$B_{\rm CSM} = \begin{cases} (0.33\ \mu{\rm G})\frac{R_{\rm WT}}{r} & \text{region 1,} \\ 1.32\ \mu{\rm G} & \text{regions 2 and 3} \\ 15.6\ \mu{\rm G} & \text{region 4} \\ 4.5\ \mu{\rm G} & \text{region 5 .} \end{cases} \tag{5.1.4}$$

The magnetic field at region 4, $B_{\rm shell}$ has been evaluated following [231],

[231]: Marle et al. (2015), 'Shape and evolution of wind-blown bubbles of massive stars: on the effect of the interstellar magnetic field'

$$B_{\rm shell} = \frac{R^2 B_{\rm ISM}}{R^2 - (R-d)^2}\ , \tag{5.1.5}$$

where $B_{\rm ISM}$ is the ISM magnetic field, and R and d are the outer radius and the thickness of region 4, respectively.
The considered magnetic field strength in the free wind is very weak and, hence, the magnetic pressure is dynamically unimportant and $B_{\rm ISM}$ is considered to provide super-Alfvénic motion of the shell in region 4 into the ISM allowing a wind bubble outer shock in the ISM.
The magnetic field in the SNR ejecta is calculated following Definition 4.3.1 considering the volume-averaged magnetic field of $B_{\rm ej,0} = 30\,{\rm G}$ initially when the SNR radius is $r_{\rm ej,0} = 10^{15}$ cm.
Finally, to achieve the subsequent evolution of the large-scale frozen-in magnetic field profile for the entire lifetime of the SNR, the induction equation, Equation 4.3.3 for ideal MHD is solved in one-dimensional spherical symmetry. This method resembles the MHD for negligible magnetic pressure.

5.1.3 Diffusion coefficient

The spatial diffusion coefficient, $D_{\rm r}$ in this study is considered to be ten times the Bohm diffusion coefficient ($D_{\rm B}$), $D_{\rm r} = 10 D_{\rm B}$ where $D_{\rm B}$ is expressed in Equation 4.3.11, in the entire region downstream of the SNR forward shock. I discuss the diffusion coefficient elaborately in Section 4.3.3.
In a more realistic approach, the transport equation of magnetic turbulence, Equation 4.3.4 should be solved at least for the resonant CR streaming instability and the corresponding study is discussed in Chapter 6.

5.1.4 Particle acceleration

The time-dependent transport equation for the differential number density of CRs expressed in Equation 4.1.1 is solved in one-dimensional spherical symmetry in test-particle approximation. A detailed description of the CR transport equation is provided in Section 4.1.

Injection of particles: The source of particles involved in the DSA process at the SNR forward shock is described in Section 4.1. Although the particle injection parameter, $\xi = 4.24$ has been estimated for SN1006 [189], in this study, $\xi = 4.4$ is taken as for smaller values of ξ, the test-particle approximation is not valid during the SNR forward shock propagation through the dense LBV shell and the shocked ISM.

The coupled equations for the HD evolution of the SNR, the evolution of the large-scale magnetic field, and the transport of CRs are solved simultaneously for this study. The time-stepping for solving the CR transport equation and magnetic field induction is 1 year except during the shock-shock interactions discussed in Section 4.4.3 whereas the standard CFL

condition, discussed in Comment 4.2.1 constraints the time-step of the hydrodynamic simulation in order of $10^{-3} - 10^{-4}$ years.

5.2 Results

5.2.1 Shock parameters

Comment 5.2.1

Here the shock velocity represents the shock propagation velocity in the simulation frame. Otherwise, I explicitly mention the frame of reference.

The evolution of the SNR with a ZAMS mass $60 M_{\odot}$ progenitor has been probed for 46 000 years, until the SNR forward shock starts to expand inside the shocked ISM region, and the sonic Mach number of the forward shock falls below 2. Figure 5.2.1 depicts the time evolution of the forward shock radius, velocity, and sub-shock compression ratio during the propagation of the SNR forward shock through the different regions of the wind bubble illustrated in Fig. 5.1.1. In the free stellar wind region, the shock velocity (see Comment 5.2.1) gradually decreases from approximately $7300\,\mathrm{km\,s^{-1}}$ to $5300\,\mathrm{km\,s^{-1}}$. After approximately 3300 years, the SNR forward shock interacts with the wind termination shock and transits to the denser shocked wind. Consequently, the shock speed sharply falls to $1500\,\mathrm{km\,s^{-1}}$ and after nearly 4830 years, the forward shock velocity increases steeply by $1400\,\mathrm{km\,s^{-1}}$ as a result of the tail-on collision between the forward shock and the reflection off the contact discontinuity between the SNR forward and reverse shocks of the reflected shock, produced during the collision between the forward shock and the wind termination shock as described in Comment 4.4.1. At later times, the shock velocity fluctuates a lot, because of the interactions between the forward shock and different weaker discontinuities, present in the shocked wind region. Further, between 19000 years and 23000 years, the forward shock evolves through the LBV shell, followed by a slight rise in shock velocity after 24000 years during the passage through the low-density shocked wind of the O and B phase of the progenitor. At last, after 32000 years, the forward shock interacts with the contact discontinuity of the wind bubble and the shock velocity plummets to $46\,\mathrm{km\,s^{-1}}$ from approximately $2000\,\mathrm{km\,s^{-1}}$.

The shock is strong and the sub-shock compression ratio is close to 4, in the free stellar region. After that, Figure 5.2.1 demonstrates a reduction of the sub-shock compression ratio to 2.9 as soon as the forward shock enters the hot shocked stellar wind and it finally reaches 1.5 right before the collision between the SNR forward shock and contact discontinuity of the wind bubble at 32000 years. The fluctuations in the sub-shock compression ratio simply depict the variation in the sonic Mach number of the forward shock. Tests verify that the numerically derived value $\mathrm{Cr_{RATPaC}} = \mathrm{V_u}/\mathrm{V_d}$, with $\mathrm{V_u}$ and $\mathrm{V_d}$ as the upstream and downstream flow speed in the forward shock rest frame matches well with the theoretical value by considering the upstream sonic Mach number $\mathscr{M}_{\mathrm{n}}$ as

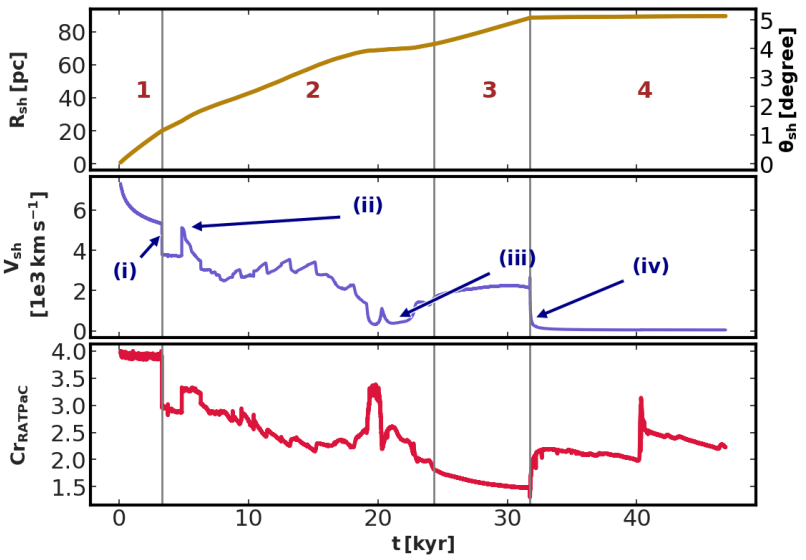

Figure 5.2.1: Behaviour of the SNR forward shock parameters: radius (R_{sh}), velocity (V_{sh}), and subshock compression ratio (Cr_{RATPaC}). In the upper panel, we also provide the angular scale, θ_{sh}, for a distance of 1000 parsec. **(i)-(iv) mark interactions of the FS with different discontinuities**, namely (i) the wind termination shock, (ii) another outgoing shock, (iii) the LBV shell, and (iv) the contact discontinuity of the wind bubble..

elaborated in Equation 3.3.3, $Cr_{Theoretical} = (1+\gamma)\mathcal{M}_n{}^2/((\gamma-1)\mathcal{M}_n{}^2+2)$, where $\gamma = 5/3$. Conclusively, the shocked wind is hot enough to reduce the sonic Mach number to single-digit numbers.

5.2.2 Particle spectra

The proton and electron spectra at different times for the respective evolution of the SNR forward shock through the different regions of the wind bubble are evaluated in terms of the volume-averaged spectra for the entire downstream region of the SNR forward shock. The large-scale transported magnetic field, discussed in Section 5.1.2 structures specifically the electron spectra by the synchrotron energy losses. Further, in the modelled large-scale magnetic field, the field strength inside the SNR reverse shock becomes approximately 0.01 μG, and consequently, inverse Compton losses dominate in the deep interior of the SNR, as expressed in Equation 3.4.7.

Forward shock in the free wind: The SNR forward shock expands through the free wind at 3000 years and reaches close to the wind termination shock located at a radius of about 20 parsecs, as illustrated in Figure 5.2.2. The first and third rows of the first column of the same Figure 5.2.2 depict the corresponding profiles of the gas number density, n, and the magnetic field (B) respectively. The magnetic field configuration demonstrates the peak field strength at the contact discontinuity between the SNR forward and reverse shocks at the radius of approximately 16 parsec and becomes moderately weaker towards the forward shock. At this age, the volume-averaged downstream spectra for protons show the p^{-2} spectra following the prediction from the test-particle DSA for strong shocks and the maximum achievable energy for protons reach 5 TeV.

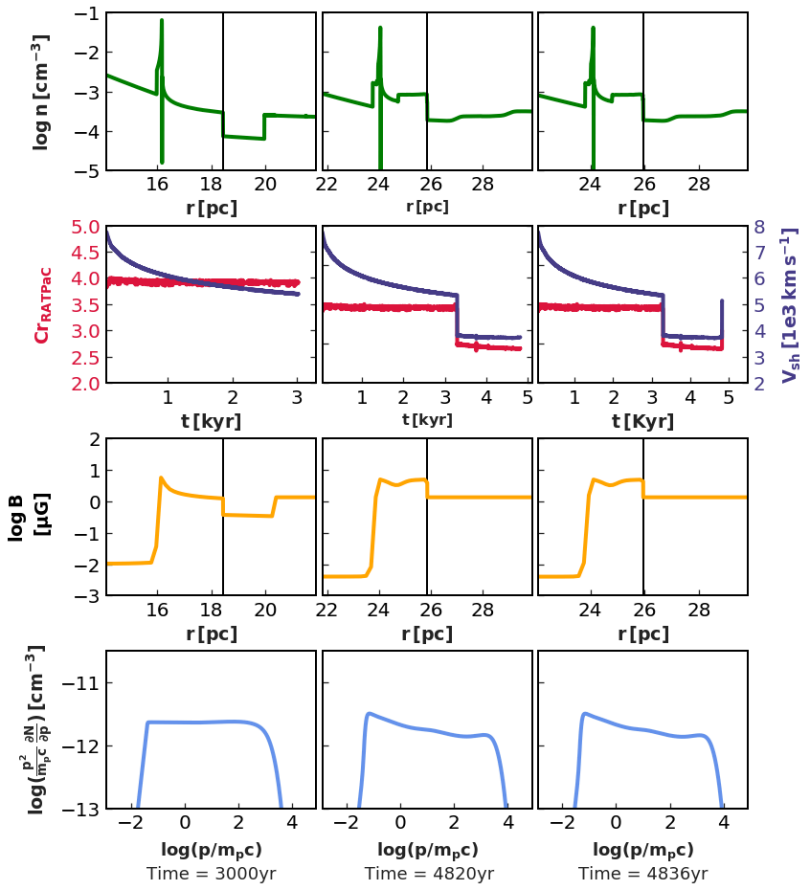

Figure 5.2.2: Proton spectra volume-averaged downstream at early ages of SNR.
The corresponding gas number density profiles, n, as a function of radius are shown in the first row. The second row displays the compression ratio (Cr_{RATPaC}) and the shock speed (V_{sh}) up to the specific age, the third row depicts the magnetic field profile (B), and the fourth row illustrates the proton spectra. The vertical lines in the first and third rows mark the forward shock position.

Forward shock in the shocked wind: The SNR forward shock propagates through the shocked wind at 4820 years. The respective proton spectrum, shown in the second column of Figure 5.2.2 starts to diverge from the standard p^{-2} spectrum and shows softness, as a consequence of the lower sonic Mach number of the forward shock in this region. Besides, the field strength in the downstream region of the SNR forward shock is very low, and hence the diffusion coefficient is large. So, sufficiently higher energetic particles can penetrate the deep downstream region and are able to interact with some of the reflected shocks as the by-products of the interaction between the forward shock and the wind termination shock. Consequently, this situation creates a weak but noticeable spectral break above 10 GeV. However, the exact structure of the spectral break may depend on the magnetic field configuration and can be slightly different for a full MHD model or the inclusion of the transport of magnetic turbulence as prescribed in 4.3.4. The corresponding electron spectrum in Figure 5.2.5 also exhibits this spectral break.
Furthermore, an outgoing shock emerging from the collision between the SNR contact discontinuity and the reflected shock, produced from the interaction between the SNR forward shock and the wind termination shock is about to merge with the forward shock. Thus, both the shock velocity and the sub-shock compression ratio increase sharply, as shown for 4836 years in the third column of Figure 5.2.2, immediately after the shock-shock tail-on collision and no

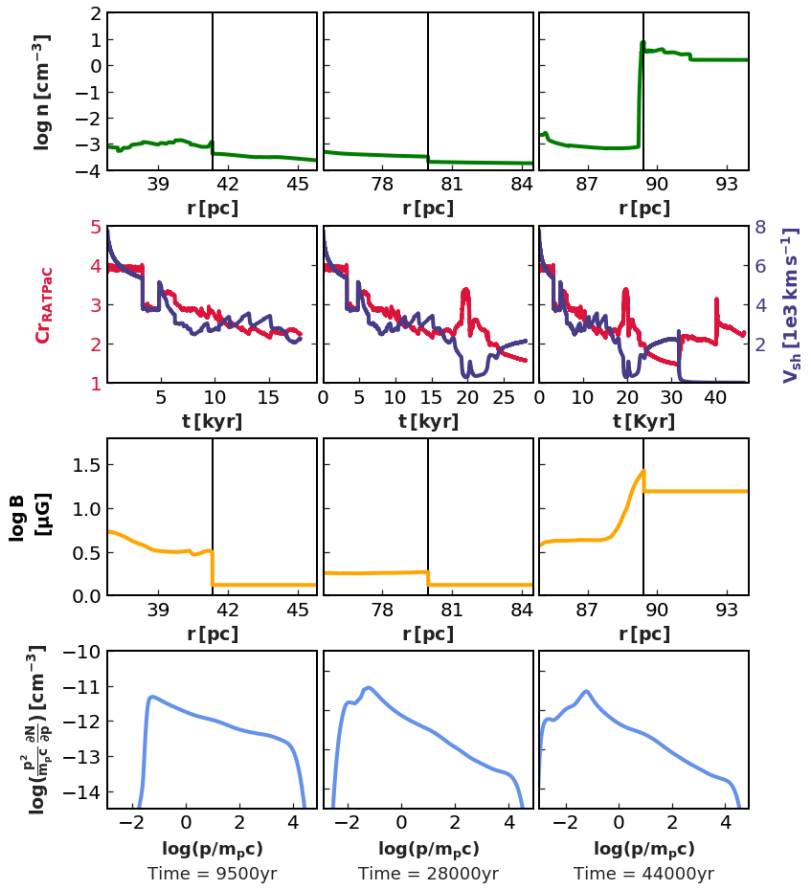

Figure 5.2.3: Proton spectra volume-averaged downstream with corresponding parameters same as Figure 5.2.2 but at later times.

visible change in the spectrum are observed. As discussed in Section 4.4.2 and Appendix B, the shock merging does not immediately shape the volume-averaged proton spectrum but this interaction will increase the acceleration rate, and therefore, the acceleration efficiency of the SNR forward shock that eventually provides higher maximum achievable energy of the particles.

The first column of Figure 5.2.3 shows the parameters and the proton spectra at 9500 years. In this stage, the SNR forward shock has already experienced several interactions with different discontinuities inside the shocked stellar wind. Around this age, the proton spectra are softer with a spectral index of approximately 2.3 with slight variations between the GeV and about 10 TeV energy bands. The running spectral index at this time is also illustrated in Figure 5.2.4. Later on, after 28000 years, the SNR forward shock passes through the shocked wind region from the O and B phases of the progenitor star after crossing the LBV shell. During the interaction of the SNR forward shock with the relatively dense and cold LBV material, the the injection rate of low-energy particles into the DSA becomes high as well as the injection momentum becomes low because of the low temperature, following the simplified injection model describe in Section 4.1. Therefore, the resulting spectrum in the second column of Figure 5.2.3 displays the pile-up at very low energy for this amplified injection. However, the spectral softness above a few tens of MeV energies is evident and originates entirely

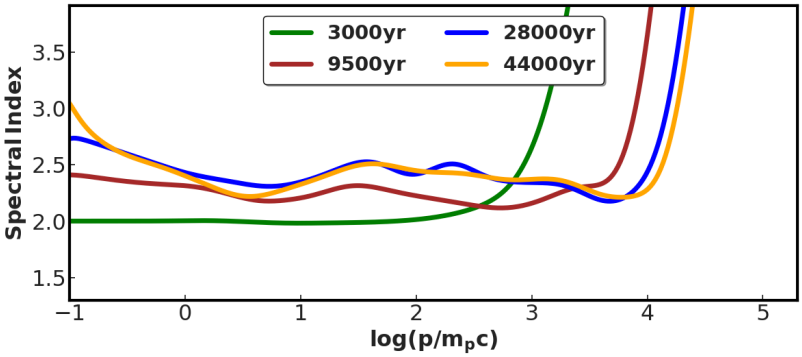

Figure 5.2.4: Variation of the spectral index for volume-averaged forward shock downstream protons spectra at different ages with as a function of momentum

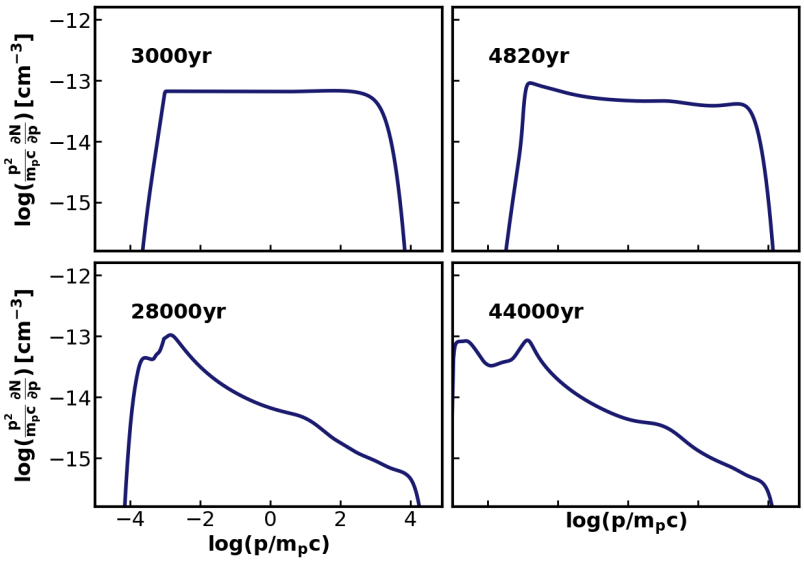

Figure 5.2.5: Volume-averaged forward shock downstream spectra at different ages of the SNR for electrons

from the small compression ratio of the SNR forward shock. At this time, the spectral index of accelerated protons reaches approximately 2.5 above 10 GeV from Figure 5.2.4.

Forward shock in the shocked ISM: The collision between the SNR forward shock and the contact discontinuity of the wind bubble significantly reduces the acceleration efficiency of the forward shock as the shocked ISM is approximately 10^4 times denser than the shocked wind region. Additionally, this collision increases the injection rate of lower energy particles and also forms a reflected shock with a velocity of approximately 2000 km s^{-1}. Therefore, the forward shock becomes too weak to accelerate particles efficiently, but the reflected shock will eventually collide with other structures and will lead to the formation of several outgoing shocks that can reach the SNR forward shock at later times. At this time, the velocity of the innermost reflected shock increases to approximately 3000 km s^{-1} during its propagation towards the ejecta and this shock may re-energise the particles that are already accelerated by the SNR forward shock. This situation is comparable to the efficient acceleration at the reverse shock of a very young SNR; for example Cas A [232]. Although, the efficient particle acceleration at the reverse shock needs magnetic amplification significantly because of the presence of the weak field in the ejecta [233, 234]. Further,

[232]: Borkowski et al. (1996), 'A Circumstellar Shell Model for the Cassiopeia A Supernova Remnant'

[233]: Ellison, D. C. et al. (2005), 'Nonlinear particle acceleration at reverse shocks in supernova remnants'

[234]: Zirakashvili et al. (2014), 'Nonthermal Radiation of Young Supernova Remnants: The Case of CAS A'

the proton and electron spectra at 44000 years, shown in the third column of Figure 5.2.3 and Figure 5.2.5, respectively are significantly softer than a p^{-2}. After this time, no further changes in proton and electron spectra are observed and the simulation is stopped after 46000 years.
The hydrodynamics within the wind bubble becomes very complex eventually with the evolution of SNR because of the multiple reflected and transmitted shocks. For modelling the particle acceleration precisely in this scenario, resolving all the shocks in the forward shock downstream region is preferable yet quite difficult to execute. Therefore, the higher energetic particles may experience two or more small shocks as one structure with smaller or larger velocity compression than the actual velocity compression and this larger velocity compression may be responsible for small spectral bumps at higher energies near cut-off.

5.2.3 Non-thermal emission

Three non-thermal emission processes such as synchrotron emission, inverse Compton scattering of CMB photons, and decay of neutral pions are considered. The spatially integrated spectra of these non-thermal emissions are calculated following the method [162], and [143], respectively. Figures 5.2.6 and 5.2.8 illustrate synchrotron and gamma-ray spectra, respectively at different times referring to the SNR forward shock propagation inside the different regions of the wind bubble. Figure 5.2.7 depicts the spectral index of synchrotron emission as a function of photon energy. Further, Figure 5.2.9 shows the energy flux for synchrotron and gamma-ray emissions during different evolutionary stages of the SNR. The non-thermal flux is calculated for the remnant located at a distance of 1 kpc.
In this simulation, the magnetic field strength is weak both upstream and downstream of the SNR forward shock until the forward shock reaches close to the shocked ISM. Consequently, a synchrotron cut-off energy above 100 eV has been achieved for the old remnant whereas, for the first few thousand years, the cut-off energy only reaches near 50 eV. In this described scenario, magnetic amplification by CR streaming instabilities or dynamo action has not been included, yet [235, 236] discussed some observational evidence for these phenomena.

[235]: Ellison (1999), 'Photons and Particle Production in Cassiopeia A: Predictions from Nonlinear Diffusive Shock Acceleration'
[236]: Fang et al. (2013), 'Gamma-ray properties of supernova remnants transporting into molecular clouds: the cases of IC 443 and W44'

Forward shock in the free wind: The flux of the synchrotron and hadronic emission decreases with time following the declining density, $\rho \propto 1/r^2$, and magnetic field profile $B \propto 1/r$ in this region. In region 1 in Panel (a) of Figure 5.2.9, the simulated radio flux at 5 GHz energy and the X-ray flux in the range $0.1\text{keV} - 10\text{keV}$ illustrates a power-law decline with different slopes. Therefore, in this considered framework, X-ray emission dominates at the very initial stage of the remnant, but as a result of the declining maximum achievable energy of electrons, the X-ray emission dims quicker than radio

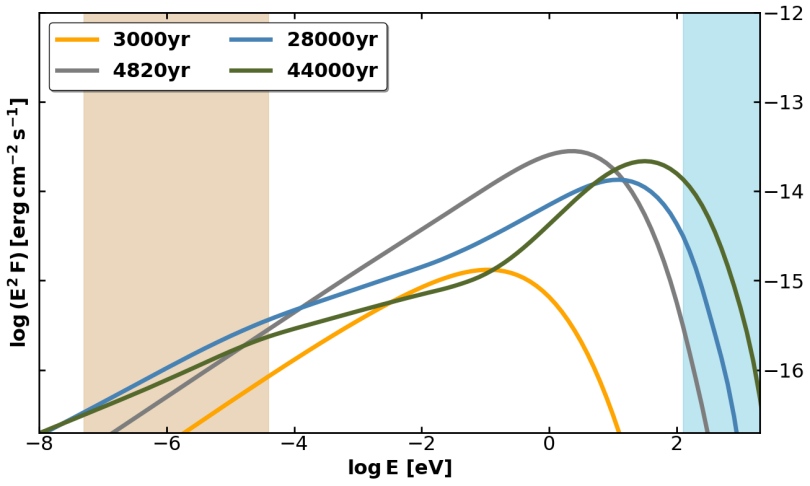

Figure 5.2.6: Spatially integrated synchrotron spectra at different ages of the SNR.
The brown band indicates the 50 MHz − 10 GHz range and the blue band denotes 0.1 keV − 40 keV.

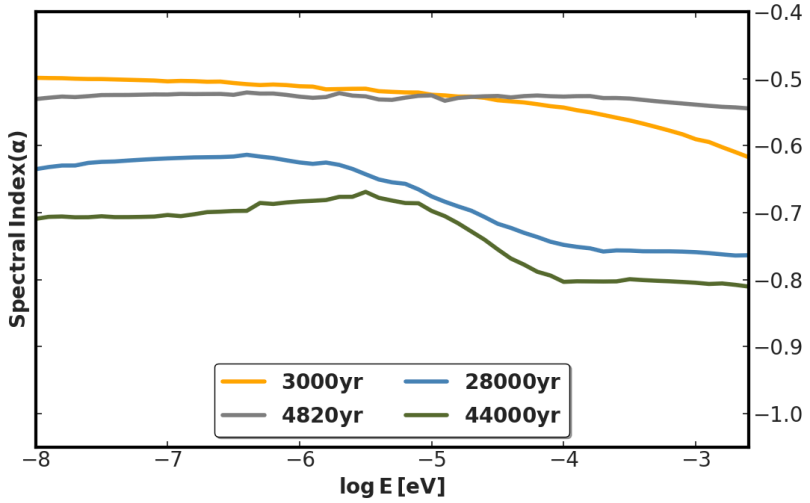

Figure 5.2.7: Variation of the spectral index (α) for synchrotron emission with energy at different ages.
where energy flux, $P_{syn}(\nu) \propto \nu^{\alpha}$ from Equation 3.4.3.

emission, and hence, radio emission begins to dominate after around 1100 years. The gamma-ray flux in panel (b) of Figure 5.2.9 illustrates the dominant inverse Compton emission for high energy gamma-ray flux (0.1 GeV − 100 GeV) except for approximately the initial 60 years and pion-decay emission is prominent in the very high energy (> 1 TeV) band. Thus, the enhanced pion-decay emission is achieved initially as the remnant passes through the dense material and the decrease in electron cut-off energy reflects the reduction in inverse Compton flux at the very high energy band.

Forward shock in the shocked wind: In this region, the synchrotron flux in the X-ray band begins to grow and eventually, dominates over the radio flux as a consequence of the increasing magnetic field strength as shown in region 2 of panel (a) of Figure 5.2.9. During this stage of the SNR forward shock evolution inside very low density, the high energy and very high energy gamma-ray emissions are dominated by inverse Compton emission. Further, the slight fluctuations shown in the non-thermal emission flux arise from the interactions between the SNR forward shock and several discontinuities present in this region of the wind bubble. For instance, the small increase in high energy pion-decay and radio emission near 20000 years as shown in Figure 5.2.9 by the blue-shaded

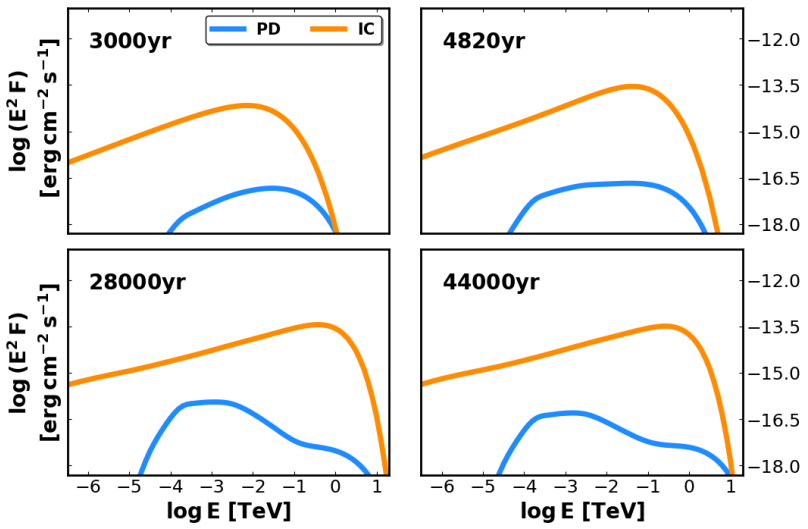

Figure 5.2.8: Spatially integrated gamma-ray spectra of pion-decay (PD) emission and inverse Compton (IC) scattering at different ages.

region between 17800 years and 23500 years suggests the collision between the SNR forward shock and the LBV shell. Further, at 4820 years the electron spectrum is slightly softer and hence, the synchrotron spectrum demonstrates an index of the synchrotron power spectrum, $\alpha \approx -0.53$ from Equation 3.4.3 in the radio band, shown in Figure 5.2.7. Figure 5.2.9 indicates that after 4820 years, the pion-decay emission increases in comparison to that at the later stage of the SNR forward shock propagation through the free wind region due to the roughly constant gas density in the shocked wind. At this stage, inverse Compton emission is in spectral agreement with, but at a lower flux than the observed emission from RX J1713.7-3946 [237] and Vela Jr. [238]. At 28000 years, the two-component structure of the synchrotron spectrum that reflects the break in the electron spectrum becomes noticeable and the radio spectral index approaches $\alpha \approx -0.7$. Additionally, the inverse Compton emission extends to the TeV scale and the pion-decay spectrum shows a weak pile-up around 1 GeV, consequently from the amplified injection in the LBV shell as discussed in Section 5.2.2.

[237]: Federici et al. (2015), 'Analysis of GeV-band gamma-ray emission from SNR RX J1713. 7-3946'

[238]: Sushch et al. (2018), 'Modeling of the spatially resolved nonthermal emission from the Vela Jr. supernova remnant'

Forward shock in the shocked ISM: After reaching the shocked ISM, the SNR forward shock starts to expand in a region with a strong magnetic field, and consequently, synchrotron emission changes. Simulated X-ray flux dominates over the radio flux in this region as displayed in Figure 5.2.9. A very soft synchrotron spectrum from the radio band with $\alpha_{\mathrm{R}} \approx -0.71$ to the infrared band with $\alpha_{\mathrm{IR}} \approx -0.83$ is obtained. The soft radio spectra in this simulation are consistent with the data for many Galactic SNRs [239], [137]. Additionally, the spectral index for pion-decay emission above 10 GeV follows the softness of the proton spectra.

[239]: Green (2009), 'A revised Galactic supernova remnant catalogue'

Morphology

Figures 5.2.10 and 5.2.11 illustrate the intensity maps for synchrotron and gamma-ray emissions, respectively considering

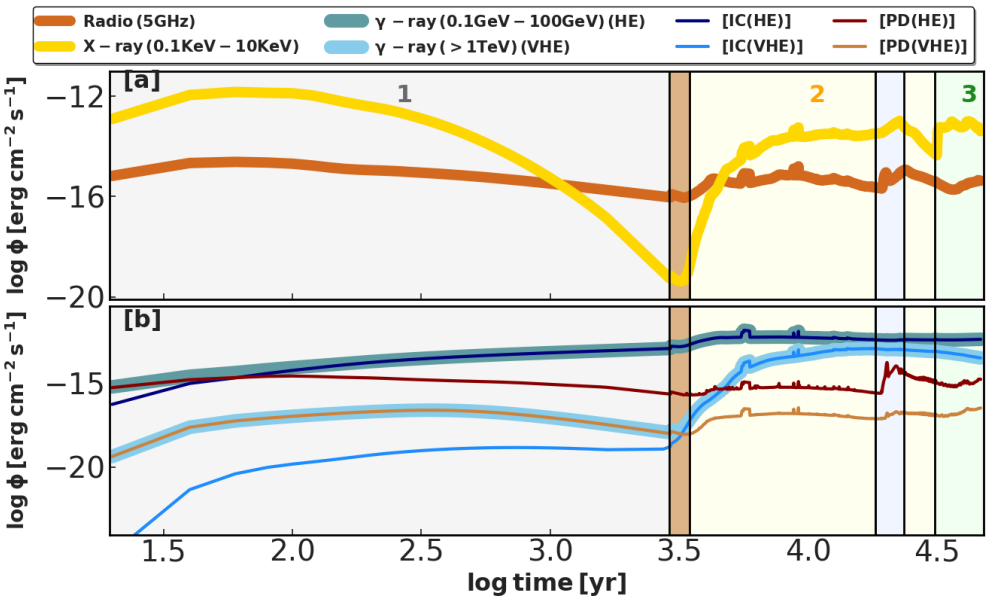

Figure 5.2.9: Evolution of energy flux (ϕ) during the lifetime of SNR for synchrotron emission and gamma-ray emission at specific energy ranges.
Region 1, Region 2, and Region 3 denote the free wind, shocked wind, and shocked ISM region, respectively, which are distinguished by different colours. The brown-shaded region around 3200 years denotes the FS transition from the free wind to the shocked wind zone, and the blue-shaded region around 20000 years denotes the interaction between the SNR forward and LBV shell

the remnant is located at 1 kpc distance. These intensity maps suggest the variation of the source morphology with time. The X-ray morphology, shown for 0.3 keV and 3 keV energies features a thin shell-like structure throughout the lifetime of the remnant, however the radio morphology, demonstrated for 1.4 GHz and 14 GHz features comparatively thicker shells that eventually becomes moderately centre-filled during the SNR forward shock propagation through the shocked wind region, displayed at 28000 years in Figure 5.2.10.
At 3000 years, when the SNR forward shock propagates through the free stellar wind, the brightest synchrotron emission in both the radio and the X-ray energy band emits from the contact discontinuity between the SNR forward and reverse shocks because of the strong magnetic field there [240]. At a later stage, during the forward shock expansion through the shocked wind, the synchrotron morphology is essentially the same as at earlier times. Further, after 28000 years the SNR forward shock approaches the contact discontinuity of the wind bubble, yet still inside the shocked wind and already collided with the LBV shell. At this stage, the brightest radio emission emanates from the region near the contact discontinuity between the SNR forward and reverse shocks as well as the region near the LBV shell whereas the contact discontinuity of the bubble looks X-ray bright as the magnetic field in shocked ISM region is almost 12 times stronger than that immediately downstream of the SNR forward shock. The forward shock is in the shocked ISM region at 44000 years and at that time, the maximum radio intensity emerges from the region near the LBV shell and X-ray emission comes from immediately downstream of the SNR forward shock. The magnetic field strength downstream

[240]: Lyutikov et al. (2004), 'The Origin of Nonthermal X-Ray Filaments and TeV Emission in Young Supernova Remnants'

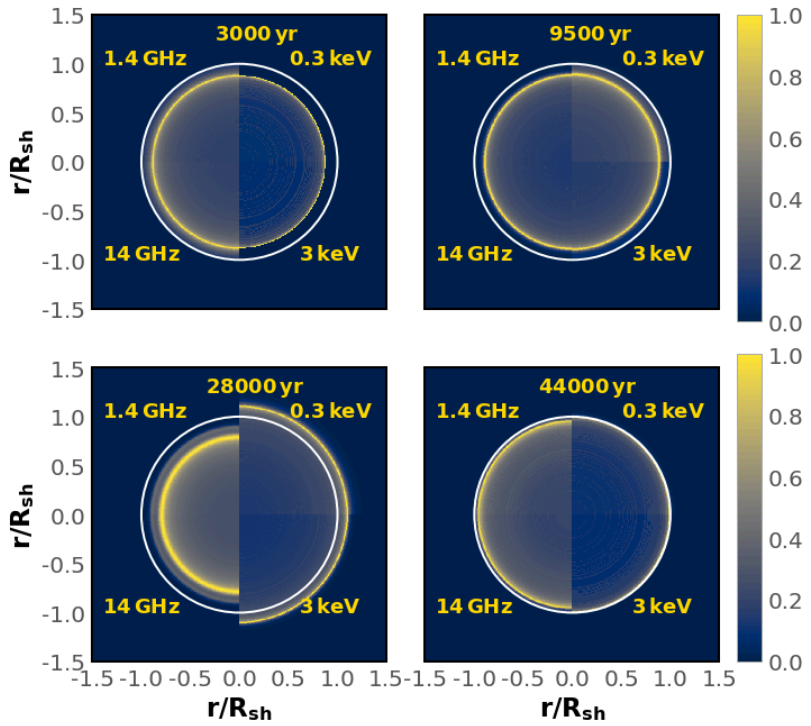

Figure 5.2.10: Normalised intensity maps of synchrotron emissions
Each panel is divided into four segments- the left hemisphere is for radio emission at 1.4 GHz in the upper half and at 14 GHz in the lower half. The right hemisphere is for the 0.3 keV and 3 keV X-ray intensity in the upper half and lower half, respectively. For each segment, the intensity is normalised to its peak value, shown by colour bars. The SNR forward shock position is marked by a white circle.

of the SNR forward shock is below 1μ *G* which is too weak to produce radio emissions significantly but the SNR appears as slightly centre-filled in the radio band for the diffusion of the higher energetic electrons in the deep downstream region.
In the scenario of the intensity maps for the gamma-ray band, the inverse Compton morphology illustrates a thick shell and the pion-decay emission appears centre-filled during the earlier evolutionary stages of the remnant inside the free wind, as shown in Figure 5.2.11 at 3000 years. The brightest inverse Compton emission comes from the region around the SNR forward shock for 10 GeV and 1 TeV energies and the interior of the remnant also looks brighter as a consequence of the penetration of the higher energetic electrons inside the deep downstream on account of the weak magnetic field. On the other hand, pion-decay emission mainly comes from two regions: the dense ejecta in the interior of the SNR and a broad region near the contact discontinuity between the SNR forward and reverse shocks. After that, at 9500 years the inverse Compton emission at 10 GeV emanates from the entire downstream region of the SNR forward shock, and at 1 TeV a shell at immediately downstream of the forward shock becomes inverse Compton bright. Similarly, the pion-decay emission is visible from almost the entire interior of the SNR forward shock, and at TeV energies most of the flux emanates from the SNR ejecta. At 28000 years, the entire region inside the SNR reverse shock is inverse Compton bright, particularly where the magnetic field is weak. Although the pion-decay emissions for 10 GeV and 1 TeV show shell-like feature, the TeV shell is located at the wind bubble contact discontinuity, while at 10 GeV the maximum pion-decay intensity comes from the region around the LBV shell. Finally, during the

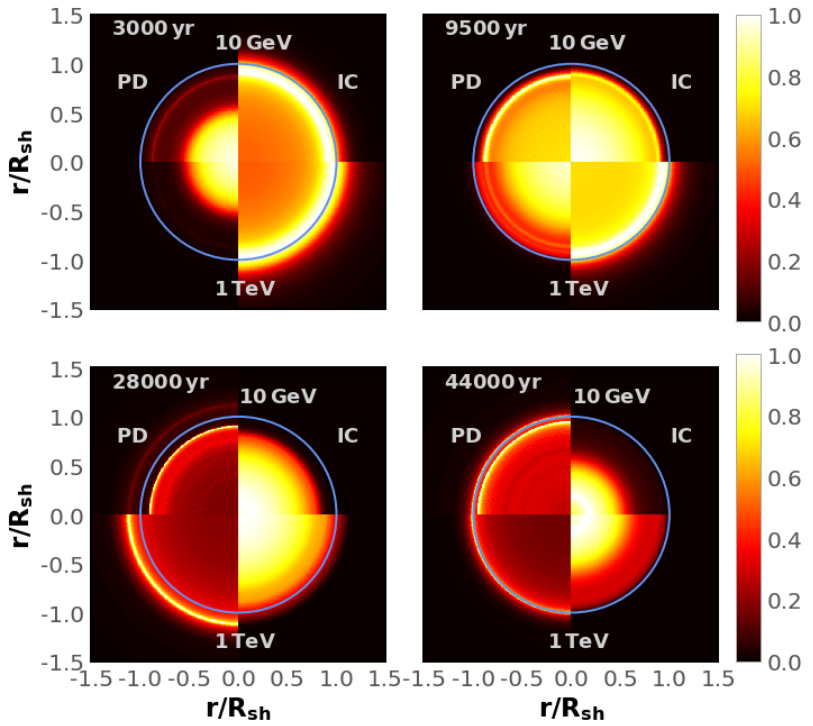

Figure 5.2.11: Normalised intensity maps of pion-decay (PD) and inverse Compton (IC) emissions.
The segments are organised to distinguish the photon energy: 10 GeV in the upper half and 1 TeV in the lower half, pion-decay on the left hemisphere and inverse Compton on the right hemisphere. In each segment, the intensity is normalised to its peak value as shown by colour bars. The SNR forward shock position is marked by a light blue circle.

expansion of the SNR forward shock inside the shocked ISM region, the inverse Compton emission appears centre-filled inside the reverse shock, similarly as earlier times, whereas the pion-decay emission shows a shell-like morphology, as displayed in Figure 5.2.11 at 44000 years.
In reality, the emission maps are very complex and patchy as a consequence of the Rayleigh-Taylor instability [241]. The distinct shell-like morphology in the calculated intensity maps in this study reflects the considered spherical symmetry in 1 dimension in the numerical modelling.

[241]: Fraschetti, F. et al. (2010), 'Simulation of the growth of the 3D Rayleigh-Taylor instability in supernova remnants using an expanding reference frame'

5.3 Conclusions

I have studied the evolution of the SNR inside the CSM, shaped by the $60\,M_\odot$ progenitor star during its lifetime. Then, the influence of the interactions between the SNR forward shock and different discontinuities in the CSM, on the particle acceleration, for instance, specifically the impact of the wind-termination shock, the dense LBV shell, the wind bubble contact discontinuity, as well as the effect of shock-shock merging are explored. The discussed simulation of particle acceleration at the SNR forward shock suggests that the spectra of accelerated particles in core-collapse SNRs significantly diverge from the standard DSA prediction for a strong shock limit.
Further, the spectra of accelerated particles depend on the CSM magnetic field structure in addition to the CSM-SNR forward shock interactions. Throughout the propagation of the SNR forward shock inside the hot wind bubble and shocked ISM, starting at an age of about 3300 years, softer

particle spectra are persistently obtained as a consequence of the relatively small sonic Mach number of the forward shock. For protons above 10 GeV energy, the spectral index reaches around 2.5. Additionally, the calculated total production spectrum at 46000 years released into the ISM, follows a broken power-law with a spectral index of $s \approx 2.4 - 2.5$ above 10 GeV energy. This is consistent with the spectral shape of the injection spectrum at higher energy needed by propagation models for the Galactic CRs [242, 243]. Apart from the impact of discussed small Mach number of the SNR forward shock, neutral particles [244, 245] in the shocked ISM and the non-linear study of DSA [246–248] can also have an effect on particle acceleration but taking into account both of these aspects is beyond the scope of this study.

In the framework of non-thermal emission, the leptonic contribution is prominent in the gamma-ray emission from the discussed SNR, and even that provides a relatively low flux. The pion-decay emission is likely, not observable but consists of a two-component structure in the spectrum after the collision of the SNR forward shock with the LBV shell. If the progenitor star is located in a high-density environment, this feature should be brighter and hence, possibly observable. The calculated intensity maps for non-thermal emissions suggest that the inverse Compton morphology varies between shell-enhanced and centre-filled, while the pion-decay emission has a centre-filled to shell-like morphology.

However, the detection of an extended object as discussed here with a radius exceeding 80 pc or 5° for a distance of 1 kpc, after 45 000 years with flux as low as this calculation is challenging. The flux may be enhanced for a high-density ISM and for efficient magnetic field amplification in the remnant and then there should be a possibility to observe such objects with the next generation of observatories, such as SKA, CTA, and LHAASO.

In this stated simulation, the considered SNR with 60 $M_\odot$ progenitor is completely based on theoretical reasoning, and the discussed analysis provides a lot of details about the expansion of the SNR inside wind bubble which can be used to further understand different observed SNRs, for example, SNR G150.3 + 4.5 [249] with angular size ∼ 3°. The very high shock velocity expected for this extended SNR propagating in a low ambient density suggests a core-collapse scenario with a large wind bubble and also the SNR forward shock is expanding in the shocked wind region. The predicted maximum cut-off energy for particles, 5 TeV and softer radio spectral index from some regions of this SNR are similar to the results of the discussed study in this Chapter. Additionally, inverse Compton-dominated gamma-ray spectra as suggested by this numerical study, are also predicted for SNR G150.3 + 4.5.

In conclusion, the evolution of an SNR with a WR progenitor is probed considering the Bohm-scaling of diffusion downstream and immediately upstream of the SNR forward shock. [215] estimated the maximum energy for accelerated

[242]: Strong et al. (2000), 'Diffuse Continuum Gamma Rays from the Galaxy'
[243]: Strong et al. (2007), 'Cosmic-Ray Propagation and Interactions in the Galaxy'

[244]: Ohira et al. (2009), 'Plasma Instabilities as a Result of Charge Exchange in the Downstream Region of Supernova Remnant Shocks'
[245]: Ohira et al. (2010), 'Effects of Neutral Particles on Modified Shocks at Supernova Remnants'

[246]: Drury et al. (1981), 'Hydromagnetic shock structure in the presence of cosmic rays'
[247]: Berezhko et al. (1999), 'A Simple Model of Nonlinear Diffusive Shock Acceleration'
[248]: Malkov et al. (2001), 'Nonlinear theory of diffusive acceleration of particles by shock waves'

[249]: Devin et al. (2020), 'High-energy gamma-ray study of the dynamically young SNR G150. 3+ 4.5'

protons and the cut-off energy for expected gamma-ray flux to be 10^{14} eV and 10^{13} eV, respectively, by considering the Bohm diffusion during the expansion of an SNR with a WR progenitor and an ejecta mass comparable to that in this discussed simulation. Although this simulation produces consistent results, the Bohm limit for CR diffusion may be too optimistic. [250, 251] considered CR streaming instability and Kolmogorov non-linearity in magneto-hydrodynamic waves and analytically estimated that for the ejecta-dominated stage, the maximum energy may exceed the "knee" but at the later Sedov phase it can be reduced to 10 GeV. Therefore, a future study including a diffusion model based on magnetic field amplification should be beneficial in this context.

[250]: Ptuskin, V. S. et al. (2003), 'Limits on diffusive shock acceleration in supernova remnants in the presence of cosmic-ray streaming instability and wave dissipation'

[251]: Ptuskin, V. S. et al. (2005), 'On the spectrum of high-energy cosmic rays produced by supernova remnants in the presence of strong cosmic-ray streaming instability and wave dissipation'

Next step: In this Chapter, I discuss the particle acceleration in the SNR with 60 $M_\odot$ progenitor, evolving inside the progenitor-modified wind bubble by considering the simplified Bohm-like diffusion coefficient. The following Chapter 6 will provide the reader with the change in particle spectra arising from the evolution of SNRs inside wind bubbles created by progenitors with different ZAMS masses by taking into account the derived time-dependent diffusion coefficient by solving the transport equation for scattering magnetic turbulence.

Particle acceleration in core-collapse SNRs with the self-consistent study of diffusion

6

The presented study in this chapter is submitted in **Astronomy & Astrophysics** and I restate this respective analysis with minor modifications.

The morphology of the CSM is structured by the massive stars through ionising radiation and stellar winds [252, 253]. The mass loss in the form of stellar winds should vary because of the evolution of massive stars through different stages as discussed in Section 2.3 [254, 255] and the evolution of mass-loss rate play an important role in shaping the environment of massive stars [198, 213]. Further, the structure of wind bubbles around massive stars is influenced by the stellar wind properties, for instance, [256, 257] studied the wind bubble around 35 $M_\odot$ and 60 $M_\odot$ stars including the interacting stellar winds from different stages of evolution. Also, the bipolar morphology of nebulae around LBV and WR stars as a result of asymmetric ambient medium from previous evolutionary stages were investigated in [258, 259].

As discussed in Section 2.2, massive star explodes as core-collapse SNRs and the resulting SNR blast waves eventually expand inside the complex ambient medium. Several observed SNRs such as Cas A, SN 1987A, and G 292 + 0.8 appear to expand inside the wind bubble. From Chapter 5, it is evident that the dynamics of the SNR blast waves should be regulated by the CSM parameters [198, 213] and should not only differ from that for a uniform ISM but can also depend on the type of progenitor star. However, the determination of the type of progenitors for SNRs from their morphology is not elementary, as the observed asymmetries in SNRs can also be created by the magnetic field and explosion mechanisms, for instance, "ear"-like structures observed in radio and X-ray emission have been explained by the interaction between the remnant and the bipolar CSM [260], while other studies [261, 262] suggested the orientation of external magnetic field and explosion mechanisms as the responsible factors in this scenario.

In the core-collapse framework, interactions between the SNR and ambient medium impact the emission from SNRs and studies [199], [263] recently probed the influence of an ambient medium modified by RSG and WR winds on the non-thermal emission from the remnants using simplified flow profiles. Furthermore, the discussed study in Chapter 5 elaborates on the spectral evolution and emission morphology for the SNR-CSM interaction using a simulated CSM structure for the stellar track of a 60 $M_\odot$ star by considering Bohm-like diffusion for accelerated particles. Although the entire HD evolution of CSM for the lifetime of the progenitor

[252]: Freyer et al. (2003), 'Massive Stars and the Energy Balance of the Interstellar Medium. I. The Impact of an Isolated 60 M_{solar} Star'
[253]: Dwarkadas (2022), 'Ionization-Gasdynamic Simulations of Wind-Blown Nebulae around Massive Stars'

[254]: Langer (2012), 'Presupernova evolution of massive single and binary stars'
[255]: Gormaz-Matamala et al. (2022), 'Evolution of massive stars with new hydrodynamic wind models'

[256]: Garcı–a-Segura et al. (1996), 'The hydrodynamic evolution of circumstellar gas around massive stars. II. The impact of the time sequence O star-> RSG-> WR star.'
[257]: Garcia-Segura et al. (1996), 'The dynamical evolution of circumstellar gas around massive stars. I. The impact of the time sequence Ostar-> LBV-> WR star.'
[258]: Dwarkadas et al. (2002), 'Radiatively Driven Winds and the Shaping of Bipolar Luminous Blue Variable Nebulae'
[259]: Meyer (2021), 'On the bipolarity of Wolf–Rayet nebulae'

[260]: Ustamujic et al. (2021), 'Modeling the Remnants of Core-collapse Supernovae from Luminous Blue Variable stars'
[261]: Townsend et al. (2005), 'A rigidly rotating magnetosphere model for circumstellar emission from magnetic OB stars'
[262]: Hungerford et al. (2005), 'Gamma rays from single-lobe supernova explosions'
[263]: Kobashi et al. (2022), 'Long-term Evolution of Nonthermal Emission from Type Ia and Core-collapse Supernova Remnants in a Diversified Circumstellar Medium'

has been considered in that study, the treatment of magnetic turbulence is not self-consistent. [105, 182] demonstrated that the self-generated magnetic field amplification influences the maximum attainable particle energies and the resulting particles spectra for type-Ia SNRs. Therefore, it is more realistic to include the combined effect of the CSM, CR streaming instabilities, and hence, time-dependent CR diffusion coefficient in the simulation, for exploring the particle acceleration and non-thermal emission in SNRs within wind bubbles.

In this Chapter, I explore the spectral evolution of accelerated particles at forward shocks of SNRs with 20 $M_\odot$, and 60 $M_\odot$ progenitors, during their propagation inside the corresponding wind bubbles, by taking into account the time-dependent evolution of self-generated magnetic turbulence. As discussed in Section 2.3, 20 $M_\odot$ star evolves through an RSG phase as the post-MS stage and 60 $M_\odot$ star has LBV and WR phases after MS. This Chapter exhibits the following aspects,
1. The difference in spectral shapes coming from the morphological dissimilarity of the CSM for both SNRs,
2. In both cases, the softening in particle spectra is obtained at higher energies during the later evolutionary ages, because of the weak driving of magnetic turbulence and the escape of highly energetic particles from the remnants.
3. The temporal evolution of the spectra for different emissions along with the emissions from the escaped particles around the remnants.
4. At last, the evolution of the morphology for the different energy bands and its dependence on the CSM structures.

6.1 Numerical methods

The DSA of particles in the test-particle approximation is modelled by using *RATPaC* and *PLUTO* code as discussed in Chapter 4. For the described study in this Chapter, the CR transport equation, HD equations, magnetic field induction equation, and transport equation for magnetic turbulence are solved simultaneously. I already presented the numerical modelling for particle acceleration at the SNR shock in Chapter 4, yet in this section, I provide a brief description of the considered parameters for this specific study.

6.1.1 Hydrodynamics

Construction of HD to study the expansion of the core-collapse SNR inside the wind bubble follows the same procedures as described in Section 5.1.1,
(a)Simulate the evolution of CSM and derive CSM structure at the pre-supernova stage: I again mention that the wind bubble simulation is not carried out by me (please see Comment 6.1.1) and I have been provided with the pre-calculated HD parameters of CSM at the pre-supernova stage for both 20 $M_\odot$ and 60 $M_\odot$ stars.

The simulation method for wind bubble around the 60 $M_\odot$ star is same as the description in Section 5.1.1. Therefore, here I only summarise the simulation method to the reader for the wind bubble around 20 $M_\odot$ star. The HD simulation with

Comment 6.1.1

Acknowledgement- Wind bubble simulations during the lifetime of massive stars 20 $M_\odot$ and 60 $M_\odot$ are performed by Dr. Dominique M.-A. Meyer.

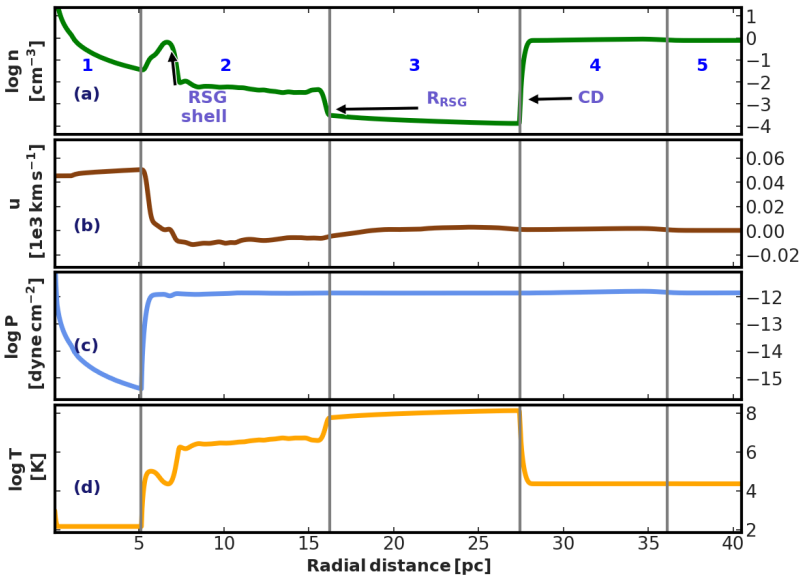

Figure 6.1.1: Pre-supernova CSM profiles of the number density, n, in panel (a), the flow speed, u, in panel (b), the thermal pressure, P, in panel (c), and the temperature, T, in panel (d), for the 20$M_\odot$ progenitor.
Vertical grey lines mark the boundary of the free RSG stellar wind region (region 1), piled-up RSG wind region (region 2), shocked MS wind region (region 3), shocked ISM region (region 4), and ISM (region 5). The RSG shell indicates the accumulation of decelerated freely expanding RSG wind, R_{RSG} denotes the transition between RSG and MS wind, and CD represents the contact discontinuity of wind bubble between shocked wind and ISM.

PLUTO code in 1-D spherical symmetry is performed with uniformly-spaced 50000 grid points in the computational domain [O, R_{max}] with origin O and R_{max} = 150 pc. For the initialisation of the simulation, the radially symmetric spherical supersonic stellar wind has been injected into a small spherical region of radius 0.06 pc at the origin, using the stellar evolutionary tracks for 20 $M_\odot$ star [35]) as described in Section 2.3 and Figure 2.3.1, assuming particle number density in ISM, n_{ISM} = 1 atom cm^{-3}. Further, for modelling the evolution of the corresponding CSM, the second-order Runge-Kutta method has been applied to integrate Equations 4.2.1, and 4.2.2 using HLL solver in *PLUTO* code. The optically thin cooling and radiative heating have been involved through the source-sink term, $S = \Phi(T, \rho)$, as expressed in Equation 5.1.1.
Figure 6.1.1 depicts the HD profiles for the pre-supernova CSM of 20 $M_\odot$ star after simulating the CSM evolution from ZAMS to the pre-supernova phase, over 8.64 million years. The created wind bubble in this scenario comprises dense RSG wind material up to approximately $r \approx 15$ pc. As the velocity of RSG is very slow in comparison to the MS wind, the deceleration of the RSG wind against the MS wind gives rise to the formation of RSG shell. The shaping of wind bubbles because of the collision between RSG and MS winds is also probed in [213] for 35 $M_\odot$ star. The main characteristic feature in this framework is the absence of a wind termination shock between the free wind and shocked wind region as shown in Figure 5.1.1 for 60 $M_\odot$ star.
As a comparison of CSM from 20 $M_\odot$ star with the wind bubble around 60 $M_\odot$, the temperature of 60 $M_\odot$-bubble is very hot in an extended region of shocked wind for almost 60pc, shown in Figure 5.1.1 while the CSM around 20 $M_\odot$

demonstrates high temperature only in the region of shocked MS wind.
(b) Modelling of the supernova ejecta profile: The supernova ejecta profile is defined following definition 4.2.2. For the simulation in this Chapter, the HD simulation for SNR evolution, the age of both remnants are considered to be $T_{\rm SN} = 3\,$yr. Further, x, $n_{\rm ej}$, and $E_{\rm ej}$ in Equations 4.2.11 and 4.2.12 are considered to be 2.5, 9, and 10^{51}erg, respectively. For $20\,M_\odot$ progenitor, $M_{\rm ej} = 3.25\,M_\odot$ and for $60\,M_\odot$ progenitor, $M_{\rm ej} = 11.75\,M_\odot$ from Equation 5.1.1. Initially, ejecta temperature is set to 10^4K.
(c) Hydrodynamic modelling to study SNR shock evolution: The supernova ejecta profile is interpolated with the pre-supernova CSM in which the SNR ejecta extends to approximately 0.043pc and 0.023pc for $20\,M_\odot$, and $60\,M_\odot$ stars, respectively depending on the progenitor masses. Further, as described in Section 5.1.1, Equations 4.2.1 and 4.2.2 are solved considering the source-sink term, S as zero using *PLUTO* code by applying HLLC solver in 1-D spherical symmetry with uniformly spaced grid cells in spatial resolution of about 4×10^{-4} pc.

6.1.2 Magnetic field

The total magnetic field strength in this simulation is given by,

$$B_{\rm tot} = \sqrt{B_0^2 + B_{\rm turb}^2}\,, \tag{6.1.1}$$

where B_0 and $B_{\rm turb}$ are the large-scale and turbulent magnetic field, respectively.

Large-scale field profile

As discussed in Section 5.1.2, simulating the CSM magnetic field for the entire lifetime of progenitors by solving MHD equations is out of the scope of this presented study. Hence, the magnetic field in the CSM around $20\,M_\odot$ star is parametrised likewise the construction of the CSM magnetic field for the $60\,M_\odot$ progenitor.
The magnetic field in the stellar wind of a rotating star is toroidal except for very close to the stellar surface and can be expressed by Equation 5.1.3.
The $20\,M_\odot$ star evolves through MS and RSG phases and during the RSG phase, the star becomes very large up to a few hundred times $R_\odot$, yet turns into a slower rotator [264], and the wind speed becomes $20-50\,{\rm km\,s^{-1}}$. An RSG is attributed to a weak surface field with $1-10\,$G from the measurements by [265, 266] and hence, $B_\star(R_\star/R_\odot) = 750\,$G is considered where $B_\star$ and $R_\star$ are the stellar surface magnetic field and radius, respectively. Then, Equation 5.1.3 describes the field strength for both free RSG wind and piled-up RSG wind regions. The transition between RSG and MS wind shown

[264]: Maeder et al. (2012), 'Rotating massive stars: From first stars to gamma ray bursts'

[265]: Aurière et al. (2010), 'The magnetic field of Betelgeuse: a local dynamo from giant convection cells?'
[266]: Tessore et al. (2017), 'Measuring surface magnetic fields of red supergiant stars'

in Figure 6.1.1, $R_{\rm RSG} = 16.3\,{\rm pc} \sim 7 \times 10^8\,R_\odot$ and MS wind has a very uncertain magnetic field. Therefore, a decrease in magnetic field strength at this transition by a factor of 3 following $B \propto \sqrt{\rho}$ and the density jump at $R_{\rm RSG}$ is considered. Further, the field strength of MS wind is considered constant for the entire region filled with the shocked MS wind. Finally, in the ISM, the field strength has been chosen as $4\,\mu$G to provide a super-Alfvenic flow to the shell indicated by region 4 in Figure 6.1.1. So, the magnetic field strength $B_{0,\,20\,{\rm M}_\odot}$ for the $20\,M_\odot$-bubble can be described as,

$$B_{0,\,20\,{\rm M}_\odot} = \begin{cases} (1.07\ \mu{\rm G})\frac{R_{\rm RSG}}{r} & \text{regions 1 \& 2} \\ 0.35\ \mu{\rm G} & \text{region 3} \\ 4.68\ \mu{\rm G} & \text{region 4} \\ 4.0\ \mu{\rm G} & \text{region 5 .} \end{cases} \tag{6.1.2}$$

For the $60\,M_\odot$ star, the CSM field is constructed using a similar methodology as discussed in Section 5.1.2, but the field strength is slightly changed to maintain the magnetic field as dynamically unimportant, for this simulation including self-consistence magnetic turbulence. Therefore, for different regions of wind bubble shown in Figure 5.1.1 the CSM magnetic field for this star is expressed as,

$$B_{0,\,60\,{\rm M}_\odot} = \begin{cases} (0.63\ \mu{\rm G})\frac{R_{\rm WT}}{r} & \text{region 1} \\ 2.52\ \mu{\rm G} & \text{regions 2 \& 3} \\ 14.8\ \mu{\rm G} & \text{region 4} \\ 4.3\ \mu{\rm G} & \text{region 5 .} \end{cases} \tag{6.1.3}$$

where $R_{\rm WT}$ is the radius of the wind termination shock. Finally, to get the subsequent evolution of large-scale frozen-in magnetic field profiles for the entire lifetime of both SNRs, the induction equation, Equation 4.3.3 for ideal MHD is solved in one-dimensional spherical symmetry and this method mimics the MHD for negligible magnetic pressure.

Magnetic turbulence

For calculating the turbulent magnetic field, the transport equation for the scattering magnetic turbulence spectrum, Equation 4.3.4 has been solved in one-dimensional spherical symmetry, considering Alfvén waves as scattering centres for CRs. The different components of this transport equation are described elaborately in Section 4.3.2.

6.1.3 Diffusion coefficient

The diffusion coefficient for CRs coupled to the magnetic spectral energy density per logarithmic bandwidth, $E_w(r, k, t)$ can be expressed by Equation 4.3.12. As in this Chapter self-consistent diffusion coefficient is applied for the simulation, a more realistic picture of CR acceleration in the SNR should be achieved in comparison to the calculation with a simplified Bohm-like diffusion coefficient described in Chapter 5.

6.1.4 Particle acceleration

The time-dependent transport equation for the differential number density of CRs is solved in one-dimensional spherical symmetry in test-particle approximation by using Equation 4.1.1.

Injection of particles

The injection of particles in the DSA process at the SNR forward shock is discussed in Section 4.1. The particle injection parameter, $\xi = 4.2$ is used in the simulations which is consistent with the observed radiation flux from SN1006 [189].

6.2 Results

The evolution of the SNRs for 20 $M_\odot$ and 60 $M_\odot$ progenitors are simulated for 30000 years and 110000 years, respectively. The behaviour of the SNR forward shock parameters and also the spectra for accelerated particles are described. Further, the spectra, achieved from the self-consistent magnetic turbulence are compared with the spectra for the Bohm-like diffusion framework, illustrated in Chapter 5. The spectra and morphology of non-thermal emissions from the SNRs are also presented.

6.2.1 Shock parameters

SNR with 20 $M_\odot$ progenitor

Figure 6.2.1 demonstrate the forward shock parameters for SNR with 20 $M_\odot$ progenitor. The forward shock velocity gradually decreases from 6300 km s^{-1} to 5300 km s^{-1}, and the sub-shock compression ratio is approximately 4, during the propagation of SNR forward shock inside free RSG stellar wind region. The interaction of forward shock and the dense RSG shell also lowers the shock velocity and the velocity drops to about 2000 km s^{-1}, and the sub-shock compression ratio reaches 3.7. Further, for the brief time spans around

1500 years and 3600 years, the compression ratio becomes approximately 4.2. This happens during the propagation of forward shock along a steeply decreasing density, once after reaching the peak of the RSG shell, and then at the transition from the piled-up RSG wind to the shocked MS wind. During this period, the rapid decrease in the upstream density in comparison to the downstream density results in a slightly higher compression ratio at the forward shock. Thus, the variations in compression ratio indicate different SNR-CSM interactions. The expansion of the SNR forward shock through the hot MS wind material in region 3, shown in Figure 6.1.1 leads to reduce the sonic Mach number of the shock, following Equation 3.3.3 and consequently, the compression ratio becomes approximately 3.5.

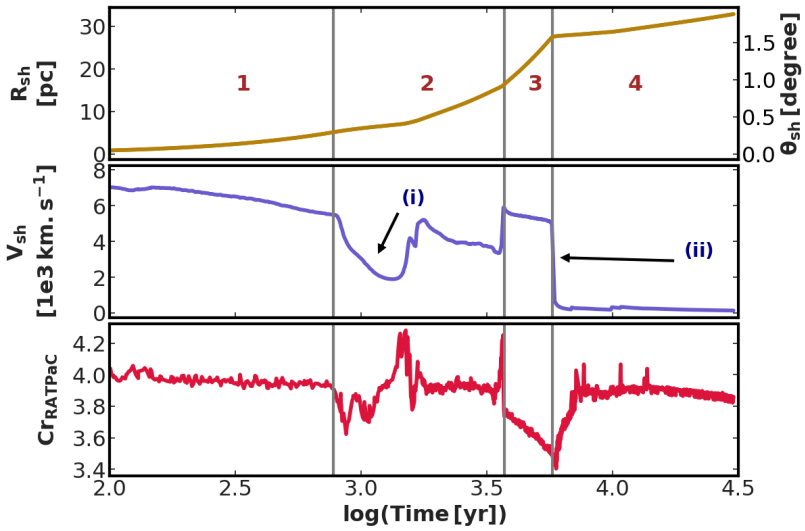

Figure 6.2.1: Behaviour of the SNR forward shock parameters for $20\,M_\odot$ **progenitor**:
radius (R_{sh}), velocity (V_{sh}), and subshock compression ratio (Cr_{RATPaC}). In the upper panel, we also provide the angular scale, θ_{sh}, for a distance of 1000 parsec. **(i), (ii) mark interactions of the forward shock with different discontinuities**, namely (i) the RSG shell, (ii) the contact discontinuity between the shocked MS wind and shocked ISM.

SNR with $60\,M_\odot$ **progenitor**

The evolution of the forward shock parameters has been described in Section 5.2.1 and in Figure 5.1.1. I mention again that in this scenario, most prominently the sub-shock compression ratio reaches approximately 1.5 when the SNR expands through the hot shocked wind. Further, in this Chapter, although the evolution of the SNR from $60\,M_\odot$ progenitor is calculated for 110000 years, no significant change in parameters for forward shock is noticed after 46000 years.

6.2.2 Particle acceleration and escape

The spectral evolution of accelerated particles is illustrated in Figures 6.2.2 and 6.2.5 for the SNRs with progenitors $20\,M_\odot$ and $60\,M_\odot$, respectively in terms of the volume-averaged downstream spectra for protons and electrons and the corresponding spectral indices are shown in Figure 6.2.3 and Figure 6.2.6, respectively. The chosen evolutionary times reflect the evolution of the SNR forward shocks through the different regions of wind bubbles. The earlier study of

type-Ia SNR with self-consistent amplification of Alfvénic turbulence [105] suggested that the spectral shape is regulated by the transport of turbulence and Alfvénic diffusion. The continuous deceleration of the shock decreases the CR flux and consequently, reduces the CR gradient which leads to a weaker driving of turbulence. For the framework of core-collapse SNRs, the resulting particle spectra should get influenced by the complicated HD of the wind bubbles as well as by the dynamics of the self-consistent turbulence. Also, the large-scale magnetic field profiles resulting from the passive transport of the CSM magnetic field, described in Section 6.1.2 can also affect particle acceleration.

SNR with $20\,M_\odot$ progenitor

The particle acceleration in the different regions of the corresponding wind bubble is as follows:
Free RSG wind: During the expansion of the SNR forward shock inside this region, the compression ratio becomes 4 and hence, the particle spectral index is around 2 as illustrated in Figures 6.2.2 and 6.2.3 at 500 years. At the end of the evolution inside this region, the maximum attainable energy for protons achieves 20 TeV.
Piled-up RSG wind: In this region, the SNR forward shock collides with the dense RSG shell and the maximum attainable energy of protons decreases to 6 TeV, because of the decrease in shock speed. During this period, displayed at 1100 years and 1500 years, spectral softening is obtained and the spectral index reaches 2.2 at energies above 100 GeV for protons. However, the spectral index comes back to 2 when the forward shock has emerged from the RSG shell. This brief spectral softening reflects the fluctuation in the sub-shock compression ratio depicted in Figure 6.2.3. After climbing the RSG shell, the forward shock velocity increases again, and so does the maximum energy of particles. During this time the compression ratio becomes 4.2 which leads to spectral hardening to an index of 1.9 at higher energies, illustrated at 2500 years. After that, the collision between the piled-up RSG wind and the forward shock produces an inward-moving reflected shock that eventually merges with the SNR reverse shock and propagates towards the interior with a speed of $\sim 3000\,\mathrm{km\,s^{-1}}$. Although particles are not injected at this inward-moving shock, this shock can re-accelerate energetic particles. Further, a complex superposition of the acceleration yield of multiple shocks is obtained in the total volume-averaged particle spectra downstream of the forward shock and at higher energies, the hardest contribution should dominate [267, 268].
Shocked MS wind: As in this region, the forward shock evolves through the hot MS wind material, the compression ratio decreases and consequently, relatively soft particle spectra are produced but these particles are so few that the volume-averaged spectra over the downstream region do not demonstrate spectral softening as shown at 5000 years in

[267]: Brecher et al. (1972), 'Extragalactic Cosmic Rays'
[268]: Büsching et al. (2001), 'Excess GeV radiation and cosmic ray origin'

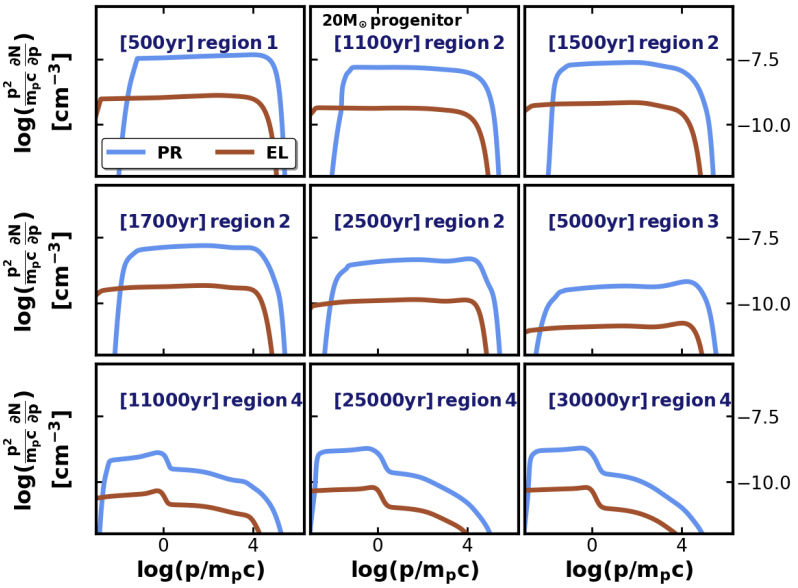

Figure 6.2.2: Proton (PR) and electron (EL) spectra volume-averaged downstream of the forward shock at different regions of the corresponding wind bubble for $\mathbf{20\,M_\odot}$ progenitor from Figure 6.1.1

Figure 6.2.2. Further, the high temperature in the shocked MS wind also provides a high injection momentum, and the volume-averaged spectrum is dominated by prior accelerated particles at all energies. The freshly accelerated particles in the MS wind cannot penetrate into the deep downstream region because of the strong magnetic field present in the piled-up RSG wind.

Shocked ISM: After the collision between the SNR forward shock and the contact discontinuity between shocked MS wind and shocked ISM, the forward shock becomes very slow and hence, becomes inefficient to accelerate particles up to very high energy. In the shocked ISM region, the maximum attainable energy for protons drops to 50 GeV at the end of the simulation. In this region, the forward shock encounters dense and cool material which reduces the injection momentum and enhances the injection rate of lower energy particles into the DSA, following the applied injection model for this simulation. However, the forward shock is too weak to accelerate these particles to very high energy and therefore, a prominent spectral break near 1 GeV is formed, as illustrated in Figure 6.2.2 at 11000 years and later. Further, the multiple merging of fast shocks with the weak forward shock enhances the acceleration efficiency and the step-like spectral feature emerges at slightly higher energies. Additionally, the electron spectra roughly follow the proton spectra, except for an additional softening arising from the synchrotron cooling.

In the time-dependent treatment of the transport of CRs and Alfvénic turbulence, the driving of turbulence becomes weaker at later stages of SNR evolution on account of the decrease in CR pressure gradient [105]. So, the diffusion coefficient along with the acceleration timescale [269] increase and hence, particles with higher energies in the shock precursor become slow to return in the vicinity of the SNR forward shock and cannot participate in further shock acceleration.

[269]: Drury (1991), 'Time-dependent diffusive acceleration of test particles at shocks'

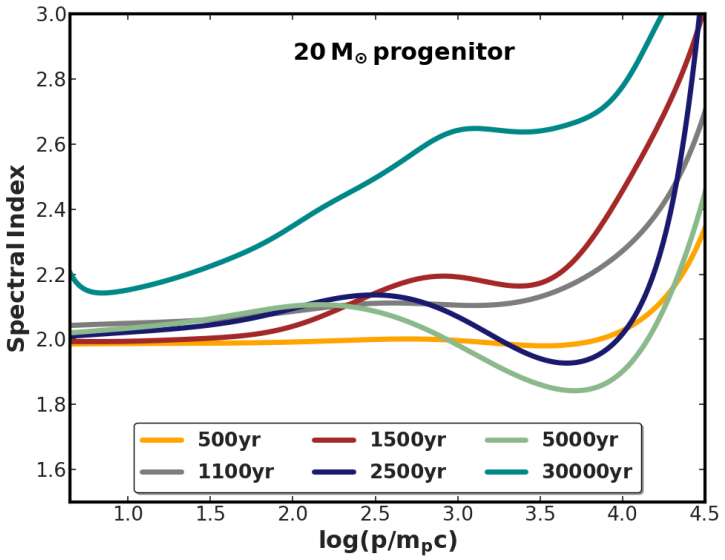

Figure 6.2.3: Variation of the spectral index for downstream protons at different ages with momentum.

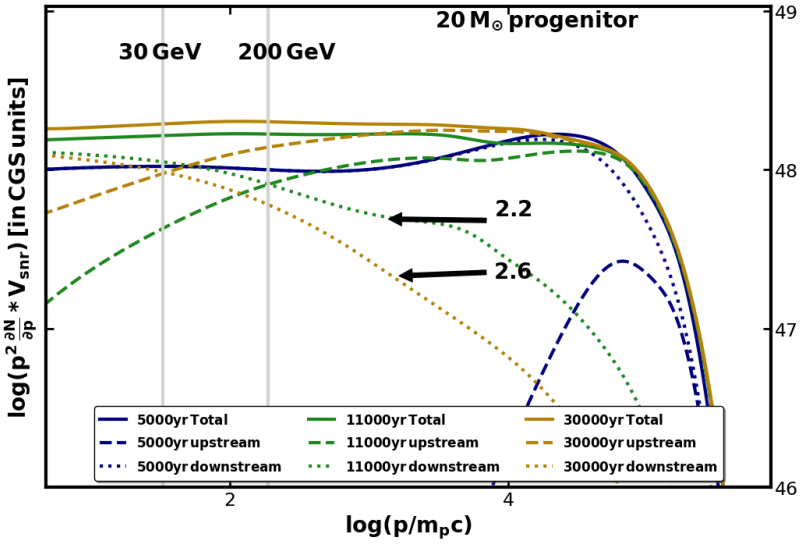

Figure 6.2.4: Proton number-spectra at late evolutionary times.
Solid lines represent the total spectra, dashed, and dotted lines indicate the forward shock upstream, and the downstream spectra, respectively. The grey vertical lines at 200 GeV and 30 GeV indicate the escape energies at 11000 years and 30000 years, respectively. The arrows point out the energy bands with spectral indices of 2.2 and 2.6.

Consequently, a break in the downstream particle spectra should appear at the currently achievable maximum energy, above which particles escape to the far-upstream region. After 30000 years, this spectral softening is clearly visible in Figure 6.2.4 and the spectral index reaches approximately 2.6 at high energy, starting from about 2.2 above 10 GeV.

Figure 6.2.4 demonstrates the total production spectra of protons, including particles outside of the SNR at different times. As the CR transport equation in *RATPaC* is solved out to several tens of shock radius, as described in Definition 4.1.1, all particles reside inside the simulation domain. Hence, integrating the particle spectra over the whole simulation domain produces the total CR production of the SNR, and that is spectrally harder than the component inside the remnant. At 5000 years, protons are accelerated up to 20 TeV energy but at 11000 years protons above 200 GeV are preferentially found in the upstream region, by softening the downstream spectra with the spectral index of ~ 2.2, shown in Figure 6.2.4. Later, the escape energy shifts to 30 GeV and the spectral

index reaches ~ 2.6 above this escape energy. At any time, the break appears at the energy up to which the particles can be currently accelerated and it reflects the interplay between the reduction in maximum energy and the escape of particles from the accelerator [270], [104, 105].

[270]: Ohira et al. (2010), 'Escape-limited model of cosmic-ray acceleration revisited'

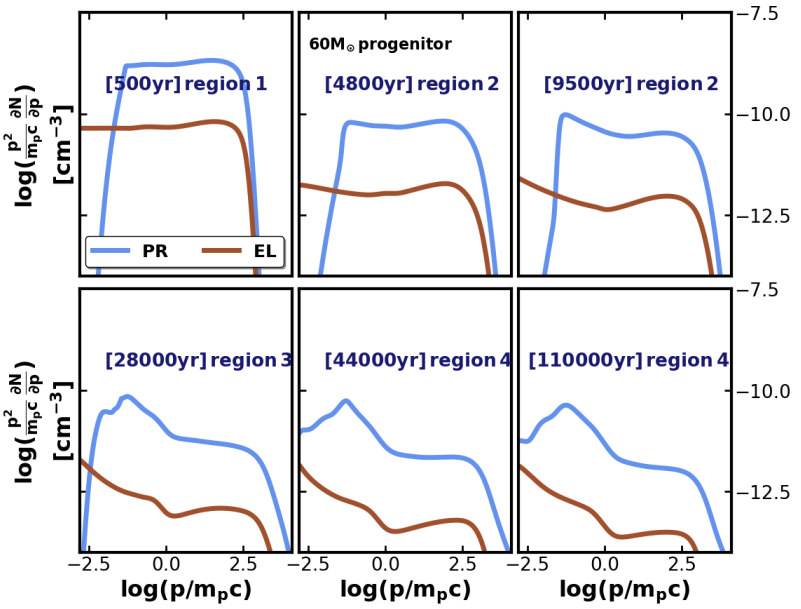

Figure 6.2.5: Proton (PR) and electron (EL) spectra volume-averaged downstream of the forward shock.
at different regions of the corresponding wind bubble for **60 $M_\odot$** progenitor from Figure 5.1.1.

SNR with 60 $M_\odot$ progenitor

Particle acceleration by the SNR forward shock at different regions of the corresponding wind bubble is elaborately described in Chapter 5 for the Bohm-like diffusion. Here, the spectral modifications deriving from the explicit treatment of turbulence transport, considering the CR streaming instability and the growth, damping, and cascading of the waves are explored. The introduction of turbulence adds non-linearity to the calculation of the diffusion coefficient. The propagation of the SNR forward shock through the hot shocked regions, region 2 and region 3 in Figure 6.2.5 results in softer spectra below roughly 10 GeV, but not as significant as for Bohm-like scenario, specifically at higher energies. After 28000 years the spectral index reaches 2.75 at lower energies, which is consistent with the result for the Bohm-like diffusion. Further, during the propagation of the SNR forward shock inside the shocked ISM, the self-consistent turbulence model provides spectral softening at higher energies arising from the evanescence of Alfvén waves. After 110000 years, the spectral index reaches approximately 2.2 above roughly 10GeV, because of the escape of particles from the vicinity of the SNR forward shock, as illustrated in Figure 6.2.7. The proton production spectra in Figure 6.2.7 suggest that the particles above 70 GeV begin to leave the remnant already after 28000 years when the forward shock is located inside the shocked MS wind. After that, the typical energy of escaping CRs is reduced to about 1.5 GeV after 110000 years as a result of the inefficient

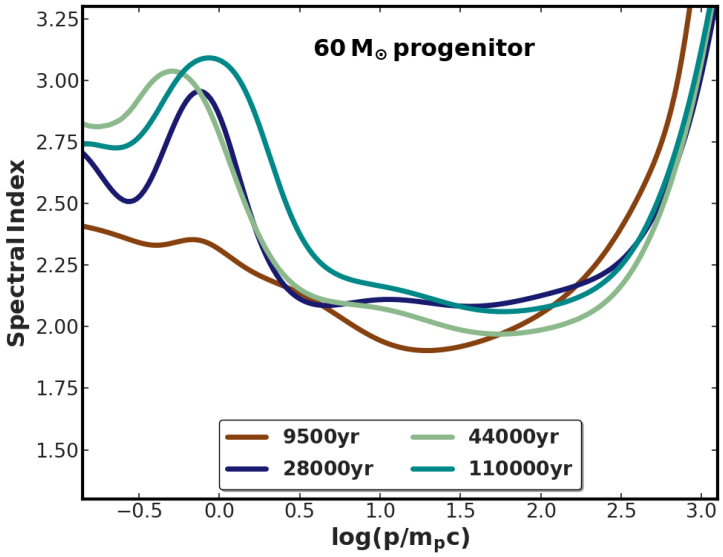

Figure 6.2.6: Variation of the spectral index for downstream protons at different ages with momentum.

confinement of high energy particles in this time-dependent treatment of diffusion regime.

The total proton production spectra for the SNR with 20 $M_\odot$ progenitor have an index of $\sim 2.1 - 2.2$ above approximately 100 GeV energies at 11000 years and 30000 years. For the 60 $M_\odot$ progenitor, the index of the total proton production spectra is ~ 1.9 near the cut-off at later evolutionary ages. Importantly, the spectral shapes of both production spectra are quite different from the production index for type-Ia SNRs, about 2.4 above 10 GeV [105]. In the study with type-Ia SNR, the downstream spectra are structured by the temporal decline of the maximum energy $E_{\rm max}$, to which the shock can accelerate. In contrast, the downstream spectra at core-collapse SNRs also show the effect of the CSM hydrodynamics, in addition to the time evolution of turbulence spectra. For instance, the SNR with 60 $M_\odot$ gives downstream spectra with index ~ 1.9 at higher energies, before the escape starts. Although at later times the downstream spectra become softer as a consequence of particle escape, the pro-

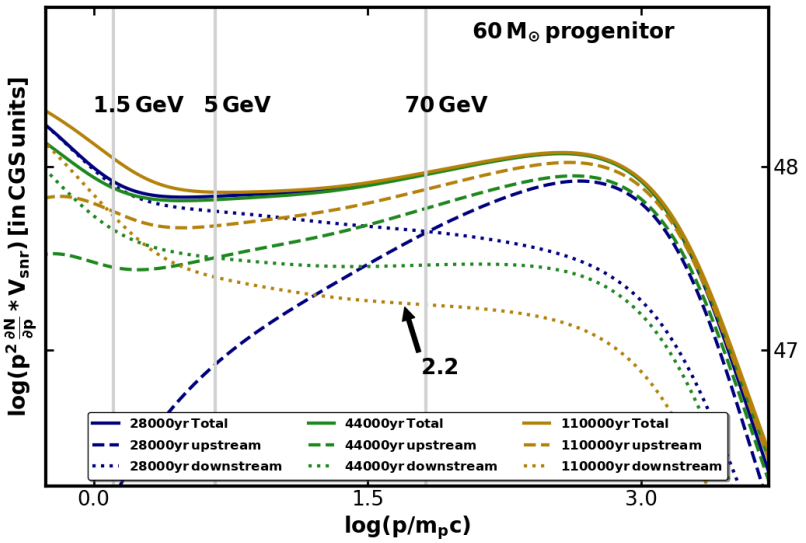

Figure 6.2.7: Proton number-spectra at later evolutionary times.
Solid lines represent the total spectra. The dashed and dotted lines indicate the spectrum upstream and downstream of the forward shock, respectively. The grey vertical lines at 70 GeV, 5 GeV, and 1.5 GeV denote the escape energies at 28000 years, 44000 years, and 110000 years, respectively. The arrow points out the energy bands with spectral index of 2.2.

ton production spectra show a slight hardness near cut-off, depicted in Figure 6.2.7.

Therefore, this study suggests that the cascading and decay of turbulence are crucial in the formation of soft particle spectra with spectral breaks for the older remnant. In contrast, in the scenario of simple Bohm-like diffusion, particles near the cut-off energy may escape the shock environment only at later stages with insignificant spectral modifications as shown in Figure 6.2.8. I emphasise that the spectral shape with Bohm-like diffusion only reflects the influence of the CSM flow profiles, while in the Alfvénic scenario, the spectra are a function of the HD parameters and the properties of the turbulence.

Probing the particle acceleration in SNRs with $20\,M_\odot$ and $60\,M_\odot$ progenitors illustrate the differences in spectral features arising from the environment of the SNRs. This is to be noted that the flow structure of wind bubbles becomes eventually very complex, on account of multiple reflected and transmitted shocks. Therefore, resolving the other shocks located downstream is preferable but out of the scope of this dissertation. Further, acceleration of particles from very low energies is possible only for the forward shock as the particles are injected into the DSA only at the forward shock. Re-acceleration of already accelerated particles at the other shocks, in particular the reverse shock, is included but this has negligible effects in the particle spectra.
Softer particle spectra at high energies for the SNR with $20\,M_\odot$ progenitor are obtained during the propagation of the SNR forward shock in the shocked ISM, while for the very massive progenitor, the signature of softness is already achieved at higher energies when the SNR shock is in the shocked wind, on account of particle escape. The enhanced driving of turbulence in the scenario with the $20\,M_\odot$ progenitor arises from the higher normalisation of the CR spectrum [105], that is caused by roughly four orders of magnitude higher density in the RSG wind. Additionally, the shock radius for the $20\,M_\odot$ progenitor is smaller than for the $60\,M_\odot$ progenitor, which increases the gradient in the cosmic-ray distribution and hence, the driving rate of turbulence.

Figures 6.2.2 and 6.2.5 demonstrate that the maximum cut-off energy for protons is $E_{\rm max} \approx 0.5\,$TeV for the $60\,M_\odot$ progenitor, which is significantly less than that for the $20\,M_\odot$ progenitor, $E_{\rm max} \approx 50\,$TeV. The reason can be imputed into the estimation of ejecta mass, $M_{\rm ej} = 11.75\,M_\odot$ for SNR with $60\,M_\odot$ progenitor, assuming the compact object as a neutron star. However, in reality, a black hole might be formed in the explosion of this very massive star, which would result in a lower ejecta mass. Therefore, in that framework, the ejecta speed and the shock speed would be higher which results in higher maximum energy of particles by a factor of a few, but not more, because the acceleration rate scales with $V_{\rm sh}^2$ and hence inversely with the ejecta mass for a given explosion energy.

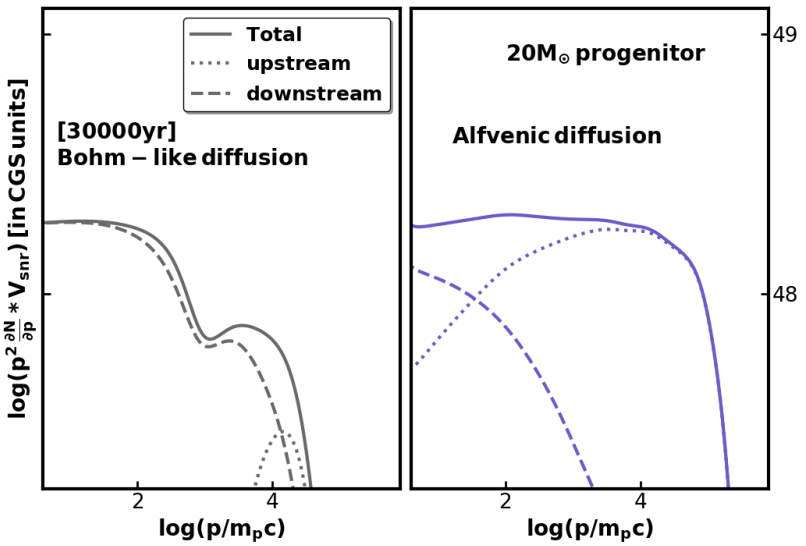

Figure 6.2.8: Proton number-spectra for Bohm-like (left panel) and self-consistent (right panel) diffusion for the SNR with 20 $M_\odot$ progenitor

Moreover, the result from SNR with 20 $M_\odot$ progenitor resemblances the estimation of maximum energy for type II progenitor discussed in [271]. Further, the spectral index at high energies obtained for the SNR with 20 $M_\odot$ progenitor at later times is roughly comparable to the deduced spectral index for IC443 and W44 ([272]).

[271]: Cristofari et al. (2020), 'The low rate of Galactic pevatrons'

[272]: Ackermann et al. (2013), 'Detection of the characteristic pion-decay signature in supernova remnants'

6.2.3 Non-thermal emission

The processes of non-thermal emission include synchrotron radiation, inverse Compton scattering, and the decay of neutral pions as described in Section 3.4. Changes in synchrotron cut-off energies with the ages of SNRs indicate the evolution of the electron acceleration efficiency depending on the magnetic field and hydrodynamics. For this study, I only consider the scattering of CMB photons to derive the inverse Compton emission from the remnants. Although additional photon fields like infrared and optical might be required to take into account in this scenario, [139] estimated that the contribution of infrared and optical photons to inverse Compton emission is not significant to that of CMB photons except for SNRs residing near the Galactic centre. However, in this Chapter, any specific SNR is not modelled and inverse Compton scattering by only considering CMB is sufficient to achieve the goal of this study. Further, the emission flux from different processes is derived by considering remnants at 1kpc distance. Figures 6.2.9 and 6.2.14 depict the synchrotron spectra from the SNRs with 20 $M_\odot$ and 60 $M_\odot$ progenitors respectively, and Figures 6.2.10, 6.2.15 illustrate the gamma-ray spectra from both the remnants. Further, these demonstrations of the spatially integrated synchrotron and gamma-ray emissions display the time-dependent total emission from the SNRs and also indicate the emission originating upstream of the SNR forward shock by the escape particles. Figure 6.2.11 shows the radio flux at 5 GHz, the non-thermal X-ray flux in the 0.1 keV − 10 keV range, as well as the gamma-ray

emission at high energy (HE) (0.1 GeV − 100 GeV) and very high energy (VHE) (> 1 TeV) as a function of time for the SNR with 20 $M_\odot$ progenitor. The intensity maps at different times for synchrotron emission by Figures 6.2.12, 6.2.16 and gamma-ray emission by Figures 6.2.13, 6.2.17 are illustrated following the method described in [162]. These maps reflect the spherical symmetry in 1-dimensional simulations but in reality, these emission maps can be very complex because of the Rayleigh-Taylor instability.

SNR with 20 $M_\odot$ progenitor

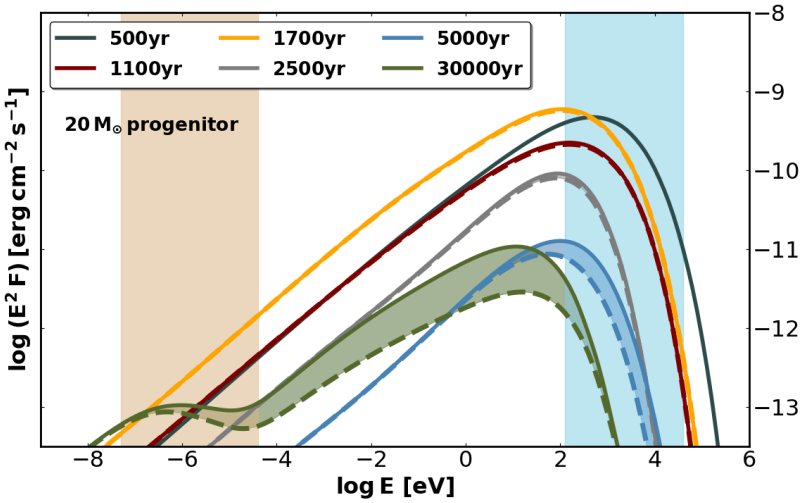

Figure 6.2.9: Spatially integrated synchrotron spectra at different ages of the SNR.
The upper boundaries of the shaded regions indicate the total emission from the remnant whether the lower ones denote emission from the downstream of SNR forward shock. The brown band indicates the 50 MHz − 10 GHz range and the blue band denotes 0.1 keV − 40 keV.

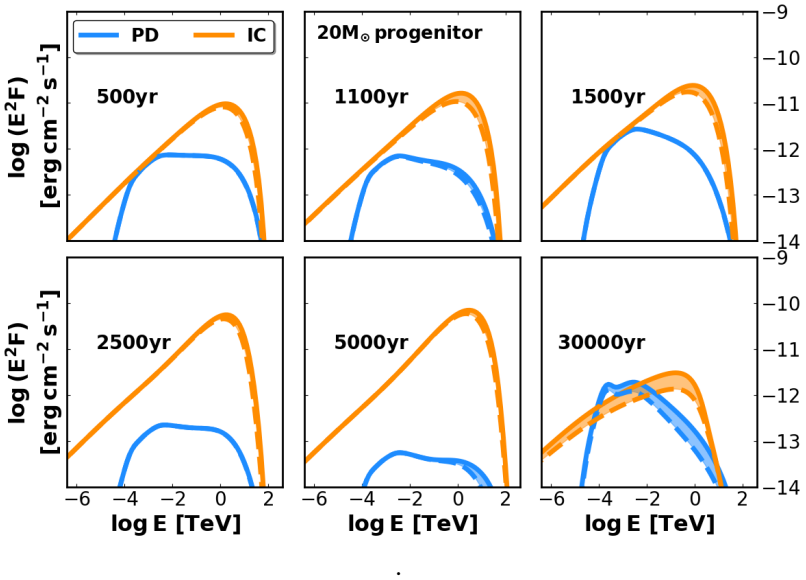

Figure 6.2.10: Spatially integrated gamma-ray spectra by pion-decay (PD) and inverse Compton (IC) scattering at different ages.
The boundaries of the shaded regions indicate the total emission and that from the interior, as in Figure 6.2.9

The entire non-thermal emissions are specifically produced in the interior of the remnant before the age of approximately 5000 years.

Free RSG wind: At the early evolutionary stage, the SNR expands through this region with a strong magnetic field $B_0 \propto 1/r$, combined with strong amplification and this results in considerable X-ray flux at this stage, shown at 500 years in Figure 6.2.9. The simulated X-ray light curve in Figure 6.2.11

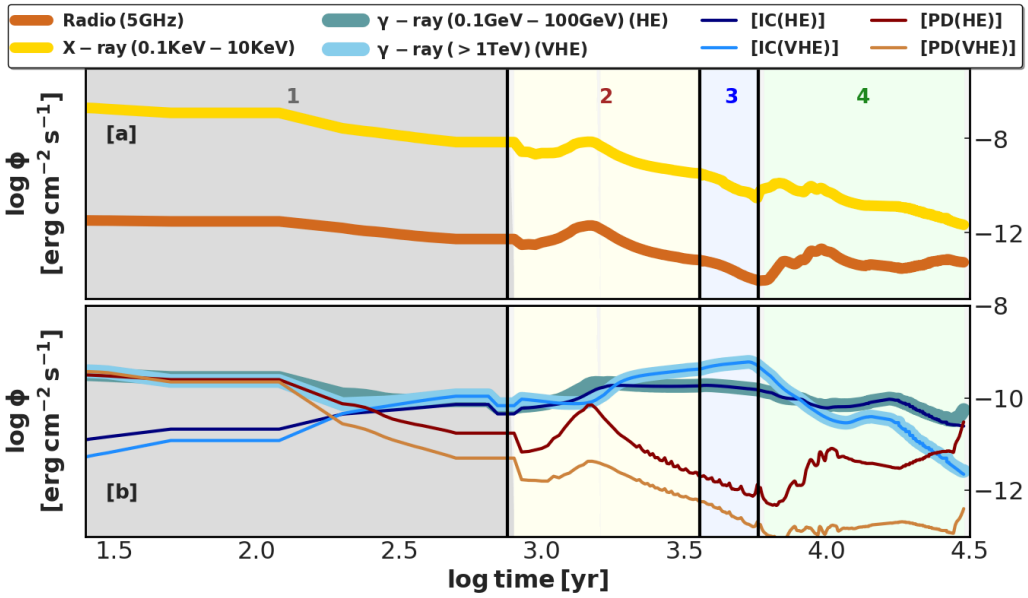

Figure 6.2.11: Evolution of energy flux (Φ) during the lifetime of SNR for synchrotron emission and gamma-ray emission at specific energy ranges inside the different regions shown in Figure 6.1.1 of wind-bubble formed by 20 $M_\odot$ progenitor. This is to be noted that the shown X-ray flux only refers to the non-thermal X-ray.

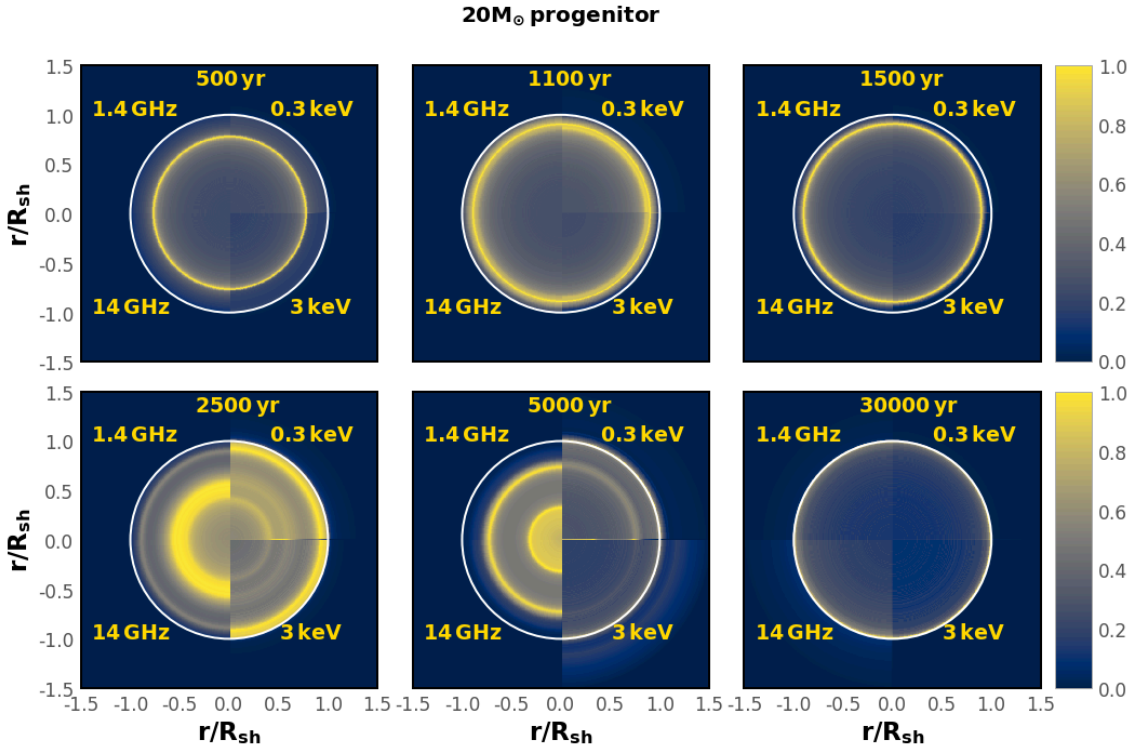

Figure 6.2.12: Normalised intensity maps for synchrotron emission at different times.
Each panel is divided into four segments: the left hemisphere is for radio emission at 1.4 GHz in the upper half and at 14 GHz in the lower half. The right hemisphere is for the 0.3 keV and 3 keV X-ray intensity in the upper half and lower half, respectively. For each segment, the intensity is normalised to its peak value indicated in the colour bar. The SNR forward shock position is marked by a white circle.

suggests the declining X-ray emission during the SNR evolution inside free RSG wind. For initial almost 200 years, pion-decay emission dominates over inverse Compton scattering during the propagation of the remnant through dense material. Furthermore, the strongest magnetic field is achieved near the contact discontinuity between SNR forward and

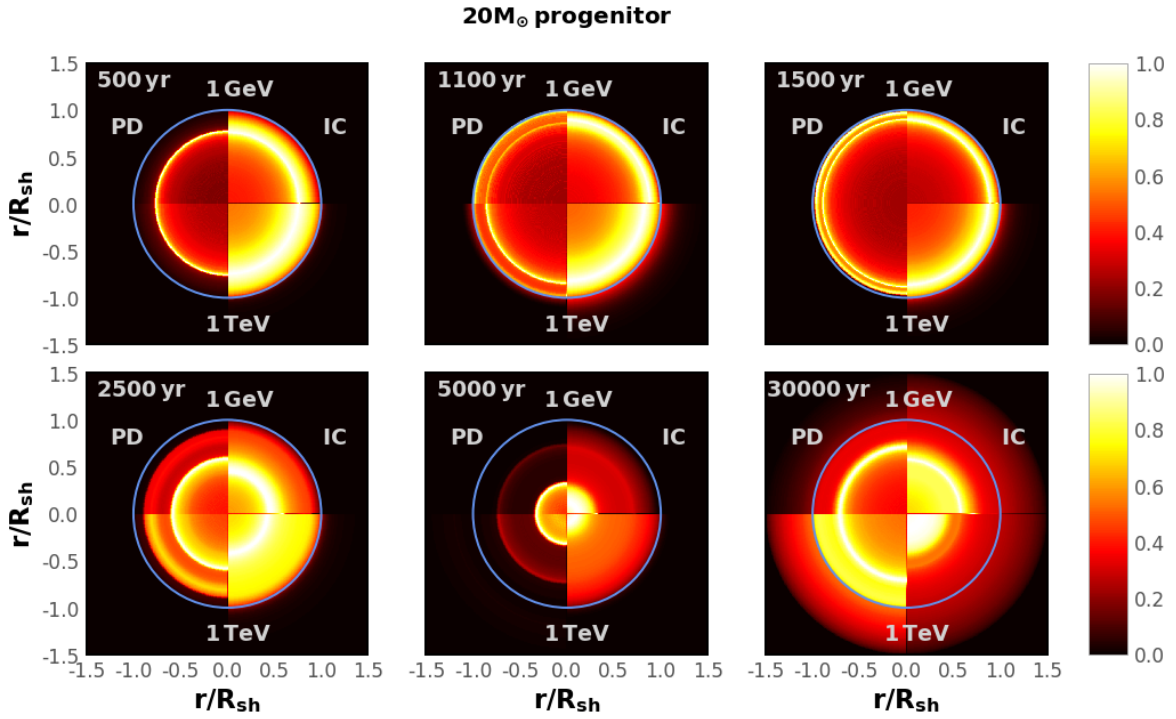

Figure 6.2.13: Normalised intensity maps for gamma-ray emission at different times.
The segments are organised to distinguish the photon energy: 1 GeV in the upper half and 1 TeV in the lower half. The Left and right hemispheres are for pion-decay and inverse Compton emission, respectively. For each segment, the intensity is normalised to its peak value indicated in the colour bar. The SNR forward shock position is marked by a light blue circle.

reverse shock and hence, the highest intensity in the radio and X-ray band is produced near this contact discontinuity as shown in Figure 6.2.12. The peak intensity of pion-decay and inverse Compton emission also coincides with the contact discontinuity between the forward and reverse shock of the SNR from Figure 6.2.13. At 1 TeV, the interior of the remnant is also inverse-Compton bright on account of the diffused high energy electrons deep downstream.

Piled-up RSG wind: During the period between 750 years and 1600 years the SNR forward shock collides with RSG shell and consequently, the radio spectra begin to soften to a spectral index $\alpha \approx -0.54$ ($S_\nu \propto \nu^\alpha$) agreeing with the low-energy spectral index of particles as shown in Figure 6.2.3 but this spectral index resumes to $\alpha = -0.5$ after the crossing of the RSG shell. In addition, the pion-decay flux also enhances because of the interaction between the forward shock and the dense RSG shell and the spectral index of pion-decay emission reaches 2.2. Importantly, the softness of the pion-decay emission extends to low gamma-ray energies, unlike the corresponding volume-averaged proton spectrum as the hadronic emission predominantly originates from the shocked RSG-shell residing immediately downstream of the shock. Also, the low-energy gamma-ray spectra appear even softer than the radio emission produced from electrons of comparable energy.

This stage of SNR evolution can be comparable to Cas A which may be expanding inside the dense RSG wind [273]. Although the ambient CSM of Cas A may differ from that

[273]: Chevalier et al. (2003), 'Cassiopeia A and Its Clumpy Presupernova Wind'

of a 20 $M_\odot$ progenitor, and the reverse shock of Cas A is an efficient accelerator [274], the spectral index for accelerated protons calculated in this study is comparable with that estimated by [275] for Cas A. The synchrotron flux in the radio and X-ray band along with the hadronic emission flux reaches its peak during the forward shock crossing through the dense RSG shell. For the next 200 years after this collision, the X-ray flux and high energy pion-decay flux decrease at rates of $\sim 0.3\%$/yr and $\sim 0.7\%$/yr, respectively, as a result of the declining density and the deceleration of the remnant. For Cas A, non-thermal X-rays in the band 4.2 keV − 6 keV declines at the rate of 1.5%/yr [276]. Therefore, it is possible that the forward shock of Cas A is propagating through piled-up RSG wind and the difference in density, age, and shock radius may indicate a much lower progenitor mass for Cas A than the 20 $M_\odot$ progenitor.

Additionally, the synchrotron morphology is centre-filled in this region. After the collision with the RSG shell, the velocity of the forward shock starts to increase and the reverse shock with the contact discontinuity moves towards the interior. After 2500 years, two radio shells are visible, the inner shell at the contact discontinuity and the outer one at the shocked RSG shell. On the other hand, the brightest X-ray band is created near the forward shock. In the gamma-ray band, the brightest emission comes from the region near the contact discontinuity between forward and reverse shock, and reverse shock. In reality, the Rayleigh-Taylor instability of the contact discontinuity can smear out the intensity peak. Later on, at 2500 years the entire remnant appears bright in inverse Compton emission, specifically at 1 TeV, as the energetic particles reach the reverse shock and may be re-energised there.

Shocked MS wind: At 5000 years, the SNR forward shock is about to collide with the contact discontinuity of the wind bubble between the shocked MS wind and the shocked ISM region. At this age from Figure 6.2.9, it is noticeable that the total X-ray synchrotron flux is slightly higher than that emerging only from the downstream region. The X-ray morphology at this time in Figure 6.2.12 indicates that this upstream emission originated near the wind bubble contact discontinuity on account of a very strong magnetic field there, almost 15 times stronger than that in the shocked MS wind. At this time, maximum radio intensity emerges from the piled-up RSG wind behind the forward shock as well as from the region inside of the contact discontinuity between the SNR forward and reverse shock. Further, in this stage, the pion-decay flux decreases because of the lower density of the medium, and the very high energy inverse Compton emission flux dominates over its high energy counterpart on account of the increase in the maximum achievable energy for electrons as the forward shock velocity increases by 2000 km s^{-1} in this region. The normalised intensity map at 5000 years indicates that both the leptonic and hadronic gamma-ray emission emanates from deep downstream.

[274]: Uchiyama et al. (2008), 'Fast Variability of Nonthermal X-Ray Emission in Cassiopeia A: Probing Electron Acceleration in Reverse-Shocked Ejecta'

[275]: Saha et al. (2014), 'Origin of gamma-ray emission in the shell of Cassiopeia A'

[276]: Patnaude et al. (2011), 'A DECLINE IN THE NONTHERMAL X-RAY EMISSION FROM CASSIOPEIA A'

Shocked ISM: As high energetic particles escape the remnant during the forward shock passage through the shocked ISM as shown in Figure 6.2.4, a significant fraction of the synchrotron flux is produced in the upstream region as shown in Figure 6.2.9 at 30000 years. At this stage, the pion-decay emission flux enhances because of the shock propagating in dense material. A fraction of the gamma-ray emission is also generated around the remnant, on account of particle escape. The spectral index for pion-decay emission reflects the soft proton spectra with the spectral index of $2.4 - 2.6$ above 10 GeV. This kind of soft gamma-ray spectra is observed from SNRs like IC443, W44, $G\,39.2 - 0.3$, etc., that are expanding in or near the dense molecular clouds [236],[277, 278]. The old remnant appears shell-like in pion-decay emission, whereas the inverse Compton emission is centre-filled, contrary to the synchrotron intensity map. This morphology of old core-collapse remnants resembles the morphology of old type-Ia SNRs [189].

[277]: Cardillo, M. et al. (2014), 'The supernova remnant W44: Confirmations and challenges for cosmic-ray acceleration'
[278]: Oña Wilhelmi et al. (2020), 'SNR G39.2–0.3, an hadronic cosmic rays accelerator'

SNR with $60\,M_\odot$ progenitor

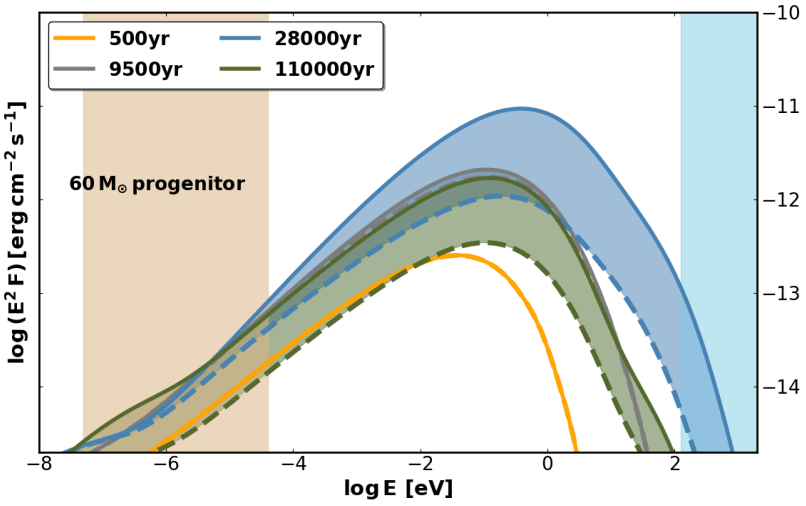

Figure 6.2.14: Spatially integrated synchrotron spectra at different ages of the SNR.
The brown band indicates the 50 MHz – 10 GHz range and the blue band denotes 0.1 keV – 40 keV. The boundaries of the shaded regions indicate the total emission and that from the interior, as in Figure 6.2.9.

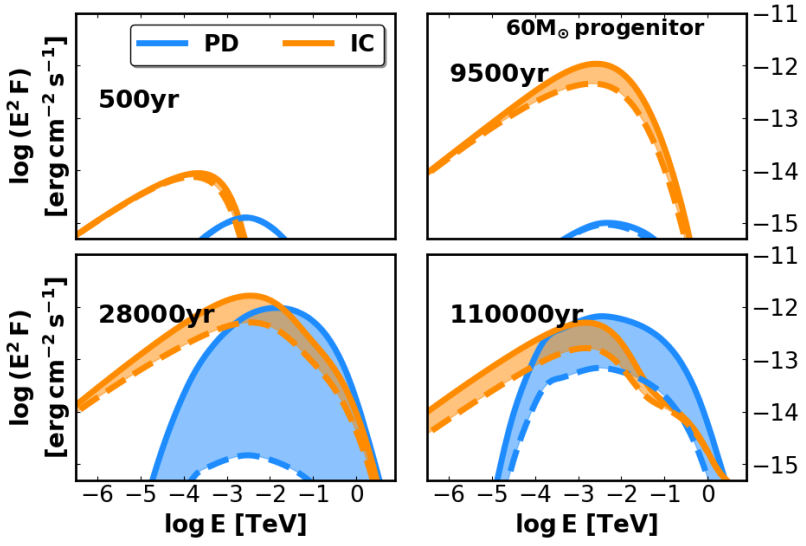

Figure 6.2.15: Spatially integrated gamma-ray spectra by pion-decay (PD) and inverse Compton (IC) scattering at different ages.
The boundaries of the shaded regions indicate the total emission and that from the interior, as in Figure 6.2.9.

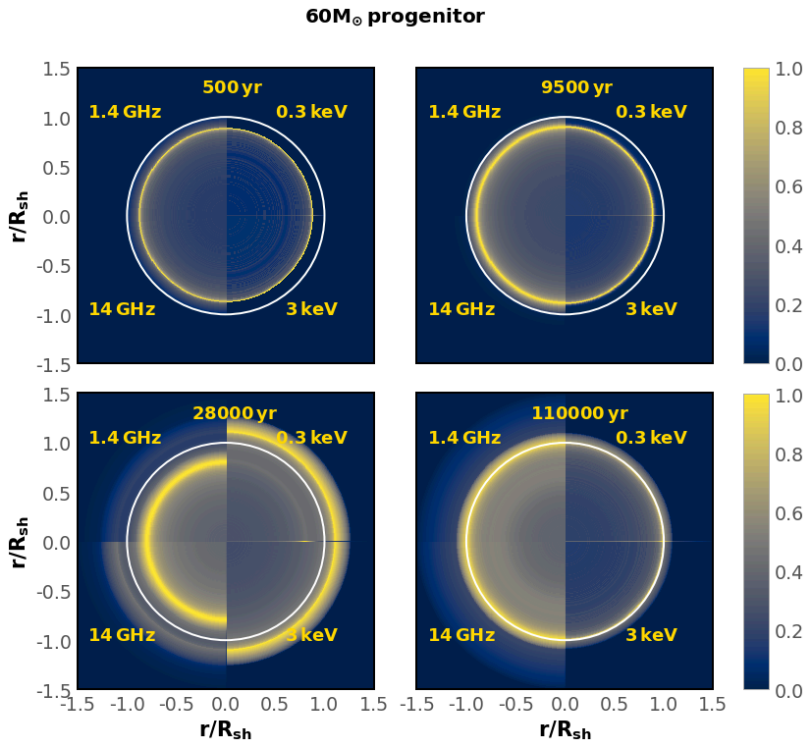

Figure 6.2.16: Normalised intensity maps for synchrotron emission at different times.
For each segment, the intensity is normalised to its peak value indicated in the colour bar. The SNR forward shock position is marked by a white circle.

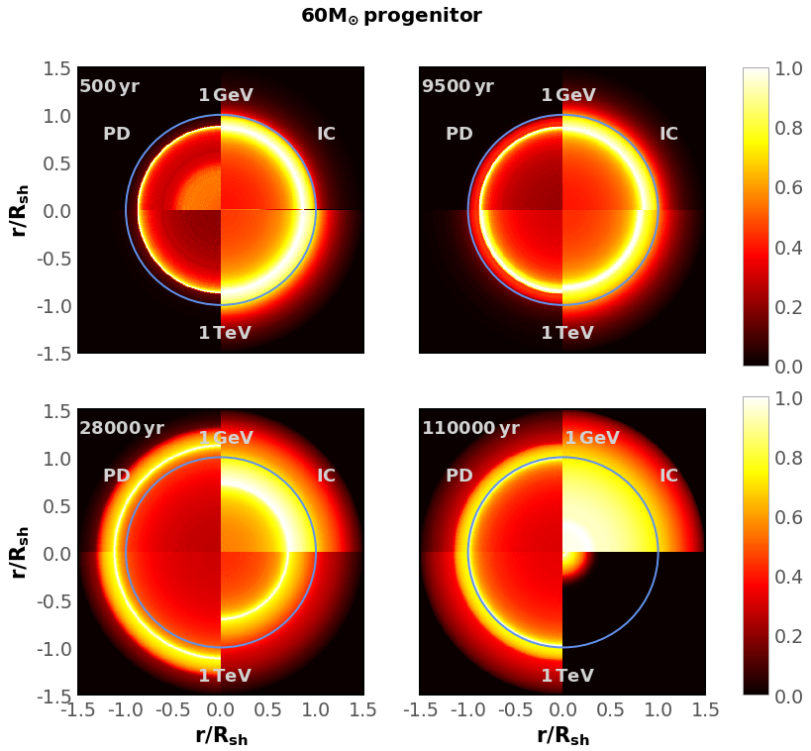

Figure 6.2.17: Normalised intensity maps for gamma-ray emission at different times.
The Left and right hemispheres are for pion-decay and inverse Compton emission, respectively. For each segment, the intensity is normalised to its peak value indicated in the colour bar. The SNR forward shock position is marked by a light blue circle.

For this SNR, I only summarise the difference in emission spectra and morphology on account of self-consistence turbulence and the time-dependent evaluation of the diffusion coefficient as a detailed description of non-thermal emission in the different regions of the bubble is already stated in Section 5.2.3 for Bohm-like diffusion.
The significant flux of synchrotron and gamma-ray emissions emerges from the upstream region of the SNR forward shock even when the SNR forward shock resides in the shocked

wind, on account of the escaped particles arising from the weak driving of turbulence, as indicated by Figure 6.2.7. The contact discontinuity between SNR forward and reverse shock looks bright in the radio and the X-ray band before the SNR approaches the shocked ISM and this is evident in the X-ray morphology at 28000 years, illustrated in Figure 6.2.16. Around 28000 years, after the collision of the SNR forward shock with the LBV shell, the wind-bubble contact discontinuity appears X-ray bright because of the very strong magnetic field there whereas the brightest radio emission still emerges from the region near the contact discontinuity between the SNR forward and reverse shock. The synchrotron morphology, illustrated in Figure 6.2.16 in the scenario of self-consistent turbulence is similar to that for Bohm-like diffusion from Figure 5.2.10, except the contribution from escaped particles around the SNR. This is to be noted that the radio spectra are softer with spectral index, $\alpha \approx -0.8$, where energy flux, $S_\nu = \nu^\alpha$, during the shock passage through the shocked wind and the shocked ISM, which resembles with the observed indices for many old Galactic SNRs [279, 280]. During the early stages of evolution, the strong magnetic field in the free wind allows efficient proton acceleration to very high energy, and the gamma-ray emission is predominantly hadronic because of the dense medium, independent of the diffusion model. At later stages, during the expansion of the SNR inside the shocked wind region, inverse Compton emission dominates and pion-decay emission specifically from the downstream region is diminished. Around 28000 years, high-energy protons residing in the shock precursor can reach the high-density material behind the contact discontinuity of the wind bubble, which causes bright hadronic TeV-scale emission from the periphery of the SNR. Thus, considerable pion-decay emission flux from the upstream of the remnant is obtained, demonstrated in Figure 6.2.15 at 28000 years. This feature is also visible in the morphology at 1 TeV, shown in Figure 6.2.17 where the pion-decay emission emerges from the shell around the wind-bubble contact discontinuity ahead of the SNR shock. This situation is comparable with the scenario of gamma-ray emission from the interaction of escaped protons with ambient molecular clouds, that has been suggested for IC 443, W44, G 39.2 − 0.3 and G 106.3 + 2.7 [236, 278]. Pion-decay dominates the gamma-ray emission from old remnants while the forward shock is in the shocked ISM, and the spectral index, 2.2-2.4 for pion-decay emission above 10 GeV reflects the softness of the proton spectra.

The gamma-ray emission morphology is shell-like at early stages, dominated by the emission from the contact discontinuity between forward and reverse shock. After the SNR forward shock encounters the wind bubble contact discontinuity, the velocity of SNR forward shock decreases, and it can no longer accelerate particles at very high energies. At that time, confined particles with very high energy can reach the reverse shock and get re-accelerated and this is to be noted that the reverse shock itself is already energised by multiple reflected shocks resulting from the SNR-CSM

[279]: Green (2014), 'A catalogue of 294 Galactic supernova remnants'
[280]: Urošević (2014), 'On the radio spectra of supernova remnants'

interaction. After 28000 years, the inverse Compton emission mainly emerges from the region around the reverse shock, and the morphology eventually becomes centre-filled. The morphology of both SNRs at later times is comparable.

6.3 Conclusions

The interaction of the SNRs with $20\,M_\odot$ and $60\,M_\odot$ progenitors with the respective CSM is explored together with the acceleration and transport of energetic particles. To do this, the time-dependent transport equations of CRs in the test-particle limit and of magnetic turbulence, as well as the induction equation for the large-scale magnetic field, all in parallel with the hydrodynamic equations for the evolution of SNRs inside the wind bubbles are solved. The self-consistent turbulence module applied in this Chapter provides a time- and momentum-dependent spatial CR diffusion coefficient which is far more realistic than the oversimplified Bohm-like diffusion coefficient considered in Chapter 5.

I have demonstrated that the inefficient confinement of higher energetic particles eventually causes spectral breaks at GeV energies, above which the spectral index becomes $2.2 - 2.6$. The simulations of particle acceleration at the SNR forward shock indicate that the spectra of the particles and their emissions are considerably influenced by the structure of the wind bubble. Also, the morphological analysis of two SNRs with $20\,M_\odot$, and $60\,M_\odot$ progenitors suggests dissimilarities in various frequency bands, that reflect the differences in the wind bubbles.

Transient softer spectra with the spectral index of 2.2 specifically at higher energy are obtained in the scenario with the $20\,M_\odot$ star, during the collision between SNR-RSG shell. Beyond this, the hydrodynamic profiles of the ambient medium do not produce any spectral softness. Later, the weak driving of turbulence for old remnants softens the proton spectra with a spectra index of around 2.6 at high energies. Similar soft proton spectra have been derived from observations of the SNRs evolving inside dense molecular clouds. Further, the synchrotron flux depends on the total magnetic field intensity in the different regions of the wind bubble as well as the maximum achievable electron energy. At later times, although the magnetic field strength is very high in the shocked ISM, because of the large diffusion coefficient, derived from the magnetic turbulence spectrum the paucity of high-energy electrons in the shock environment causes the synchrotron cut-off energy to decline from 10 keV to 0.1 keV. The flux of pion-decay emission changes throughout the evolution, whereas the inverse Compton flux shows a steady trend and slightly increases until the SNR enters the shocked ISM. SNRs with a $20\,M_\odot$ progenitor have a shell-like morphology in the X-ray band and pion-decay emission except at middle age, while in the radio band, the SNR looks more

centre-filled, except at very old age. The inverse-Compton morphology is that of a thick shell, which transitions to a more centre-filled configuration at late times.

For the SNR with 60 $M_\odot$ progenitor star, softer spectra specifically at low energies are obtained because of the low sonic Mach number of the SNR forward shock inside the hot shocked wind regions. Later, the spectra become soft at higher energies as well, on account of the inefficient driving of turbulence and the associated rapid decline in the currently achievable maximum particle energy. In terms of non-thermal emissions, the synchrotron cut-off frequency increases with time because of the high magnetic field intensity in the shocked wind, until the high-energy electrons start to escape from the remnant. Inverse Compton emission dominates the gamma-ray emission until the SNR reaches the vicinity of the contact discontinuity of the wind bubble, and the pion-decay emission is prominent for the old remnant. For both SNRs, the gas density of the ambient medium determines the dominant contribution in the gamma-ray band [281]. The X-ray morphology resembles a thick shell, whereas the radio emission evolves with time from the shell-like to the centre-filled configuration. In the gamma-ray band, the pion-decay intensity profile is shell-like, and that of inverse Compton emission eventually transitions from shell-like to a centre-filled structure. For both SNRs, the morphology looks similar for old remnants and also resembles the type-Ia SNRs [189].

[281]: Yuan et al. (2012), 'An Attempt at a Unified Model for the Gamma-Ray Emission of Supernova Remnants'

In conclusion, evidently the spectra of accelerated particles are shaped by both the hydrodynamics of the ambient medium and the time-dependent diffusion coefficients. This study suggests that non-thermal emission and its morphology can provide information about the progenitor stars and the current state of evolution of the remnant, at least until it reaches the shocked ISM. Further, the SNR with lower-mass progenitor star (20 $M_\odot$) is more likely to be detected with current-generation observations, on account of the high density of the RSG wind.

Conclusions and future prospects 7

Galactic CRs are widely assumed to be accelerated at shocks in SNRs by the DSA mechanism. If these shocks expand in a complex environment, which happens generally in the core-collapse scenario, then accelerated particles in this situation may carry spectral signatures of that complexity.
From this motivation, particle acceleration and non-thermal emissions from SNRs with massive progenitors have been studied numerically in this dissertation by considering the corresponding ambient medium structured by the massive stars. To attain this objective, *RATPaC* has been executed for solving the HD evolution, the evolution of large-scale frozen in the magnetic field, and transport equation of CRs and scattering magnetic field in one-dimensional spherical symmetry and to calculate the non-thermal emissions from the accelerated particles.
In this context, Chapter 4 describes the functionality of *RATPaC* and implemented changes in the code to deal with the interaction between the SNR and discontinuities present in the wind bubble. Besides, the achieved optimisation of the code to obtain results for older remnants within reasonable computational time is specified, particularly while the transport equation of scattering magnetic turbulence is involved.
In Chapter 5, particle acceleration at the SNR with 60 $M_\odot$ progenitor is investigated by considering the simplified Bohm-like diffusion coefficient which has provided insights into the emission from the SNR depending on the region of wind bubble in which the SNR forward shock resides. From this study, the important conclusions are as follows:
1. Softer particle spectra with spectral index close to 2.5 are generated during the propagation of the SNR inside the hot shocked wind region of the wind bubble. Consequently, the softer electron spectra give rise to the softer radio spectra with spectral index, $\alpha \sim -0.7$ where synchrotron energy flux, $S_\nu \propto \nu^\alpha$ during late evolutionary stages.
2. Spectral index for pion-decay emission above 10 GeV reaches $\sim$ 2.6 while the remnant evolves inside the dense shocked interstellar medium.
3. In terms of the morphology of gamma-ray emission, the remnant evolves from centre-filled to shell-like in pion-decay emission. In contrast, inverse-Compton morphology appears centre-filled from the shell-like structure during later evolutionary stages as soon as the maximum attainable energy of freshly accelerated electrons starts to reduce.

I want to indicate that observing SNRs with this very massive progenitor is not usual but this study gives information about the effects of interactions between the SNR and different discontinuities in CSM on particle acceleration and emissions which are generic and also applicable to other SNRs residing in wind bubbles. After that, in Chapter 6 the

change in particle spectra and emission on account of the evolution of SNRs in wind bubbles around 20 $M_\odot$ and 60 $M_\odot$ stars are elaborately discussed along with the inclusion of the time-dependent diffusion coefficient. This study infers:
1. Hydrodynamics of the wind bubbles along with the magnetic field configuration and self-generated magnetic turbulence regulate the spectral shape of accelerated particles for both SNRs.
2. For the SNR with 60 $M_\odot$ progenitor, particle spectra show softness at lower energies ($<$ 10 GeV) with spectral index $\sim$ 2.4 while the SNR forward shock resides in the hot shocked wind region. However, in the other scenario, the hydrodynamics do not give rise to persistent spectral softness except for a brief period during the SNR-RSG shell interaction. Therefore, the SNRs with lower massive progenitors are not likely to provide spectral softness during early evolutionary stages on account of the presence of comparatively colder wind bubbles. But, at later stages, the particle spectra become softer at higher energies because of the escape of highly energetic particles from the remnant on account of the weak driving of magnetic turbulence.
3. Further, the emission morphology of SNRs from different non-thermal processes is strongly influenced by the type of progenitors and also the wind bubble region where the SNR forward shocks reside. However, when the SNR forward shock reaches the shocked ISM region, the morphology for both SNRs is consistent and also similar to that of the type-Ia SNRs at later times.

Therefore, in this dissertation I provide a very detailed study of the particle acceleration and emission from the core-collapse remnant and different aspects of the SNR-CSM interactions which can be beneficial to understand the emission from observed SNRs expanding in wind bubbles.

Future prospects
This work opens different future possibilities that can be studied by using *RATPaC* with modification to some extent. These prospects are as follows,

[282]: Perez-Rendon et al. (2009), 'Supernova progenitor stars in the initial range of 23 to 33 solar masses and their relation with the SNR Cas A'
[283]: Weil et al. (2020), 'Detection of the Red Supergiant Wind from the Progenitor of Cassiopeia A'

1. Particle acceleration in Cas A: Understanding the dynamics of the forward and reverse shock of the young SNR Cas A can be interesting by modelling this scenario as the SNR expansion inside the wind bubble of lower massive progenitor [282, 283] in *RATPaC*. Observationally, for Cas A, in the West, the reverse shock moves towards the SNR interior with a very high velocity and [284] predicted that such a situation may arise from the collision of the forward shock with a dense shell. This scenario is quite similar to the SNR evolution inside the wind bubble from the 20 $M_\odot$ progenitor explained in Chapter 6 where the SNR reverse shock evolves towards the SNR interior after the encounter of the forward shock with the dense RSG shell but of course, this situation occurs in the simulation after around 1900 years. So, modelling the CSM with a lower massive progenitor may

[284]: Vink et al. (2022), 'The Forward and Reverse Shock Dynamics of Cassiopeia A'

cause the formation of a shell near the SNR ejecta and the reverse shock motion towards SNR interior can happen at early times. Further, this fast inward-moving reverse shock in Cas A gives rise to synchrotron X-ray emitting filaments which suggests that it would be beneficial to study the particle acceleration at the reverse shock along with the magnetic field amplification together with the modelling of the DSA at the forward shock.

2. Particle acceleration at core-collapse SNRs in different environments: In Chapter 6, I have studied the effect of the CSM shaped by different massive progenitors on the particle acceleration of SNRs. However, the evolution of massive stars depends on metallicity, for instance, metal-poor stars hardly reach the red supergiant stage as the metallicity directly connects to opacity which regulates the stellar luminosity [285, 286]. Therefore, it might be interesting to probe the acceleration of particles at SNRs with massive progenitors at different metallicities. This study may also provide information about the emission from SNRs in different local galaxies, such as the Large Magellanic Cloud (LMC), Small Magellanic Cloud (SMC), and Messier 33.

[285]: Hirschi et al. (2007), 'Stellar Evolution at Low Metallicity'
[286]: Sanyal, D. et al. (2017), 'Metallicity dependence of envelope inflation in massive stars'

3. CRs in massive stellar clusters: Massive star clusters are expected to accelerate particles to higher energies by the combined effect of interacting powerful stellar winds and also their lifespan is longer than individual SNRs. Therefore, these clusters can be the potential sources of CRs [287], but [288, 289] suggested that considering star clusters along with the discrete supernova explosions would be the realistic approach for exploring CR acceleration in this scenario. Therefore, it would be fascinating to study CR acceleration by star cluster specifically at the superbubbles, considering the details of the injection from stellar wind and supernovae [290].

[287]: Yang et al. (2019), 'Massive star clusters as the an alternative source population of galactic cosmic rays'

[288]: Maurin et al. (2016), 'Embedded star clusters as sources of high-energy cosmic rays-Modelling and constraints'
[289]: Bhadra et al. (2022), 'Cosmic rays from massive star clusters: a close look at Westerlund 1'

[290]: Vieu et al. (2022), 'Cosmic ray production in superbubbles'

Linearised MHD equations and dispersion relation

A

In the ideal MHD fluids, all dissipative processes like thermal conductivity, viscous dissipation, non-adiabatic heating or cooling etc. can be neglected and these fluids can be described by the following equations:

Continuity equation $$\frac{\partial \rho}{\partial t} + \nabla.(\rho\,\mathbf{u}) = 0 \tag{A.0.1}$$

Momentum equation

$$\rho\frac{\partial \mathbf{u}}{\partial t} + \rho\,(\mathbf{u}.\nabla)\,\mathbf{u} = \frac{1}{4\pi}(\nabla\times\mathbf{B})\times\mathbf{B} - \nabla P \tag{A.0.2}$$

Induction equation $$\frac{\partial \mathbf{B}}{\partial t} = \nabla\times(\mathbf{u}\times\mathbf{B}) \tag{A.0.3}$$

Gauss law $$\nabla.\mathbf{B} = 0 \tag{A.0.4}$$

Adiabatic energy equation $$\left(\frac{\partial}{\partial t} + \mathbf{u}.\nabla\right) P = -\gamma\rho\,\nabla.\mathbf{u} \tag{A.0.5}$$

where $\mathbf{u}$ is the fluid velocity, ρ is the fluid density, P is the thermal pressure, $\mathbf{B}$ refers to the frozen-in magnetic field and γ is the adiabatic index.
Decomposing flow density, flow velocity and magnetic field in terms of the background initial values and space- and time-dependent fluctuations by ignoring second and higher-order terms,

$$\begin{aligned}\rho &= \rho_0 + \rho_1\\ \mathbf{u} &= \mathbf{u_0} + \mathbf{u_1}\\ \mathbf{B} &= \mathbf{B_0} + \mathbf{B_1}\end{aligned} \tag{A.0.6}$$

Therefore, considering the uniform background the linearised MHD equations become,

$$\frac{\partial \rho_1}{\partial t} = -\rho_0\nabla.\mathbf{u_1} \tag{A.0.7}$$

$$\rho_0\frac{\partial \mathbf{u_1}}{\partial t} = \frac{(\nabla\times\mathbf{B_1})\times\mathbf{B_0}}{4\pi} - \nabla\mathbf{P_1} \tag{A.0.8}$$

$$\frac{\partial \mathbf{B_1}}{\partial t} = \nabla \times (\mathbf{u_1} \times \mathbf{B_0}) \tag{A.0.9}$$

$$\frac{\partial P_1}{\partial t} = -\gamma P_0 \nabla . \mathbf{u_1} \tag{A.0.10}$$

Differentiating Equation A.0.8 and using Equations A.0.7 and A.0.9, a wave equation for $\mathbf{u_1}$ can be developed,

$$\frac{\partial^2 \mathbf{u_1}}{\partial t} - c_s^2 \nabla (\nabla . \mathbf{u_1}) + v_A \times [\nabla \times \{\nabla \times (\mathbf{u_1} \times v_A)\}] = 0 \tag{A.0.11}$$

where c_s and v_A are sound speed and Alfvén speed, respectively. Assuming a plane wave solution,

$$\mathbf{u_1}(\mathbf{r}, t) = \mathbf{u_1} \exp\{(i\mathbf{k}.\mathbf{r} - i\omega t)\} \tag{A.0.12}$$

and $\nabla = i\mathbf{k}$, $\partial/\partial t = -i\omega$, Equation A.0.11 reads,

$$-\omega^2 \mathbf{u_1} + c_s^2 (\mathbf{k}.\mathbf{u_1})\, \mathbf{k} - v_A \times [\mathbf{k} \times \{\mathbf{k} \times (\mathbf{u_1} \times v_A)\}] = 0. \tag{A.0.13}$$

For $\mathbf{k} = k_\perp \widehat{\mathbf{y}} + k_\parallel \widehat{\mathbf{z}}$, Equation A.0.13 gives,

$$\begin{pmatrix} \omega^2 - k_\parallel^2 v_A^2 & 0 & 0 \\ 0 & \omega^2 - k_\perp^2 c_s^2 - k^2 v_A^2 & -k_\perp k_\parallel c_s^2 \\ 0 & -k_\perp k_\parallel c_s^2 & \omega^2 - k_\parallel c_s^2 \end{pmatrix} \begin{pmatrix} u_{1x} \\ u_{1y} \\ u_{1z} \end{pmatrix} = 0 \tag{A.0.14}$$

Then, for the non-trivial solution of $\mathbf{u_1}$ Equation A.0.14 gives the dispersion relations MHD waves,

$$(\omega^2 - k_\parallel^2 v_A^2) \left[\omega^4 - k^2 \left(c_s^2 + v_A^2\right) \omega^2 + k^2 k_\parallel c_s^2 v_A^2\right] = 0 \tag{A.0.15}$$

as expressed in Equation 3.3.24.

Effect of shock-shock tail-on merging

B

Figure B.0.1 shows a two-shock system schematically. I consider that shock 1 and shock 2 propagate with velocities $V_{\rm sh,1}$ and $V_{\rm sh,2}$, respectively in the simulation frame and these shocks are separated by distance L at a particular time. There should be a limited time span $t_{\rm i}$ during which particles with particular energies may able to cross both shocks diffusively and "feel" the total compression ratio of this system which is $r_{\rm tot} = r_1 . r_2$, where r_1 and r_2 are the compression ratio of shock 1 and shock 2, respectively and as $r_{\rm tot}$ should typically larger than four and hence, a spectral hardening may happen. But the particle spectrum should be affected if the interaction time ($t_{\rm i}$) is larger than the acceleration time of the particles ($t_{\rm acc}$).

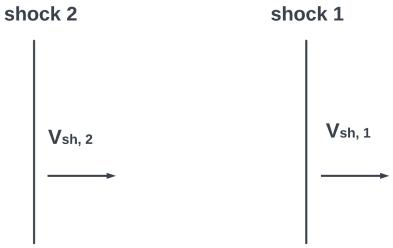

Figure B.0.1: Schematic of two-shock system

If particles with momentum p cross shock 2 towards its upstream region and reach shock 1, then the distance L between two shocks can be expressed as, $L = \frac{D(p)}{V_2}$ following the definition of precursor length in Definition 3.3.2, where V_2 is the velocity of shock 2 in its upstream rest frame and D is the spatial diffusion coefficient between shock 1 and shock 2. Therefore, in this system, the collision time reads,

$$t_{\rm i} = \frac{L}{V_{\rm sh,2} - V_{\rm sh,1}} = \frac{D\,(p)}{V_2\,(V_{\rm sh,2} - V_{\rm sh,1})} \tag{B.0.1}$$

considering $V_{\rm sh,1}$ and $V_{\rm sh,2}$ remain constant. Further, in the simulation frame, $u_{\rm d,1} = u_{\rm u,2}$ where u is the flow velocity in the simulation reference frame and subscripts, u and d denote the upstream and downstream regions, respectively and subscripts 1, 2 represent the corresponding shocks. Then, from Equation 4.4.5,

$$r_1 = \frac{V_{\rm sh,1} - u_{\rm u,1}}{V_{\rm sh,1} - u_{\rm d,1}} \Rightarrow V_{\rm sh,2} - V_{\rm sh,1} = V_2 - \frac{V_1}{r_1} \tag{B.0.2}$$

where V_1 is the velocity of shock 1 in the rest frame of its upstream. Additionally, shock 2 should have sonic Mach number, $\mathcal{M}_{\rm n,2} > 1$ and hence, from Equation 3.3.2 by using $\rho_{\rm d,1} = \rho_{\rm u,2}$ and $P_{\rm d,1} = P_{\rm u,2}$, where P and ρ refer the thermal pressure and flow density, respectively and considering shock 1 as a strong shock and $\gamma = 5/3$,

$$\mathcal{M}_{\rm n,2} = \sqrt{\frac{\rho_{\rm d,1} V_2^2}{\gamma P_{\rm d,1}}} = \sqrt{\frac{3V_2^2}{5}\frac{16}{3V_1^2}\left(1 + \frac{16}{5\mathcal{M}_{\rm n,1}^2}\right)^{-1}} \sim \frac{4}{\sqrt{5}}\frac{V_2}{V_1} \tag{B.0.3}$$

if $\gamma = 5/3$.
From Equations B.0.2 and B.0.3,

$$t_{\rm i} = \frac{D(p)}{V_2\left(1-\frac{1}{\sqrt{5}\mathcal{M}_{\rm n,2}}\right)} = \frac{D(p)}{V_1^2}\frac{16}{5\mathcal{M}_{\rm n,2}^2}\frac{1}{\left(1-\frac{1}{\sqrt{5}\mathcal{M}_{\rm n,2}}\right)} \tag{B.0.4}$$

Now, the average energy gained by particles per cycle in the two-shock system can be written in terms of the total compression ratio of the system, $r_{\rm tot}$ from Equation 3.3.7,

$$\left\langle\frac{\Delta p}{p}\right\rangle = \frac{4}{3}\frac{r_{\rm tot}-1}{r_{\rm tot}}\frac{V_1}{c} \tag{B.0.5}$$

In this shock-shock merging system, the diffusion coefficient will change in the downstream region of shock 2 and in the upstream region of shock 1. Therefore, only considering the region between two shocks with constant diffusion coefficient $D(p)$ and taking into account the residence time of particles in this region ignoring the time spent upstream of shock 1 and downstream of shock 2, a lower limit of the acceleration time to gain momentum p from Equations 3.3.20 and 3.3.21 can be expressed by,

$$\begin{aligned} t_{\rm acc} &= \frac{\left\langle t_{\rm cycle}\right\rangle}{\frac{\Delta p}{p}} > \frac{4D(p)}{c\left(V_{\rm sh,1}-u_{\rm d,1}\right)}\Big/\left\langle\frac{\Delta p}{p}\right\rangle \\ &> \frac{16D(p)}{V_1}\Big/\left\langle\frac{\Delta p}{p}\right\rangle = \frac{12D(p)}{V_1^2}\frac{r_{\rm tot}}{r_{\rm tot}-1} \end{aligned} \tag{B.0.6}$$

Hence, from Equations B.0.4 and B.0.6,

$$\frac{t_{\rm i}}{t_{\rm acc}} < \frac{4}{3}\frac{r_{\rm tot}-1}{r_{\rm tot}}\frac{1}{5\mathcal{M}_{\rm n,2}^2\left(1-\frac{1}{\sqrt{5}\mathcal{M}_{\rm n,2}}\right)} \tag{B.0.7}$$

Now, $r_{\rm tot} = \frac{\rho_{\rm d,2}}{\rho_{\rm u,1}}$ and for $r_1 = 4$ along with using Equation 3.3.3,

$$r_{\rm tot} = 16\frac{\mathcal{M}_{\rm n,2}^2}{\mathcal{M}_{\rm n,2}^2+3} \tag{B.0.8}$$

Then using this, Equation B.0.7 can be written as,

$$\frac{t_{\rm i}}{t_{\rm acc}} < \frac{1}{4\mathcal{M}_{\rm n,2}^2}\left(1+\frac{1}{\sqrt{5}\mathcal{M}_{\rm n,2}}\right) \tag{B.0.9}$$

where $\frac{1}{4\mathcal{M}_{\rm n,2}^2}\left(1+\frac{1}{\sqrt{5}\mathcal{M}_{\rm n,2}}\right) < 1$ for $\mathcal{M}_{\rm n,2} > 1$ which is required for shock 2 to be a shock. Hence, particles can "feel" the $r_{\rm tot}$ for less than a single acceleration time. Therefore, the tail-on collision of shocks cannot produce any significant spectral features.

The effect of shock-shock tail on collision is also described in [202].

Bibliography

[1] M. Walter and A. W. Wolfendale. 'Early history of cosmic particle physics'. In: *Eur. Phys. J. H* 37 (2012), pp. 323–358. DOI: 10.1140/epjh/e2012-30020-1 (cited on page 1).

[2] C. T. R. Wilson. 'On the Ionisation of Atmospheric Air'. In: *Proceedings of the Royal Society of London* 68 (1901), pp. 151–161. (Visited on 01/17/2023) (cited on page 1).

[3] Victor F. Hess. 'Über Beobachtungen der durchdringenden Strahlung bei sieben Freiballonfahrten'. In: *Phys. Z.* 13 (1912), pp. 1084–1091 (cited on page 1).

[4] W. Baade and F. Zwicky. 'On Super-Novae'. In: *Proceedings of the National Academy of Sciences* 20.5 (1934), pp. 254–259. DOI: 10.1073/pnas.20.5.254 (cited on page 1).

[5] W. Baade and F. Zwicky. 'Cosmic Rays from Super-Novae'. In: *Proceedings of the National Academy of Sciences* 20.5 (1934), pp. 259–263. DOI: 10.1073/pnas.20.5.259 (cited on pages 1, 3).

[6] Gloria Dubner and Elsa Giacani. 'Radio emission from Supernova Remnants'. In: *Astron. Astrophys. Rev.* 23.1 (2015), p. 3. DOI: 10.1007/s00159-015-0083-5 (cited on page 1).

[7] H. Alfvén and N. Herlofson. 'Cosmic Radiation and Radio Stars'. In: *Phys. Rev.* 78 (5 June 1950), pp. 616–616. DOI: 10.1103/PhysRev.78.616 (cited on page 1).

[8] K. O. Kiepenheuer. 'Cosmic Rays as the Source of General Galactic Radio Emission'. In: *Phys. Rev.* 79 (4 Aug. 1950), pp. 738–739. DOI: 10.1103/PhysRev.79.738 (cited on page 1).

[9] Enrico Fermi. 'On the Origin of the Cosmic Radiation'. In: *Physical Review* 75.8 (Apr. 1949), pp. 1169–1174. DOI: 10.1103/PhysRev.75.1169 (cited on pages 1, 19, 67).

[10] A. R. Bell. 'The acceleration of cosmic rays in shock fronts - I.' In: 182 (Jan. 1978), pp. 147–156. DOI: 10.1093/mnras/182.2.147 (cited on pages 1, 19, 29, 53, 67).

[11] A. R. Bell. 'The acceleration of cosmic rays in shock fronts - II.' In: 182 (Feb. 1978), pp. 443–455. DOI: 10.1093/mnras/182.3.443 (cited on pages 1, 19).

[12] R. D. Blandford and J. P. Ostriker. 'Supernova shock acceleration of cosmic rays in the Galaxy.' In: 237 (May 1980), pp. 793–808. DOI: 10.1086/157926 (cited on page 1).

[13] J. A. Toalá et al. 'The Bubble Nebula NGC 7635 - testing the wind-blown bubble theory'. In: 495.3 (July 2020), pp. 3041–3051. DOI: 10.1093/mnras/staa752 (cited on page 2).

[14] J. Chadwick. 'Possible Existence of a Neutron'. In: *Nature* 129 (1932), p. 312. DOI: 10.1038/129312a0 (cited on page 3).

[15] D. G. Yakovlev et al. 'L D Landau and the concept of neutron stars'. In: *Phys. Usp.* 56.3 (2013), pp. 289–295. DOI: 10.3367/UFNe.0183.201303f.0307 (cited on page 3).

[16] J. H. Elias et al. 'Type I supernovae in the infrared and their use as distance indicators.' In: 296 (Sept. 1985), pp. 379–389. DOI: 10.1086/163456 (cited on page 3).

[17] Weidong Li et al. 'Nearby supernova rates from the Lick Observatory Supernova Search - II. The observed luminosity functions and fractions of supernovae in a complete sample'. In: 412.3 (Apr. 2011), pp. 1441–1472. DOI: 10.1111/j.1365-2966.2011.18160.x (cited on page 3).

[18] Patrick L. Kelly, Robert P. Kirshner, and Michael Pahre. 'Long γ-Ray Bursts and Type Ic Core-Collapse Supernovae Have Similar Locations in Hosts'. In: 687.2 (Nov. 2008), pp. 1201–1207. DOI: 10.1086/591925 (cited on page 3).

[19] Stephen J Smartt. 'Progenitors of core-collapse supernovae'. In: *Annual Review of Astronomy and Astrophysics* 47 (2009), pp. 63–106 (cited on page 3).

[20] Oliver Krause et al. 'The cassiopeia A supernova was of type IIb'. English (US). In: *Science* 320.5880 (May 2008), pp. 1195–1197. DOI: 10.1126/science.1155788 (cited on page 4).

[21] R. Minkowski. 'Spectra of Supernovae'. In: 53.314 (Aug. 1941), p. 224. DOI: 10.1086/125315 (cited on page 4).

[22] Avishay Gal-Yam. 'Observational and Physical Classification of Supernovae'. In: (Nov. 2016). DOI: 10.1007/978-3-319-20794-0_35-1 (cited on page 4).

[23] N. Langer. 'Presupernova Evolution of Massive Single and Binary Stars'. In: *Annual Review of Astronomy and Astrophysics* 50.1 (2012), pp. 107–164. DOI: 10.1146/annurev-astro-081811-125534 (cited on page 4).

[24] S. E. Woosley, A. Heger, and T. A. Weaver. 'The evolution and explosion of massive stars'. In: *Rev. Mod. Phys.* 74 (4 Nov. 2002), pp. 1015–1071. DOI: 10.1103/RevModPhys.74.1015 (cited on page 4).

[25] Georg G Raffelt. 'Supernova neutrino observations: What can we learn?' In: *arXiv preprint astro-ph/0701677* (2007) (cited on page 5).

[26] A. Odrzywolek, M. Misiaszek, and M. Kutschera. 'Future neutrino observations of nearby pre-supernova stars before core-collapse'. In: *AIP Conference Proceedings* 944.1 (Nov. 2007), pp. 109–118. DOI: 10.1063/1.2818538 (cited on page 5).

[27] Adam Burrows. 'Colloquium: Perspectives on core-collapse supernova theory'. In: *Rev. Mod. Phys.* 85 (1 Feb. 2013), pp. 245–261. DOI: 10.1103/RevModPhys.85.245 (cited on page 5).

[28] Hans-Thomas Janka, Tobias Melson, and Alexander Summa. 'Physics of Core-Collapse Supernovae in Three Dimensions: A Sneak Preview'. In: *Annual Review of Nuclear and Particle Science* 66.1 (2016), pp. 341–375. DOI: 10.1146/annurev-nucl-102115-044747 (cited on page 5).

[29] Sean M. Couch. 'The mechanism(s) of core-collapse supernovae'. In: *Philosophical Transactions of the Royal Society A: Mathematical, Physical and Engineering Sciences* 375.2105 (2017), p. 20160271. DOI: 10.1098/rsta.2016.0271 (cited on page 5).

[30] James R. Wilson. 'Supernovae and Post-Collapse Behavior'. In: *Numerical Astrophysics*. Jan. 1985, p. 422 (cited on page 5).

[31] H. -Th. Janka et al. 'Theory of core-collapse supernovae'. In: 442.1-6 (Apr. 2007), pp. 38–74. DOI: 10.1016/j.physrep.2007.02.00210.48550/arXiv.astro-ph/0612072 (cited on page 6).

[32] Raphael Hirschi et al. 'Stellar Evolution at Low Metallicity'. In: *Massive Stars as Cosmic Engines*. Ed. by F. Bresolin, P. A. Crowther, and J. Puls. Vol. 250. June 2008, pp. 217–230. DOI: 10.1017/S1743921308020528 (cited on page 7).

[33] Georges Meynet and Andre Maeder. 'Stellar evolution with rotation. 5. Changes in all the outputs of massive star models'. In: *Astron. Astrophys.* 361 (2000), p. 101 (cited on page 7).

[34] Sanyal, D. et al. 'Metallicity dependence of envelope inflation in massive stars'. In: *A&A* 597 (2017), A71. DOI: 10.1051/0004-6361/201629612 (cited on page 7).

[35] Ekström, S. et al. 'Grids of stellar models with rotation - I. Models from 0.8 to 120 M solar metallicity (Z = 0.014)'. In: *A&A* 537 (2012), A146. DOI: 10.1051/0004-6361/201117751 (cited on pages 7, 89).

[36] Norhasliza Yusof et al. 'Grids of stellar models with rotation VII: models from 0.8 to 300–M– at supersolar metallicity (Z = 0.020)'. In: *Monthly Notices of the Royal Astronomical Society* 511.2 (Jan. 2022), pp. 2814–2828. DOI: 10.1093/mnras/stac230 (cited on page 7).

[37] S. E. Woosley, Norbert Langer, and Thomas A. Weaver. 'The evolution of massive stars including mass loss - Presupernova models and explosion'. In: *The Astrophysical Journal* 411 (1993), pp. 823–839 (cited on page 7).

[38] J. J. Eldridge et al. 'The circumstellar environment of Wolf-Rayet stars and gamma-ray burst afterglows'. In: 367.1 (Mar. 2006), pp. 186–200. DOI: 10.1111/j.1365-2966.2005.09938.x (cited on page 8).

[39] Sam Geen et al. 'The geometry and dynamical role of stellar wind bubbles in photoionized H–ii regions'. In: *Monthly Notices of the Royal Astronomical Society* 501.1 (Nov. 2020), pp. 1352–1369. DOI: 10.1093/mnras/staa3705 (cited on pages 8, 11).

[40] VS Avedisova. 'Formation of Nebulae by Wolf-Rayet Stars.' In: *Soviet Astronomy* 15 (1972), p. 708 (cited on page 8).

[41] R. Weaver et al. 'Interstellar bubbles. II. Structure and evolution.' In: 218 (Dec. 1977), pp. 377–395. DOI: 10.1086/155692 (cited on pages 8, 9).

[42] A. Mignone et al. 'PLUTO: A Numerical Code for Computational Astrophysics'. In: 170.1 (May 2007), pp. 228–242. DOI: 10.1086/513316 (cited on pages 9, 42, 44).

[43] Gary M. Heiligman. 'Planetary nebulae and the interstellar magnetic field'. In: *Monthly Notices of the Royal Astronomical Society* 191.4 (Aug. 1980), pp. 761–766. DOI: 10.1093/mnras/191.4.761 (cited on page 10).

[44] van Marle, A. J., Meliani, Z., and Marcowith, A. 'Shape and evolution of wind-blown bubbles of massive stars: on the effect of the interstellar magnetic field'. In: *A&A* 584 (2015), A49. DOI: 10.1051/0004-6361/201425230 (cited on page 10).

[45] L. L. Cowie and C. F. McKee. 'The evaporation of spherical clouds in a hot gas. I. Classical and saturated mass loss rates.' In: 211 (Jan. 1977), pp. 135–146. DOI: 10.1086/154911 (cited on page 10).

[46] L. Spitzer. *Physics of Fully Ionized Gases*. 1962 (cited on page 10).

[47] Tim Freyer, Gerhard Hensler, and Harold W Yorke. 'Massive Stars and the Energy Balance of the Interstellar Medium. I. The Impact of an Isolated 60 M– Star'. In: *The Astrophysical Journal* 594.2 (2003), p. 888 (cited on page 10).

[48] Tim Freyer, Gerhard Hensler, and Harold W Yorke. 'Massive Stars and the Energy Balance of the Interstellar Medium. II. The 35 M– Star and a Solution to the "Missing Wind Problem"'. In: *The Astrophysical Journal* 638.1 (2006), p. 262 (cited on page 10).

[49] J. A. Toalá et al. 'X-RAY EMISSION FROM THE WOLF–RAYET BUBBLE S 308*'. In: *The Astrophysical Journal* 755.1 (2012), p. 77. DOI: 10.1088/0004-637X/755/1/77 (cited on page 11).

[50] Dave van Buren and Richard McCray. 'Bow Shocks and Bubbles Are Seen around Hot Stars by IRAS'. In: 329 (June 1988), p. L93. DOI: 10.1086/185184 (cited on page 11).

[51] T. R. Gull and S. Sofia. 'Discovery of two distorted interstellar bubbles.' In: 230 (June 1979), pp. 782–785. DOI: 10.1086/157137 (cited on page 11).

[52] Pereira, V. et al. 'Modeling nonthermal emission from stellar bow shocks'. In: *A&A* 588 (2016), A36. DOI: 10.1051/0004-6361/201527985 (cited on page 11).

[53] D. M.-A. Meyer et al. 'Models of the circumstellar medium of evolving, massive runaway stars moving through the Galactic plane'. In: *Monthly Notices of the Royal Astronomical Society* 444.3 (Sept. 2014), pp. 2754–2775. DOI: 10.1093/mnras/stu1629 (cited on page 11).

[54] William J Henney and S J Arthur. 'Bow shocks, bow waves, and dust waves – I. Strong coupling limit'. In: *Monthly Notices of the Royal Astronomical Society* 486.3 (Apr. 2019), pp. 3423–3433. DOI: 10.1093/mnras/stz1043 (cited on page 11).

[55] Cintia Soledad Peri, Paula Benaglia, and Natacha Laura Isequilla. 'E-boss: An extensive stellar bow shock survey-ii. catalogue second release'. In: *Astronomy & Astrophysics* 578 (2015), A45 (cited on page 11).

[56] Henry A. Kobulnicky et al. 'A COMPREHENSIVE SEARCH FOR STELLAR BOWSHOCK NEBULAE IN THE MILKY WAY: A CATALOG OF 709 MID-INFRARED SELECTED CANDIDATES'. In: *The Astrophysical Journal Supplement Series* 227.2 (2016), p. 18. DOI: 10.3847/0067-0049/227/2/18 (cited on page 11).

[57] V. B. Baranov, K. V. Krasnobaev, and A. G. Kulikovskii. 'A Model of the Interaction of the Solar Wind with the Interstellar Medium'. In: *Soviet Physics Doklady* 15 (Mar. 1971), p. 791 (cited on page 11).

[58] Francis P. Wilkin. 'Exact Analytic Solutions for Stellar Wind Bow Shocks'. In: 459 (Mar. 1996), p. L31. DOI: 10.1086/309939 (cited on page 11).

[59] J. A. Toalá et al. 'X-RAY OBSERVATIONS OF BOW SHOCKS AROUND RUNAWAY O STARS. THE CASE OF ζ OPH AND BD+43°3654'. In: *The Astrophysical Journal* 821.2 (2016), p. 79. DOI: 10.3847/0004-637X/821/2/79 (cited on page 12).

[60] V. V. Gvaramadze, N. Langer, and J. Mackey. '– Oph and the weak-wind problem'. In: *Monthly Notices of the Royal Astronomical Society: Letters* 427.1 (2012), pp. L50–L54. DOI: https://doi.org/10.1111/j.1745-3933.2012.01343.x (cited on page 12).

[61] J Van den Eijnden, P Saikia, and S Mohamed. 'Radio detections of IR-selected runaway stellar bow shocks'. In: *Monthly Notices of the Royal Astronomical Society* 512.4 (Mar. 2022), pp. 5374–5389. DOI: 10.1093/mnras/stac823 (cited on page 12).

[62] Mackey, Jonathan et al. 'Detecting stellar-wind bubbles through infrared arcs in Hregions'. In: *A&A* 586 (2016), A114. DOI: 10.1051/0004-6361/201527569 (cited on page 12).

[63] Samuel Green et al. 'Thermal emission from bow shocks-II. 3D magnetohydrodynamic models of ζ Ophiuchi'. In: *Astronomy & Astrophysics* 665 (2022), A35 (cited on page 12).

[64] Jonathan Mackey. 'Interaction between massive star winds and the interstellar medium'. In: *arXiv e-prints*, arXiv:2211.08808 (Nov. 2022), arXiv:2211.08808. DOI: 10.48550/arXiv.2211.08808 (cited on page 12).

[65] L. Woltjer. 'Supernova Remnants'. In: *Annual Review of Astronomy and Astrophysics* 10.1 (1972), pp. 129–158. DOI: 10.1146/annurev.aa.10.090172.001021 (cited on page 13).

[66] D. A. Leahy and J. E. Williams. 'A Python Calculator for Supernova Remnant Evolution'. In: 153.5, 239 (May 2017), p. 239. DOI: 10.3847/1538-3881/aa6af6 (cited on page 13).

[67] Jacco Vink. 'Supernova remnants: the X-ray perspective'. In: *The Astronomy and Astrophysics Review* 20 (2012), pp. 1–120 (cited on pages 13, 14).

[68] Brian J. Williams et al. 'RCW 86: A TYPE Ia SUPERNOVA IN A WIND-BLOWN BUBBLE'. In: *The Astrophysical Journal* 741.2 (2011), p. 96. DOI: 10.1088/0004-637X/741/2/96 (cited on page 13).

[69] E. A. Helder, J. Vink, and C. G. Bassa. 'TEMPERATURE EQUILIBRATION BEHIND THE SHOCK FRONT: AN OPTICAL AND X-RAY STUDY OF RCW 86'. In: *The Astrophysical Journal* 737.2 (2011), p. 85. DOI: 10.1088/0004-637X/737/2/85 (cited on page 13).

[70] R. A. Chevalier. 'Self-similar solutions for the interaction of stellar ejecta with an external medium.' In: 258 (July 1982), pp. 790–797. DOI: 10.1086/160126 (cited on pages 13, 42, 46).

[71] J. Kelly Truelove and Christopher F. McKee. 'Evolution of Nonradiative Supernova Remnants'. In: 120.2 (Feb. 1999), pp. 299–326. DOI: 10.1086/313176 (cited on page 14).

[72] Leonid Ivanovich Sedov. 'Propagation of strong shock waves'. In: *Journal of Applied Mathematics and Mechanics* 10 (1946), pp. 241–250 (cited on page 14).

[73] Geoffrey Taylor. 'The Formation of a Blast Wave by a Very Intense Explosion. I. Theoretical Discussion'. In: *Proceedings of the Royal Society of London Series A* 201.1065 (Mar. 1950), pp. 159–174. DOI: 10.1098/rspa.1950.0049 (cited on page 14).

[74] Daniel J Patnaude and Robert A Fesen. 'Proper motions and brightness variations of nonthermal X-ray filaments in the Cassiopeia A supernova remnant'. In: *The Astrophysical Journal* 697.1 (2009), p. 535 (cited on page 14).

[75] Fraschetti, F. et al. 'Simulation of the growth of the 3D Rayleigh-Taylor instability in supernova remnants using an expanding reference frame'. In: *A&A* 515 (2010), A104. DOI: 10.1051/0004-6361/200912692 (cited on page 15).

[76] Bahaa T Chiad, Lana Ali, and Abdhreda Hassani. 'Determination of Velocity and Radius of Supernova Remnant after 1000 yrs of Explosion'. In: *International Journal of Astronomy and Astrophysics* 05 (Jan. 2015), pp. 125–132. DOI: 10.4236/ijaa.2015.52016 (cited on page 15).

[77] M. V. del Valle and M. Pohl. 'Nonthermal Emission from Stellar Bow Shocks'. In: 864.1, 19 (Sept. 2018), p. 19. DOI: 10.3847/1538-4357/aad333 (cited on page 15).

[78] Aharonian, F. et al. 'A deep spectromorphological study of the emission surrounding the young massive stellar cluster Westerlund 1'. In: *A&A* 666 (2022), A124. DOI: 10.1051/0004-6361/202244323 (cited on page 15).

[79] Thibault Vieu et al. 'Cosmic ray production in superbubbles'. In: *Mon. Not. Roy. Astron. Soc.* 512.1 (2022), pp. 1275–1293. DOI: 10.1093/mnras/stac543 (cited on page 15).

[80] Isabelle A Grenier, John H Black, and Andrew W Strong. 'The nine lives of cosmic rays in galaxies'. In: *Annual Review of Astronomy and Astrophysics* 53 (2015), pp. 199–246 (cited on pages 17, 18).

[81] Pasquale Blasi. 'The origin of galactic cosmic rays'. In: *The Astronomy and Astrophysics Review* 21 (2013), pp. 1–73 (cited on pages 17, 67).

[82] Russell M. Kulsrud. *Plasma Physics for Astrophysics*. 2005 (cited on page 17).

[83] O. Adriani et al. 'PAMELA Measurements of Cosmic-Ray Proton and Helium Spectra'. In: *Science* 332.6025 (Apr. 2011), p. 69. DOI: 10.1126/science.1199172 (cited on page 17).

[84] M. Aguilar et al. 'First Result from the Alpha Magnetic Spectrometer on the International Space Station: Precision Measurement of the Positron Fraction in Primary Cosmic Rays of 0.5–350 GeV'. In: *Phys. Rev. Lett.* 110 (14 Apr. 2013), p. 141102. DOI: 10.1103/PhysRevLett.110.141102 (cited on page 17).

[85] O. Ganel et al. 'Beam tests of the balloon-borne ATIC experiment'. In: *Nuclear Instruments and Methods in Physics Research Section A: Accelerators, Spectrometers, Detectors and Associated Equipment* 552 (Nov. 2005), pp. 409–419. DOI: 10.1016/j.nima.2005.06.081 (cited on page 17).

[86] Karl-Heinz Kampert and Alan A Watson. 'Extensive air showers and ultra high-energy cosmic rays: a historical review'. In: *The European Physical Journal H* 37.3 (2012), pp. 359–412 (cited on page 17).

[87] Ralph Engel. 'Indirect Detection of Cosmic Rays'. In: *Handbook of Particle Detection and Imaging*. Ed. by Claus Grupen and Irène Buvat. Berlin, Heidelberg: Springer Berlin Heidelberg, 2012, pp. 593–632. DOI: 10.1007/978-3-642-13271-1_24 (cited on page 17).

[88] Marius S Potgieter. 'Solar modulation of cosmic rays'. In: *Living Reviews in Solar Physics* 10 (2013), pp. 1–66 (cited on page 18).

[89] L. A. Fisk and G. Gloeckler. 'ACCELERATION OF GALACTIC COSMIC RAYS IN THE INTERSTELLAR MEDIUM'. In: *The Astrophysical Journal* 744.2 (2011), p. 127. DOI: 10.1088/0004-637X/744/2/127 (cited on page 18).

[90] Kenneth Greisen. 'End to the Cosmic-Ray Spectrum?' In: *Phys. Rev. Lett.* 16 (17 Apr. 1966), pp. 748–750. DOI: 10.1103/PhysRevLett.16.748 (cited on page 18).

[91] Carmelo Evoli. *The Cosmic-Ray Energy Spectrum*. Dec. 2020. DOI: 10.5281/zenodo.4396125. URL: https://doi.org/10.5281/zenodo.4396125 (cited on page 18).

[92] Thomas K. Gaisser. *Cosmic rays and particle physics*. 1990 (cited on page 19).

[93] Seán Prunty. 'Conditions Across the Shock: The Rankine-Hugoniot Equations'. In: *Introduction to Simple Shock Waves in Air: With Numerical Solutions Using Artificial Viscosity*. Cham: Springer International Publishing, 2021, pp. 89–130. DOI: 10.1007/978-3-030-63606-7_3 (cited on page 19).

[94] R. Li et al. 'Electron shock-surfing acceleration in the presence of magnetic field'. In: *Physics of Plasmas* 25.8 (July 2018). 082103. DOI: 10.1063/1.5030184 (cited on page 21).

[95] Artem Bohdan et al. 'Kinetic Simulations of Nonrelativistic Perpendicular Shocks of Young Supernova Remnants. II. Influence of Shock-surfing Acceleration on Downstream Electron Spectra'. In: *The Astrophysical Journal* 885.1 (2019), p. 10. DOI: 10.3847/1538-4357/ab43cf (cited on page 21).

[96] Malcolm S. Longair. *High Energy Astrophysics*. 2011 (cited on pages 21, 32).

[97] Andrew W Strong and Igor V Moskalenko. 'Propagation of cosmic-ray nucleons in the galaxy'. In: *The Astrophysical Journal* 509.1 (1998), p. 212 (cited on page 22).

[98] ZHONGHUI FAN and SIMING LIU. 'STOCHASTIC ELECTRON ACCELERATION IN SNR RX J1713.7-3946'. In: *International Journal of Modern Physics: Conference Series* 23 (2013), pp. 319–323. DOI: 10.1142/S2010194513011550 (cited on page 22).

[99] Wilhelm, A. et al. 'Stochastic re-acceleration and magnetic-field damping in Tycho´s supernova remnant'. In: *A&A* 639 (2020), A124. DOI: 10.1051/0004-6361/201936079 (cited on page 22).

[100] G. F. Krymskii. 'A regular mechanism for the acceleration of charged particles on the front of a shock wave'. In: *Akademiia Nauk SSSR Doklady* 234 (June 1977), pp. 1306–1308 (cited on page 22).

[101] R. D. Blandford and J. P. Ostriker. 'Particle acceleration by astrophysical shocks.' In: 221 (Apr. 1978), pp. L29–L32. DOI: 10.1086/182658 (cited on page 22).

[102] A R Bell et al. 'Fast electron transport in laser-produced plasmas and the KALOS code for solution of the Vlasov–Fokker–Planck equation'. In: *Plasma Physics and Controlled Fusion* 48.3 (2006), R37. DOI: 10.1088/0741-3335/48/3/R01 (cited on page 24).

[103] B. Reville and A. R. Bell. 'Universal behaviour of shock precursors in the presence of efficient cosmic ray acceleration'. In: *Monthly Notices of the Royal Astronomical Society* 430.4 (Feb. 2013), pp. 2873–2884. DOI: 10.1093/mnras/stt100 (cited on page 24).

[104] S. Celli et al. 'Exploring particle escape in supernova remnants through gamma rays'. In: 490.3 (Dec. 2019), pp. 4317–4333. DOI: 10.1093/mnras/stz2897 (cited on pages 26, 67, 97).

[105] Robert Brose et al. 'Cosmic-ray acceleration and escape from post-adiabatic supernova remnants'. In: *Astronomy & Astrophysics* 634 (2020), A59 (cited on pages 26, 30, 55, 67, 68, 88, 94, 95, 97–99).

[106] P Cristofari, P Blasi, and D Caprioli. 'Cosmic ray protons and electrons from supernova remnants'. In: *Astronomy & Astrophysics* 650 (2021), A62 (cited on pages 26, 29).

[107] L. Oc. Drury. 'REVIEW ARTICLE: An introduction to the theory of diffusive shock acceleration of energetic particles in tenuous plasmas'. In: *Reports on Progress in Physics* 46.8 (Aug. 1983), pp. 973–1027. DOI: 10.1088/0034-4885/46/8/002 (cited on pages 26, 67).

[108] Parizot, E. et al. 'Observational constraints on energetic particle diffusion in young supernovae remnants: amplified magnetic field and maximum energy'. In: *A&A* 453.2 (2006), pp. 387–395. DOI: 10.1051/0004-6361:20064985 (cited on pages 26, 27).

[109] Berezhko, E. G., Ksenofontov, L. T., and Völk, H. J. 'Confirmation of strong magnetic field amplification and nuclear cosmic ray acceleration in SN 1006'. In: *A&A* 412.1 (2003), pp. L11–L14. DOI: 10.1051/0004-6361:20031667 (cited on page 26).

[110] Donald C Ellison, Anne Decourchelle, and Jean Ballet. 'Hydrodynamic simulation of supernova remnants including efficient particle acceleration'. In: *Astronomy & Astrophysics* 413.1 (2004), pp. 189–201 (cited on page 27).

[111] Hyesung Kang and Dongsu Ryu. 'DIFFUSIVE SHOCK ACCELERATION IN TEST-PARTICLE REGIME'. In: *The Astrophysical Journal* 721.1 (2010), p. 886. DOI: 10.1088/0004-637X/721/1/886 (cited on pages 27, 41).

[112] MA Malkov and L O'C Drury. 'Nonlinear theory of diffusive acceleration of particles by shock waves'. In: *Reports on Progress in Physics* 64.4 (2001), p. 429 (cited on page 27).

[113] E. Berezhko and Donald Ellison. 'A Simple Model of Nonlinear Diffusive Shock Acceleration'. In: *The Astrophysical Journal* 526 (Jan. 2009), p. 385. DOI: 10.1086/307993 (cited on pages 27, 28).

[114] M. L. Ahnen et al. 'A cut-off in the TeV gamma-ray spectrum of the SNR Cassiopeia A'. In: *Monthly Notices of the Royal Astronomical Society* 472.3 (Aug. 2017), pp. 2956–2962. DOI: 10.1093/mnras/stx2079 (cited on page 28).

[115] MA Malkov, PH Diamond, and RZ Sagdeev. 'Mechanism for spectral break in cosmic ray proton spectrum of supernova remnant W44'. In: *Nature Communications* 2.1 (2011), p. 194 (cited on page 28).

[116] Damiano Caprioli, Colby C. Haggerty, and Pasquale Blasi. 'Kinetic Simulations of Cosmic-Ray-modified Shocks. II. Particle Spectra'. In: *The Astrophysical Journal* 905.1 (2020), p. 2. DOI: 10.3847/1538-4357/abbe05 (cited on page 28).

[117] J. G. Kirk et al. *Plasma astrophysics / J.G. Kirk, D.B. Melrose, E.R. Priest ; edited by A.O. Benz and T.J.-L. Courvoisier*. English. Springer-Verlag Berlin ; New York, 1994, xii, 324 p. : (cited on page 28).

[118] Pohl, M., Wilhelm, A., and Telezhinsky, I. 'Reacceleration of electrons in supernova remnants'. In: *A&A* 574 (2015), A43. DOI: 10.1051/0004-6361/201425027 (cited on page 29).

[119] J. Skilling. 'Cosmic Ray Streaming—III SELF-CONSISTENT SOLUTIONS'. In: *Monthly Notices of the Royal Astronomical Society* 173.2 (Nov. 1975), pp. 255–269. DOI: 10.1093/mnras/173.2.255 (cited on page 29).

[120] S. G. Lucek and A. R. Bell. 'Non-linear amplification of a magnetic field driven by cosmic ray streaming'. In: *Monthly Notices of the Royal Astronomical Society* 314.1 (May 2000), pp. 65–74. DOI: 10.1046/j.1365-8711.2000.03363.x (cited on page 29).

[121] A. R. Bell. 'Turbulent amplification of magnetic field and diffusive shock acceleration of cosmic rays'. In: 353.2 (Sept. 2004), pp. 550–558. DOI: 10.1111/j.1365-2966.2004.08097.x (cited on page 29).

[122] Mario A. Riquelme and Anatoly Spitkovsky. 'NONLINEAR STUDY OF BELL'S COSMIC RAY CURRENT-DRIVEN INSTABILITY'. In: *The Astrophysical Journal* 694.1 (2009), p. 626. DOI: 10.1088/0004-637X/694/1/626 (cited on page 29).

[123] Oleh Kobzar et al. 'Spatio-temporal evolution of the non-resonant instability in shock precursors of young supernova remnants'. In: *Monthly Notices of the Royal Astronomical Society* 469.4 (May 2017), pp. 4985–4998. DOI: 10.1093/mnras/stx1201 (cited on page 29).

[124] Jacek Niemiec et al. 'Production of Magnetic Turbulence by Cosmic Rays Drifting Upstream of Supernova Remnant Shocks'. In: *The Astrophysical Journal* 684.2 (2008), p. 1174. DOI: 10.1086/590054 (cited on page 30).

[125] Martin Pohl. 'Time-dependent treatment of cosmic-ray spectral steepening due to turbulence driving'. In: *The Astrophysical Journal* 921.2 (2021), p. 121 (cited on page 30).

[126] Tsuyoshi Inoue et al. 'Direct Numerical Simulations of Cosmic-ray Acceleration at Dense Circumstellar Medium: Magnetic-field Amplification and Maximum Energy'. In: *The Astrophysical Journal* 922.1 (2021), p. 7. DOI: 10.3847/1538-4357/ac21ce (cited on page 30).

[127] Elena Amato and Pasquale Blasi. 'Non-linear particle acceleration at non-relativistic shock waves in the presence of self-generated turbulence'. In: *Monthly Notices of the Royal Astronomical Society* 371.3 (2006), pp. 1251–1258 (cited on page 30).

[128] V. N. Zirakashvili and V. S. Ptuskin. 'Diffusive Shock Acceleration with Magnetic Amplification by Nonresonant Streaming Instability in Supernova Remnants'. In: *The Astrophysical Journal* 678.2 (2008), p. 939. DOI: 10.1086/529580 (cited on page 30).

[129] Martin C. Weisskopf et al. 'Chandra X-ray Observatory (CXO): overview'. In: *X-Ray Optics, Instruments, and Missions III*. Ed. by Joachim E. Truemper and Bernd Aschenbach. Vol. 4012. Society of Photo-Optical Instrumentation Engineers (SPIE) Conference Series. July 2000, pp. 2–16. DOI: 10.1117/12.391545 (cited on page 30).

[130] W. B. Atwood et al. 'The Large Area Telescope on the Fermi Gamma-Ray Space Telescope Mission'. In: 697.2 (June 2009), pp. 1071–1102. DOI: 10.1088/0004-637X/697/2/1071 (cited on page 30).

[131] F. Aharonian et al. 'First ground-based measurement of atmospheric Cherenkov light from cosmic rays'. In: 75.4, 042004 (Feb. 2007), p. 042004. DOI: 10.1103/PhysRevD.75.042004 (cited on page 30).

[132] H Salazar and L Villasenor. 'Ground detectors for the study of cosmic ray showers'. In: *Journal of Physics: Conference Series* 116.1 (2008), p. 012008. DOI: 10.1088/1742-6596/116/1/012008 (cited on page 30).

[133] Stephen P. Reynolds. 'Models of Synchrotron X-Rays from Shell Supernova Remnants'. In: *The Astrophysical Journal* 493.1 (1998), p. 375. DOI: 10.1086/305103 (cited on page 30).

[134] Kazimierz J Borkowski et al. 'Thermal and nonthermal X-ray emission in supernova remnant RCW 86'. In: *The Astrophysical Journal* 550.1 (2001), p. 334 (cited on page 30).

[135] GEORGE R. BLUMENTHAL and ROBERT J. GOULD. 'Bremsstrahlung, Synchrotron Radiation, and Compton Scattering of High-Energy Electrons Traversing Dilute Gases'. In: *Rev. Mod. Phys.* 42 (2 Apr. 1970), pp. 237–270. DOI: 10.1103/RevModPhys.42.237 (cited on page 31).

[136] Julian Schwinger. 'Quantum Electrodynamics. III. The Electromagnetic Properties of the Electron—Radiative Corrections to Scattering'. In: *Phys. Rev.* 76 (6 Sept. 1949), pp. 790–817. DOI: 10.1103/PhysRev.76.790 (cited on pages 31, 32).

[137] V Domček et al. 'Mapping the spectral index of Cas A: evidence for flattening from radio to infrared'. In: *arXiv preprint arXiv:2005.12677* (2020) (cited on pages 32, 80).

[138] P. S. Coppi and R. D. Blandford. 'Reaction rates and energy distributions for elementary processes in relativistic pair plasmas'. In: 245.3 (Aug. 1990), pp. 453–453. DOI: 10.1093/mnras/245.3.453 (cited on page 32).

[139] Troy A Porter, Igor V Moskalenko, and Andrew W Strong. 'Inverse compton emission from galactic supernova remnants: effect of the interstellar radiation field'. In: *The Astrophysical Journal* 648.1 (2006), p. L29 (cited on pages 33, 100).

[140] JA Hinton and W Hofmann. 'Teraelectronvolt astronomy'. In: *Annual Review of Astronomy and Astrophysics* 47 (2009), pp. 523–565 (cited on page 34).

[141] L O'C Drury, FA Aharonian, and HJ Völk. 'The gamma-ray visibility of supernova remnants: a test of cosmic ray origin'. In: *arXiv preprint astro-ph/9305037* (1993) (cited on page 34).

[142] Szécsi, Dorottya et al. 'Low-metallicity massive single stars with rotation - Evolutionary models applicable to I Zwicky'. In: *A&A* 581 (2015), A15. DOI: 10.1051/0004-6361/201526617 (cited on page 34).

[143] Maulik Bhatt et al. 'Production of secondary particles in heavy nuclei interactions in supernova remnants'. In: *Astroparticle Physics* 123 (Dec. 2020), p. 102490. DOI: 10.1016/j.astropartphys.2020.102490 (cited on pages 34, 35, 78).

[144] Manami Sasaki. 'Multi-Wavelength View of Supernova Remnants'. In: *Acta Polytechnica CTU Proceedings* 1 (Dec. 2014), pp. 194–199. DOI: 10.14311/APP.2014.01.0194 (cited on page 36).

[145] M. Ackermann et al. 'Detection of the Characteristic Pion-Decay Signature in Supernova Remnants'. In: *Science* 339.6121 (Feb. 2013), pp. 807–811. DOI: 10.1126/science.1231160 (cited on page 36).

[146] Takanobu Amano and Masahiro Hoshino. 'ELECTRON SHOCK SURFING ACCELERATION IN MULTIDIMENSIONS: TWO-DIMENSIONAL PARTICLE-IN-CELL SIMULATION OF COLLISIONLESS PERPENDICULAR SHOCK'. In: *The Astrophysical Journal* 690.1 (2008), p. 244. DOI: 10.1088/0004-637X/690/1/244 (cited on page 37).

[147] Takayuki Umeda, Masahiro Yamao, and Ryo Yamazaki. 'ELECTRON ACCELERATION AT A LOW MACH NUMBER PERPENDICULAR COLLISIONLESS SHOCK'. In: *The Astrophysical Journal* 695.1 (2009), p. 574. DOI: 10.1088/0004-637X/695/1/574 (cited on page 37).

[148] A Marcowith et al. 'The microphysics of collisionless shock waves'. In: *Reports on Progress in Physics* 79.4 (2016), p. 046901. DOI: 10.1088/0034-4885/79/4/046901 (cited on page 37).

[149] M. Pohl, M. Hoshino, and J. Niemiec. 'PIC simulation methods for cosmic radiation and plasma instabilities'. In: *Progress in Particle and Nuclear Physics* 111, 103751 (Mar. 2020), p. 103751. DOI: 10.1016/j.ppnp.2019.103751 (cited on page 37).

[150] C. K. Birdsall and A. B. Langdon. *Plasma Physics via Computer Simulation*. 1991 (cited on page 37).

[151] Mario Riquelme and Anatoly Spitkovsky. 'Electron Injection by Whistler Waves in Non-relativistic Shocks'. In: *The Astrophysical Journal* 733 (Sept. 2010). DOI: 10.1088/0004-637X/733/1/63 (cited on page 38).

[152] D. Caprioli and A. Spitkovsky. 'Simulations of Ion Acceleration at Non-relativistic Shocks. I. Acceleration Efficiency'. In: 783.2, 91 (Mar. 2014), p. 91. DOI: 10.1088/0004-637X/783/2/91 (cited on page 38).

[153] Allard Jan van Marle, Fabien Casse, and Alexandre Marcowith. 'On magnetic field amplification and particle acceleration near non-relativistic astrophysical shocks: particles in MHD cells simulations'. In: *Monthly Notices of the Royal Astronomical Society* 473.3 (2018), pp. 3394–3409 (cited on page 38).

[154] Allard Jan van Marle et al. 'Diffusive Shock Acceleration at Oblique High Mach Number Shocks'. In: *The Astrophysical Journal* 929.1 (2022), p. 7. DOI: 10.3847/1538-4357/ac5962 (cited on page 38).

[155] Naveen Kumar and Brian Reville. 'Nonthermal Particle Acceleration at Highly Oblique Nonrelativistic Shocks'. In: *The Astrophysical Journal Letters* 921.1 (2021), p. L14 (cited on page 38).

[156] C. Pfrommer et al. 'Simulating cosmic ray physics on a moving mesh'. In: 465.4 (Mar. 2017), pp. 4500–4529. DOI: 10.1093/mnras/stw2941 (cited on page 38).

[157] M Pais et al. 'The effect of cosmic ray acceleration on supernova blast wave dynamics'. In: *Monthly Notices of the Royal Astronomical Society* 478.4 (May 2018), pp. 5278–5295. DOI: 10.1093/mnras/sty1410 (cited on page 38).

[158] Matteo Pais et al. 'Constraining the coherence scale of the interstellar magnetic field using TeV gamma-ray observations of supernova remnants'. In: *Monthly Notices of the Royal Astronomical Society* 496.2 (June 2020), pp. 2448–2461. DOI: 10.1093/mnras/staa1678 (cited on page 38).

[159] Vladimir Ptuskin, Vladimir Zirakashvili, and Eun-Suk Seo. 'SPECTRUM OF GALACTIC COSMIC RAYS ACCELERATED IN SUPERNOVA REMNANTS'. In: *The Astrophysical Journal* 718.1 (2010), p. 31. DOI: 10.1088/0004-637X/718/1/31 (cited on page 39).

[160] V. N. Zirakashvili and V. S. Ptuskin. 'Numerical simulations of diffusive shock acceleration in SNRs'. In: *Astroparticle Physics* 39 (Dec. 2012), pp. 12–21. DOI: 10.1016/j.astropartphys.2011.09.003 (cited on page 39).

[161] Telezhinsky, I., Dwarkadas, V. V., and Pohl, M. 'Time-dependent escape of cosmic rays from supernova remnants, and their interaction with dense media'. In: *A&A* 541 (2012), A153. DOI: 10.1051/0004-6361/201118639 (cited on page 39).

[162] I Telezhinsky, VV Dwarkadas, and M Pohl. 'Acceleration of cosmic rays by young core-collapse supernova remnants'. In: *Astronomy & Astrophysics* 552 (2013), A102 (cited on pages 39, 49, 50, 67, 78, 101).

[163] Jonathan E. Guyer, Daniel Wheeler, and James A. Warren. 'FiPy: Partial Differential Equations with Python'. In: *Computing in Science and Engineering* 11.3 (May 2009), pp. 6–15. DOI: 10.1109/MCSE.2009.52 (cited on pages 39, 49).

[164] Christine M. Simpson et al. 'The Role of Cosmic-Ray Pressure in Accelerating Galactic Outflows'. In: 827.2, L29 (Aug. 2016), p. L29. DOI: 10.3847/2041-8205/827/2/L29 (cited on page 41).

[165] P Blasi, Stefano Gabici, and Giulia Vannoni. 'On the role of injection in kinetic approaches to non-linear particle acceleration at non-relativistic shock waves'. In: *Monthly Notices of the Royal Astronomical Society* 361.3 (2005), pp. 907–918 (cited on page 41).

[166] M Pohl. 'On the predictive power of the minimum energy condition. I-Isotropic steady-state configurations'. In: *Astronomy and Astrophysics* 270 (1993), pp. 91–101 (cited on page 42).

[167] Donald P. Cox. 'Cooling and Evolution of a Supernova Remnant'. In: 178 (Nov. 1972), pp. 159–168. DOI: 10.1086/151775 (cited on page 42).

[168] Randall J. LeVeque. *Finite Volume Methods for Hyperbolic Problems*. Cambridge Texts in Applied Mathematics. Cambridge University Press, 2002 (cited on page 42).

[169] Eleuterio Toro. 'Riemann Solvers and Numerical Methods for Fluid Dynamics: A Practical Introduction'. In: Jan. 2009. DOI: 10.1007/b79761 (cited on page 42).

[170] Sergei Konstantinovich Godunov. 'A difference method for the numerical computation of discontinuous solutions of hydrodynamic equations'. In: *Math. Sbornik* 47.89 (1959), pp. 271–306 (cited on page 43).

[171] Florian Haider, Bernard Courbet, and Jean-Pierre Croisille. 'A high-order interpolation for the finite volume method: The Coupled Least Squares reconstruction'. In: *Computers Fluids* 176 (2018), pp. 20–39. DOI: https://doi.org/10.1016/j.compfluid.2018.09.009 (cited on page 43).

[172] Guang-Shan Jiang and Chi-Wang Shu. 'Efficient Implementation of Weighted ENO Schemes'. In: *Journal of Computational Physics* 126.1 (1996), pp. 202–228. DOI: https://doi.org/10.1006/jcph.1996.0130 (cited on page 44).

[173] 'Restoration of the contact surface in the HLL-Riemann solver'. In: *Shock waves* 4 (1994), pp. 25–34 (cited on page 45).

[174] Antony Jameson, Wolfgang Schmidt, and Eli Turkel. 'Numerical Solution of the Euler Equations by Finite Volume Methods Using Runge-Kutta Time Stepping Schemes'. In: *AIAA Paper* 81 (July 1981). DOI: 10.2514/6.1981-1259 (cited on page 45).

[175] R. Courant, K. Friedrichs, and H. Lewy. 'On the Partial Difference Equations of Mathematical Physics'. In: *IBM Journal of Research and Development* 11 (Mar. 1967), pp. 215–234. DOI: 10.1147/rd.112.0215 (cited on page 45).

[176] David Gottlieb and Chi-Wang Shu. 'On the Gibbs Phenomenon and its Resolution'. In: *SIAM Review* 39.4 (1997), pp. 644–668. (Visited on 04/03/2023) (cited on page 45).

[177] Robert Brose. 'From dawn till dusk : modelling particle acceleration in supernova remnants'. PhD thesis. Potsdam U., 2020. DOI: 10.25932/publishup-47086 (cited on page 45).

[178] Daniel Whalen et al. 'The destruction of cosmological minihalos by primordial supernovae'. In: *The Astrophysical Journal* 682.1 (2008), p. 49 (cited on page 47).

[179] Marcowith, A. and Casse, F. 'Postshock turbulence and diffusive shock acceleration in young supernova remnants'. In: *A&A* 515 (2010), A90. DOI: 10.1051/0004-6361/200913022 (cited on page 48).

[180] Martin Pohl, Huirong Yan, and Alexander Lazarian. 'Magnetically limited X-ray filaments in young supernova remnants'. In: *The Astrophysical Journal* 626.2 (2005), p. L101 (cited on pages 48, 53).

[181] Sushch, Iurii, Brose, Robert, and Pohl, Martin. 'Modeling of the spatially resolved nonthermal emission from the Vela Jr. supernova remnant'. In: *A&A* 618 (2018), A155. DOI: 10.1051/0004-6361/201832879 (cited on page 49).

[182] Robert Brose, Igor Telezhinsky, and Martin Pohl. 'Transport of magnetic turbulence in supernova remnants'. In: *Astronomy & Astrophysics* 593 (2016), A20 (cited on pages 51, 88).

[183] A. N. Kolmogorov. 'Dissipation of Energy in the Locally Isotropic Turbulence'. In: *Proceedings: Mathematical and Physical Sciences* 434.1890 (1991), pp. 15–17. (Visited on 04/05/2023) (cited on page 51).

[184] Lewis Fry Richardson and Peter Lynch. *Weather Prediction by Numerical Process*. 2nd ed. Cambridge Mathematical Library. Cambridge University Press, 2007 (cited on page 51).

[185] Ye Zhou and William H. Matthaeus. 'Models of inertial range spectra of interplanetary magnetohydrodynamic turbulence'. In: *Journal of Geophysical Research: Space Physics* 95.A9 (1990), pp. 14881–14892. DOI: https://doi.org/10.1029/JA095iA09p14881 (cited on page 51).

[186] Reinhard Schlickeiser. *Cosmic Ray Astrophysics*. 2002 (cited on page 51).

[187] E. Amato and P. Blasi. 'A kinetic approach to cosmic-ray-induced streaming instability at supernova shocks'. In: 392.4 (Feb. 2009), pp. 1591–1600. DOI: 10.1111/j.1365-2966.2008.14200.x (cited on page 52).

[188] J. Skilling. 'Cosmic ray streaming - I. Effect of Alfvén waves on particles.' In: 172 (Sept. 1975), pp. 557–566. DOI: 10.1093/mnras/172.3.557 (cited on page 52).

[189] Brose, R., Pohl, M., and Sushch, I. 'Morphology of supernova remnants and their halos'. In: *A&A* 654 (2021), A139. DOI: 10.1051/0004-6361/202141194 (cited on pages 52, 72, 92, 105, 109).

[190] Alexandre Marcowith et al. 'Core-collapse supernovae as cosmic ray sources'. In: *Monthly Notices of the Royal Astronomical Society* 479.4 (2018), pp. 4470–4485 (cited on page 53).

[191] Robert Brose, Iurii Sushch, and Jonathan Mackey. 'Core-collapse supernovae in dense environments–particle acceleration and non-thermal emission'. In: *Monthly Notices of the Royal Astronomical Society* 516.1 (2022), pp. 492–505 (cited on page 53).

[192] James Threlfall, Ken Mcclements, and I. De Moortel. 'Alfvèn wave phase-mixing and damping in the ion cyclotron range of frequencies'. In: *Astronomy and Astrophysics* 525 (July 2010). DOI: 10.1051/0004-6361/201015479 (cited on page 53).

[193] Russell Kulsrud and William P. Pearce. 'The Effect of Wave-Particle Interactions on the Propagation of Cosmic Rays'. In: 156 (May 1969), p. 445. DOI: 10.1086/149981 (cited on page 53).

[194] F. -K. Thielemann et al. 'Massive Stars and Their Supernovae'. In: *Lecture Notes in Physics, Berlin Springer Verlag*. Ed. by Roland Diehl, Dieter H. Hartmann, and Nikos Prantzos. Vol. 812. 2011, pp. 153–232 (cited on page 53).

[195] P. O. Lagage and C. J. Cesarsky. 'The maximum energy of cosmic rays accelerated by supernova shocks'. In: *Astron. Astrophys.* 125 (1983), pp. 249–257 (cited on page 54).

[196] KM Schure et al. 'Time-dependent particle acceleration in supernova remnants in different environments'. In: *Monthly Notices of the Royal Astronomical Society* 406.4 (2010), pp. 2633–2649 (cited on page 54).

[197] Telezhinsky, I., Dwarkadas, V. V., and Pohl, M. 'Time-dependent escape of cosmic rays from supernova remnants, and their interaction with dense media'. In: *A&A* 541 (2012), A153. DOI: 10.1051/0004-6361/201118639 (cited on page 55).

[198] Vikram V. Dwarkadas. 'The Evolution of Supernovae in Circumstellar Wind-Blown Bubbles. I. Introduction and One-Dimensional Calculations'. In: 630.2 (Sept. 2005), pp. 892–910. DOI: 10.1086/432109 (cited on pages 55, 67, 87).

[199] Iurii Sushch et al. 'Leptonic Nonthermal Emission from Supernova Remnants Evolving in the Circumstellar Magnetic Field'. In: *The Astrophysical Journal* 926.2 (2022), p. 140. DOI: 10.3847/1538-4357/ac3cb8 (cited on pages 62, 67, 87).

[200] Tomoyuki Okuno et al. 'Time Variability of Nonthermal X-Ray Stripes in Tycho's Supernova Remnant with Chandra'. In: *The Astrophysical Journal* 894.1 (2020), p. 50. DOI: 10.3847/1538-4357/ab837e (cited on page 62).

[201] T. Vieu, S. Gabici, and V. Tatischeff. 'Particle acceleration at colliding shock waves'. In: 494.3 (Apr. 2020), pp. 3166–3176. DOI: 10.1093/mnras/staa799 (cited on page 62).

[202] Samata Das et al. 'Spectral softening in core-collapse supernova remnant expanding inside wind-blown bubble'. In: *Astronomy & Astrophysics* 661 (2022), A128 (cited on pages 67, 119).

[203] W. Baade and F. Zwicky. 'Cosmic Rays from Super-novae'. In: *Proceedings of the National Academy of Science* 20.5 (May 1934), pp. 259–263. DOI: 10.1073/pnas.20.5.259 (cited on page 67).

[204] Donald C. Ellison, Luke O'C. Drury, and Jean-Paul Meyer. 'Galactic Cosmic Rays from Supernova Remnants. II. Shock Acceleration of Gas and Dust'. In: 487.1 (Sept. 1997), pp. 197–217. DOI: 10.1086/304580 (cited on page 67).

[205] V. A. Acciari et al. 'Observation of Extended Very High Energy Emission from the Supernova Remnant IC 443 with VERITAS'. In: 698.2 (June 2009), pp. L133–L137. DOI: 10.1088/0004-637X/698/2/L133 (cited on page 67).

[206] A. A. Abdo et al. 'Fermi-Lat Discovery of GeV Gamma-Ray Emission from the Young Supernova Remnant Cassiopeia A'. In: 710.1 (Feb. 2010), pp. L92–L97. DOI: 10.1088/2041-8205/710/1/L92 (cited on page 67).

[207] F. Acero et al. 'First detection of VHE gamma-rays from SN 1006 by HESS'. In: *Astronomy Astrophysics, v.516, 1-7 (2010)* (Jan. 2010) (cited on page 67).

[208] V. A. Acciari et al. 'Discovery of TeV Gamma-ray Emission from Tycho's Supernova Remnant'. In: 730.2, L20 (Apr. 2011), p. L20. DOI: 10.1088/2041-8205/730/2/L20 (cited on page 67).

[209] Martina Cardillo, Elena Amato, and Pasquale Blasi. 'Supernova remnant W44: a case of cosmic-ray reacceleration'. In: *Astronomy & Astrophysics* 595 (2016), A58 (cited on page 67).

[210] Emma de Oña Wilhelmi et al. 'SNR G39.2-0.3, an hadronic cosmic rays accelerator'. In: 497.3 (Sept. 2020), pp. 3581–3590. DOI: 10.1093/mnras/staa2045 (cited on page 67).

[211] Pohl, M., Wilhelm, A., and Telezhinsky, I. 'Reacceleration of electrons in supernova remnants'. In: *A&A* 574 (2015), A43. DOI: 10.1051/0004-6361/201425027 (cited on page 67).

[212] Damiano Caprioli, Colby C. Haggerty, and Pasquale Blasi. 'Kinetic Simulations of Cosmic-Ray-modified Shocks. II. Particle Spectra'. In: 905.1, 2 (Dec. 2020), p. 2. DOI: 10.3847/1538-4357/abbe05 (cited on page 67).

[213] Vikram V. Dwarkadas. 'The Evolution of Supernovae in Circumstellar Wind Bubbles. II. Case of a Wolf-Rayet Star'. In: 667.1 (Sept. 2007), pp. 226–247. DOI: 10.1086/520670 (cited on pages 67, 87, 89).

[214] VS Berezinskii and VS Ptuskin. 'Radiation from young SN II shells produced by cosmic rays accelerated in shock waves'. In: *Astronomy and Astrophysics* 215 (1989), pp. 399–408 (cited on page 67).

[215] Evgeny G Berezhko and Heinrich J Völk. 'Kinetic theory of cosmic ray and gamma-ray production in supernova remnants expanding into wind bubbles'. In: *arXiv preprint astro-ph/0002411* (2000) (cited on pages 67, 84).

[216] Zachary G. Jennings et al. 'The Supernova Progenitor Mass Distributions of M31 and M33: Further Evidence for an Upper Mass Limit'. In: 795.2, 170 (Nov. 2014), p. 170. DOI: 10.1088/0004-637X/795/2/170 (cited on page 68).

[217] Groh, Jose H. et al. 'The evolution of massive stars and their spectra - I. A non-rotating 60 Mar from the zero-age main sequence to the pre-supernova stage'. In: *A&A* 564 (2014), A30. DOI: 10.1051/0004-6361/201322573 (cited on page 69).

[218] DM-A Meyer et al. 'Models of the circumstellar medium of evolving, massive runaway stars moving through the Galactic plane'. In: *Monthly Notices of the Royal Astronomical Society* 444.3 (2014), pp. 2754–2775 (cited on page 69).

[219] N. G. Bochkarev. 'Book Review: D. E. Osterbrock Astrophysics of Gaseous Nebulae and Active Galactic Nuclei'. In: 33 (Dec. 1989), p. 694 (cited on page 69).

[220] Robert PC Wiersma, Joop Schaye, and Britton D Smith. 'The effect of photoionization on the cooling rates of enriched, astrophysical plasmas'. In: *Monthly Notices of the Royal Astronomical Society* 393.1 (2009), pp. 99–107 (cited on page 69).

[221] D. M. -A. Meyer, M. Petrov, and M. Pohl. 'Wind nebulae and supernova remnants of very massive stars'. In: 493.3 (Apr. 2020), pp. 3548–3564. DOI: 10.1093/mnras/staa554 (cited on page 70).

[222] J. Mackey, S. Green, and M. Moutzouri. 'Simulations of Magnetised Stellar-Wind Bubbles'. In: *Journal of Physics Conference Series*. Vol. 1620. Journal of Physics Conference Series. Sept. 2020, 012012, p. 012012. DOI: 10.1088/1742-6596/1620/1/012012 (cited on page 70).

[223] J. P. Cassinelli. 'Wolf-Rayet Stellar Wind Theory (review)'. In: *Wolf-Rayet Stars and Interrelations with Other Massive Stars in Galaxies*. Ed. by Karel A. van der Hucht and Bambang Hidayat. Vol. 143. Jan. 1991, p. 289 (cited on page 71).

[224] R. Ignace, J. P. Cassinelli, and J. E. Bjorkman. '"WCFields": A Magnetic Rotating Stellar Wind Model from Wind Compression Theory'. In: 505.2 (Oct. 1998), pp. 910–920. DOI: 10.1086/306189 (cited on page 71).

[225] Roger A. Chevalier and D. Luo. 'Magnetic shaping of planetary nebulae and other stellar wind bubbles'. In: *The Astrophysical Journal* 421 (1994), pp. 225–235 (cited on page 71).

[226] G. Garcı–a-Segura et al. 'Hydrodynamics of ring nebulae: magnetic vs. non-magnetic hydro-models'. In: *Wolf-Rayet Phenomena in Massive Stars and Starburst Galaxies*. Ed. by Karel A. van der Hucht, Gloria Koenigsberger, and Philippe R. J. Eenens. Vol. 193. Jan. 1999, p. 325 (cited on page 71).

[227] Tsuyoshi Inoue et al. 'Direct Numerical Simulations of Cosmic-ray Acceleration at Dense Circumstellar Medium: Magnetic-field Amplification and Maximum Energy'. In: 922.1, 7 (Nov. 2021), p. 7. DOI: 10.3847/1538-4357/ac21ce (cited on page 71).

[228] Paul A Crowther. 'Physical properties of Wolf-Rayet stars'. In: *Annu. Rev. Astron. Astrophys.* 45 (2007), pp. 177–219 (cited on page 71).

[229] R. Ignace, J. P. Cassinelli, and J. E. Bjorkman. 'Equatorial Wind Compression Effects across the H-R Diagram'. In: 459 (Mar. 1996), p. 671. DOI: 10.1086/176932 (cited on page 71).

[230] A. -N. Chené and N. St-Louis. 'Large-scale Periodic Variability of the Wind of the Wolf-Rayet Star WR 1 (HD 4004)'. In: 716.2 (June 2010), pp. 929–941. DOI: 10.1088/0004-637X/716/2/929 (cited on page 71).

[231] Allard Jan van Marle, Zakaria Meliani, and Alexandre Marcowith. 'Shape and evolution of wind-blown bubbles of massive stars: on the effect of the interstellar magnetic field'. In: *Astronomy & Astrophysics* 584 (2015), A49 (cited on page 71).

[232] Kazimierz Borkowski et al. 'A Circumstellar Shell Model for the Cassiopeia A Supernova Remnant'. In: 466 (Aug. 1996), p. 866. DOI: 10.1086/177560 (cited on page 77).

[233] Ellison, D. C., Decourchelle, A., and Ballet, J. 'Nonlinear particle acceleration at reverse shocks in supernova remnants'. In: *A&A* 429.2 (2005), pp. 569–580. DOI: 10.1051/0004-6361:20041668 (cited on page 77).

[234] V. N. Zirakashvili et al. 'Nonthermal Radiation of Young Supernova Remnants: The Case of CAS A'. In: 785.2, 130 (Apr. 2014), p. 130. DOI: 10.1088/0004-637X/785/2/130 (cited on page 77).

[235] Donald Ellison. 'Photons and Particle Production in Cassiopeia A: Predictions from Nonlinear Diffusive Shock Acceleration'. In: *26th International Cosmic Ray Conference (ICRC26), Volume 3*. Vol. 3. International Cosmic Ray Conference. Aug. 1999, p. 468 (cited on page 78).

[236] Jun Fang et al. 'Gamma-ray properties of supernova remnants transporting into molecular clouds: the cases of IC 443 and W44'. In: *Monthly Notices of the Royal Astronomical Society* 435.1 (Aug. 2013), pp. 570–574. DOI: 10.1093/mnras/stt1318 (cited on pages 78, 105, 107).

[237] S Federici et al. 'Analysis of GeV-band gamma-ray emission from SNR RX J1713. 7-3946'. In: *arXiv preprint arXiv:1502.06355* (2015) (cited on page 80).

[238] Iurii Sushch, Robert Brose, and Martin Pohl. 'Modeling of the spatially resolved nonthermal emission from the Vela Jr. supernova remnant'. In: *Astronomy Astrophysics* 618 (Aug. 2018). DOI: 10.1051/0004-6361/201832879 (cited on page 80).

[239] D. A. Green. 'A revised Galactic supernova remnant catalogue'. In: *Bulletin of the Astronomical Society of India* 37.1 (Mar. 2009), pp. 45–61 (cited on page 80).

[240] M. Lyutikov and M. Pohl. 'The Origin of Nonthermal X-Ray Filaments and TeV Emission in Young Supernova Remnants'. In: 609.2 (July 2004), pp. 785–796. DOI: 10.1086/421290 (cited on page 81).

[241] Fraschetti, F. et al. 'Simulation of the growth of the 3D Rayleigh-Taylor instability in supernova remnants using an expanding reference frame'. In: *A&A* 515 (2010), A104. DOI: 10.1051/0004-6361/200912692 (cited on page 83).

[242] Andrew W. Strong, Igor V. Moskalenko, and Olaf Reimer. 'Diffuse Continuum Gamma Rays from the Galaxy'. In: 537.2 (July 2000), pp. 763–784. DOI: 10.1086/309038 (cited on page 84).

[243] Andrew W. Strong, Igor V. Moskalenko, and Vladimir S. Ptuskin. 'Cosmic-Ray Propagation and Interactions in the Galaxy'. In: *Annual Review of Nuclear and Particle Science* 57.1 (Nov. 2007), pp. 285–327. DOI: 10.1146/annurev.nucl.57.090506.123011 (cited on page 84).

[244] Yutaka Ohira, Toshio Terasawa, and Fumio Takahara. 'Plasma Instabilities as a Result of Charge Exchange in the Downstream Region of Supernova Remnant Shocks'. In: 703.1 (Sept. 2009), pp. L59–L62. DOI: 10.1088/0004-637X/703/1/L59 (cited on page 84).

[245] Yutaka Ohira and Fumio Takahara. 'Effects of Neutral Particles on Modified Shocks at Supernova Remnants'. In: 721.1 (Sept. 2010), pp. L43–L47. DOI: 10.1088/2041-8205/721/1/L43 (cited on page 84).

[246] L. O'C. Drury and J. H. Voelk. 'Hydromagnetic shock structure in the presence of cosmic rays'. In: 248 (Aug. 1981), pp. 344–351. DOI: 10.1086/159159 (cited on page 84).

[247] E. G. Berezhko and Donald C. Ellison. 'A Simple Model of Nonlinear Diffusive Shock Acceleration'. In: 526.1 (Nov. 1999), pp. 385–399. DOI: 10.1086/307993 (cited on page 84).

[248] M. A. Malkov and L. O'C. Drury. 'Nonlinear theory of diffusive acceleration of particles by shock waves'. In: *Reports on Progress in Physics* 64.4 (Apr. 2001), pp. 429–481. DOI: 10.1088/0034-4885/64/4/201 (cited on page 84).

[249] Justine Devin et al. 'High-energy gamma-ray study of the dynamically young SNR G150. 3+ 4.5'. In: *Astronomy & Astrophysics* 643 (2020), A28 (cited on page 84).

[250] Ptuskin, V. S. and Zirakashvili, V. N. 'Limits on diffusive shock acceleration in supernova remnants in the presence of cosmic-ray streaming instability and wave dissipation'. In: *A&A* 403.1 (2003), pp. 1–10. DOI: 10.1051/0004-6361:20030323 (cited on page 85).

[251] Ptuskin, V. S. and Zirakashvili, V. N. 'On the spectrum of high-energy cosmic rays produced by supernova remnants in the presence of strong cosmic-ray streaming instability and wave dissipation'. In: *A&A* 429.3 (2005), pp. 755–765. DOI: 10.1051/0004-6361:20041517 (cited on page 85).

[252] Tim Freyer, Gerhard Hensler, and Harold W. Yorke. 'Massive Stars and the Energy Balance of the Interstellar Medium. I. The Impact of an Isolated 60 M_{solar} Star'. In: 594.2 (Sept. 2003), pp. 888–910. DOI: 10.1086/376937 (cited on page 87).

[253] Vikram V. Dwarkadas. 'Ionization-Gasdynamic Simulations of Wind-Blown Nebulae around Massive Stars'. In: *Galaxies* 10.1 (Feb. 2022), p. 37. DOI: 10.3390/galaxies10010037 (cited on page 87).

[254] N Langer. 'Presupernova evolution of massive single and binary stars'. In: *Annual Review of Astronomy and Astrophysics* 50 (2012), pp. 107–164 (cited on page 87).

[255] A. C. Gormaz-Matamala et al. 'Evolution of massive stars with new hydrodynamic wind models'. In: *arXiv e-prints*, arXiv:2207.04786 (July 2022), arXiv:2207.04786 (cited on page 87).

[256] Guillermo Garcı–a-Segura, Norbert Langer, and M-M Mac Low. 'The hydrodynamic evolution of circumstellar gas around massive stars. II. The impact of the time sequence O star-> RSG-> WR star.' In: *Astronomy and Astrophysics, v. 316, p. 133-146* 316 (1996), pp. 133–146 (cited on page 87).

[257] G Garcia-Segura, M-M Mac Low, and N Langer. 'The dynamical evolution of circumstellar gas around massive stars. I. The impact of the time sequence Ostar-> LBV-> WR star.' In: *Astronomy and Astrophysics* 305 (1996), p. 229 (cited on page 87).

[258] Vikram V. Dwarkadas and Stanley P. Owocki. 'Radiatively Driven Winds and the Shaping of Bipolar Luminous Blue Variable Nebulae'. In: *The Astrophysical Journal* 581.2 (2002), pp. 1337–1343. DOI: 10.1086/344257 (cited on page 87).

[259] D M-A Meyer. 'On the bipolarity of Wolf–Rayet nebulae'. In: *Monthly Notices of the Royal Astronomical Society* 507.4 (Aug. 2021), pp. 4697–4714. DOI: 10.1093/mnras/stab2426 (cited on page 87).

[260] S. Ustamujic et al. 'Modeling the Remnants of Core-collapse Supernovae from Luminous Blue Variable stars'. In: *arXiv e-prints*, arXiv:2108.01951 (Aug. 2021), arXiv:2108.01951 (cited on page 87).

[261] R. H. D. Townsend and S. P. Owocki. 'A rigidly rotating magnetosphere model for circumstellar emission from magnetic OB stars'. In: *Monthly Notices of the Royal Astronomical Society* 357.1 (Feb. 2005), pp. 251–264. DOI: 10.1111/j.1365-2966.2005.08642.x (cited on page 87).

[262] Aimee L Hungerford, Chris L Fryer, and Gabriel Rockefeller. 'Gamma rays from single-lobe supernova explosions'. In: *The Astrophysical Journal* 635.1 (2005), p. 487 (cited on page 87).

[263] Ryosuke Kobashi, Haruo Yasuda, and Shiu-Hang Lee. 'Long-term Evolution of Nonthermal Emission from Type Ia and Core-collapse Supernova Remnants in a Diversified Circumstellar Medium'. In: *The Astrophysical Journal* 936.1 (2022), p. 26. DOI: 10.3847/1538-4357/ac80f9 (cited on page 87).

[264] André Maeder and Georges Meynet. 'Rotating massive stars: From first stars to gamma ray bursts'. In: *Rev. Mod. Phys.* 84 (1 Jan. 2012), pp. 25–63. DOI: 10.1103/RevModPhys.84.25 (cited on page 90).

[265] M Aurière et al. 'The magnetic field of Betelgeuse: a local dynamo from giant convection cells?' In: *Astronomy & Astrophysics* 516 (2010), p. L2 (cited on page 90).

[266] Benjamin Tessore et al. 'Measuring surface magnetic fields of red supergiant stars'. In: *Astronomy & Astrophysics* 603 (2017), A129 (cited on page 90).

[267] K. Brecher and G. R. Burbidge. 'Extragalactic Cosmic Rays'. In: 174 (June 1972), p. 253. DOI: 10.1086/151488 (cited on page 94).

[268] Ingo Büsching, Martin Pohl, and Reinhard Schlickeiser. 'Excess GeV radiation and cosmic ray origin'. In: *Astronomy & Astrophysics* 377.3 (2001), pp. 1056–1062 (cited on page 94).

[269] L. O'C. Drury. 'Time-dependent diffusive acceleration of test particles at shocks'. In: 251 (July 1991), pp. 340–350. DOI: 10.1093/mnras/251.2.340 (cited on page 95).

[270] Yutaka Ohira, Kohta Murase, and Ryo Yamazaki. 'Escape-limited model of cosmic-ray acceleration revisited'. In: *Astronomy & Astrophysics* 513 (2010), A17 (cited on page 97).

[271] Pierre Cristofari, Pasquale Blasi, and Elena Amato. 'The low rate of Galactic pevatrons'. In: *Astroparticle Physics* 123, 102492 (Dec. 2020), p. 102492. DOI: 10.1016/j.astropartphys.2020.102492 (cited on page 100).

[272] Markus Ackermann et al. 'Detection of the characteristic pion-decay signature in supernova remnants'. In: *Science* 339.6121 (2013), pp. 807–811 (cited on page 100).

[273] Roger A. Chevalier and Jeffrey Oishi. 'Cassiopeia A and Its Clumpy Presupernova Wind'. In: 593.1 (Aug. 2003), pp. L23–L26. DOI: 10.1086/377572 (cited on page 103).

[274] Yasunobu Uchiyama and Felix A. Aharonian. 'Fast Variability of Nonthermal X-Ray Emission in Cassiopeia A: Probing Electron Acceleration in Reverse-Shocked Ejecta'. In: 677.2 (Apr. 2008), p. L105. DOI: 10.1086/588190 (cited on page 104).

[275] L Saha et al. 'Origin of gamma-ray emission in the shell of Cassiopeia A'. In: *Astronomy & Astrophysics* 563 (2014), A88 (cited on page 104).

[276] Daniel J. Patnaude et al. 'A DECLINE IN THE NONTHERMAL X-RAY EMISSION FROM CASSIOPEIA A'. In: *The Astrophysical Journal Letters* 729.2 (2011), p. L28. DOI: 10.1088/2041-8205/729/2/L28 (cited on page 104).

[277] Cardillo, M. et al. 'The supernova remnant W44: Confirmations and challenges for cosmic-ray acceleration'. In: *A&A* 565 (2014), A74. DOI: 10.1051/0004-6361/201322685 (cited on page 105).

[278] Emma de Oña Wilhelmi et al. 'SNR G39.2–0.3, an hadronic cosmic rays accelerator'. In: *Monthly Notices of the Royal Astronomical Society* 497.3 (July 2020), pp. 3581–3590. DOI: 10.1093/mnras/staa2045 (cited on pages 105, 107).

[279] DA Green. 'A catalogue of 294 Galactic supernova remnants'. In: *arXiv preprint arXiv:1409.0637* (2014) (cited on page 107).

[280] Dejan Urošević. 'On the radio spectra of supernova remnants'. In: *Astrophysics and Space Science* 354 (2014), pp. 541–552 (cited on page 107).

[281] Qiang Yuan, Siming Liu, and Xiaojun Bi. 'An Attempt at a Unified Model for the Gamma-Ray Emission of Supernova Remnants'. In: 761.2, 133 (Dec. 2012), p. 133. DOI: 10.1088/0004-637X/761/2/133 (cited on page 109).

[282] B Perez-Rendon, G Garcia-Segura, and N Langer. 'Supernova progenitor stars in the initial range of 23 to 33 solar masses and their relation with the SNR Cas A'. In: *arXiv preprint arXiv:0905.1101* (2009) (cited on page 112).

[283] Kathryn E. Weil et al. 'Detection of the Red Supergiant Wind from the Progenitor of Cassiopeia A'. In: 891.2, 116 (Mar. 2020), p. 116. DOI: 10.3847/1538-4357/ab76bf (cited on page 112).

[284] Jacco Vink, Daniel J. Patnaude, and Daniel Castro. 'The Forward and Reverse Shock Dynamics of Cassiopeia A'. In: 929.1, 57 (Apr. 2022), p. 57. DOI: 10.3847/1538-4357/ac590f (cited on page 112).

[285] Raphael Hirschi et al. 'Stellar Evolution at Low Metallicity'. In: *Proceedings of the International Astronomical Union* 3.S250 (2007), pp. 217–230. DOI: 10.1017/S1743921308020528 (cited on page 113).

[286] Sanyal, D. et al. 'Metallicity dependence of envelope inflation in massive stars'. In: *A&A* 597 (2017), A71. DOI: 10.1051/0004-6361/201629612 (cited on page 113).

[287] Rui-zhi Yang, Felix Aharonian, and Emma de Oña Wilhelmi. 'Massive star clusters as the an alternative source population of galactic cosmic rays'. In: *Rendiconti Lincei. Scienze Fisiche e Naturali* 30 (Dec. 2019), pp. 159–164. DOI: 10.1007/s12210-019-00819-3 (cited on page 113).

[288] Gilles Maurin et al. 'Embedded star clusters as sources of high-energy cosmic rays-Modelling and constraints'. In: *Astronomy & Astrophysics* 591 (2016), A71 (cited on page 113).

[289] Sourav Bhadra et al. 'Cosmic rays from massive star clusters: a close look at Westerlund 1'. In: *Monthly Notices of the Royal Astronomical Society* 510.4 (Jan. 2022), pp. 5579–5591. DOI: 10.1093/mnras/stac023 (cited on page 113).

[290] Thibault Vieu et al. 'Cosmic ray production in superbubbles'. In: *Monthly Notices of the Royal Astronomical Society* 512.1 (2022), pp. 1275–1293 (cited on page 113).